Ferritin nanocages used as programmable bricks for biomolecular electronics

Luis Lechaptois

Sorbonne Université

Nanyang Technological University

Ecole doctoral ED 397 – Physique et Chimie des Matériaux

Institut des NanoSciences / Equipe Physico-Chimie et Dynamique des Surfaces

Ferritin nanocages used as programmable bricks for biomolecular electronics

Par Luis Lechaptois

Thèse de doctorat de Physique et Chimie des Matériaux

Dirigée par Pr. Olivier Pluchery et Pr. Sierin Lim

Présentée et soutenue publiquement le 06 Décembre 2023

Devant un jury composé de :

Rosine COQ GERMANICUS, Professeure associée, Université de Caen, Rapporteure
Sabine SZUNERITS, Professeure, Université de Lille, Rapporteure
Anna PROUST, Professeure, Sorbonne Université, Examinatrice
Shuzhou LI, Professeur associé, Nanyang Technological University, Examinateur
Sierin LIM, Professeure associée, Nanyang Technological University, Co-directrice de thèse
Olivier PLUCHERY, Professeur, Sorbonne Université, Directeur de thèse

« Au bord du texte le plus ambitieux
Que je n'ai jamais tenté
Je fais partie de ceux qui
N'ont pas peur de sauter »

- Disiz

Acknowledgements

The joint PhD project presented in this manuscript has been carried out between the Institut des NanoSciences de Paris (INSP), at Sorbonne Université, in the PHYSURF (Physico-chimie et dynamique des surfaces) group, and at the Nanyang Technological University (NTU), at the School of Chemistry, Chemical engineering and biotechnology (CCEB), in the SlimResearch Lab.

I sincerely thank Pr. Rosine Coq Germanicus and Pr. Sabine Szunerits who kindly dedicated their time reviewing this manuscript. I would also like to thank Pr. Anna Proust and Pr. Shuzhou Li for being part of my thesis committee.

I would like to express my profound gratitude to my PhD supervisors who were involved in this project and who brought me so much knowledge in these 3 years. I sincerely thank Pr. Olivier Pluchery who welcomed me to the PhD journey with patient and calmness and make me feel comfortable from the beginning. Your knowledge in gold nanoparticles, KPFM, and scientific writing was invaluable to me, and I am deeply grateful for the skills you hand down to me. I sincerely thank Pr. Sierin Lim who welcomed me with some much and kindness in Singapore. I am profoundly thankful for accompanying me along the biological knowledges which I was not familiar with. I was always impressed by your optimism and energy that you dedicated to my PhD. Thank you to the two of you for all the discussion we had to overcome the difficulties, for your open-mindedness and for all the skills you taught me.

The measurements of carried out during the whole project were possible thanks to the involvement of the following people. I sincerely thank Yoann Prado for carrying out the synthesis of the gold nanoparticles. I would like to thank the responsible of the AFM platforms Hervé Cruguel (SU) and Elaine Yao (NTU) for the formation, and Erwan Dandeu for the help on the SEM image.

During my time at NTU, the bioengineering processes were made possible thanks to the involvements of the following person. I sincerely like to thank Dr. Rupali Reddy, Dr. Sathya Moorthy Bhaskar, Tanvi Kaku and Ruoxuan Sun for teaching me all your knowledges and skills

on the production and mutations of the ferritin, and for helping me when I was at an impasse. Your help was deeply invaluable for me.

Now, I would like to thank the fellow labmates from the INSP. Very big thank to Azmat Ali, I sincerely thank you for the moments, talks and (the many) coffee breaks we had together. It was a real pleasure to have you around during this PhD. I also like to thank the fellow PhD/Master student who followed me during these 3 years: Guillaume Diot, Jean de Dieu Niyonzima, Pedro Ribeiro Silva, Frederick Johanson, Kelly Trinh, Angeline Dileseigres, Pedro Lourenço, Ayoub Badri.

I would like to thank the fellow labmates from NTU. Big shout out to Tanvi Kaku and Keerthi Pinchi for the help in the laboratory, but mostly for the special times we had together at Singapore. It was a real pleasure to discover this new city with you, and I will always remember our trip to Indonesia and Malaysia. My time at Singaore would have been completely different without you and I am really grateful for that. Also, I would like to thank all the members of the SlimResearch Lab: Sathya Moorthy Bhaskar, Rupali Reddy, Vishnu Vadanan, Usha Rani, Samuel Watts, Lui Lung Lim , Aditya Setiawibawa, Adam Abdurrahman, Haryo Himan, , Jyngyuan Wang, Chase Chow Jia Jing, Parth Rajendra. Thank you all

Last, thank you to my family and friends who supported me throughout all these 3 years, and gave me revitalising moment out of the laboratory. It was very essential to me and helped a lot to motivate me during the hardest time. I love you so much.

Thank you all for taking part in my wonderful journey.

Table of contents

Abbreviations

AFM	Atomic Force Microscopy
AfFtn	*Archaeglobus fulgidus* Ferritin
AfFtn-AA	Closed-pores *Archaeglobus fulgidus* Ferritin K150A/R151A
AfFtn-AA M0	AfFtn-AA unmutated
AfFtn-AA M3	AfFtn-AA E131K/E123K/E133K
AfFtn-AA M9	AfFtn-AA E76K/E77K/E81K/E90K/E131K/E123K/E133K/E148K/D149K
AfFtn-WT	Open-Pores Wild-Type *Archaeglobus fulgidus* Ferritin
Ala (A)	Alanine
Arg (R)	Arginine
AM	Amplitude modulation
APTES	(3-aminopropyl)triethoxysilane
AuNP	Gold nanoparticle
BSC	BioSafetyCabinet
c-AFM	Conductive Atomic Force Microscopy
CD	Circular Dichroism
CPD	Contact Potential Difference
DFOM	Dark-Field Optical Microscopy
DLS	Dynamic Light Scattering
DNA	Deoxyribonucleic Acid
dNTP	Deoxynucleotide Triphosphate
E.coli	*Escherichia coli*
EDTA	Ethylenediaminetetraacetic Acid
ELS	Electrophoresis Light Scattering
ESP	Electrostatic Surface Potential
ET	Electron Transfer
ETp	Electron Transport
FET	Field-Effect Transistor
FeNP	Iron Nanoparticle
FM	Frequency Modulation
FPLC	Fast Protein Liquid Chromatography
FTIR	Fourier Transform Infrared Spectroscopy
FZ	Float Zone
HEPES	4-(2-hydroxyethyl)-1-piperazineethanesulfonic acid
HIC	Hydrophobic Interaction Column
IEP	IsoElectric Point

ICP-MS	Inductively Coupled Plasma – Mass Spectroscopy
IPTG	Isopropyl-β-d-thiogalactopyranoside
KPFM	Kelvin Probe Force Microscopy
LB	*Luriani-Bertani* or Lysogeny Broth
LSH	Lift Scan Height
LSPR	Localized Surface Plasmon Resonance
Lys (K)	Lysine
MRI	Magnetic Resonance Imaging
M-I-M	Metal-Insulator-Metal
MOPS	3-(N-morpholino)propanesulfonic acid
MOSFET	Metal Oxide Semiconductor Field-Effect Transistor
NDR	Negative Differential Resistance
NMR	Nuclear Magnetic Resonance
n-Si	N-doped Silicon
OD	Optical Density
PB	Poisson-Boltzmann
PCR	Polymerase Chain Reaction
p-Si	P-Doped Silicon
RNA	Ribonucleic Acid
RNase	Ribonuclease
SAM	Self-Assembled Monolayer
SB	Schottky Barrier
SBH	Schottky Barrier Height
SCR	Space Charge Region
SEM	Scanning Electron Microscopy
SDM	Site-Directed Mutagenesis
SDS-PAGE	Sodium Dodecyl Sulphate-PolyAcrylamide Gel Electrophoresis
STM	Scanning Tunnelling Microscopy
STS	Scanning Tunnelling Spectroscopy
TEM	Transmission Electronic Microscopy
UV-Vis	UV-visible
VB	Valence Band
WF	Work Function
ζ	Zeta potential
ϕ	Potential

Chapter I: Overview of the project

Introduction

The first chapter introduces the topic and field of work of this thesis. First, a fairly detailed description of the protein, and in particular the ferritin protein, is given in order to help the non-biologist reader. Then, we describe the different goals, the organisation and the division of the thesis work in each chapter.

The main purpose of this thesis is the study of the electrostatic behaviour of a particular protein, the **ferritin**, known for its iron handling capacity and particular caged shape. The ferritin is produced via bioengineering tools and deposited onto a **silicon surface**. The study of this system will give us insight into the electrostatic interactions between ferritin and the surface of a solid-state electronic device such as a **transistor**. In addition, we performed a **modulation of the charge** of ferritin using **mutagenesis** tools (modification of the gene of ferritin). The ferritins were characterised in solution via **light scattering** techniques and in a dry state using the **Kelvin Probe Force Microscopy** (KPFM), which can generate topography and surface potential images of nanoparticles (NPs) on a surface. Therefore, it provides a spatial mapping of the surface and can be performed on monolayers or on individual particles. Prior to the work with ferritin, a KPFM study was carried out using gold nanoparticles (AuNPs) to mimic ferritin. This allows us to understand in detail the phenomena that are involved in the particle-silicon interaction. By KPFM measurement, the **structure** and **conformation** of the ferritin are studied, as well as the **adsorption mechanisms** of the ferritin on a solid surface. These three parameters are important to understand the electrostatic behaviour of ferritin and, moreover, understand the **charge transport mechanism** (transport of electron) across the ferritin. Finally, this study will provide strong knowledge about the possible incorporation of the ferritin protein as an electronic component that can be developed into bioinspired systems for future electronic device technology.

During the three years, the work was carried out in two different laboratories. All the bioengineering experiments and in-solution characterisation of the ferritin were carried out at the Nanyang Technological University (NTU) in Singapore. On the other side, most of the electrical characterisations of the ferritin on surfaces were carried out at the Sorbonne University (SU) in France.

1. Protein, the building block of life

Proteins are ubiquitous molecules present in all living cells and were first described in 1838 by G. J. Mulder. One century later, F. Sanger (Nobel Prize in 1958) sequenced the first protein: the insulin (a hormonal protein). He demonstrated that proteins are formed by linear polymers, or amino acid chains.[1,2] The amino acids are the building blocks of the proteins; although 300 amino acids have been listed, only 20 have a role in the protein processes (see the Appendix I-1). Each of them contains a carboxylic group (−COOH), an amino group ($-NH_2$), and a side chain that defines its function inside the protein. Some amino acid side chains bear an electrical charge at physiological pH (7.4), while others are polar or hydrophobic. The amino acids are linked together via peptide bonds (covalent bonds) to form a short chain (from 2 to 10 amino acids) called a peptide. The assemblage of peptides into a longer chain (a polypeptide) forms **the primary structure of the protein**. Driven by the residue groups, the chain arranges itself in the space along two possible conformations: in an α-helix or β-pleated sheet shape (or β-strand). This arrangement forms the **secondary structure of the protein** and involves hydrogen bonds between amino acids. The secondary structure folds through various interactions (hydrogen bonds, disulphide bonds, salt bridges) into a compact subunit to form **the tertiary structure**. This latter is, for some proteins, the final structure. However, a **quaternary structure** exists that refers to the global structure of linked subunits (Figure 1).[3] The complex process of protein folding makes them as diverse as the functions they serve. The role of proteins is mainly to effectuate every task of cellular life: cell shapes, catalysis, enzymatic behaviour, waste clean-up, and even signal receptors. The three-dimensional conformation of the protein and its interaction with neighbouring non-protein molecules define its function inside the cell. Many protein structures and functions inside cells have been widely described. An interesting property that has been attracting interests in the biomolecular electronic field is the charge transport. This thesis focuses on one particular protein: the ferritin. A description is given in the next section.

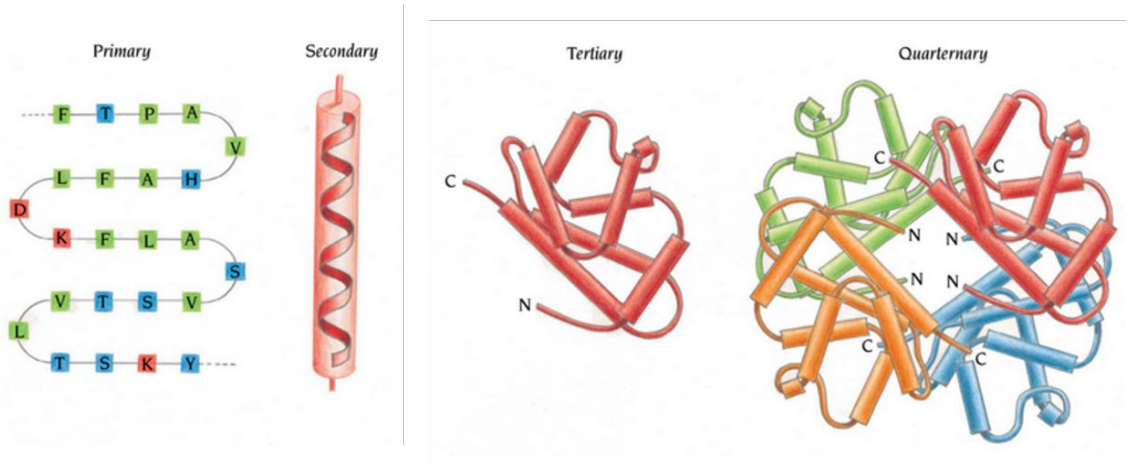

Figure 1 : The four structural levels of a protein. The amino acid sequence of the polypeptide chain of a protein is called the primary structure. The chain forms local regular secondary structures, such as α-helices or β-strands. The tertiary structure is formed by packing such structural elements into one or several compact globular units. The final protein may contain several polypeptide chains arranged in a quaternary structure.[3]

2. Ferritin: the iron-storage protein

In this part, a detailed description of the ferritin is given. The different types of ferritins, their functions, shapes and electronic properties are described. Then, we will focus more precisely on a particular ferritin extracted from the thermophilic archaea species *Archaeglobus fulgidus*, which was the model ferritin investigated for this thesis.

2.1. Ferritin for chemistry and for life

Ferritins are a group of large protein cages (475 kDa) first described by Laufberger in 1937.[4] They are responsible for the iron homeostasis inside many living bodies by sequestering di-iron (Fe^{2+}) via an oxidoreduction process into an oxyhydroxide mineral core ($Fe_2O_3{\cdot}H_2O$), similar to the ferrihydrite mineral, that can accommodate up to 4800 iron atoms (the amount of iron atoms inside the core is noted with the suffix -Fe, e.g., 1200Fe). A ferritin protein is formed by 24 ferritin polypeptides (called subunits) folded in a 5-α helix bundle (Figure 2.a), which self-assembles into a 12 nm highly symmetrical nanocage (Figure 2.b) with a 4, 3, 2 symmetry and an 8 nm diameter cavity. At the 3-fold symmetry axes, three subunits form hydrophilic channels (or pores) that connect the exterior (solvent) to the inner cavity and participate in the di-iron exchange. Through these pores, Fe^{2+} ions flow toward the ferroxidase centers buried inside the α-helix bundle subunits (Figure 2.c−d). Actually, there is one ferroxidase center

buried inside each subunit that binds two Fe^{2+}, which react with O_2 to form a μ-diiron ferric (Fe^{3+}-O-O-Fe^{3+}) complex that moves to the cavity surface for nucleation and formation of the core (Figure 2.e). At the 4-fold symmetry axes, four subunits form hydrophobic channels that might transport protons but do not seem to be involved in ion exchange.[5]

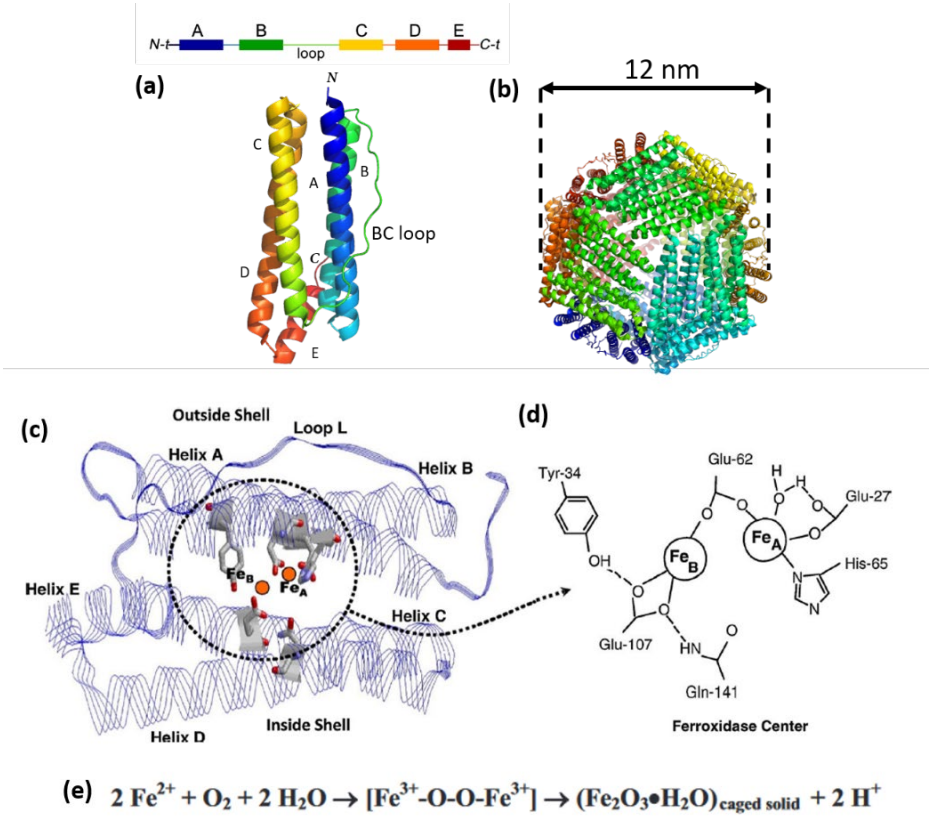

Figure 2: Structural aspects of the ferritin and the ferroxidase center. (a) ferritin subunits folded in a 5-α helix bundle. (b) 24 ferritin subunits self-assemble into a 12 nm nanocage, shown here from the 3-fold axis view. (c) schematic of the ferroxidase center inside an α-helix bundle subunit. (d) highlights of the residues forming the ferroxidase center. (e) the oxidation reaction occurring at the ferroxidase center.[6,7]

The ferritin protein is found in many species, such as archaea, plants, bacteria, and animals. Its major role is to concentrate the iron inside its inner cavity in a safe form and make it available when needed. For instance, iron from the ferritin can be released for the synthesis of proteins with an iron cofactor, like the porphyrin molecule inside the azurin or the cytochrome c. Numerous mechanisms explain the release of iron from the mineral core, which appears to be mainly driven by a reduction process followed by Fe^{2+} exit through the 3-fold axes.[8] However, the *in vivo* process is still under investigation. Moreover, ferritin also acts as an antioxidant: by

retrieving iron released from proteins, it hinders the potential spontaneous Fe^{2+} oxidation that donates single electrons to transform reactive oxygen species (e.g., H_2O_2) into highly toxic radicals. The DNA-binding proteins from starved cells (called Dps) are a class of "mini-ferritin" formed by 12 self-assembled subunits, with a 9 nm diameter. Their only function is to detoxify cells through di-iron sequestration and H_2O_2 removal. They usually move to the nucleus of the cell for DNA protection.[9]

Since the last decades, *in* vitro ferritin proteins have been used in various fields such as nanomaterials, nanoparticle templating, imaging, and drug delivery. In fact, ferritins are water-soluble molecules but can also be stabilized in organic solvents (toluene, dichloromethane). At neutral pH, its external surface has a net negative surface charge due to the distribution of amino acids in the shell, which can be modified for different applications. Furthermore, the hollow cavity of the ferritin can host inorganic nanoparticles, alongside iron, in a controlled amount. From the different types of ferritin, depending on which species it is extracted, ferritin presents different thermal and chemical stability. All these features have made the ferritin protein a good candidate for nanochemistry and technology. Ferritin has been widely used as a template for nanoparticle (NP) synthesis as it can incorporate a variety of metals (Fe, Au, Pd, Pt, Ni, Zn, Cu, Rh, Pd, Cr, Ti, Tb, and Co), and several works showed immobilization of ferritins on various substrates to produce a size-controlled array of NPs after removing the amino acid shell by heat treatment (Figure 3.a).[10,11] The inner cavity of the ferritin can also be used to trap various drugs, imaging agents or radionuclides, as well as its external surface, onto which specific ligands or peptides are attached for targeted drug delivery. The introduction of drugs is realized by the disassembly of the cage at low pH and its reassembly at neutral pH (Figure 3.b).[12] Moreover, ferritin is used for applications such as magnetic resonance imaging (MRI) contrast agents since ferritin is superparamagnetic, and catalysis applications (Figure 3.c−d).[13,14] The ferritin superfamily is composed of numerous types of ferritin with different properties that can be used for different applications. In this thesis, we chose to focus on the ferritin from the thermophilic archaea specie *Archaeglobus fulgidus* (designated AfFtn). This particular ferritin is described in the next part.

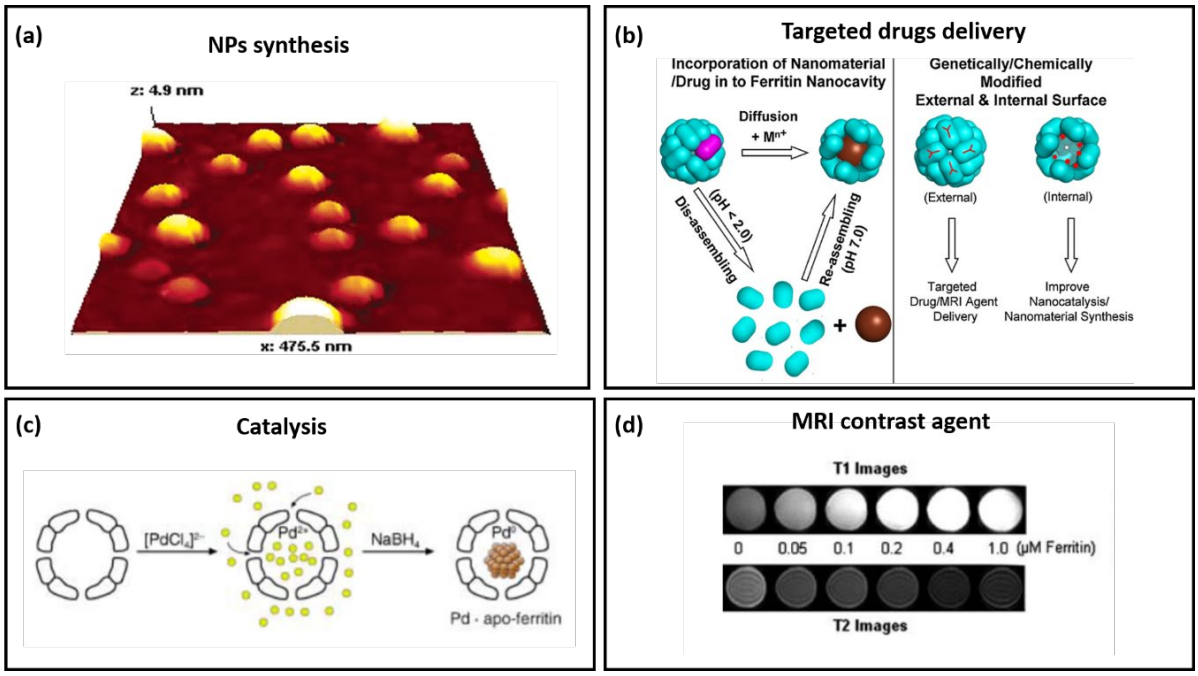

Figure 3 : Ferritin applications in nanotechnology. (a) AFM acoustic AC mode micrograph of FeOOH NPs prepared by UV-ozone treatment of 1000Fe loaded ferritin. (b) synthesis and incorporation of nanoparticles inside the multi-subunit ferritin nano cavity for catalysis and targeted drug delivery. (c) schematic of the preparation of Pd-apoferritin for hydrogenation catalysis. (d) images of iron loading as a contrast agent, at different concentrations.[7,10,13,14]

2.2. AfFtn-AA the thermophilic ferritin

AfFtn was extracted from the thermophilic species *Archaeglobus fulgidus*, an archaea (a prokaryote microorganism) found in hydrothermal environments such as hot springs, oil wells, and hydrothermal vents.[15] This ferritin is the only known ferritin to form a unique tetrahedral cage, which contradicts the octahedral cage of the typical ferritin. As a result of its tetrahedral 2-3 symmetry, four openings (≈ 45 Å in diameter) are formed in the cage at the 3-fold axes (Figure 4.a), and the 4-fold axe channels are absent. On each apex of these openings, there is a positive electrostatic potential due to the presence of amino acids with long and positively charged side chains: A lysine (noted Lys or K) and an arginine (noted Arg or R) at positions 150 and 151, respectively, of the primary structure of each ferritin subunit. These amino acids are designated Lys150 and Arg151. Therefore, they create steric clashes and repulsive charges that form the large openings. Sana *et al.* (2013)[16] studied the role of these two amino acids by site-directed mutagenesis, where Lys150 and Arg151 were substituted with alanine (A) amino-acids, which have short and uncharged side chains. These mutations are noted as K150A and R151A for lysine and arginine, respectively. By x-ray measurement, they showed that these

mutations trigger a symmetry switch, from tetrahedral to octahedral, and the closing of the four openings resulting from the removal of steric clashes and repulsive charges (Figure 4.b−c). The mutant closed-pore ferritin, noted AfFtn-AA (in reference to the two alanine substitutions), presents a slower reductive iron release compared to the open-pore ferritin, noted AfFtn-WT (for wild-type ferritin). During this thesis, ferritins are used at precise iron loading; the amount of iron inside the cage is an important parameter, and therefore, the AfFtn-AA was preferred to be used as a model ferritin throughout the thesis.

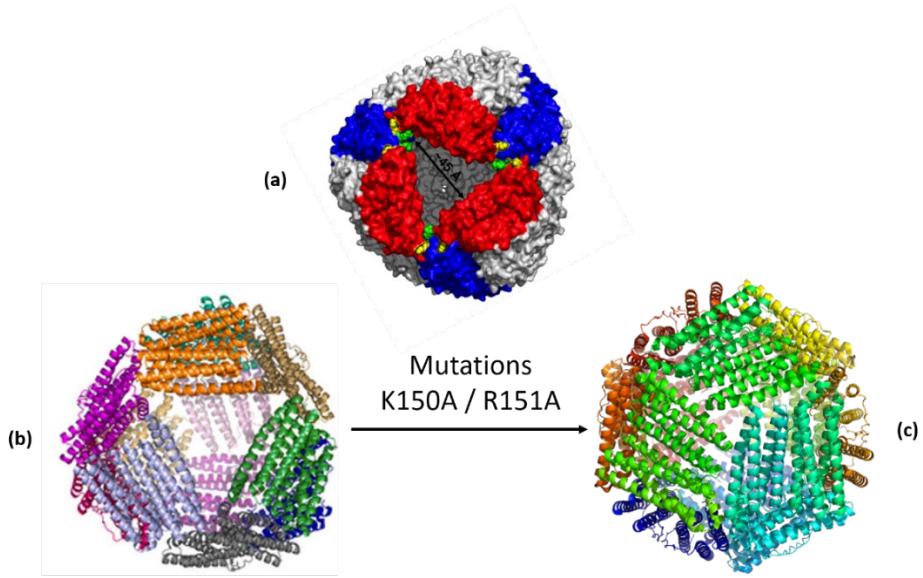

Figure 4 : 3D structures of the wild-type Archaeglobus fulgidus ferritin with open pores (AfFtn-WT), and with closed pores (AfFtn-AA). (a) surface representation of the tetrahedral AfFtn-WT showing one of the four large pores. The Lys150 and Arg151 residues are drawn in yellow and green, respectively. (b) AfFtn-WT representation at one of the four large pores before mutation. (c) representation of AfFtn-AA at the 3-fold axis.[16]

3. Goals and organisation of the project

3.1. Gold nanoparticles to mimic the ferritin

The first year of the thesis took place at SU. The main work was about the study of the electrostatic behaviour of gold nanoparticles (AuNPs). The goal was to mimic the ferritin particles with AuNPs immobilized on a doped silicon substrate, which were first observed by dark-field optical microscopy (DFOM) and probed by KPFM. Our interest was to investigate the different question that comes with a KPFM measurement: how to understand and interpret

the “contact potential difference” (potential) of a single “dry” nanoparticle on a surface. As well, we investigated the various phenomena that occur due to the interaction of a “conductive” nanoparticle with a semiconductor surface. The benefit of using AuNP as a mimic particle is that its electronic features are widely studied and understood through multiple measurements of AuNPs on different surfaces (Si, TiO_2).[17,18] By using the KPFM tool, we showed for the first time the potential image of a Schottky barrier (SB) induced by a metallic nanoparticle (AuNP) on a semiconductor (Si) (Figure 5). We proposed a model using the electrostatic approach to explain the effects observed. Finally, the results of this study were published in the *Nanoscale* journal on March 2023, and presented at the *Material Research Society* conference in San Francisco on April 2023. The results and discussion are presented in the Chapter IV of this manuscript.

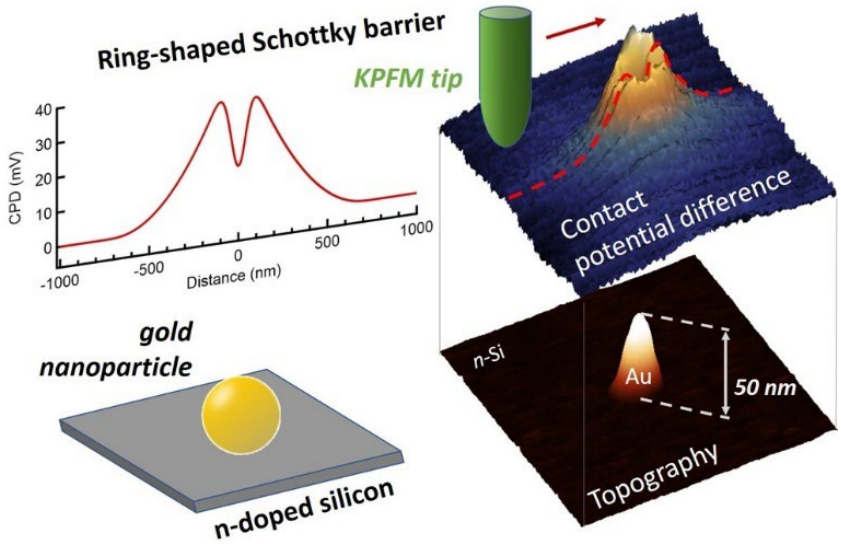

Figure 5 : KPFM study of gold nanoparticles (AuNPs) on doped silicon (n-Si). A Schottky barrier effect was detected on the contact potential difference image with an increase in the potential at the junction of AuNPs/n-Si.

3.2. Production and mutation of the ferritin

The second-year work was about the bioengineering of the AfFtn-AA nanocages in the NTU laboratory. During this year, the first goal was the production, purification, and characterization of AfFtn-AA nanocages, which were loaded with different iron contents. The production and purification of the ferritins were carried out by following precise protocols, which involved the use of numerous techniques such as fast protein liquid chromatography (FPLC) and UV-Vis spectrometry. The characterisations of the purified proteins were carried

out by using gel electrophoresis (SDS-PAGE), dynamic and electrophoresis light scattering (DLS and ELS), and mass spectroscopy (ICP-MS) techniques. The second goal was to modulate the surface charge of the AfFtn-AA through multiple mutations that substitute the negatively charged amino acids, which compose the ferritin shell, with positively charged amino acids (Figure 6.b). The goal of the mutations was to shift the isoelectric point (IEP) of the ferritin so that at neutral pH, we obtain a positively charged ferritin. Before performing the mutation experiments, we investigated the variation of the electrostatic potential distribution at the surface of the ferritin in solution while substituting different amino acids. This study was carried out using the *PyMol* software to calculate and simulate the electrostatic potential of the molecular surface of the ferritin. The mutated ferritins were produced, and the electrostatic charge surface was monitored by measuring the zeta potential of the ferritin at different pHs. All the production, purification and characterisation techniques are described in the Chapter III of this manuscript.

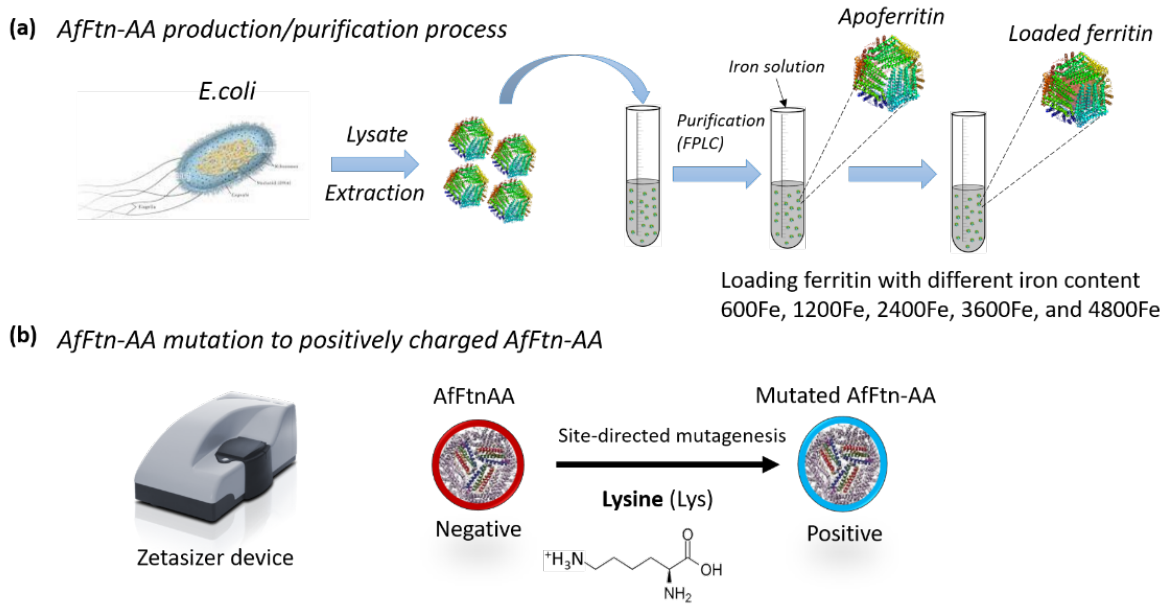

Figure 6 : Schematics of the bioengineering of the ferritin (AfFtn-AA). (a) production and purification steps for the production of AfFtn-AA from the E.coli bacteria. (b) mutation of the negative AfFtn-AA to obtain a positively charged AfFtn-AA.

3.3. Study of the electrostatic behaviour of the ferritin

The third-year work took place in both the SU and the NTU laboratories. Produced ferritins and mutants were brought from the NTU laboratory to the SU laboratory. The goal was to investigate the morphology and the nanoscale electrical properties of AfFtn-AA deposited onto a doped silicon substrate using the KPFM technique. We investigated both individual AfFtn-AA and AfFtn-AA monolayers (Figure 7.a) on silicon, to seek links between the structure, size and shape of the ferritin and its electrostatic properties. Our goal is to fully understand the morphological and electrostatic behaviour and the adsorption mechanisms of ferritins on solid surfaces. These are important parameters to perform charge transport through ferritins in a solid-state junction. The results and discussions about this study are described in the Chapter V. Furthermore, we characterise the ferritin mutants on a silicon surface by KPFM (Figure 7.a). Here, we aim to gather valuable information about the effect of the mutation on the electrostatic properties of the ferritin. The results and discussion of this study are described in the Chapter VI. For future work, successful mutations of the ferritin will allow us to form an active monolayer of mixed positive and negative ferritin that will be drop-casted on top of a transistor (Figure 7.b–c). This monolayer will act as a second gate, and the current source-drain could be modulated by adjusting the ratio of positive and negative ferritin.

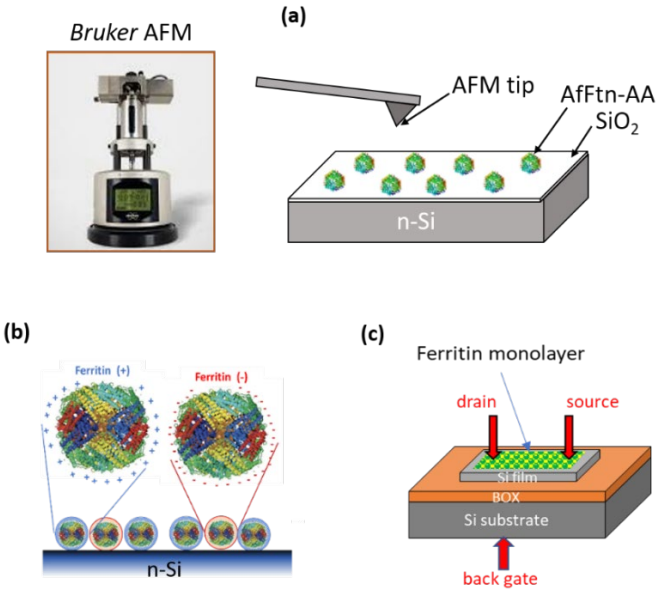

Figure 7 : Study of the electrostatic behaviour of the ferritin (AfFtn-AA). (a) schematic of a KPFM measurement of AfFtn-AA nanocages immobilized on a doped silicon substrate. An image of the Bruker AFM used in this thesis is shown on the left. (b) schematic of a mixed monolayer of positive (mutant) and negative AfFtn-AA on doped silicon. (c) schematic of the fully-depleted transistor in a silicon on insulator (SOI) configuration.

4. References

[1] Harold Hartley, « Origin of the word “Protein” », *Nature*, (1951), Vol.168, 244.

[2] Frederick Sanger, The chemistry of insulin, *Nobel Lecture*, (1958).

[3] Brändén Carl-Ivar and John Tooze. *Introduction to Protein Structure*. 2nd edition, (1999).

[4] Laufberger V., « Sur la Cristallisation de la Ferritine », *Bull. Soc. Chim. Biol*, (1937) 19, 1575-1582.

[5] Douglas Trevor and Daniel R. Ripoll. « Calculated Electrostatic Gradients in Recombinant Human H-Chain Ferritin ». *Protein Science* 7, nº 5 (1998): 1083-91.

[6] Finazzi Dario and Paolo Arosio, « Biology of Ferritin in Mammals: An Update on Iron Storage, Oxidative Damage and Neurodegeneration ». *Archives of Toxicology,* 88, nº 10 (2014): 1787-1802.

[7] Theil Elizabeth C., Rabindra K. Behera, Takehiko Tosha, « Ferritins for Chemistry and for Life ». *Coordination Chemistry Reviews*, (2013), 257, 579-586.

[8] Sirivech Somjai, Earl Frieden and Shigemasa Osaki. « The Release of Iron from Horse Spleen Ferritin by Reduced Flavins ». *Biochemical Journal* 143, nº 2 (1974): 311-15.

[9] Chiancone Emilia and Pierpaolo Ceci. « The Multifaceted Capacity of Dps Proteins to Combat Bacterial Stress Conditions: Detoxification of Iron and Hydrogen Peroxide and DNA Binding ». *Biochimica et Biophysica Acta (BBA) - General Subjects* 1800, nº 8 (2010): 798-805.

[10] Yamashita Ichiro. « Fabrication of a Two-Dimensional Array of Nano-Particles Using Ferritin Molecule ». *Thin Solid Films,* 393, nº 1-2 (2001): 12-18.

[11] Yoshii Shigeo, Kiyohito Yamada, Nozomu Matsukawa, and Ichiro Yamashita. « Making Monolayer of Inorganic Nanoparticles on Silicon Substrate ». *Japanese Journal of Applied Physics* 44, nº 3 (2005): 1518-23.

[12] Aihui MaHam, Zhiwen Tang, Hong Wu, Jun Wang, and Yuehe Lin, «Protein-Based Nanomedicine Platforms for Drug Delivery », *Small*, (2009), 5 , n°15, 1706-1721

[13] Sana Barindra, Eric Johnson, Kenneth Sheah, Chueh Loo Poh, et Sierin Lim. « Iron-Based Ferritin Nanocore as a Contrast Agent » 5, nº 3 (2010): 5.

[14] Takafumi Ueno, Masako Suzuki, Toshiaki Goto, Tomoharu Matsumoto, Kuniaki Nagayama, and Yoshihito Watanabe, « Size-Selective Olefin Hydrogenation by a Pd Nanocluster Provided in an Apo-Ferritin Cage », Angew. Chemi., (2004), 116, 2581-2584

[15] Lapaglia C and P L Hartzell. « Stress-Induced Production of Biofilm in the Hyperthermophile Archaeoglobus Fulgidus ». *Applied and Environmental Microbiology* 63, nº 8 (1997): 3158-63.

[16] Sana Barindra, Eric Johnson, Pierre Le Magueres, Angela Criswell, Duilio Cascio and Sierin Lim. « The Role of Nonconserved Residues of Archaeoglobus Fulgidus Ferritin on Its Unique Structure and Biophysical Properties ». *Journal of Biological Chemistry* 288, nº 45 (2013): 32663-72.

[17] Zhang Yingjie, Olivier Pluchery, Louis Caillard, Anne-Félicie Lamic-Humblot, Sandra Casale, Yves J. Chabal and Miquel Salmeron. « Sensing the Charge State of Single Gold Nanoparticles via Work Function Measurements ». *Nano Letters* 15, nº 1 ,(2015): 51-55.

[18] Wang Shengyang, Yuying Gao, Shu Miao, Taifeng Liu, Linchao Mu, Rengui Li, Fengtao Fan and Can Li. « Positioning the Water Oxidation Reaction Sites in Plasmonic Photocatalysts ». *Journal of the American Chemical Society* 139, nº 34, (2017): 11771-78.

Chapter II: Ferritin for biomolecular electronics in the literature

Introduction

The second chapter will provide the reader of this manuscript with a literature review. First, the state of the art in the biomolecular electronic field will be presented, and we will focus on the applications and uses of proteins in this field. The phenomenon of electron transport through proteins and the adsorption mechanisms of proteins on solid surfaces will be discussed. Secondly, the electronic behaviour of ferritins embedded in various devices will be described, in particular the electron transport. And finally, we will illustrate with examples from recent articles how KPFM brought new insight in biomolecular electronics, mainly to visualize and characterise individual nanobiomaterials.

1. The biomolecular electronics field: State of the art

In 1791, Luigi Galvani, an Italian physicist and physiologist, introduced the concept of "biological electricity", by observing the twitching of a frog's leg upon application of a potential difference. Such phenomena are known to be the result of neurons that use electrical current to send signals to specific muscles. To reach this explanation, scientists have deeply examined miscellaneous biophysical systems to understand the detailed pathway of electron transfer. Mainly by studying biological functions such as photosynthesis or aerobic respiration that involve redox reactions.[19,20] Throughout the years, the biomolecular electronics field has arisen from the desire to exploit and explore the electronic behaviour of such molecular systems of biological origin by combining them with the processing power of modern electronics for two major purposes. First, use their electrical nature and charge transport mechanisms to build new hybrid devices that are more sustainable and biocompatible. And secondly, to understand more in detail the chemical interactions involved in biological processes and to better comprehend disease mechanisms linked to charge transport. For instance, the malfunction of mitochondria, which is strongly related to Parkinson's disease, has been linked to a disorder in the electron transport chain.[21] The biomolecular electronic field frames all the native and modified biological molecules that can be differentiated by their molecular weight. These biological molecules can be classified into two families: small and large. The small biological molecules (Figure 8), with a molecular weight below 1 kDa form crystalline materials and the large biological molecules, with a molecular weight above 1 kDa (and could reach over 3.8 MDa such as the connectin protein, which is responsible for the passive elasticity of muscle), that are mainly formed by polymeric building blocks (Figure 8), of various types of molecules

(e.g., amino-acids, nucleic acids (DNA), and monosaccharides (sugar)). A few examples of the use of small and large biomolecules in electronic systems are described hereafter.

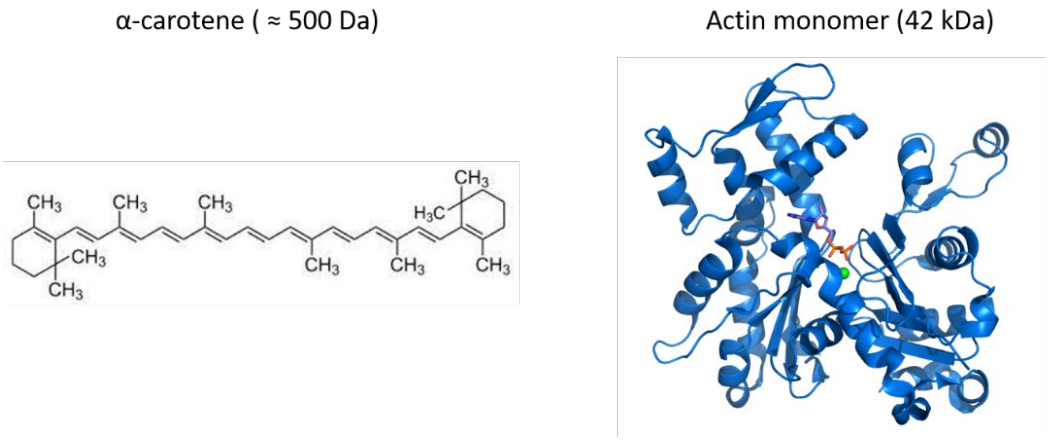

Figure 8 : Example of small (left) and large (right) biological molecules. The α-carotene is a pigment molecule from the carotene family. The actin is a globular protein.

1.1. Small Molecules

Indigo as ambipolar semiconducting materials

Within the small biological molecule family, indigos and indigoid have shown interest in the biomolecular field. These natural dyes, extracted from plants and animals, have proven to be natural intrinsic semiconductors, ambipolar charge carriers, and electrochemically active.[22,23] The readily redox process of indigo (Figure 9.a) makes it an ambipolar and semiconductor material suitable for various electronic devices. Either as an active electronic material (thin film) in an Al/Indigo/Au photovoltaic cell[24] or crystallized and incorporated as solid-state electrodes in lithium and sodium rechargeable batteries.[25,26] Moreover, Irimia-Vladu *et al.* (2012)[27] reported the fabrication of an ambipolar organic field effect transistor (OFET) with a thin film indigo active layer on a natural shellac resin substrate (Figure 9.b−c). The indigo film showed good electron mobility (10^{-2} $cm^2.V^{-1}.s^{-1}$) and its low band gap (E_g = 1.65 eV) allowed carrier injection from the gold electrode. Furthermore, the OFET has proven to have good stability in the air, to be nontoxic (biocompatible) and biodegradable. These latter features are widely spread among all electronic systems carrying biomolecules, as they are strong aspects sought by the researchers to create new devices. Indigo and its derivatives keep showing, over the years, a strong interest in organic electronics with increasing mobility (0.95

cm².V^{-1}.s^{-1} for electron)[28,29] and more recently for neuromorphic sciences embedded in a brain-like functioning device (Sreelakshmi et *al.* (2023)).[30]

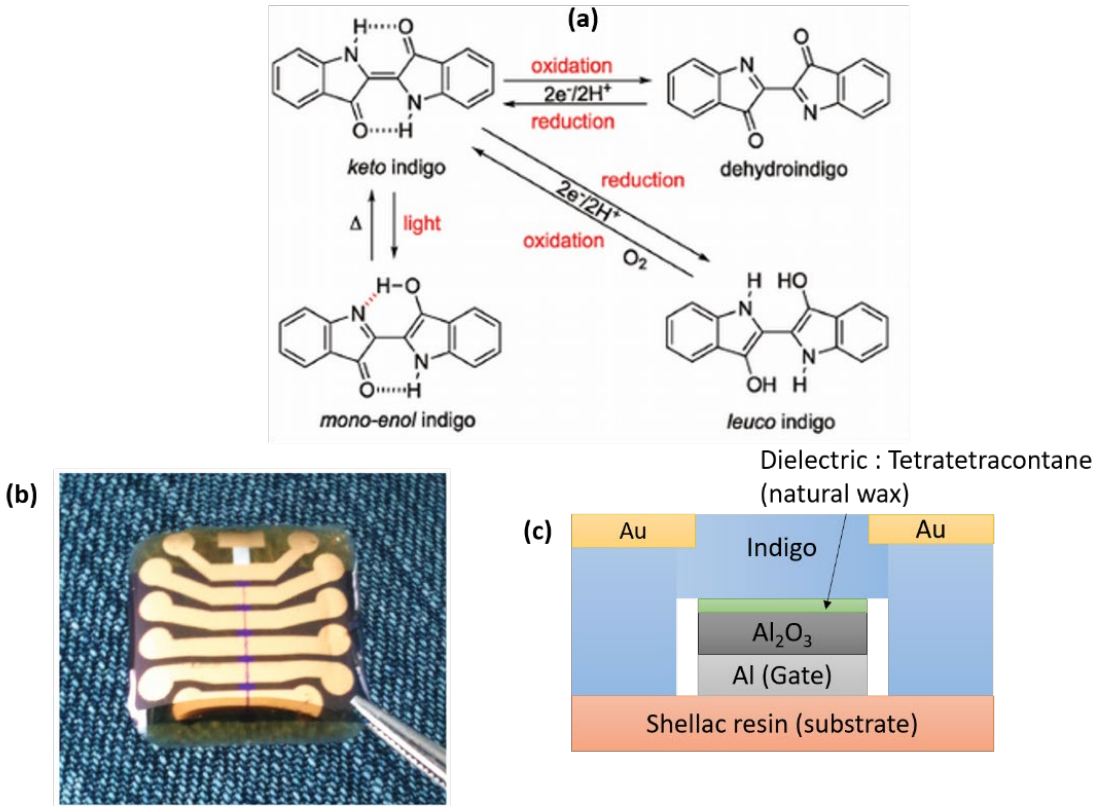

Figure 9 : The redox properties and electronic application of the indigo dye. (a) the (photo)-redox properties of indigo show the reduced and oxidized forms of indigo and the photo-induced proton transfer. (b) indigo-based organic field effect transistor, W/L = 1 mm/ 120 µm. (c) schematic of the transistor structure.[19,27]

Carotenoids for photovoltaics

Carotenoids are another class of pigment responsible for multiple biologic processes such as light harvesting, energy transfer, and photo-protective functions (and the colour of some vegetables). Their potential electronic transport properties come from their polyene chain structure, which is very similar to that of conductive polymers. One of the most studied carotenoids is the β-carotene. Upon charge-transfer doping, β-carotene stores charge in pairs of spatially delocalized solitons (Figure 10.a).[31] It demonstrated a *p*-type mobility of 4.10^{-4} cm².V^{-1}.s^{-1}, measured in transistors. Moreover, a heterojunction diode Au/β-carotene/*n*-Si (Figure 10.b) was reported by Yakuphanoglu *et al.* (2006)[32] for the fabrication of organic solar cells, which presented a 23.3 % conversion efficiency. Furthermore, in 2013 it was reported the

fabrication of an organic solar cells with β-carotene layer as an electron-donor molecule and a fullerene derivative as an electron-acceptor molecule.[33] The use of such carotenoid pigment in electronic devices is suitable due to its ease of fabrication, low cost, light weight, and ability to produce flexible devices. Carotenoids as sensitizers for dye-sensitized solar cells have been reported in many studies and even recently showed a high conversion efficiency (photo-to-electron) of 33 % (Calogero et *al*. (2018)).[34] The carotenoid family contains more than 700 known molecules, but only a few of them have been investigated so far, opening the field of possibilities for developing new optoelectronic devices.[35]

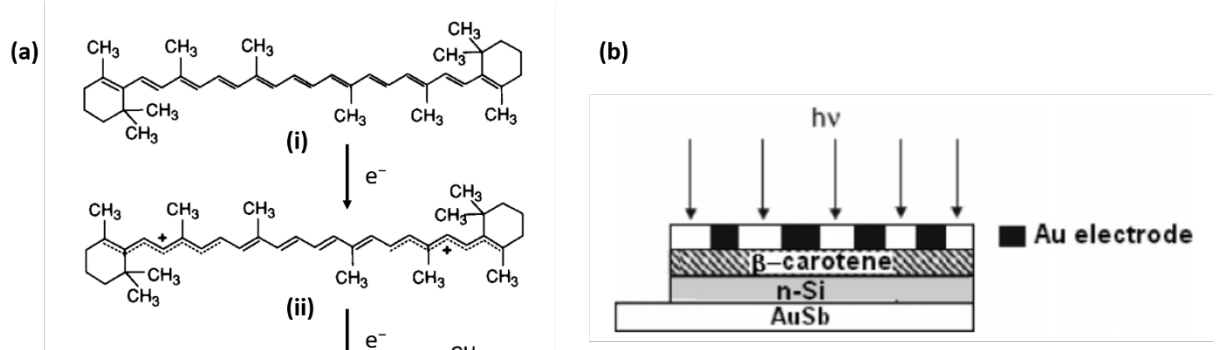

Figure 10 : Chemical properties and electronic application of the β-carotene. (a) chemical structure diagram of (i) neutral β-carotene, (ii) the dication β-C^{2+}, and (c) the cation radical β-C^{+}. (b) structure of the Au/β-carotene/n-Si organic solar cell.[31,32]

1.2. Large Molecules

Polysaccharides in field effect transistors

In the large biomolecule category, natural polysaccharides were the first biopolymers to be studied for their conductivity properties. They are formed by long chains of monosaccharides, which perform energy storage in many cells of plants, fungi, and bacteria. Among the rich catalogue of polysaccharide molecules, only two have risen a strong interest for their conductance properties: the cellulose, an organic polymer, which was first studied in 1960 (Murphy)[36], and the chitin(−chitosan), whose conductivity was described 43 years later by Creber *et al.* (2003)[37] (Figure 11.a). However, in their natural state, these biopolymers have an intrinsic conductivity ranging from insulator to partially conductive. The conductance across

the polysaccharide has been tuned using different modifications involving the addition of doping molecules and coatings to form polymer blends. One interesting strategy is the modification of chitosan with proline and maleic acid (Figure 11.c−d) that was incorporated as a channel in a field effect transistor (FET) (Figure 11.b). It showed a reverse response of the current-voltage gate with an ionic mobility of $\mu_{H+} = 5.3.10^{-3}$ $cm^2.V^{-1}.s^{-1}$ for the maleic acid and $\mu_{OH-} = 0.4.10^{-3}$ $cm^2.V^{-1}.s^{-1}$ for the proline.[38]

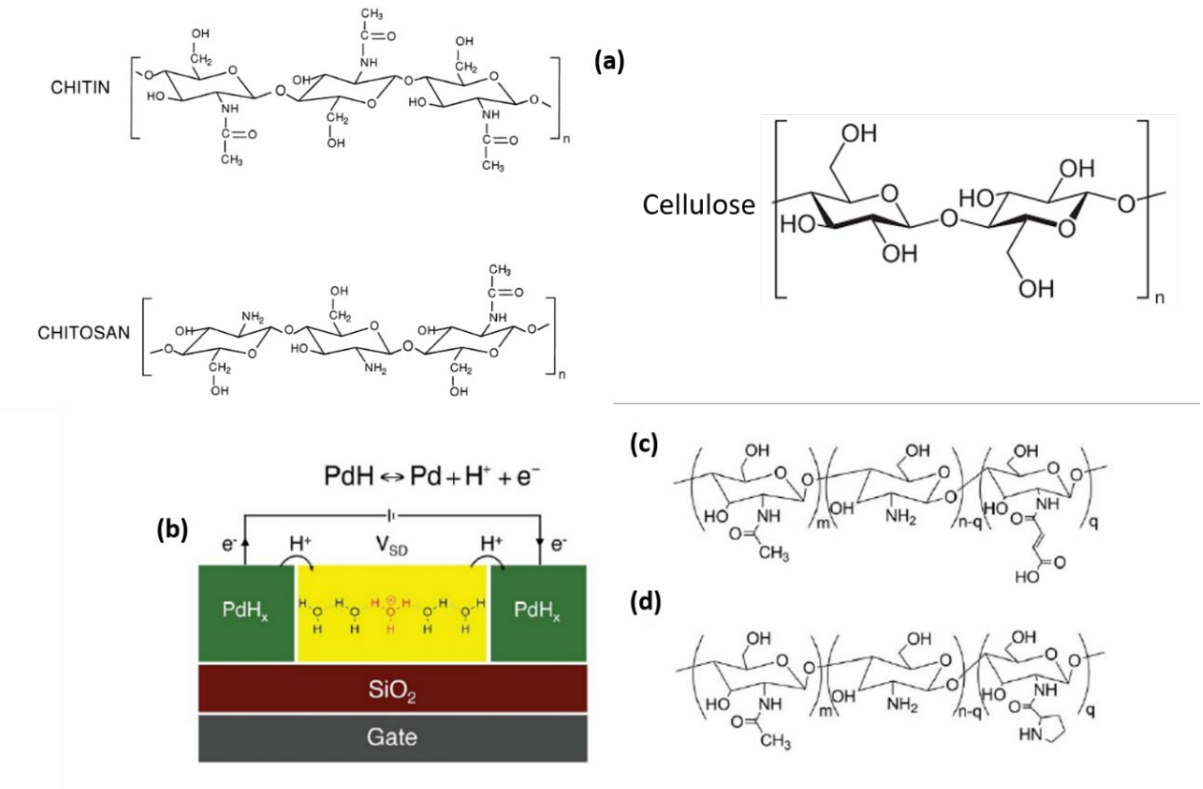

Figure 11 : Molecular representation of chitin, chitosan, and cellulose and their application in an electronic device. (a) molecular structure of natural polysaccharides. The chitosan is the N-deacetylated derivative of chitin.[37] (b) FET-structured device with PdH_x as a source and drain. The channel is made of maleic chitosan (c) or proline chitosan (d).[38]

Protein-based biopolymers

As large biological molecules, proteins have been particularly focused on by researchers in the biomolecular electronic field. Their functions are essential for various chemical processes like photosynthesis, water oxidation, nitrogen fixation, and iron transport. Such processes involve electron transfer driven by the redox centers carried by the proteins. The redox activity of a protein is extremely linked to its structure (i.e., folding), and phenomena that change the electrostatic interaction within the protein may lead to the denaturation of the protein, i.e., the

loss of its structural order. Particular assets of the protein, like biocompatibility, biodegradability, and especially its size (nanometer scale), made it a good candidate for electronic. Even though there are few early works about electrical studies on protein-based materials like keratin protein (Murphy, 1975)[39] and globular or fibrous protein films (Powell *et al.*, 1970)[40], the emergence of the protein subfield occurred in the early 2000s with the measurement of protein conductance in molecular junction configuration. This subfield started with modified protein-based biopolymers like silk fibrils coated with organic conductive polymers (PEDOT: PSS) (Figure 12.a−b) or graphene/carbon nanotubes to increase their conductivity (to 0.1 $S.cm^{-1}$), [41,42] and also the deeply studied amyloid-like fibril proteins, formed by the self-assembling of peptides into a cross-beta structure. Like the silk, amyloid fibrils were coated with PEDOT or polyaniline. One engineering strategy reported by Altamura *et al.* (2016)[43] was to form a chimeric protein of amyloid fibril and rubredoxin (an iron-containing redox protein) (Figure 12.c). The self-assembly process of the amyloid fibril creates an ordered 1D assembly of redox proteins (Figure 12.d) that is capable of electron transport over a dozen micrometers (measured by electrochemical measurements), but with a relatively low conductivity around 2.3 $\mu S.cm^{-1}$. Furthermore, non-fibrillar proteins have become more attractive in the past decade. The reflectin, a structure protein of cephalods, was used for its high percentage of charged amino acids to form proton-conducting films deposited onto Pd electrodes (Odrinario *et al.*)[44]. The albumen, a protein from the albumin family found in vertebrate blood, was deposited on indium tin oxide electrodes by spin coating (Wu *et al.*).[45]

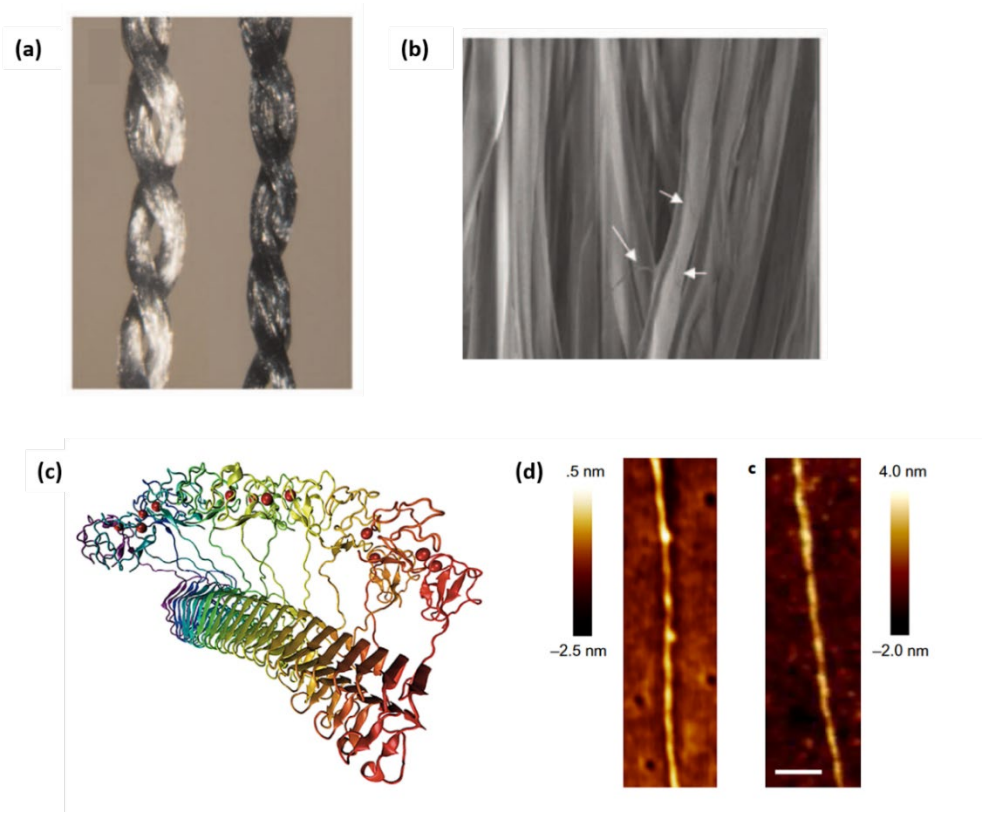

Figure 12 : Silk threads and their application in electronics. (a) macroscopic images of a silk thread (left) and a PEDOT-PSS coated silk thread (right). (b) SEM image of a PEDOT-PSS coated silk thread. (c) 3D structural model of amyloid fibrils combined with rubredoxin (red dots). (d) tapping AFM images (scale bar, 50 nm) of an amyloid fibril nanowire used for electrochemistry.[41,43]

1.3. Metalloproteins

This section describes the last class of large biomolecules: the metalloprotein. This category is described in detail in the section below, as it is strongly linked to the topic of this thesis. An description of the electron transport through biomolecules and protein adsorption on solid surface is given in this section. It introduces different notions that are used for the study of the electrostatic behaviour of metalloproteins, which includes the ferritin as well.

The complexity of electric transport phenomena through biomolecules

The electronic conduction across individual biomolecules can be distinguished either as electron transfer (ET) or electron transport (ETp). Almost all the important biochemistry processes involve ET, which refers to a redox event with the exchange of an electron (or hole) between an ionic solution (solvent) and a protein in contact with it (Figure 13.a). Conversely, ETp refers to electrons that flow through a protein without the participation of a solvent. The

electrons flow across the protein between two electronically conducting electrodes (Figure 13.b).[46–48] The latter phenomenon is linked to the topic of this thesis as we are investigating proteins on solid surfaces; however, the fundamental processes of ETp via protein are still in their infancy and are less understood than ET. To describe the different ETp phenomena, we consider a molecular junction with a protein containing various amino acid residues between two metallic electrodes. The residues affect the potential that the electron encounters as it flows through the protein (Figure 13.c). By applying a potential at the electrodes, the electron can transport between the electrodes, which can be described with different models. The ETp can occur via the hopping mechanism (Figure 13.e), a multistep process in which the transport of the electron between the electrodes is realized across intermediate energy states that are potential wells for the electron, requiring activation energy to escape. The transport is thermally activated and temperature-dependent (incoherent). On the other hand, ETp can occur via direct (coherent) (Figure 13.d) or indirect (sequential) tunnelling, which are considered temperature-independent. The determination of the transport mechanism is performed by measuring the current density vs. voltage (J(V)) characteristic of the junction as a function of the temperature and the distance *d* between both electrodes. The coherent (or sequential) ETp across a junction is usually a short-range mechanism. However, long-range ETp was reported for long-conjugated molecular wire or graphene, with a distance of up to 3.5 nm,[49,50] and also for biomolecules like bacteriorhodopsin, azurin or ferritin.[51,52] The ETp distance is determined by the shape and size of the molecule between the electrode, as well as the interaction of molecule-electrode (here, protein-electrode). These parameters are important to fully understand the transport mechanism across such a junction. Therefore, the study of the adsorption phenomena of the protein onto a solid substrate and its electrostatic properties is necessary. In this thesis, we propose a new method to measure, at the nanoscale (at the single molecule level), the electrical phenomena involved when a protein is adsorbed on a substrate.

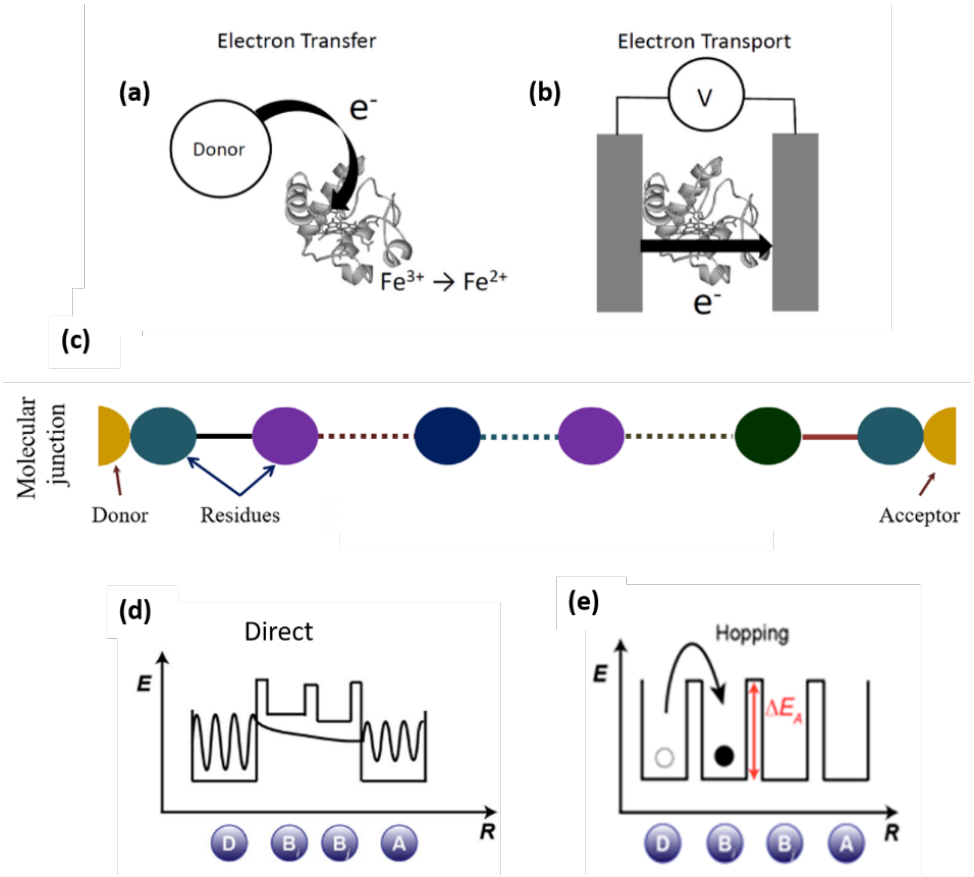

Figure 13 : Schematic of the electron transport mechanism through biomolecules. (a) schematic of the electron transfer (ET) process, whereby an electron is transferred to/from a site on a protein that becomes ionized (oxidized or reduced). (b) schematic of the electron transport (ETp) process, whereby electrons pass from one electron (donor) to another (acceptor) via protein. (c) schematic of a molecular junction with a protein between two electrodes. At the bottom are the energy diagrams representing the wave function of the electron in relation to the donor D, acceptor A, and bridge B states during direct coherent tunnelling (d) and hopping (e).

Metalloprotein conduction inside junction

Metalloproteins are a class of proteins that contain a metal ion cofactor, a chemical compound that is required for the protein to achieve a specific role (enzyme, catalysis). About one-third of the known proteins are metalloproteins, which are involved in many electron transfers through their redox active sites. Metalloproteins have been extensively characterized

once immobilized on solid substrates, mainly inside junctions, by using probe techniques such as conductive atomic force microscopy (c-AFM) and scanning tunnelling microscopy (STM). These techniques were performed to measure the topography and ETp of protein assemblies at the nanoscale. Among metalloproteins, the azurin protein has been substantially studied for its electron-mediating function, it operates as an electron shuttle in various biological systems (photosynthesis in bacteria and plants).[53] This protein contains a Cu^{2+} ion, which undergoes a redox process with the transfer of an electron. Li *et al.* (2012)[54] reported the measurement of electron transport in an azurin monolayer deposited onto a gold substrate by c-AFM (Figure 14.a). The results show a switch in the ETp process from temperature-independent for the holoazurin form to thermally activated for the apoazurin form. For metalloproteins, the prefix holo- is used to name the metal-containing form, and the prefix apo- is used to name the metal-free form. Furthermore, Amdursky *et al.* (2013)[55] studied ETp through the electron carrier protein cytochrome-c (CytC). This protein contains a porphyrin cofactor molecule (a macrocycle organic compound) that can handle one Fe atom. CytC was electrostatically formed as a monolayer on an H-terminated silicon surface, and the current density through the monolayer was measured between two electrodes. The results showed that ETp is strongly related to the conformation of the protein. The apoCytC showed a large difference in current compared to the holoCytC, attributed to the loss of its structure (Figure 14.b). Moreover, a single myoglobin metalloprotein, which handles O_2 molecules inside muscles, was deposited on a Si/SiO_2 substrate between two Pt electrodes to form a single electron transistor device (Figure 14.c) (Li *et al*, 2012).[56] As for the CytC, the myoglobin contains a porphyrin cofactor, and single-electron transport measurements showed resonant tunnelling through it. A change in the protein conformation during the tunnelling process is also reported. The few examples of ETp investigations presented above clearly show an interest in the metalloprotein in electronics. Interestingly, the conformation and orientation of the protein on a solid surface appears to influence the ETp. During this thesis, we focused on one of the metalloproteins: the iron-storage ferritin protein, presented in detail in the next section of this chapter.

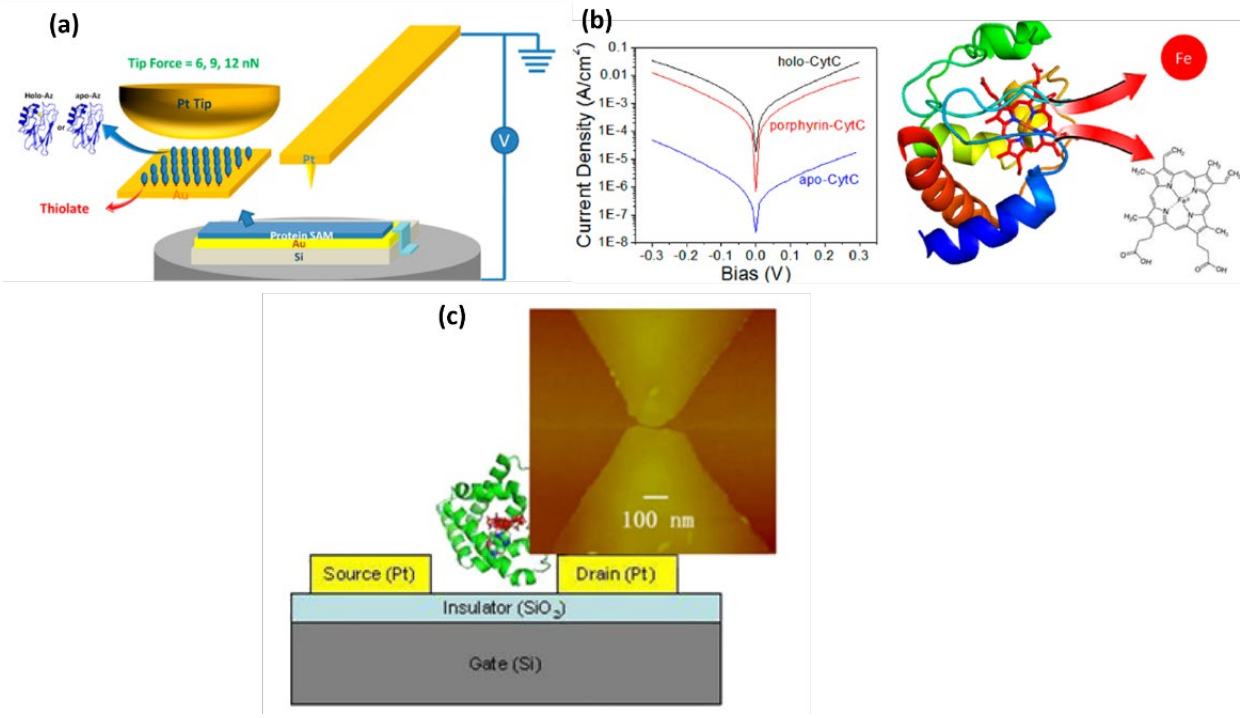

Figure 14: Electron transport (ETp) measurements through metalloproteins. (a) schematic (not to scale) of a junction employed in ETp measurement via azurin proteins. (b) ETp via the cytochrome-c derivative and ribbon representation of the cytochrome-c. (c) sketch of the single-electron transistor with myoglobin protein. In the inset, an AFM image of the bare Pt junction is shown.[54–56]

Local electric charge in protein and adsorption mechanisms

Proteins are both amphiphilic and charged molecules due to the multiple amino acids of varying hydrophobicity or with positive/negative charges they are composed of. This divides the protein surface into different patches, either hydrophobic, hydrophilic, positively charged, or negatively charged. Due to the complexity of their structure, the local arrangement of amino acids in the shell creates different affinities in different areas. Therefore, the charge distribution on the protein is considered anisotropic, and the protein adsorption cannot be explained by its overall net charge.[57] For instance, on a negatively charged surface, proteins expose their positively charged domains to the surface, and conversely, on a positively charged surface. A simplified representation of this phenomenon is displayed in Figure 15. The β-lactoglobulin protein exhibits positive and negative domains due to the positive and negative amino acids. The protein rearranges itself in the space to adsorb on the negative surface.[58,59] To visualize the distribution of charges at the surface of a protein, a numerical model that solves the Poisson-

Boltzmann equation is used. This latter describes the electrostatic potential distributions at the surface, which consist of charged amino acids in an ionic solution,[57] and therefore gives a map of the potential distributions around the protein. This numerical model was used during this thesis to observe the charge modification induced by the mutation of the ferritin. Protein particles in an ionic solution are colloidal systems whose stability is characterised by the zeta potential (ζ in volts). This value not only gives the stability of the colloidal solution but also the sign of the surface charge of the protein as a function of the pH. The pH at which the protein particle has a neutral charge, i.e., $\zeta = 0$ mV, is the isoelectric point (IEP). At pH > IEP, the surface charge is negative, and at pH < IEP, the surface charge is positive. Each protein has a proper IEP that indicates its net surface charge at a given pH. Thereby, the determination of the IEP is important to investigate the charged distributions of the protein as well as the adsorption of protein on charged surfaces.[60]

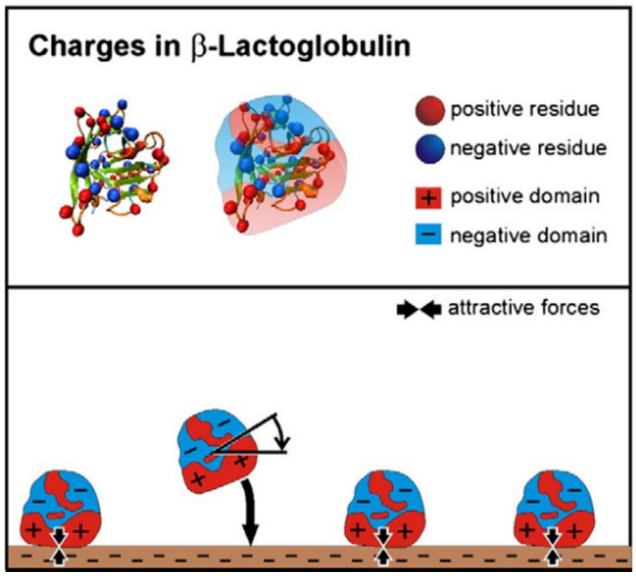

Figure 15 : Schematic representation of orientation changes of surface-adsorbing proteins. Top: a cartoon representation of β-Lactoglobulin depicts the distribution of positively (red spheres) and negatively (blue spheres) charged amino acids. After strong simplification, the protein is represented as a globular entity consisting of positive and negative domains. Bottom: the protein orientation is solely determined by surface-protein interactions.[58]

The immobilization of proteins on solid substrates is an important challenge for reliable measurements, and the adsorption of proteins is a phenomenon that is widely studied in many research areas, such as biomedical[61], food industry[62], and bioelectronic[47]. It is a very common phenomenon that occurs in countless systems (natural or artificial), and is often describes as “complicated to avoid”. Proteins contrast with small molecules, which behave like

rigid particles, as their adsorption is caused by complex mechanisms still being investigated nowadays. Proteins are adsorbed on a surface via electrostatic or hydrophobic interactions driven by a combination of enthalpic (attractive interaction) and entropic contributions.[58,63,64] In fact, it is now accepted that proteins undergo a rearrangement of their structure (secondary or tertiary) to relax in an energetically favoured state. This driven force is what makes possible the adsorption of proteins on an electrostatically repelling surface (Figure 16). Proteins that lose their conformation upon adsorption are called "soft proteins", whereas those that resist conformational changes are called "hard proteins".[65]

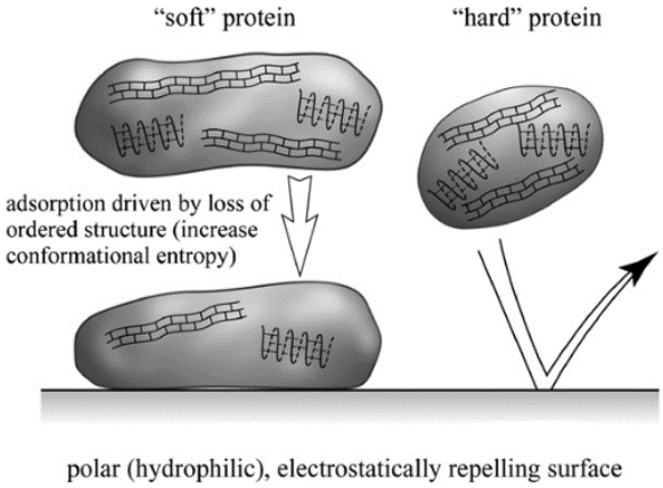

Figure 16: Loss of ordered (secondary) structure (α-helix and/or β-sheet) may drive proteins to adsorb onto a hydrophilic and electrostatically repelling surface.[65]

As shown in a previous section, the conformation and orientation of a protein on a solid surface are parameters that can significantly influence the ETp. Once deposited on a surface, a protein must remain in its native conformation to conserve its activity. Protein adsorption is therefore of great interest and should be investigated. In fact, there are multiple analytical techniques that can be performed to analyse the conformation of immobilized proteins, such as Fourier transform infrared spectroscopy (FTIR), ultraviolet-visible spectroscopy (UV-Vis), RAMAN spectroscopy or circular dichroism (CD).[64] In our work, the FTIR technique was used to confirm the adsorption of our protein onto the surface. However, such a technique only provides an analysis of the chemical composition of a protein assembly. In this thesis, we propose a novel method to determine the conformation and orientation of an individual protein directly on a solid surface using a KPFM.

2. Applications of the ferritin to the biomolecular electronic field

This part reviews the applications of the ferritin nanocages inside various electronic systems, such as junctions or solid-state transistors, in order to probe the electronic properties of the ferritin. Furthermore, we present the long-range mechanism of electron transport that occurs across ferritin assemblies.

2.1. Ferritin in electronic devices

By its nature of metalloprotein, the ferritin possesses suitable features to be incorporated into a tunnel junction. First, the loading of metal inside its core is driven by a redox process involving ET and therefore gives the possibility to switch the electronic state of the molecule via the application of an external potential. Secondly, the iron core can be substituted with other metals without alteration of the structure of the ferritin and allowed to tune the electric properties of the ferritin. Thirdly, it has the ability to stay in its active form in an aqueous buffer with a wide pH range (4.0 to 9.0) and well up to 85 °C in temperature.[66] Fourth and finally, its particular shape facilitates the electron tunnelling and making it naturally capable of ETp.[67] The nature of the electron transport process across ferritin has been characterized in various systems described in studies that propose the introduction of ferritin onto a solid support or inside a junction. To study and understand the ETp across ferritin, it is first necessary to characterise its structure, conformation and the way it adsorbed on solid surfaces. The shape and size of the ferritin will greatly affect the ETp. In addition, the ETp may vary depending on the form of the ferritin assembly (bulk, organised or disorganised monolayer, single particle).

2.2. Electron transport through ferritin monolayers

Electron transport to and from the mineral core was demonstrated by electrochemical measurements on ferritin adsorbed onto different surfaces (gold, silicon), using voltammetry[68], or probing techniques such as c-AFM, STM, and KPFM.[69–71] The benefit of such probe techniques is that they can perform electrical measurements down to the single-molecule level by using the metal tip as an electrode. Then, we can consider the ferritin as incorporated into a metal-insulator-metal (M-I-M) junction, which is the main configuration that has been used for electrochemical measurement. The electrical conductivity through the metal core of the ferritin has been mainly deduced by comparing the conductivities and band gaps of the iron-containing ferritin (holoferritin) and iron-free (apoferritin) forms. We can notice the work of Bera *et al.*

(2017)[72], who reported transport band gap measurements of equine spleen holoferritin, apoferritin and different substituted ferritins (ferritin with a metal core of nickel (Ni), manganese (Mn), and gold (Au)). A monolayer of each ferritin type was anchored onto a thiol-functionalized *n*-doped silicon substrate (Figure 17.a), and gaps were determined from c-AFM measurement and UV-Vis absorption. The current vs. voltage curves (I-V), obtained by c-AFM, showed a clear band gap value difference between apoferritin (2.6 eV), holoferritin (2.0 eV), and other reconstituted ferritins (2.2 eV for Mn-ferritin, 1.43 eV for Ni-ferritin, and 0.8 eV for Au-ferritin) (Figure 17.b). Interestingly, the band gap value of holoferritin reported here differs from the reported band gap of an ultra-small iron oxide nanoparticle (2.2 eV).[73] The contribution of the amino acid shell to the electron transport could be an explanation for this difference in values. However, direct band gap values were measured by optical absorption and showed 2.4 eV (holoferritin) and 2.8 eV (apoferritin) band gaps. Previous studies reported values of ferritin band gaps measured by optical absorption in solution, of 2.14 eV (indirect) and 3.05 eV (direct) (Colton *et al.*, 2014).[74] The position of the Fermi level relative to the conduction band indicates a *n*-type semiconductor nature for the ferrihydrite core of the ferritin. Therefore, the electronic property of the ferritin can be tuned by core modification, which is potentially useful for band gap engineering. Also, this study demonstrated the viable compatibility of the silicon as a solid support to detect the electron transport activities of the ferritin, reinforcing the incorporation of ferritin in modern devices. The silicon is the type of substrate that we used in this thesis. Furthermore, it has been shown that the core of the ferritin participates in the retention of its structure once it is deposited in a “dry” state on surfaces. Highly oriented pyrolytic graphite (HOPG) was used as a substrate for the physisorption of holo- and apoferritin and on which tapping AFM measurements were performed. The results here showed that apoferritin tends to collapse on the surface (vertical compression and lateral spread) when high force is applied (10-50 nN) by the tip (Figure 17.c), whereas holoferritin only undergoes small compression. However, these deformations were shown to be reversible, and ferritins return to their original heights under a small applied (10 nN).[69,75] In such c-AFM measurements, the applied compressional force also varies the magnitude of the ETp through ferritins due to the mechanical compression of the nanocage (i.e., compression of the amino-acids shell), which reduces the atom-to-atom distances and increases the ETp rate.

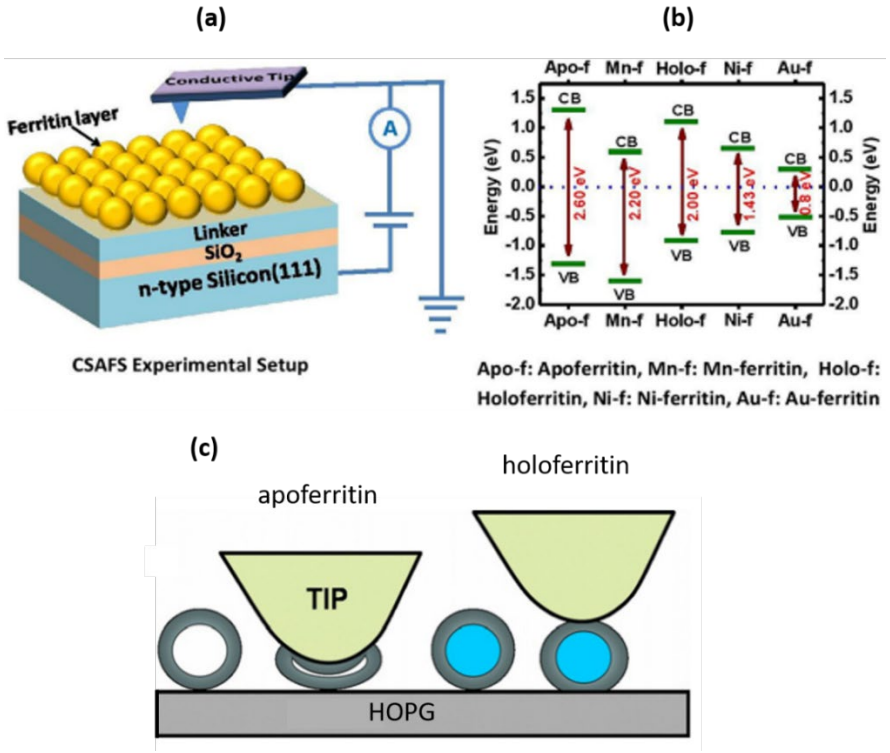

Figure 17 : Electron transport measurements. (a) schematic of a c-AFM measurement of a horse spleen ferritin monolayer on a n-silicon substrate. (b) band diagram for iron-loaded ferritin (holo-f), apo-ferritin (apo-f) and different reconstituted ferritins (Ni-f, Au-f, and Mn-f). The dashed line represents each molecular semiconductor's Fermi energy, which was aligned to 0V. (c) schematic showing the different responses to AFM tip induced compression from the (left) apoferritin and (right) holoferritin. [69,72]

Negative differential resistance induced by a ferritin assembly

Through multiple I-V curve results, ferritin demonstrated a quantum electrical phenomenon known as negative differential resistance (NDR): a sharp decrease in current with progressive increasing voltage and vice versa. Such a phenomenon relates to an ON-OFF behaviour and indicates utilizable electronic signals to make a potential molecular switch. In the literature, it was reported for the first time for a germanium *p-n* junction (Esaki *et al.*, 1958)[76] and was observed in organic molecules with an active redox center embedded in a nanoscale molecular junction (Chen *et al.*, 2000).[77] Ferritin assemblies have shown NDR behaviour via I-V curves from STS and voltammetry measurements. Such curves were reported by Kolay *et al.* (2018)[78] for apo- and holoferritin films deposited onto a gold substrate (Figure 18.a). It showed a reversible NDR, but only for the holoferritin indicating the role of the iron core in the ETp. Although reproducible NDR was also spotted on holoferritins embedded between single-walled carbon nanotube (SWNT) electrodes on a silicon substrate (Tang *et al.*,

2007)[79] (Figure 18.c–d). The difference in the voltages where NDR peaks appear comes from the difference in the origin of the NDR behaviour, which in the case of the SWNT-ferritin-SWNT device arises from the reversible redox process of the core with reduction of Fe (III) and oxidation of Fe (II) during the I-V scan. In this configuration, ferritin nanocages are in a substantially hydrated state; moisture surrounding the protein acts as a solvent medium, which forms an electrochemical system more favourable for redox processes to occur. Whereas for the holoferritin film on gold, the NDR behaviour comes from the resonant tunnelling between the tip electronic state and the molecular energy band of the ferritin. In the ferritin differential conductance spectra (see the inset in Figure 18.b), some local density of states (DOS) were observed to be missing in both the conduction band (CB) and the valence band (VB). Therefore, the tunnel current reaches its maximum value (NDR peak) when the Fermi level of the STM tip is aligned with the DOS of ferritin (resonance conditions), and a decrease of the tunnel current (NDR valley) appears when the Fermi level of the STM tip is aligned with the DOS missing regions in both CB and VB (off-resonance conditions).

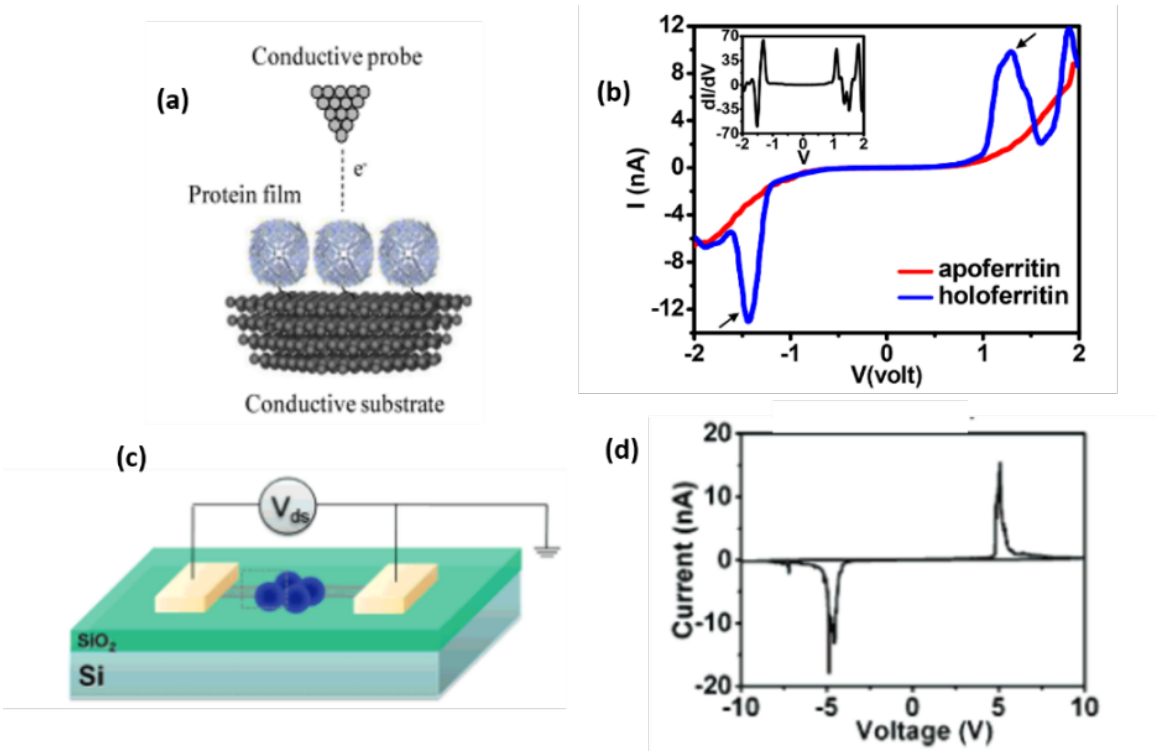

Figure 18: Negative differential resistance of ferritins embedded in solid-state junctions. (a) schematic of a local probe technique configuration to study electron transport through a protein film. (b) NDR peaks (shown by black arrows) from STS-derived current (I) vs. voltage (V) curves for holoferritin (blue line) and apoferritin (red line). The differential conductance response of holoferritin is shown in the inset of the figure. (c) schematic view of the SWNT-ferritin-SWNT device with, (d) representative I-V curve recorded at room temperature.[78,79]

Ferritin in Field-Effect Transistor

In the range of applications that could include the ferritin as an electric component, the transistor is a promising type of device. This widely studied type of electronic device is commonly used to amplify or switch electric signals and power. It was invented in 1947 by John Bardeen, Walter Brattain, and William Shockley at Bell Labs (an invention that won them the Nobel Prize in 1956), and has remained, since then, one of the building blocks of the modern electronics. Nowadays, the field-effect transistor (FET) is by far the most commonly used transistor, and it is usually composed of a doped silicon substrate and three metallic electrodes. Many studies have reported the use of ferritin nanoparticles in transistor-like devices. Inside this type of device, it was proposed to use ferritin layers as floating nanodot gates for non-volatile memory applications. In fact, the fabrication of floating nanodot gates presents issues regarding the size uniformity and dot density with conventional methods. By having the capacity to form and keep a metal NP inside its core in a very stable way, ferritin has raised strong interest in fabricated nanodots with high uniformity and high density at low temperatures and under ambient conditions. The ferritin was used as a template to encapsulate a metal NP in its core, and after its immobilization on a solid surface, it can release the metal NP by removing its amino acid shell. Therefore, it forms arrays of metallic nanodots. In 2006, Matsui *et al.*[80] realized a two-dimensional ordered array of ferritin onto a silicon substrate from the perspective of making a metal oxide FET (MOSFET). A low-temperature polycrystalline silicon thin film transistor (LTPS-TFT) flash memory was reported by Ichikawa *et al.* (2008)[81], where ferritins were deposited onto an APTES functionalised Si/SiO_2 substrate (Figure 19.a–b). After a heating process, the amino acid shells of the ferritins were removed, and the remaining cores formed a floating gate embedded in the control oxide. The LTPS-TFT showed a drain current-gate voltage with a hysteresis (threshold voltage shift) due to the charging and discharging of the ferritin cores. More recently, it was reported that the fabrication of a reduced graphene oxide (rGO)-based FET (Figure 19.c) for detection of orthophosphate ions (HPO_4^{2-}) in water.[82] Inside this device, ferritins were labelled on rGO nanosheets deposited onto a silicon surface. In the sensing process, HPO_4^{2-} binds with the ferritin core, leading to a change in the electrical conductivity of the rGO sheet (Figure 19.d).

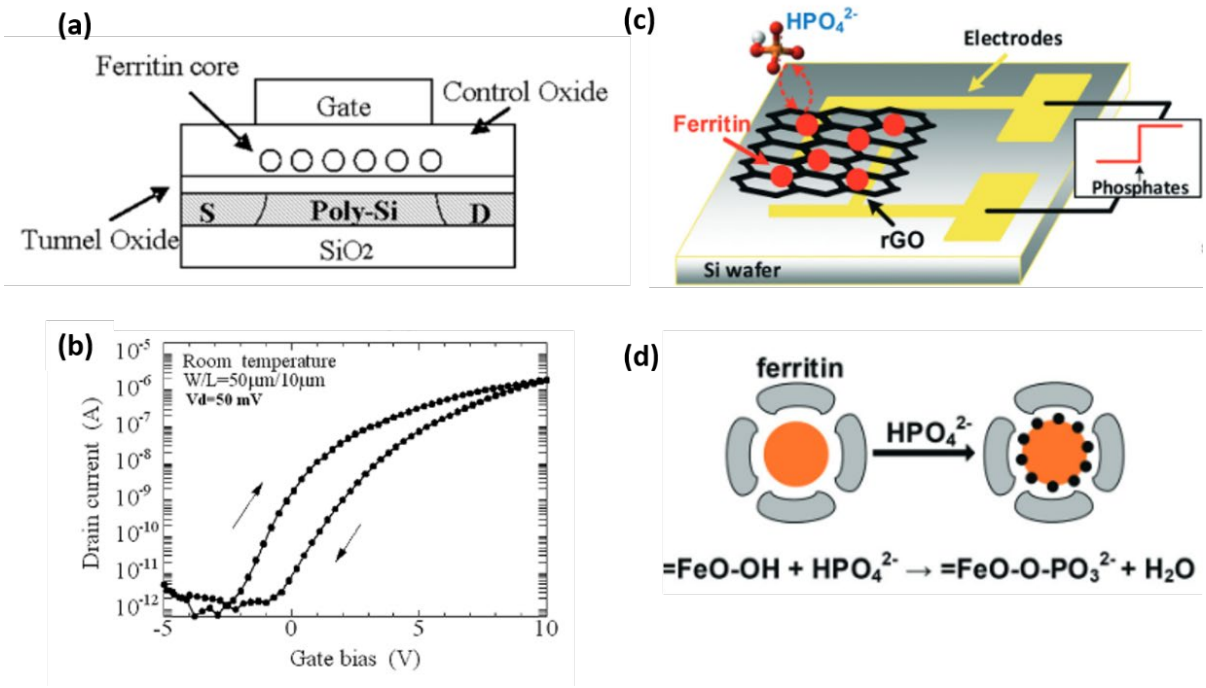

Figure 19 : Ferritin in transistor-like devices. (a) structure of the LTPS-TFT flash memory transistor. (b) drain current-gate voltage characteristics of the LTPS-TFT transistor with ferritin cores. (c) schematic of the rGO/ferritin FET for HPO_4^{2-} detection. (d) schematic of the sensing process. HPO_4^{2-} binds to the iron core of the ferritin. [81,82]

2.3. Long-range electron transport through ferritin

The latter part presented some results about ETp through ferritin inside junctions that prompt us to look closer at it, especially for the long-range transport of electrons. In fact, redox metalloproteins possess the ability to transport single electrons over long distances.[83] In the case of the ferritin, it was first shown from STM measurements that ETp is temperature-induced and therefore indicates a hopping mechanism (Rakshit *et al.*, 2010).[84] Furthermore, a 100 nm route for ETp was reported for an assembled multilayer based on ferritin nanocages with polyallylamine hydrochloride (PAH) (Ko *et al.*, 2011).[85] In this configuration, the assembly is operating as a nanoscale memory device (switching mechanism) where ferrihydrites cores act as trapping sites that capture electrons from electrodes, which are released by applying a high electric field. The charge trap/release state of the assembly multilayer was investigated by KPFM. By applying positive and negative potential on the surface, they created ferritin in charge-trap states (yellow regions) and release states (dark regions), respectively. The clear contrast measured by KFPM and shown in Figure 20.a confirms the strong non-volatile memory effect of the assembled multilayer. Moreover, the ON-OFF behaviour of ferritin nanoparticles

was investigated by c-AFM on one bare ferritin deposited on a Pt-coated silicon substrate. As shown in Figure 20.b, the bipolar switching behaviour of ferritin is confirmed by the I-V curve shape. The ferrihydrite core of ferritin is a conductive path formed by electron hopping between charge trap sites.

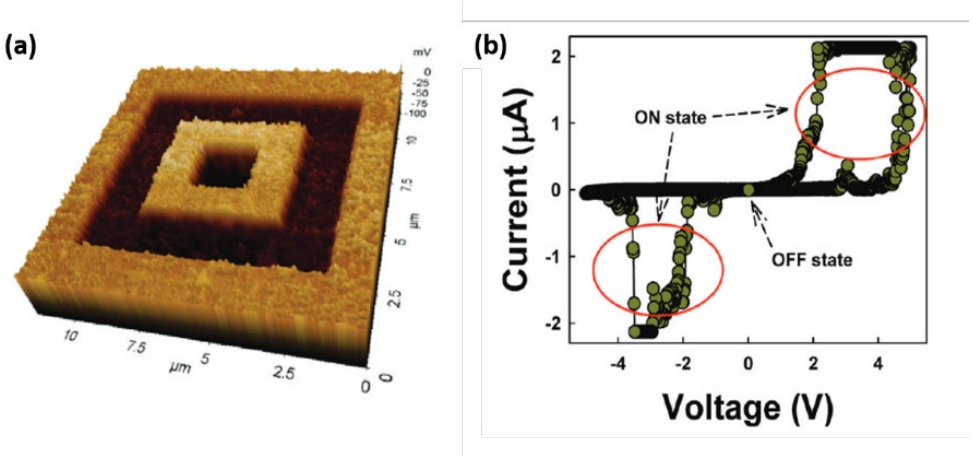

Figure 20 : Electron transport between ferritin senses by KPFM and c-AFM. (a) 3D KPFM image of PAH/ferritin multilayer. The yellow region corresponds to the charge-trap state and the dark region to the release state of the ferritin assembly. (b) I-V curve of one bare ferritin measured by c-AFM with current set at 2.1 µA.[85]

Electron transport over a length of one micrometer (or several micrometers) is the longest transport length reported so far for a ferritin assembly, by Bera *et al.* (2019).[86] In their study, they performed electrostatic layer-by-layer adsorption of cationized and negatively charged ferritin on a *n*-silicon substrate. They showed ETp across 40 nm of ferritin layers by c-AFM (vertical) and over 40 µm along the ferritin layers by interdigitated electrode-based measurement (lateral). Such long-range vertical transport is made possible by the stacking of ferritin layers to form an electronic bulk material that lowers the values of the indirect band gap as the number of ferritin layers increases, until the sixth layer, where it gets saturated. Also, compared to the holoferritin monolayer, the holoferritin multilayer showed fewer variations in band gap value (< 0.1 eV) as it presents fewer void areas, which exposed the substrate and interfered with the electron transport measurement. The substrate influence is clearly identified by KPFM, which showed a larger variation of the surface potential for a holoferritin monolayer than for holoferritin higher layers (Figure 21.a). The CPD image of a 15 µm² area recorded on a cationized holoferritin monolayer showed a relatively equipotential area with 40 mV variation (Figure 21.b). For lateral current measurements, a ferritin multilayer was deposited on a silicon

surface inside a 40 µm channel positioned between two Ni/Au electrodes. This configuration provides a lower contact resistance compared to the contact with the c-AFM tip. It showed a current at the nA level for apoferritin (Figure 21.c) and 1000 times higher for holoferritin (Figure 21.d). Considering the transport length scale of the ferritin multilayer presented before, the electron transport mechanism that has the highest possibility of occurring here is the inelastic hopping between trap sites of Fe^{2+}/Fe^{+3}.

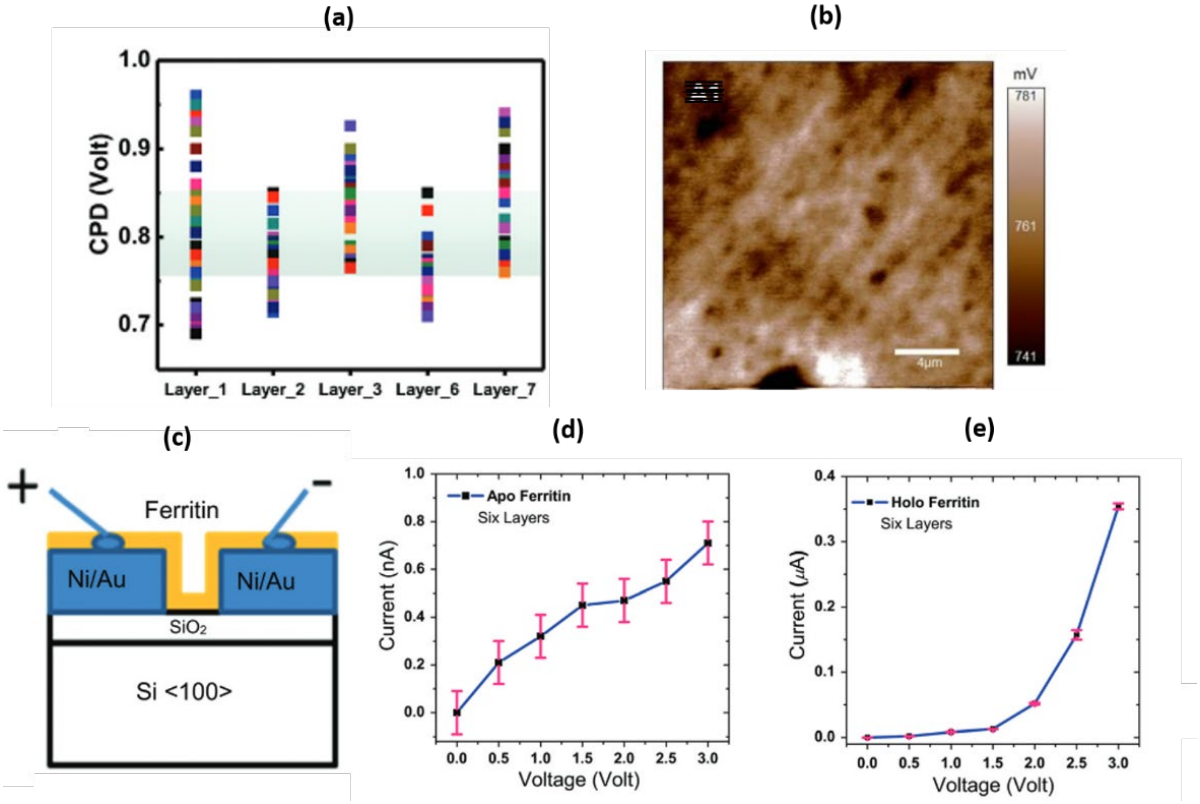

Figure 21 : KPFM and c-AFM measurements of ferritin multilayer. (a) data sets of surface potential (CPD) measured on holoferritin layers. The shaded area indicated that a high percentage of CPD data sets belong to this range. (b) KPFM image of a large area (10 – 20 µm²) of a cationized holoferritin monolayer. (c) schematic of the protein-coated electrode configuration for lateral conductivity measurement with lateral I-V response for a six-layer apoferritin multilayer (d) and a six-layer holoferritin multilayer (e).

However, the ETp across a single AfFtn-AA monolayer was recently studied inside junctions with an EGaIn (eutectic gallium indium) as a top electrode and various types of bottom electrodes: gold template-stripped (Au^{TS})[52], copper (Cu)[87], and nickel template-stripped (Ni^{TS})(Figure 22.a–c).[88] Ferritins with different amounts of iron content (from the apoferritin to the fully loaded holoferritin with 4800Fe) were immobilized on the bottom electrode via an organic or graphene linker. By AFM measurement, it appears that the size of

the ferritin, once "dry" and deposited on the surface, tends to reduce as the iron content decreases. For an apoferritin, the size is about 2-3 nm and increases to 10-12 nm for a 4800Fe ferritin (the diameter of the ferritin in solution is around 12 nm) (Figure 22.d–e). Therefore, the size of the ferritin is strongly related to the amount of iron inside its core.

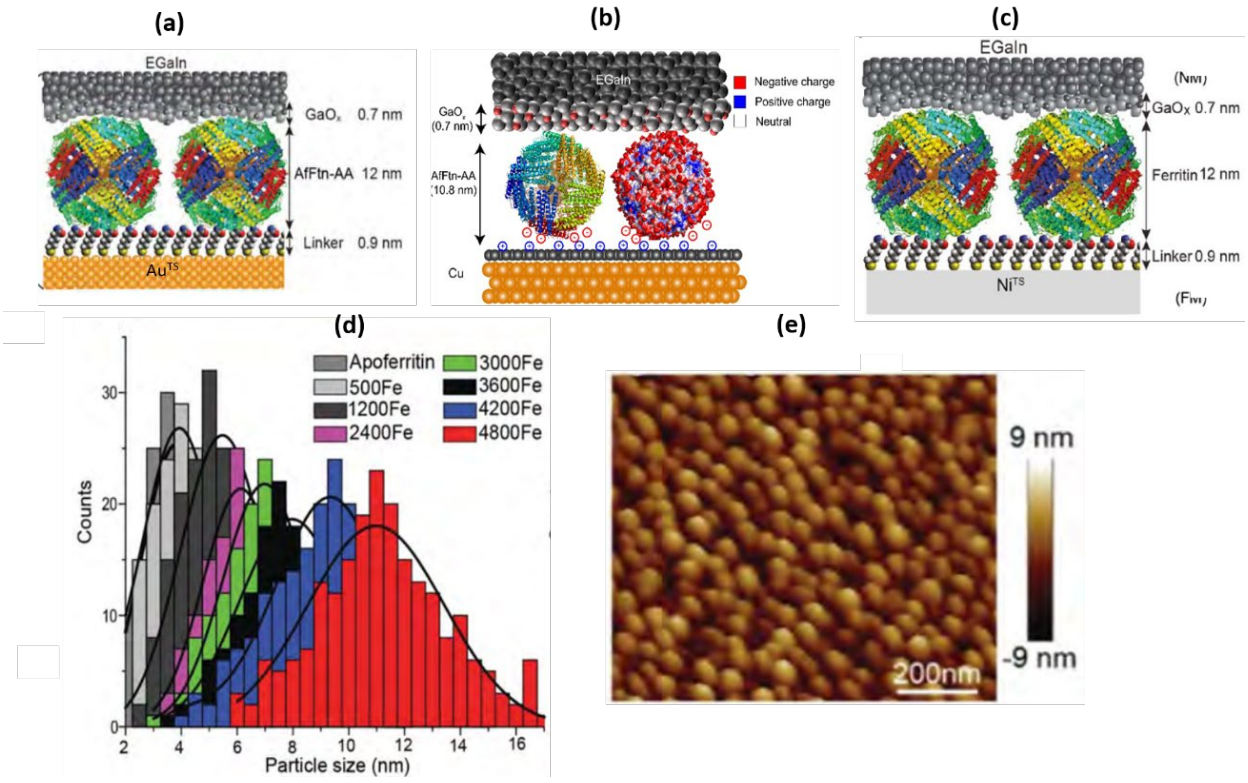

Figure 22 : Ferritins (AfFtn-AA) in various tunnel junctions and AFM measurements. Schematics of AfFtn-AA in different tunnel junctions with an EGaIn (eutectic gallium indium) top electrode and Au (a), Cu (b), and Ni (c) bottom electrodes. (d) size distribution of AfFtn-AA with different iron content immobilized on an Au surface. Gaussian fits are represented on the distributions. (e) topography image of a gold surface with AfFtn-AA 2400Fe covalently immobilized on a linker self-assembled monolayer.[52,87,88]

When the ferritin is in the junction, the variation of diameter as a function of the iron loading allows studying the electron transport dependence of the distance between the two electrodes d (in nm), via measurement of the current density J (in A.cm^{-2}). Kumar *et al.* (2016)[52] reported the current density for Au^{TS}/linker/AfFtn-AA/GaOx/EGaIn junctions with different sizes of ferritin. The results showed a graphic of measured J (for a given potential) as a function of d (Figure 23.a), which indicates a transition in the ETp mechanism from temperature-independent direct (coherent) tunnelling to temperature-independent indirect (sequential) tunnelling, for d = 6 nm (i.e., for AfFtn-AA 2400Fe). Similar results were reported

for Ni^{TS} and Cu bottom electrodes. Furthermore, by varying the temperature T (in K) of the current density measurements, it was shown that the transport mechanism of apoferritin is inelastic hopping (Figure 23.b−c). Thereby, the ETp across one ferritin monolayer is temperature-independent due to the presence of the iron oxide core and exhibits coherent or sequential tunnelling as a function of its size, which is related to the loading of its iron core. Therefore, the configuration of the iron core impacts the overall electronic behaviour of the ferritin. It is believed that there are intrinsic interactions between the amino acid shell and the iron core that dictate the regime of tunnelling. Therefore, it is interesting to turn toward an analysis of the ferritin's electronic properties in a "dry" state and immobilized on a substrate. First, by studying the effect of the iron core loading on the charge state of the ferritin and its interaction with a given substrate. During this thesis, we studied the electrostatic behaviour of dry ferritin in both single and dense configurations using a KPFM.

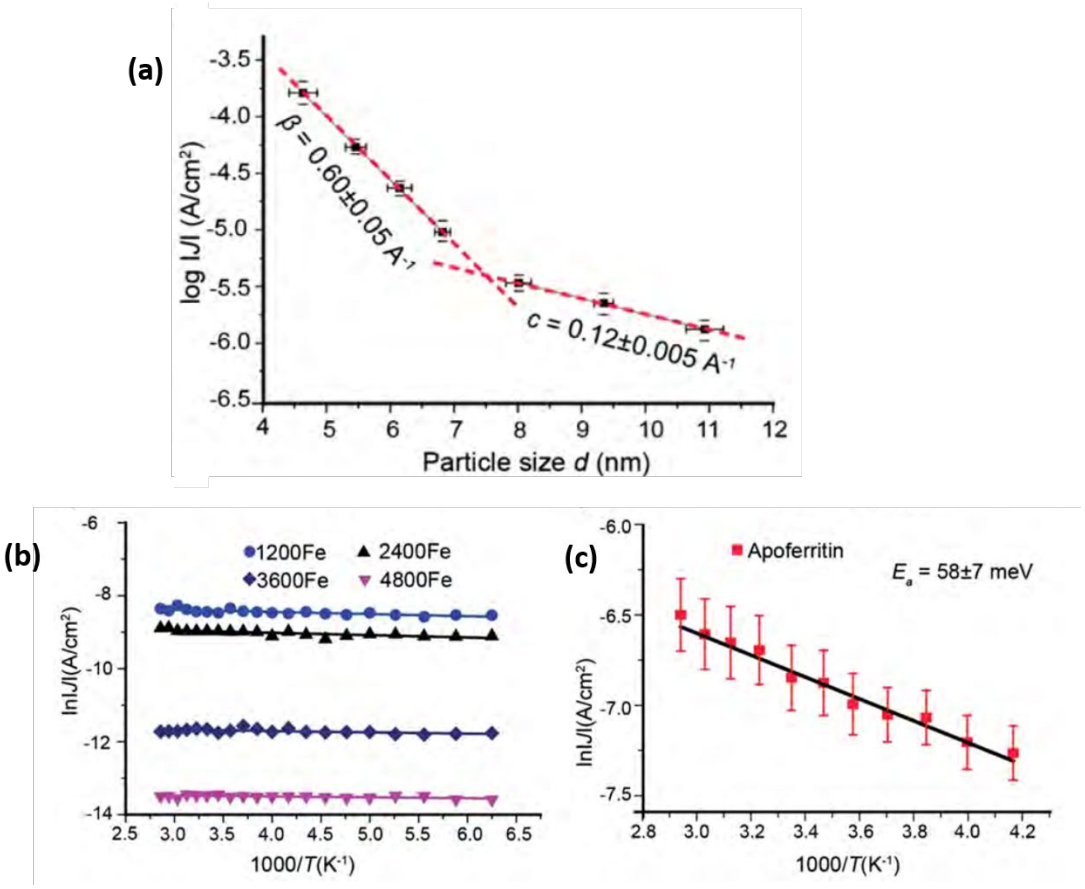

Figure 23 : Long-range tunnelling transport of the loaded ferritin (AfFtn-AA) embedded in a tunnel junction as a function of the size of the ferritin and temperature T (K). (a) graphic of the current density J (A.cm^{-2}) measured at a given potential as a function of the electrode-electrode distance d (nm). (b) J measured at a given potential as a function of the temperature for tunnel junctions with AfFtn-AA at different loadings. (c) J measured at a given potential as a function of the temperature for a tunnel junction with apoferritin.[52]

3. Application of the Kelvin Probe Force Microscopy

During this thesis, Kelvin Probe Force Microscopy (KPFM) was the key instrument to measure the local charges and electrostatic effects on nanoparticles (AuNPs and AfFtn-AAs) once immobilized on a surface. The KPFM is an advanced technique of the atomic force microscopy (AFM), one of the many probing techniques using a sharp tip to scan a surface and gather sample information. In this section, we review the reported work using the KPFM to visualize and measure the surface potential of nanoobjects, particularly biomaterials. The analysis of a sample surface with the KPFM provides valuable information such as the work function and the surface potential.

3.1. KPFM to detect local charge of nanoparticles

The KPFM device was invented in 1991 and became an important tool to measure the work function and surface charge distribution of metal/semiconductor surfaces[81,82] and semiconductor devices.[91,92] By scanning the surface, the KPFM can visualize many electrostatic effects with high spatial resolution. Tal *et al.* (2004)[93] clearly identified interfacial potential dipoles across a metal/organic/metal layered structure, and these results are inferred from potential profiles that can only be performed with a KPFM. The simultaneously detection of the work function with the topography shows various areas on the potential images with distinguishable work functions depending on the material. Unlike conventional macroscopic techniques such as photoelectron spectroscopy, which deduces an averaged work function of an unknown topography, the KPFM can detect local electrical properties at complex areas (e.g., the interface of nanomaterials), and this asset makes it suitable to detect local charges of single nanoparticles on a surface. Previous work reported the KPFM measurement of gold nanoparticles with varying diameters deposited on doped silicon grafted with an organic monolayer (Zhang *et al.*,(2014))[17]. By scanning one sample only, they could determine the work functions of the AuNPs as a function of their size (Figure 24.b), which were different from the bulk one. Furthermore, the KPFM was used to determine the work function variation as a function of the thickness of 2D nanomaterials such as graphene[94] and molybdenum disulphide (MoS_2).[95] In view of the above features, the KPFM device appears to be an appropriate tools to probe biomaterials such as DNA, proteins and nucleotides, which are molecules with a complex structure.

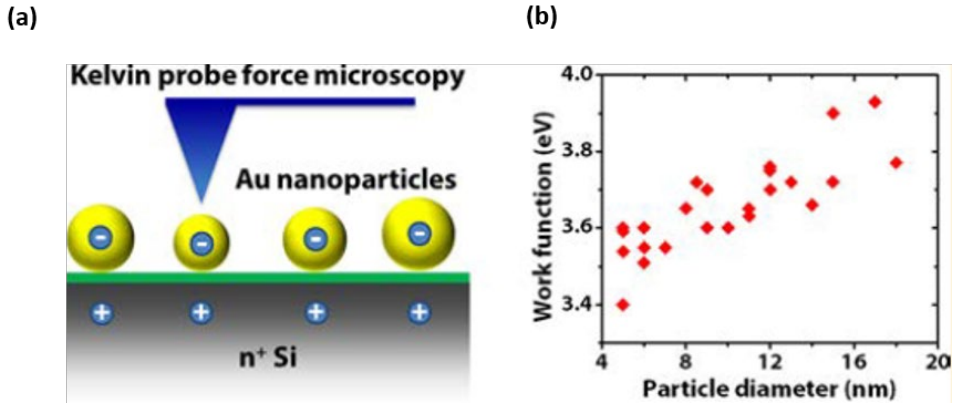

Figure 24 : KPFM measurement of gold nanoparticles (AuNPs) on silicon (Si). (a) schematic of the KPFM measurement of the AuNPs deposited on a Si substrate covered with a grafter organic monolayer (GOM). (b) Work function of the AuNPs as a function of their diameter.[17]

3.2. KPFM for biomolecular electronics

The use of the KPFM tool on biomaterials came from the desire to understand the interactions between biomolecules. In fact, many functions of these biomolecules are driven by electrostatic interactions with other molecules, which are closely related to their surface potential.[96] This latter also brings strong insight into the molecular structure of biomolecules. To understand these interactions, the electrostatic properties of individual biomolecules need to be known. Primary KPFM work on biomaterials revealed the surface potential of biomolecules such as proteins[97], DNA,[98] and lipids,[99] but at a low resolution or assembly level. However, Leung *et al.*(2009-2010)[100,101] showed topography (Figure 25.a) and surface potential (Figure 25.b) images at the molecular level of silicon and mica surfaces covered with avidin proteins (a 58 kDa tetrameric protein) and DNAs. At a low density of coverage, the positive potential of a single avidin was distinguishable, surrounded by a more negative substrate (Figure 25.c). Therefore, it showed that we can visualize complex biomaterials at the nanoscale in a straightforward manner, using KPFM. In fact, this is a non-contact and label-free technique that does not damage the structure, spatial configuration, or local properties of the analysed biomaterials. It has been presented as a promising alternative technique to the conventional fluorescence or mass spectroscopy detection method for microarrays of oligonucleotides or proteins.[102,103] However, the KPFM visualisation of biomolecule at the single particle level is still in its early stages. During this thesis, we showed well resolved potential images of individual ferritin nanocages.

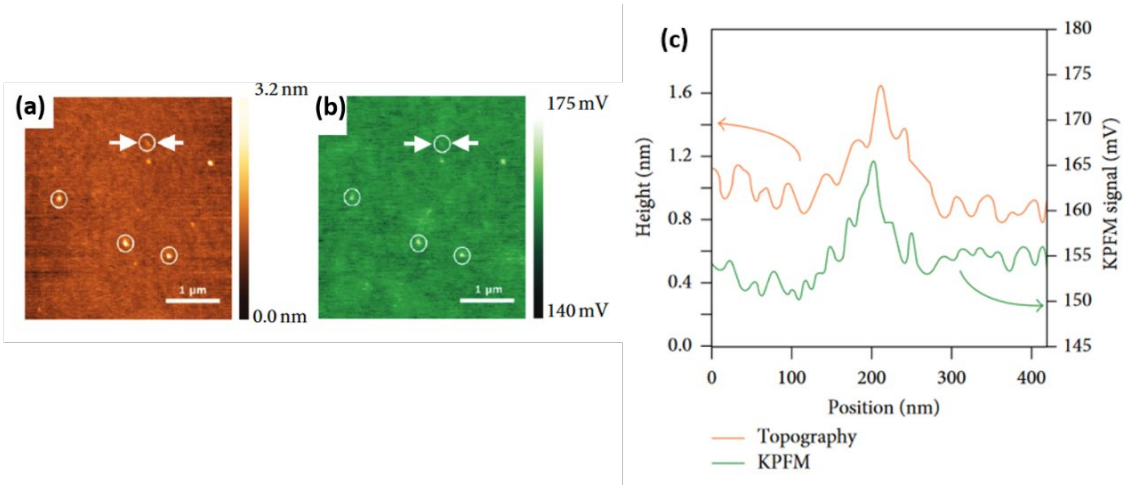

Figure 25 : KPFM images of avidin deposited on a silicon surface. (a) AFM topography image and the corresponding surface potential image of avidin on silicon. (c) Height and potential profiles of one avidin. Line profiles correspond to the topographic and potential data at the location indicated by arrows.[100]

4. References

[19] Amdursky Nadav, Eric Daniel Głowacki, and Paul Meredith. « Macroscale Biomolecular Electronics and Ionics ». *Advanced Materials* 31, nº 3 (2019): 1802221.

[20] Facci Paolo. « Biomolecular Electronics », *Biomolecular Electronics*, 1-17. (2014).

[21] Li Jeng-Lin, Tai-Yi Lin, Po-Lin Chen, Ting-Ni Guo, Shu-Yi Huang, Chun-Hong Chen, Chin-Hsien Lin and Chih-Chiang Chan. « Mitochondrial Function and Parkinson's Disease: From the Perspective of the Electron Transport Chain ». *Frontiers in Molecular Neuroscience* 14 (2021): 797833.

[22] Vuorema Anne, Philip John, Marjo Keskitalo, M. Anbu Kulandainathan, and Frank Marken. « Electrochemical and Sonoelectrochemical Monitoring of Indigo Reduction by Glucose ». *Dyes and Pigments* 76, nº 2 (2008): 542-49.

[23] Głowacki Eric Daniel, Gundula Voss, and Niyazi Serdar Sariciftci. « 25th Anniversary Article: Progress in Chemistry and Applications of Functional Indigos for Organic Electronics ». *Advanced Materials* 25, nº 47 (2013): 6783-6800.

[24] Uehara, K, K Takagishi, et M Tanaka. « The Al/indigo/Au photovoilaic cell », *Solar Cells*, 22 (1987), 295-301

[25] Yao Masaru, Kentaro Kuratani, Toshikatsu Kojima, Nobuhiko Takeichi, Hiroshi Senoh, and Tetsu Kiyobayashi. « Indigo Carmine: An Organic Crystal as a Positive-Electrode Material for Rechargeable Sodium Batteries ». *Scientific Reports* 4, nº 1 (2014): 3650.

[26] Sultana Irin, Md. Mokhlesur Rahman, Jiazhao Wang, Caiyun Wang, Gordon G. Wallace, and Hua-Kun Liu. « All-Polymer Battery System Based on Polypyrrole (PPy)/Para (Toluene Sulfonic Acid) (PTS) and Polypyrrole (PPy)/Indigo Carmine (IC) Free Standing Films ». *Electrochimica Acta* 83 (2012): 209-15.

[27] Mihai Irimia-Vladu, Eric D. Głowacki, Pavel A. Troshin, Günther Schwabegger, Lucia Leonat, Diana K. Susarova, Olga Krystal, Mujeeb Ullah, Yasin Kanbur, Marius A. Bodea, Vladimir F. Razumov, Helmut Sitter, Siegfried Bauer, and Niyazi Serdar Sariciftci, « Indigo - A Natural Pigment for High Performance Ambipolar Organic Field Effect Transistors and Circuits », *Adv. Material,* (2012), 24, 375-380

[28] Klimovich Irina V., Alexander V. Zhilenkov, Lidiya I. Kuznetsova, Lubov A. Frolova, Olga R. Yamilova, Sergey I. Troyanov, Konstantin A. Lyssenko, and Pavel A. Troshin. « Novel Functionalized Indigo Derivatives for Organic Electronics ». *Dyes and Pigments* 186 (2021): 108966.

[29] Pitayatanakul Oratai, Toshiki Higashino, Tomofumi Kadoya, Masaki Tanaka, Hirotaka Kojima, Minoru Ashizawa, Tadashi Kawamoto, Hidetoshi Matsumoto, Ken Ishikawa, and Takehiko Mori. « High Performance Ambipolar Organic Field-Effect Transistors Based on Indigo Derivatives ». *J. Mater. Chem. C* 2, nº 43 (2014): 9311-17.

[30] Sreelakshmi B., and R. Thamankar. « Coexistence of Synaptic Behaviour and Negative Differential Resistance at Room Temperature in the Resistive Switching Device Based on Natural Indigo Molecules ». *Dyes and Pigments* 219 (2023): 111638.

[31] Ehrenfreund E, D Moses, A J Heeger, J Cornil, and J L Brddas. « Doped -Carotene Films: Spinless Charge Storage Stabilized by Structural Relaxation ». *CHEMICAL PHYSICS LETTERS* 196, nº 1 (1992).

[32] Yakuphanoglu F., M. E. Aydin, and T. Kiliçoğlu. « Photovoltaic Properties of Au/β -Carotene/n-Si Organic Solar Cells ». *The Journal of Physical Chemistry B* 110, nº 20 (2006): 9782-84.

[33] Wang Xiao-Feng, Li Wang, Zhongqiang Wang, Yuwei Wang, Naoto Tamai, Ziruo Hong, and Junji Kido. « Natural Photosynthetic Carotenoids for Solution-Processed Organic Bulk-Heterojunction Solar Cells ». *The Journal of Physical Chemistry C,* 117, nº 2 (2013): 804-11.

[34] Calogero Giuseppe, Jessica Barichello, Ilaria Citro, Paolo Mariani, Luigi Vesce, Antonino Bartolotta, Aldo Di Carlo, and Gaetano Di Marco. « Photoelectrochemical and Spectrophotometric Studies on Dye-Sensitized Solar Cells (DSCs) and Stable Modules (DSCMs) Based on Natural Apocarotenoids Pigments ». *Dyes and Pigments* 155 (2018): 75-83.

[35]Singh, Ajay, et Trinetra Mukherjee. « Application of Carotenoids in Sustainable Energy and Green Electronics ». *Materials Advances* 3, nº 3 (2022): 1341-58.

[36] Murphy E.J. « The Temperature Dependence of the Conductivity of Dry Cellulose ». *Journal of Physics and Chemistry of Solids* 15, nº 1-2 (1960): 66-71.

[37] Wan Ying, Katherine A.M Creber, Brant Peppley, and V.Tam Bui. « Ionic Conductivity of Chitosan Membranes ». *Polymer* 44, nº 4 (2003): 1057-65.

[38] Deng Yingxin, Erik Josberger, Jungho Jin, Anita Fadavi Roudsari, Brett A. Helms, Chao Zhong, M. P. Anantram, and Marco Rolandi. « H+-Type and OH−-Type Biological Protonic Semiconductors and Complementary Devices ». *Scientific Reports* 3, nº 1 (2013): 2481.

[39] Murphy E.J., « Ionic Conduction in Keratin (Wool) ». *Journal of Colloid and Interface Science* 54, nº 3 (1976): 400-408.

[40] Powell Michael R., and Barnett Rosenberg, « The Nature of the Charge Carriers in Solvated Biomacromolecules ». *Journal of Bioenergetics* 1, nº 6 (1970): 493-509.

[41] Bo Liang, Lu Fang, Yichuan Hu, Guang Yang, Qin Zhu, and Xuesong Ye, « Fabrication and application of flexible graphene silk composite film electrodes decorated with spiky Pt nanospheres », *Nanoscale*, (2013), 00, 1-3.

[42] Tsukada Shingo, Hiroshi Nakashima, and Keiichi Torimitsu. « Conductive Polymer Combined Silk Fiber Bundle for Bioelectrical Signal Recording », *PLOS ONE,* 7, nº 4 (2012)

[43] Altamura Lucie, Christophe Horvath, Saravanan Rengaraj, Anaëlle Rongier, Kamal Elouarzaki, Chantal Gondran, Anthony L. B. Maçon, *et al.* « A Synthetic Redox Biofilm Made

from Metalloprotein–Prion Domain Chimera Nanowires ». *Nature Chemistry* 9, nº 2 (2017): 157-63.

[44] Ordinario David D., Long Phan, Jonah-Micah Jocson, Tam Nguyen, and Alon A. Gorodetsky. « Protonic Transistors from Thin Reflectin Films ». *APL Materials* 3, nº 1 (2015): 014907.

[45] Wu Guodong, Ping Feng, Xiang Wan, Liqiang Zhu, Yi Shi, and Qing Wan. « Artificial Synaptic Devices Based on Natural Chicken Albumen Coupled Electric-Double-Layer Transistors ». *Scientific Reports* 6, nº 1 (2016): 23578.

[46] Ing Nicole L., Mohamed Y. El-Naggar, and Allon I. Hochbaum. « Going the Distance: Long-Range Conductivity in Protein and Peptide Bioelectronic Materials ». *The Journal of Physical Chemistry B* 122, nº 46 (2018): 10403-23.

[47] Bostick Christopher D, Sabyasachi Mukhopadhyay, Israel Pecht, Mordechai Sheves, David Cahen, and David Lederman. « Protein Bioelectronics: A Review of What We Do and Do Not Know ». *Reports on Progress in Physics* 81, nº 2 (2018): 026601.

[48] Ron Izhar, Israel Pecht, Mordechai Sheves, and David Cahen. « Proteins as Solid-State Electronic Conductors ». *Accounts of Chemical Research* 43, nº 7 (2010): 945-53.

[49] Koch Matthias, Francisco Ample, Christian Joachim, et Leonhard Grill. « Voltage-Dependent Conductance of a Single Graphene Nanoribbon ». *Nature Nanotechnology* 7, nº 11 (2012): 713-17.

[50] Lafferentz, Leif, Francisco Ample, Hao Yu, Stefan Hecht, Christian Joachim, et Leonhard Grill. « Conductance of a Single Conjugated Polymer as a Continuous Function of Its Length ». *Science* 323, nº 5918 (2009): 1193-97.

[51] Sepunaru Lior, Israel Pecht, Mordechai Sheves, et David Cahen. « Solid-State Electron Transport across Azurin: From a Temperature-Independent to a Temperature-Activated Mechanism ». *Journal of the American Chemical Society* 133, nº 8 (2011): 2421-23.

[52] Kumar, Karuppannan Senthil, Rupali Reddy Pasula, Sierin Lim, et Christian A. Nijhuis. « Long-Range Tunneling Processes across Ferritin-Based Junctions ». *Advanced Materials* 28, nº 9 (2016): 1824-30.

[53] De Rienzo F., R.R. Gabdoulline, M. C. Menziani, and R.C. Wade. « Blue Copper Proteins: A Comparative Analysis of Their Molecular Interaction Properties ». *Protein Science* 9, nº 8 (2000): 1439-54.

[54] Li Wenjie, Lior Sepunaru, Nadav Amdursky, Sidney R. Cohen, Israel Pecht, Mordechai Sheves, and David Cahen. « Temperature and Force Dependence of Nanoscale Electron Transport *via* the Cu Protein Azurin ». *ACS Nano* 6, nº 12 (2012): 10816-24.

[55] Amdursky Nadav, Israel Pecht, Mordechai Sheves, and David Cahen. « Electron Transport via Cytochrome C on Si–H Surfaces: Roles of Fe and Heme ». *Journal of the American Chemical Society* 135, nº 16 (2013): 6300-6306.

[56] Li Debin, Peter M Gannett, and David Lederman. « An Investigation into the Feasibility of Myoglobin-Based Single-Electron Transistors », *Nanotechnology* 23, nº 39 (2012): 395705.

[57] Hartvig Rune A., Marco Van De Weert, Jesper Østergaard, Lene Jorgensen and Henrik Jensen. « Protein Adsorption at Charged Surfaces: The Role of Electrostatic Interactions and Interfacial Charge Regulation ». *Langmuir* 27, nº 6 (2011): 2634-43.

[58] Rabe Michael. « Understanding Protein Adsorption Phenomena at Solid Surfaces ». *Advances in Colloid and Interface Science*, (2011).

[59] Rabe Michael, Dorinel Verdes, Michael Rankl, Georg R. J. Artus, and Stefan Seeger. « A Comprehensive Study of Concepts and Phenomena of the Nonspecific Adsorption of β-Lactoglobulin ». *ChemPhysChem* 8, nº 6 (2007): 862-72.

[60] Meissner Jens, Albert Prause, Bhuvnesh Bharti and Gerhard H. Findenegg. « Characterization of Protein Adsorption onto Silica Nanoparticles: Influence of PH and Ionic Strength ». *Colloid and Polymer Science* 293, nº 11 (2015): 3381-91.

[61] Silva-Bermudez P., and S.E. Rodil. « An Overview of Protein Adsorption on Metal Oxide Coatings for Biomedical Implants ». *Surface and Coatings Technology* 233 (2013): 147-58.

[62] Elofsson Ulla M, Marie A Paulsson, and Thomas Arnebrant. « Adsorption of [-Lactoglobulin A and B: Effects of Ionic Strength and Phosphate Ions », *Colloid and Surfaces B: Biointerface*, (1997) 163-169

[63] Secundo Francesco. « Conformational Changes of Enzymes upon Immobilisation ». *Chemical Society Reviews,* 42, nº 15 (2013): 6250.

[64] Norde Willem. « Adsorption of Proteins from Solution at the Solid-Liquid Interface ». *Advances in Colloid and Interface Science* 25 (1986) : 267-340.

[65] Norde Willem. « My Voyage of Discovery to Proteins in Flatland …and Beyond ». *Colloids and Surfaces B: Biointerfaces* 61, nº 1 (2008): 1-9.

[66] Granick S., « FERRITIN ». *Journal of Biological Chemistry*, 146, nº 2 (1942): 451-61.

[67] Rakshit Tatini, Sudipta Bera, Jayeeta Kolay andRupa Mukhopadhyay. « Nanoscale Solid-State Electron Transport via Ferritin: Implications in Molecular Bioelectronics ». *Nano-Structures & Nano-Objects,* 24 (2020): 100582.

[68] Zapien Donald C. and Michael A. Johnson, « Direct Electron Transfer of Ferritin Adsorbed at Bare Gold Electrodes ». *Journal of Electroanalytical Chemistry* 494, nº 2 (2000): 114-20.

[69] Axford Danny N and Jason J Davis. « Electron Flux through Apo-and Holoferritin ». *Nanotechnology*, 18, nº 14 (2007): 145502.

[70] Rakshit T., S. Banerjee and R. Mukhopadhyay. « Near-Metallic Behavior of Warm Holoferritin Molecules on a Gold (111) Surface ». *Langmuir* 26, nº 20 (2010): 16005-12.

[71] Xu Degao, Gerald D. Watt, John N. Harb and Robert C. Davis. « Electrical Conductivity of Ferritin Proteins by Conductive AFM ». *Nano Letters* 5, nº 4 (2005): 571-77.

[72] Bera Sudipta, Jayeeta Kolay, Siddhartha Banerjee and Rupa Mukhopadhyay. « Nanoscale On-Silico Electron Transport via Ferritins ». *Langmuir* 33, nº 8 (2017): 1951-58.

[73] Kumar Manish, Anjna Sharma, Indresh Kumar Maurya, Alpana Thakur and Sunil Kumar. « Synthesis of Ultra Small Iron Oxide and Doped Iron Oxide Nanostructures and Their Antimicrobial Activities ». *Journal of Taibah University for Science* 13, nº 1 (2019): 280-85.

[74] Colton J S, S D Erickson, T J Smith and R K Watt. « Sensitive Detection of Surface- and Size-Dependent Direct and Indirect Band Gap Transitions in Ferritin ». *Nanotechnology* 25, nº 13 (2014) : 135703.

[75] Rakshit Tatini and Rupa Mukhopadhyay. « Solid-State Electron Transport in Mn-, Co-, Holo-, and Cu-Ferritins: Force-Induced Modulation Is Inversely Linked to the Protein Conductivity ». *Journal of Colloid and Interface Science* 388, nº 1 (2012): 282-92.

[76] Esaki Leo. « New Phenomenon in Narrow Germanium p − n Junctions ». *Physical Review* 109, nº 2 (1958): 603-4.

[77] Chen J, W Wang, M A Reed, A M Rawlett, D W Price and J M Tour. « Room-Temperature Negative Differential Resistance in Nanoscale Molecular Junctions », *Applied Physics Letters*, (2000), V.77, n°8.

[78] Kolay J., S. Bera, T. Rakshit and R. Mukhopadhyay. « Negative Differential Resistance Behavior of the Iron Storage Protein Ferritin ». *Langmuir* 34, nº 9 (2018): 3126-35.

[79] Tang Qun, Hye Kyung Moon, Yoonmi Lee, Seok Min Yoon, Hyun Jae Song, Hyunseob Lim and Hee Cheul Choi. « Redox-Mediated Negative Differential Resistance Behavior from Metalloproteins Connected through Carbon Nanotube Nanogap Electrodes ». *Journal of the American Chemical Society* 129, nº 36 (2007): 11018-19.

[80] Matsui Takuro, Nozomu Matsukawa, Kenji Iwahori, Ken-Ichi Sano, Kiyotaka Shiba, and Ichiro Yamashita. « Realizing a Two-Dimensional Ordered Array of Ferritin Molecules Directly on a Solid Surface Utilizing Carbonaceous Material Affinity Peptides ». *Langmuir* 23, nº 4, (2007): 1615-18.

[81] Ichikawa Kazunori, Mami Fujii, Yukiharu Uraoka, Prakaipetch Punchaipetch, Hiroshi Yano, Tomoaki Hatayama, Takashi Fuyuki, and Ichiro Yamashita. « Nonvolatile Thin Film Transistor Memory with Ferritin ». *Journal of the Korean Physical Society* 54, nº 9(5) (2009): 554-57.

[82] Mao Shun, Haihui Pu, Jingbo Chang, Xiaoyu Sui, Guihua Zhou, Ren Ren, Yantao Chen, and Junhong Chen. « Ultrasensitive Detection of Orthophosphate Ions with Reduced Graphene Oxide/Ferritin Field-Effect Transistor Sensors ». *Environnemental Science: Nano* 4, nº 4 (2017): 856-63.

[83] Willner Itamar and Bilha Willner. « Biomaterials Integrated with Electronic Elements: En Route to Bioelectronics ». *Trends in Biotechnology* 19, nº 6 (2001): 222-30.

[84] Rakshit T., S. Banerjee and R. Mukhopadhyay. « Near-Metallic Behavior of Warm Holoferritin Molecules on a Gold (111) Surface ». *Langmuir* 26, nº 20 (2010): 16005-12.

[85] Ko Yongmin, Younghoon Kim, Hyunhee Baek and Jinhan Cho. « Electrically Bistable Properties of Layer-by-Layer Assembled Multilayers Based on Protein Nanoparticles ». *ACS Nano* 5, nº 12 (2011) : 9918-26.

[86] Bera Sudipta, Jayeeta Kolay, Pallabi Pramanik, Anirban Bhattacharyya and Rupa Mukhopadhyay. « Long-Range Solid-State Electron Transport through Ferritin Multilayers ». *Journal of Materials Chemistry C* 7, nº 29 (2019): 9038-48.

[87] Gupta Nipun Kumar, Senthil Kumar Karuppannan, Rupali Reddy Pasula, Ayelet Vilan, Jens Martin, Wentao Xu, Esther Maria May, *et al.* « Temperature-Dependent Coherent Tunneling across Graphene–Ferritin Biomolecular Junctions ». *ACS Applied Materials & Interfaces* 14, nº 39 (2022): 44665-75.

[88] Karuppannan Senthil Kumar, Rupali Reddy Pasula, Tun Seng Herng, Jun Ding, Xiao Chi, Enrique Del Barco, Stephan Roche, *et al.* « Room-Temperature Tunnel Magnetoresistance across Biomolecular Tunnel Junctions Based on Ferritin ». *Journal of Physics: Materials* 4, nº 3 (2021): 035003.

[89] Lee, Sangyeob, Aniketa Shinde, and Regina Ragan. « Morphological Work Function Dependence of Rare-Earth Disilicide Metal Nanostructures ». *Nanotechnology* 20, nº 3 (2009): 035701.

[90]Zerweck U, Ch Loppacher, T Otto, S Grafström, and L M Eng. « Kelvin Probe Force Microscopy of C_{60} on Metal Substrates: Towards Molecular Resolution ». *Nanotechnology* 18, nº 8 (2007): 084006.

[91] Buh G. H., H. J. Chung, C. K. Kim, J. H. Yi, I. T. Yoon, and Y. Kuk. « Imaging of a Silicon Pn Junction under Applied Bias with Scanning Capacitance Microscopy and Kelvin Probe Force Microscopy ». *Applied Physics Letters* 77, nº 1 (2000): 106-8.

[92] Ankudinov A. V., V. P. Evtikhiev, K. S. Ladutenko, A. N. Titkov, and R. Laiho. « Kelvin Probe Force Microscopy of Hole Leakage from the Active Region of a Working Injection-Type Semiconductor Laser Diode ». *Semiconductors* 40, nº 8 (2006): 982-89.

[93] Tal O., W. Gao, C. K. Chan, A. Kahn, and Y. Rosenwaks. « Measurement of Interface Potential Change and Space Charge Region across Metal/Organic/Metal Structures Using Kelvin Probe Force Microscopy ». *Applied Physics Letters* 85, nº 18 (2004): 4148-50.

[94] Panchal, Vishal, Ruth Pearce, Rositza Yakimova, Alexander Tzalenchuk, and Olga Kazakova. « Standardization of Surface Potential Measurements of Graphene Domains ». *Scientific Reports* 3, nº 1 (2013): 2597.

[95] Ochedowski Oliver, Kolyo Marinov, Nils Scheuschner, Artur Poloczek, Benedict Kleine Bussmann, Janina Maultzsch, and Marika Schleberger. « Effect of Contaminations and Surface Preparation on the Work Function of Single Layer MoS_2 ». *Beilstein Journal of Nanotechnology* 5 (2014): 291-97.

[96] Honig Barry, and Anthony Nicholls. « Classical Electrostatics in Biology and Chemistry ». *Science* 268, nº 5214 (1995): 1144-49.

[97] Gao Pei, and Yuguang Cai. « Label-Free Detection of the Aptamer Binding on Protein Patterns Using Kelvin Probe Force Microscopy (KPFM) ». *Analytical and Bioanalytical Chemistry* 394, nº 1 (2009): 207-14.

[98] Valdrè Giovanni. « Natural Nanoscale Surface Potential of Clinochlore and Its Ability to Align Nucleotides and Drive DNA Conformational Change ». *European Journal of Mineralogy* 19, nº 3 (2007): 309-19.

[99] Leonenko Zoya, Mathias Rodenstein, Jana Döhner, Lukas M. Eng, and Matthias Amrein. « Electrical Surface Potential of Pulmonary Surfactant ». *Langmuir* 22, nº 24 (2006): 10135-39.

[100] Leung Carl, Helen Kinns, Bart W. Hoogenboom, Stefan Howorka, and Patrick Mesquida. « Imaging Surface Charges of Individual Biomolecules ». *Nano Letters* 9, nº 7 (2009): 2769-73.

[101] Leung Carl, Dario Maradan, Armin Kramer, Stefan Howorka, Patrick Mesquida, and Bart W. Hoogenboom. « Improved Kelvin Probe Force Microscopy for Imaging Individual DNA Molecules on Insulating Surfaces ». *Applied Physics Letters* 97, nº 20 (2010): 203703.

[102] Thompson Michael, Larisa-Emilia Cheran, Mingquan Zhang, Melissa Chacko, Hong Huo, and Saman Sadeghi. « Label-Free Detection of Nucleic Acid and Protein Microarrays by Scanning Kelvin Nanoprobe ». *Biosensors and Bioelectronics* 20, nº 8 (2005): 1471-81.

[103] Sinensky Asher K., and Angela M. Belcher. « Label-Free and High-Resolution Protein/DNA Nanoarray Analysis Using Kelvin Probe Force Microscopy ». *Nature Nanotechnology* 2, nº 10 (2007): 653-59.

Chapter III: Experimental methods. Production and characterisation of ferritin nanocages and surface characterisation techniques for nanoparticles on silicon

Introduction

This chapter will describe the experimental methods, protocols, and numerous apparatus used during this thesis. All the biochemistry around the production and characterisation of proteins was performed at the NTU laboratory in Singapore. Surface characterisation of particles on silicon (optical, topography, and electrical) were performed in the SU laboratory in France.

The first part of this chapter will be related to the production of the AfFtn-AA protein, introduced in the previous chapter, starting with the well-established recombinant DNA process with the *Escherichia coli* bacteria cell as host, and the experimental protocols followed to produce and purify AfFtn-AA proteins. After that, the purity, the size, and the surface charge characterisation techniques will be developed. The second part will describe the process of modulating the surface charge of AfFtn-AA by amino-acid substitution using the site-directed mutagenesis process. Finally, the third part will describe the optical Dark-Field Optical Microscopy (DFOM), the *Fourier* Transform Infrared Spectroscopy (FTIR) and the Kelvin Probe Force Microscopy (KPFM) used for the characterisation of immobilized nanoparticles on silicon.

1. AfFtn-AA protein production from *Escherichia coli* bacteria

1.1. Protein synthesis: introduction to the cell machinery

The ferritin proteins, like other proteins, are made of many amino acids joined end to end. Inside the cells, protein synthesis is carried out by the DNA (deoxyribonucleic acid) and the RNA (ribonucleic acid) polymerase. The DNA can be considered as the memory of the cell; it stores all the information for the production of proteins in the form of nucleotide (organic molecule) sequences, much like chains of zeros and ones store information in a computer. A given nucleotide sequence that codes for one protein is called a gene (all the genes of an organism are called the genome). The protein synthesis (or gene expression) is a two-step process. In the first step, the gene sequence from the DNA is transcribed by an RNA polymerase molecule (transcription step). On the second step, the transcribed sequence is read by a ribosome, a huge molecular machine that builds up the chain of amino acids that matches the instructions from the DNA (Figure 26.a) (translation step). In a genetic code, an amino acid is encoded by a nucleotide triples or codon.[104,105] The amino acid chain folds up in an α-helix or

a β-sheets structure (the secondary structure) via hydrogen bonds between the amino hydrogen and carboxyl hydrogen. It forms the polypeptide backbone, which in turn folds into a complex molecular shape (the tertiary structure) via interactions between the side chains of the amino acids. In some cases, two or more chains of proteins (also called subunits) self-assemble to form a quaternary structure. In the case of AfFtn-AA, 24 subunits self-assembled into a nanocage structure.[106] All the process described above is how the AfFtn-AA proteins are produced inside cells.

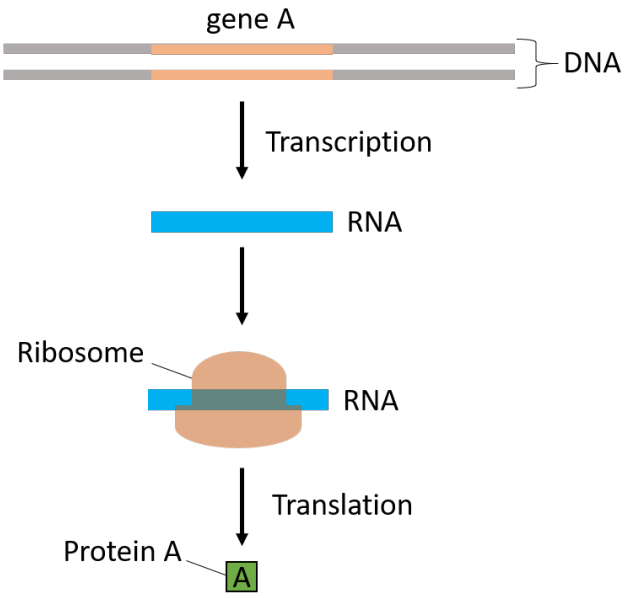

Figure 26 : Schematic of the gene expression process. The protein A is produced by the ribosome which reads the RNA copy of the gene A.[106]

1.2. Principle of recombinant DNA: from *A.fulgidus* genome to *E.coli* bacteria

The *Escherichia coli* (*E.coli)* species is a prokaryotic bacterium widely spread among mammalian, first described and isolated in 1885 by Escherich.[107] There are various types of *E.coli* strains that differ in their hazardous nature and are nowadays among the most studied organisms.[108] They are specifically studied in the biotechnology field, for which the *E.coli* bacteria presents many features: the availability of its complete genome sequence, its facility of handling, and its ability to grow fast and under both aerobic and anaerobic conditions. Such characteristics make it an essential host for microorganisms, and it is mostly used for the recombinant DNA process. This technique allows the *in vitro* modification of genetic material that is reintroduced inside a living organism afterwards to obtain improved and specific

characteristics.[109–111] Typically, a recombinant DNA process involves the modification of a DNA sequence with a desired gene, which is then introduced into a host cell that possesses the ability to express this specific gene.

Here, the AfFtn-AA expression gene sequence (AF0834) was extracted from the *A. fulgidus* genome (Figure 27.a) and cloned in a pET vector system (pET-11a): a double-stranded DNA sequence also called plasmid. The pET-11a is a powerful and widely used vector system for expression of recombinant protein. It was engineered to restrain specific gene between restriction site. The beginning and the end of the cloned gene sequence are marked by special "start" and "stop" signals, called T7 promoter and T7 terminator, respectively. The T7 promoter can be activated by reaction with a chemical inducer to drive high-level and specific expression of the gene of interest. The pET plasmid also carries an antibiotic resistant gene (AmpR) required for the cells to grow inside a culture media (Figure 27.b).[112] Afterwards, the pET vector was inserted into *E.coli* competent cells (DNA permeable cells) by a transformation step (see the detailed protocol in the Appendix III-1.5), a process in which a plasmid penetrates the membrane of a competent cell, generally via heat-shock[113] or electroporation[114]. For our study, the bacterial host cell strain chosen to upkeep the plasmids is the *E. coli* DH5-α strain and for the production of protein is the *E. coli* BL21(DE3)C + RIL strain. Then, bacterial host cells were grown in a culture media, mixed with glycerol ($C_3H_8O_3$) and frozen at −80 °C to make a long-term cell stock that can be reuse later.

For the AfFtn-AA, the recombinant DNA process was realized only once many years ago. Afterwards, the plasmid containing the ferritin expression gene sequence was extracted from the original bacterial host cell and transformed into other bacterial host cells. From which, in turn, the plasmid is extracted and transformed into another bacterial host cell, thus avoiding the contamination of the original stock. For this project, we made our own stock of *E.coli* BL21(DE3)C + RIL cells containing the ferritin expression gene (AF0834) with the two mutations K150A/R151A used for all the future experiments.

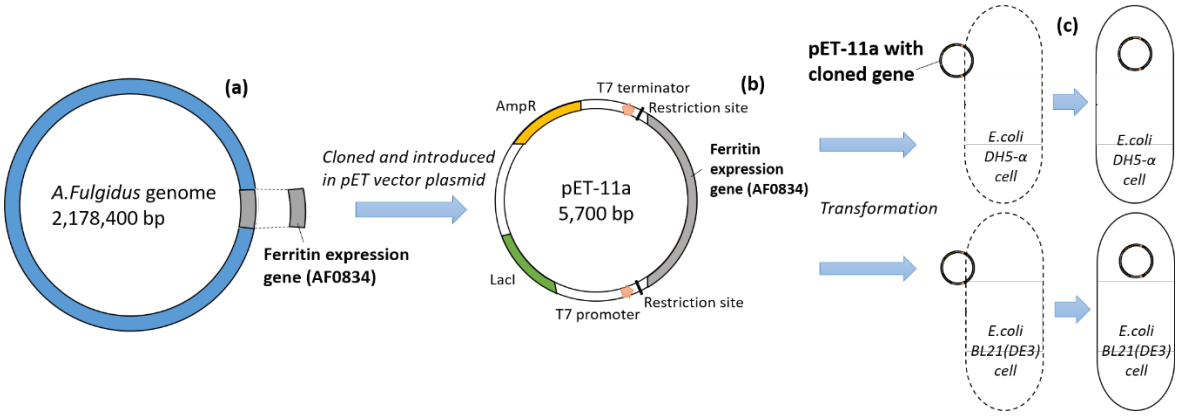

Figure 27 : Schematic of the recombinant DNA process for the AfFtn protein. (a) the ferritin expression gene from the A.fulgidus genome is extracted, and (b) cloned in an expression vector system, pET-11a. (c) the pET-11a vector is transformed into a DH5-α competent cell for maintain or BL21(DE3)C+ RIL competent cell for expression. The length of the genome sequence and the plasmid sequence is indicated in base-pair (bp) (1 bp = 1 nucleotide pair)

1.3. Production and purification of AfFtn-AA proteins

This part describes the experimental protocols for the production, purification, and characterisation of AfFtn-AA proteins. The Biochemistry methods performed in the NTU laboratory are described here, and the detailed protocols are in the Appendices III.

E.coli cell culture and expression of the AfFtn-AA gene

Before the expression of the AfFtn-AA gene, *E.coli* bacterial host cells need to multiply to reach a significant number and therefore maximize the concentration of protein that will be produced (see the detailed protocol in the Appendix III-1.1). For this, *E.coli* BL21(DE3)C+ RIL cells from our glycerol stock were inoculated in a LB ("lysogeny broth" or "*Luria-Bertani*") medium: an aqueous solution containing the required nutrients (peptides, yeast and NaCl)[115] for the cells to perform cellular division.[116] Cells were grown for 3 hours at 37 °C in air until the OD_{600} (the optical density measured at 600 nm with a spectrophotometer) of the cell culture was between 0.6 and 1. This interval corresponds to the end of the exponential growth phase, after which the number of dying cells equals the number of new cells formed, and therefore, the concentration of cells inside the culture remains steady (Figure 28).[117,118] Subsequently, when enough cells were produced, the overexpression of the ferritin gene was induced by adding a few milliliters of IPTG (isopropyl-β-D-thiogalactopyranoside) solution inside the cell culture. Each bacterium cell carrying the ferritin gene expression will start

producing AfFtn-AA dimers inside its membrane. After that, cells were harvested by centrifugation of the cell culture, collected in the form of pellets, and stored at −80 °C for future experiments.

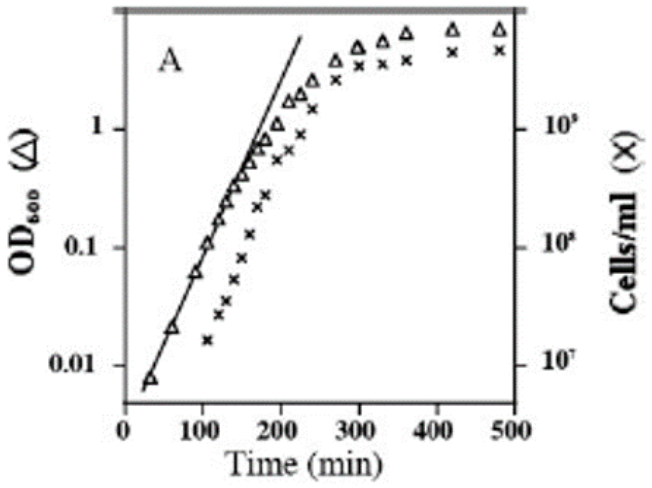

Figure 28 : Growth of E. coli in Luria-Bertani culture media. An overnight cell culture was diluted 5,000-fold in Luria-Bertani broth and cultivated at 37 °C with vigorous aeration. The OD_{600} (triangles) and cell concentration (crosses) were measured periodically.[118]

AfFtn-AA extraction and purification processes

The extraction of the ferritin dimers was performed by sonication of the cell pellets resuspended in a buffer solution (NaCl + HEPES solution at pH 7.4). The sonication is a lysis method which uses high-frequency ultrasound waves to break open the membranes of the cells and extracts their contents (Figure 29.a). Therefore, the ferritin dimers were dispersed in a HEPES buffer solution, but some impurities (membrane fragments, nucleic acids, bacterium proteins…) remain inside. To purify the solution, few steps were required. First, the lysate solution was heated at 85 °C for 10 minutes to denature proteins and to remove impurities (Figure 29). AfFtn-AA protein being produced from a thermophilic specie, it has therefore a high thermal stability and is not affected by the heat-treatment. Secondly, the lysate solution was centrifugated to separate the solubilized ferritins from the impurities (Figure 29.c). Only the supernatant is collected, and purified by the HIC method (hydrophobic interaction chromatography). This technique is one of the many FPLC (fast protein liquid chromatography) methods used to purify protein solutions (Figure 29.d). The HIC exploits the interaction between the hydrophobic areas of a protein and the hydrophobic ligands present in the base

matrix of the HIC column. When the solution to be purified flows inside the column, only the proteins are retained by the ligands of the base matrix due to hydrophobic interactions. In our case, the AfFtn-AA dimer protein has low hydrophobic interactions, and it is necessary to increase its hydrophobicity by adding a high concentration of ammonium sulphate ($NH_2SO_4^{2-}$).[119] Finally, ferritin dimers retained in the column are eluted with a HEPES buffer and stored at 4 °C for later experiments. (see the detailed protocol in the Appendix III-1.2). The purification of ferritins was performed with an *ÄKTA pure*^{TM} chromatography system from *Cytiva*. The purity of the protein solution was controlled by SDS-PAGE and the protein concentration was measured by the Bradford technique (see the detailed protocols in the Appendix III-2.1 and III-2.2, respectively).

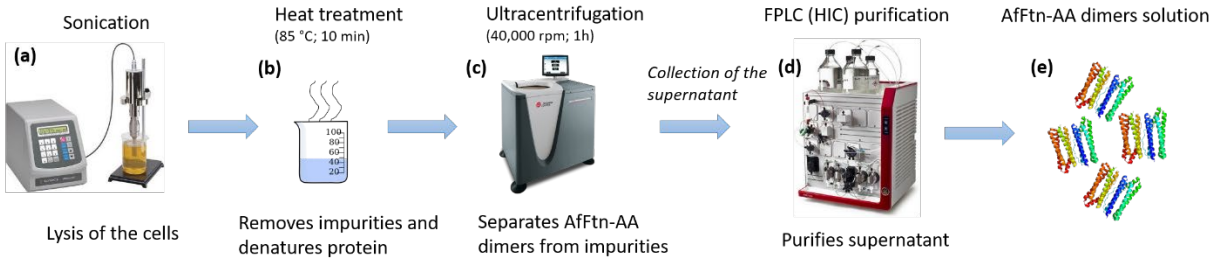

Figure 29 : Ferritin extraction and purification processes. (a) extraction of ferritin proteins by lysis of the E.coli cells. (b) heat-treatment to remove the impurities. (c) ultracentrifugation step to separate solubilized proteins from impurities. (d) HIC purification of the ferritin solution. (e) purified AfFtn-AA dimers solution.

SDS-PAGE (sodium dodecyl sulphate-polyacrylamide gel electrophoresis) is an analytical technique used to separate proteins in a mixed solution based on their molecular weights. The principle is based on the migration of the proteins inside a polyacrylamide gel, in response to an applied electrical field. Light proteins will flow faster than heavy ones, resulting in their separation inside the gel.[120,121] To control the purity of the ferritin solution, a small volume (≈ 3 µL) of the solution was swabbed at every step of the extraction and purification protocol (Figure 29) and loaded inside the gel. In the Figure 30 below, we see an image of an SDS-PAGE gel performed after AfFtn-AA purification. In the sample well (d), a purified AfFtn-AA solution was loaded, and one intense band around 20 kDa is seen, showing that we obtained a relatively pure protein solution.

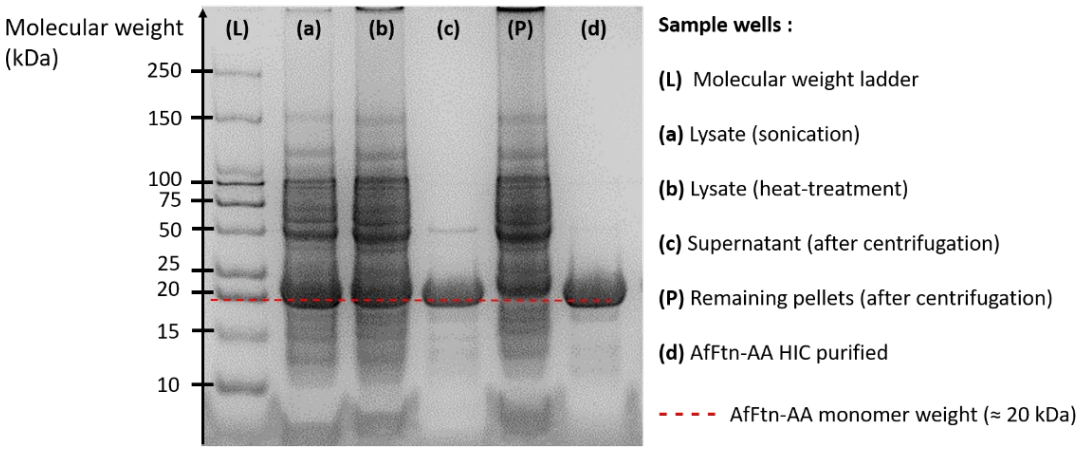

Figure 30: Image of a SDS-PAGE gel. In each well, a sample corresponding to a step of the purification process was introduced. A ladder (L) is added to control the molecular weight of the separated species. The remaining pellets (P), collected from the centrifugation and resuspended in a buffer solution, are added to control the unextracted proteins.

The **Bradford assay** is a rapid and accurate method for measuring the concentration of a protein solution. This assay was described first by Bradford (1976)[122] and has become one of the favourite assays for quantifying protein. The Bradford assay relies on the binding of the Coomassie blue G250 dye to proteins. This blue colour dye forms a protein-dye complex that has an absorbance maximum at 595 nm. Thus, protein concentration measurement is achieved by adding the Coomassie blue G250 dye solution to a protein solution and measuring its absorbance at 595 nm (Figure 31).[123] For our experiments, the concentration of the AfFtn-AA solution is measured after both the purification and loading steps using a SpectraMax M5 plate reader from *Molecular Devices*. The protein concentration value is crucial for the mineralization of AfFtn-AA nanocage. Typically, the AfFtn-AA concentration was measured between 0.5 and 1.0 $mg.mL^{-1}$ for one batch of protein (≈ 80 mL of protein solution).

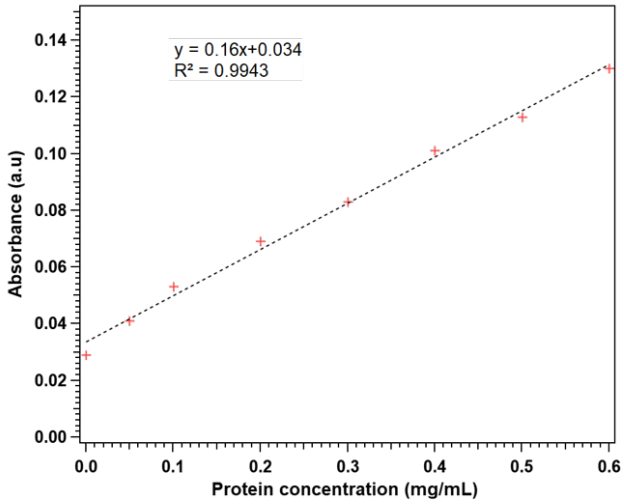

Figure 31 : Calibration curve for the Bradford assay. The dots represent the measured absorbance at 595 nm for different protein concentrations (mg/mL) of a bovine serum albumin (BSA) solution.

Mineralization of the AfFtn-AA core

In solution, AfFtn-AAs are in a dimeric form (two subunits). They can self-assemble into 24-mer nanocages in the presence of iron. For this, a solution of iron (II) sulphate heptahydrate ($FeSO_4 \cdot 7H_2O$) with 0.1 % hydrochloric acid (HCl) was slowly added to the ferritin protein solution. Then, the solution was left at room temperature for 1 hour and kept at 4 °C overnight. After that, unbound iron atoms were removed by FPLC using a desalting column. This column relies on the principle of size exclusion chromatography with matrix beads containing pores. For this study, the amount of iron atoms loaded inside the core was precisely controlled by adjusting the volume of iron (II) solution added to the protein solution (see the detailed protocol in the Appendix III-1.2.). For our experiments, AfFtn-AA nanocages were loaded with 600, 1200, 2400, 3600, and 4800 iron atoms. To control the iron content inside loaded ferritins, the protein cages were broken open by the addition of nitric acid (HNO_3) , and the amount of iron inside the solution was measured by Inductively Coupled Plasma – Mass Spectroscopy (ICP-MS). The formation of the AfFtn-AA cage was confirmed by dynamic light scattering (DLS) and the colloidal stability was controlled by electrophoretic light scattering (ELS). Both last techniques are developed in the next part.

1.4. Characterisation techniques of AfFtn-AA proteins in solution

Measurement of the hydrodynamic diameter by dynamic light scattering

The dynamic light scattering is a common technique used to measure the hydrodynamic diameter of particles in solution. The hydrodynamic diameter (d_h) is defined as "the diameter of a hard sphere that diffuses through the solvent at the same velocity as the particle or molecule being measured" (Figure 32.a).[124] For an ionic solution, it corresponds to the sum of the particle diameter and the thickness of the electrical double layer that surrounds the particle. The principle of DLS relies on the measurement of the Brownian motion of the particles by a laser. The intensity of the fluctuations of the scattered laser light arising from the Brownian motion is measured, which gives access to the diffusion coefficient (D) (Figure 32.b). This physical quantity, related to the diffusion of matter, is inversely proportional to d_h (at a constant temperature).[125] Although, the intensity of light scattered by the particles is sensitive to the presence of large particles, aggregates, or dust, and therefore the results are transformed into volume (or number) distributions using the Mie theory.[126] This allows a better interpretation of the particle size inside the solution. DLS measurement also gives information about the dispersity of the particles in the solutions through the polydispersity index (PDI, or *Đ)* defined as $PDI = \Delta D/D$.

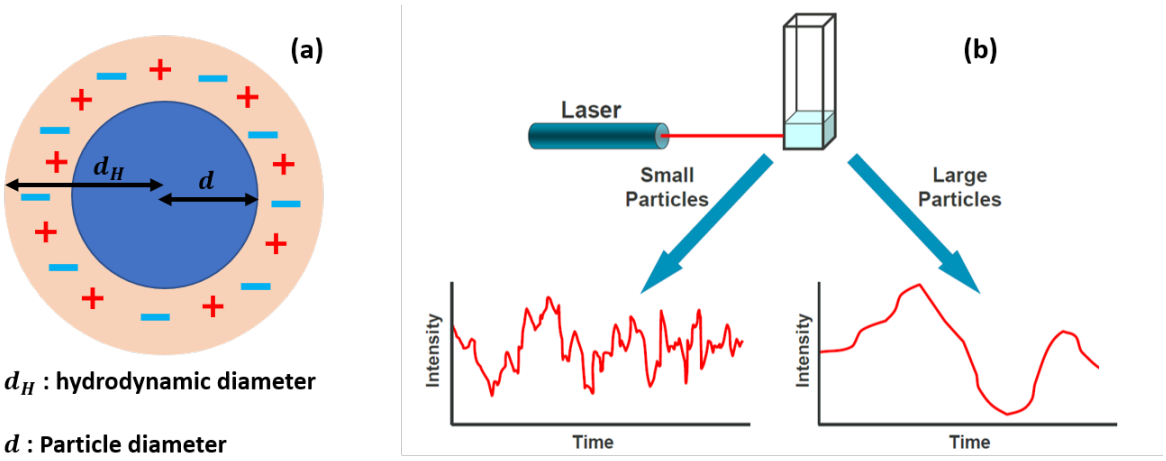

Figure 32 : (a) Schematic of the hydrodynamic diameter of a particle in ionic solution. (b) DLS measurement principle.[127]

To measure the size of iron-loaded ferritin nanocages, one milliliter of ferritin solution was poured into a quartz cuvette and introduced into a Nano-ZS Particle Sizer device from *Malvern Instruments*. The hydrodynamic diameter was then recorded at 25 °C (see the detailed protocol in the Appendix III-2.3). In Figure 33 below, DLS results are displayed for AfFtn-AA nanocages at different loadings. The volume size distributions show peaks ranging from 12 to 14 nm. These results are coherent with the expected size of a ferritin (12 nm) and allow us to confirm the formation of the nanocages post-iron loading. Furthermore, we noticed that the size of the ferritin in solution is not significantly affected by its iron content. The *Đ* measured around 0.2 indicates a relatively low dispersion of particle size.

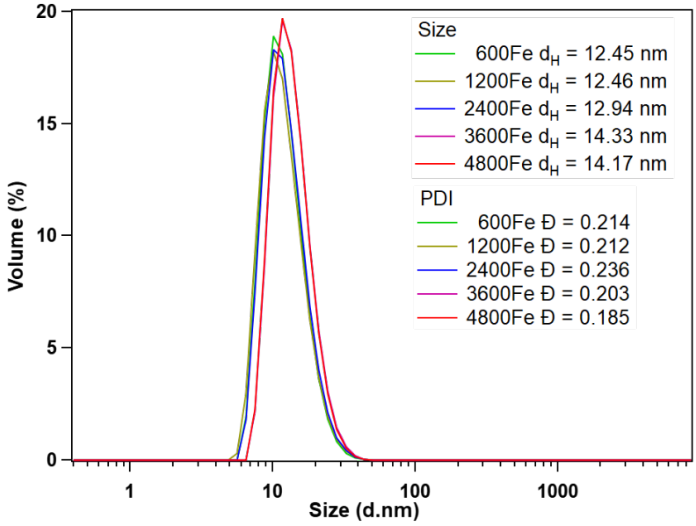

Figure 33 :Dynamic light scattering results from AfFtn-AA at different loadings. The hydrodynamic diameters and PDI measured are displayed in the insert.

Measurement of the zeta potential by electrophoretic light scattering

The stability of a colloidal dispersion is controlled by the electrostatic interactions between particles and is characterized by one major parameter: the zeta potential (ζ). It is defined as the average potential at the slipping plane: an imaginary boundary around the particle, inside which counter-ions accumulate and form an electrical double layer linked to the particle (Figure 34.a). When the particle moves, the ions inside the double layer move with it.[128] On this surface, ions participate in the electrostatic repulsion of other particles. Therefore, the zeta potential indicates the magnitude of repulsion between the dispersed particles, which is responsible for the good stability of the colloidal dispersion. A high zeta potential ($|\zeta| > 40$ mV) is characteristic of good colloidal stability.[129]

The zeta potential is routinely measured via electrophoretic light scattering (ELS). Under an external potential, a particle in a colloidal solution will move relatively to the liquid in which it is suspended; we say that this particle undergoes electrophoresis. The measurement of the electrophoretic mobility (i.e., velocity of the particle per unit of the electric field) gives the net charge on the solid particle, therefore its zeta potential. Electrophoretic mobility is obtained by measuring the frequency shift between a laser passing through the particle dispersion, undergoing electrophoresis, and a reference laser routed around the cell (Figure 34.b) (laser Doppler electrophoresis process). This frequency shift Δf is related to the particle velocity ν, as shown in Equation 1. The zeta potential is therefore calculated with the Henry's equation (Equation 2).

$$\Delta f = 2\nu.\sin(\frac{\theta}{2})/\lambda$$

Equation 1: Frequency shift $\Delta f\,(s^{-1})$ between the scattered light from the moving particle and the reference light. ν $(m.s^{-1})$ is the particle velocity, λ (m) the laser wavelength, and θ (°) the scattering angle.

$$\nu = \frac{2\varepsilon.\zeta.F(\kappa a)}{3\,\eta}$$

Equation 2 : Henry's equation. The relationship between the zeta potential $\zeta(mV)$ and the particle velocity ν (or electrophoretic mobility). ε is the dielectric constant of the dispersant, $F(\kappa a)$ is the Henry function, and η the viscosity.

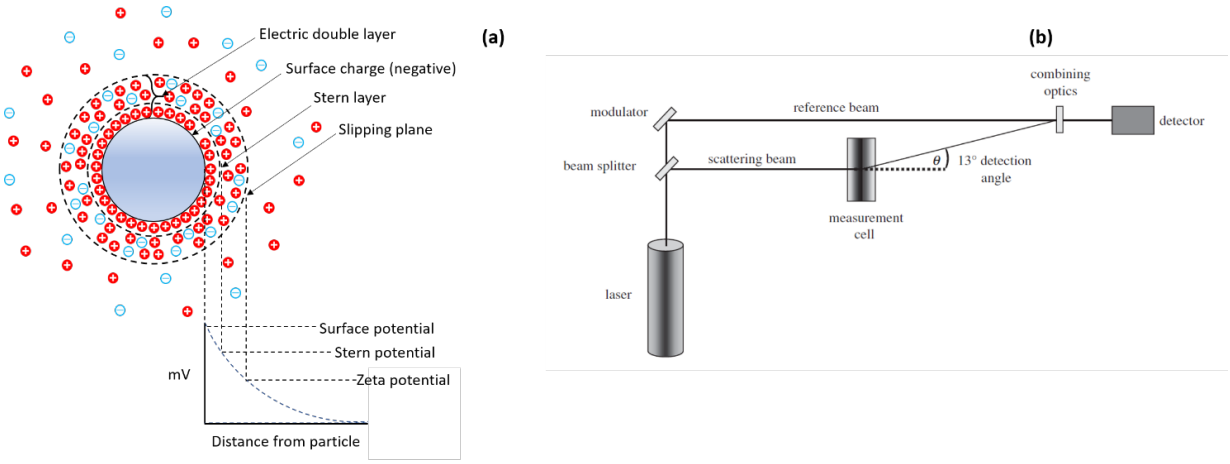

Figure 34 : Measurement of zeta potential by electrophoretic light scattering. (a) schematic of the electrical double layer that surrounds the particle. (b) schematic of a typical optical configuration for a laser Doppler electrophoresis instrument.[130]

Zeta potential measurements of loaded AfFtn-AA nanocages were performed not only to control the stability of the colloidal dispersion (ferritins in a buffer solution with Na^+ and Cl^- as counter-ions) but to measure its surface charge as well. One milliliter of ferritin solution was injected into a folded capillary cell (DTS1080) and introduced into a Nano-ZS Particle Sizer device from *Malvern Instruments*. The zeta potential of AfFtn-AA proteins was measured at different pH values ranging from 3 to 10 (see the detailed protocol in the Appendix III-2.4) to obtain its isoelectric point (IEP).

2. AfFtn-AA mutation by site-directed mutagenesis

2.1. Site-directed mutagenesis principle

Site-directed mutagenesis (SDM) is a technique developed in 1978 by Michael Smith (Nobel Prize in 1993) to characterize gene and protein structures. In this technique, a nucleotide sequence of interest, present on a DNA strand, is modified using a synthetic short sequence of nucleotides called an oligonucleotide or a primer. This latter is complementary to the interest DNA strand but presents an internal mismatch to direct the mutation, i.e., one (or many) different codons that will be translated in a new amino acid.[131,132] Primers are usually in a complimentary pair, as they are used for double-stranded DNA. We talk about the forward primer, from the 5' end to the 3' end, and the reverse primer, from the 3' end to the 5' end. Primers will stand in front of the interest area on the parent DNA and will start to extend through a polymerase chain reaction (PCR) process, copying the DNA sequence. After that, the parent DNA is removed by digestion using a restriction enzyme. Finally, the mutated DNA is transformed in a host cell (e.g., *E.coli* DH5-α) to be expressed later (Figure 35).

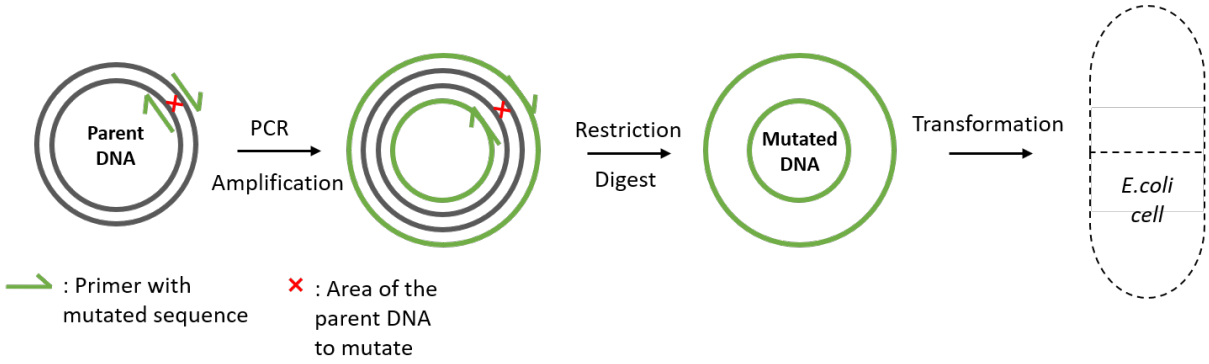

Figure 35 : Schematic of the site-directed mutagenesis procedure. The parent DNA is the DNA where the nucleotide sequence of interest is present (red cross). The amplification by polymerase chain reaction adds nucleotides on each side of the primers, by copying the nucleotide sequence of the parent DNA. The digest step removes the parent DNA, and the transformation step inserts the mutated DNA into a competent cell.

AfFtn-AA proteins were mutated using the SDM principle. The designed primers with the mutation of interest were bought from the *IDT* company. To confirm each SDM, AfFtn-AA mutated plasmids were sent for sequencing to the *1st Base* company.

2.1.1. Polymerase Chain Reaction principle

Experimentally, the modification of the DNA by site-directed mutagenesis is driven by a PCR. This reaction was discovered in 1986 by Kary Mullis (who won the Nobel Prize in 1993 with Michael Smith). It has revolutionized the molecular biology field and is nowadays widely used in medicine, for instance, to detect specific viruses (COVID, HIV, hepatitis, etc.). The PCR technique allows a high amplification (with a factor of a billion) of a known DNA (or RNA) sequence from a small quantity (minimum a picogram), using a complementary primer of the parent DNA and a specific enzyme called DNA polymerase. The principle required a three-step cycling process. First, the denaturation separates the parent DNA held together by heating to 95 °C. Then, primers are annealed to the dissociated parent DNA strands. The primers are introduced in molar excess so that they are more likely to anneal to the denatured DNA strand than the DNA strands are to anneal to each other. Thirdly and finally, the primers are extended by the DNA polymerase, which adds the nucleotides complementary to those in the unpaired parent DNA strand, onto the annealed primers (Figure 36). After each three-step cycle, the number of DNA strands is doubled. Therefore, after 30 cycles, the parent DNA is multiplied by 1 000 000.[133]

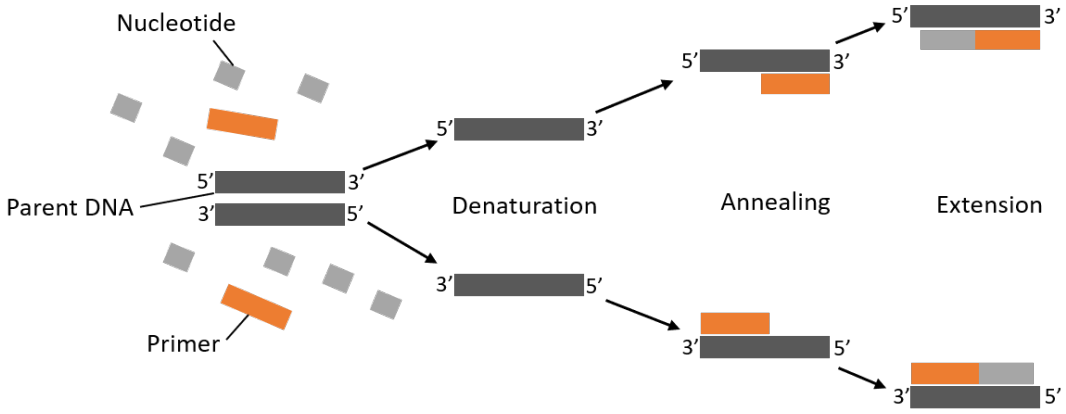

Figure 36: Schematic of the polymerase chain reaction (PCR) principle. The denaturation step separates the double-stranded DNA. The primers are then annealed to each DNA strand and extended with nucleotides by the DNA polymerase.

For our experiment, PCR was used for the site-directed mutagenesis of an AfFtn-AA plasmid (parent DNA) previously extracted from a host cell (see the detailed plasmid extraction protocol in the Appendix III-1.3). The experiment was carried out with an Veriti 96-well programmable thermocycler from *Applied Biosystem*^{TM} (see the detailed protocol in the Appendix III-1.4).

3. Characterisation techniques for nanoparticles immobilized on silicon

In this part, the surface characterisation techniques used during this thesis are presented: Kelvin Probe Force Microscopy (KPFM), Dark-Field Optical Microscopy (DFOM), and Fourier Transform Infrared Spectroscopy (FTIR). These techniques were used to characterise nanoparticles (AuNPs and AfFtn-AAs) immobilized on a silicon wafer.

3.1. Kelvin Probe Force Microscopy: an advanced technique of the Atomic Force Microscopy

AFM principle

The KPFM is an advanced technique of the Atomic Force Microscopy (AFM) that measures both the topography of the sample and the local contact potential difference (CPD) between an AFM tip and the sample. Therefore, it allows the mapping of the surface potential

of the sample with high spatial resolution. Since its introduction in 1991, the KPFM has been a method mainly used to characterize the electrical properties of metal and semiconductor surfaces. Recently, it has been used to measure the electrical properties of biological materials like DNA microarrays[134] or protein films. The KPFM principle is based on the operational principles of an AFM apparatus. Like other scanning probe microscopes, it uses a sharp probe that scans across the surface of a sample. The tip interacts directly with the surface, probing repulsive and attractive forces that exist to produce a three-dimensional image of the surface. The tip is put at the end of a flexible cantilever, which is itself mounted on a piezo crystal, which allows the tip to move. The upper surface of the cantilever is coated with a reflective surface onto which a laser beam is directed and reflected to a photodiode. The deflection of the cantilever is monitored by the change in the amount of laser light reflected into the photodiode. This deflection can be used to calculate the interaction force between probe and sample (Figure 37).[135]

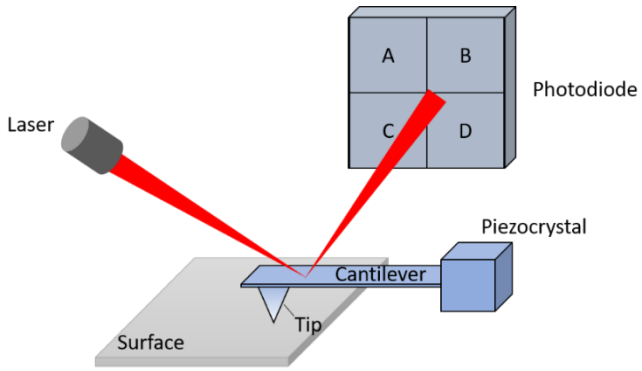

Figure 37 : Schematic of the AFM principle. The cantilever deflection is monitored by the change in the path of the laser light beam to the photodiode.

Many AFM modes exist to record the topography of a surface sample, with each mode depending on the force it involves. An AFM can operate in contact mode (repulsive forces), intermediate mode (also called tapping mode), or non-contact mode (attractive and repulsive forces). One of the most commonly used modes is the tapping mode, in which the cantilever is externally oscillated close to its resonance frequency. The tip-sample interaction will change the oscillation amplitude, which is used, with respect to the reference amplitude, as a feed-back signal to obtain the topography (Figure 38).[135]

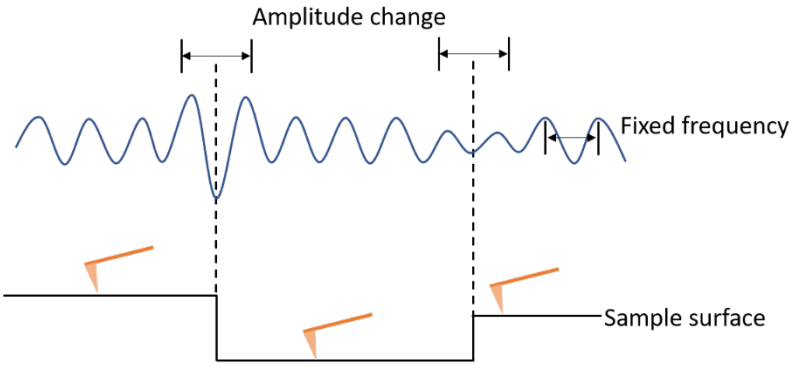

Figure 38 : Schematic of the AFM tapping mode principle. As the surface is scanned, the amplitude will change as it passes through different topographies. By using a feedback mechanism, the z-height of the cantilever is constantly adjusted to remain constant. This provides the z-topography of the surface.

PeakForce Tapping mode

Our experiments in INSP were carried out with a *Bruker* Multimode-8 AFM purchased in 2015 and equipped with the options KPFM and TUNA (conductive AFM). In Singapore, KPFM experiments were carried out with a *Bruker* Dimension XR Icon AFM.

For our experiments, topography was recorded by *PeakForce Tapping*®, an intermediate mode developed by *Bruker* mainly for the study of biomaterials and soft materials. In this mode, the cantilever does not oscillate, but it approaches and interacts with the surface until a given force set point is reached and then retracts. During the approach and retraction of the cantilever, the probe of the AFM senses the near-field surface forces acting between the atoms of the probe and the atoms of the sample. A force response curve (Figure 39.a) is recorded, which represents the sum of the attractive forces and repulsive forces as a function of the distance of the cantilever from the surface. In the approach part, the tip descends to the surface, and the tip-surface interaction is dominated by long-range attractive forces such as van der Waals interactions, magnetic forces, and electrostatic forces. The tip is attracted by the surface until contact. At the contact point, the tip-surface interaction is dominated by a repulsive short-range interatomic force (Coulomb interaction). The tip continues to push on the surface until the force set point is reached, at which point it retracts. To obtain a topographic image, a force-distance curve (or ramp curve) is recorded (Figure 39.b) at each scanning point (x, y), and the tip-sample interaction is controlled by maintaining the applied force. From the produced force curve, the topography and other information about the sample can be extracted: deformation, adhesion

force, elastic modulus, and dissipated energy.[136] This technique allows to precisely control the force applied by the tip on the sample, and is very suitable for fragile material. To control the applied force, the tip was calibrated prior to every experiment to convert the photodetector signal (relative to the deflection of the cantilever) into a quantitative value of force. From a ramp curve, the deflection sensitivity (nm/V) of the cantilever is extracted from the contact part of the force curve, where the deflection rises steeply upwards (Figure 39.b; points C to D). Usually, the calibration of the tip is done on a hard surface. Here, we calibrated the tip on a bare silicon surface.

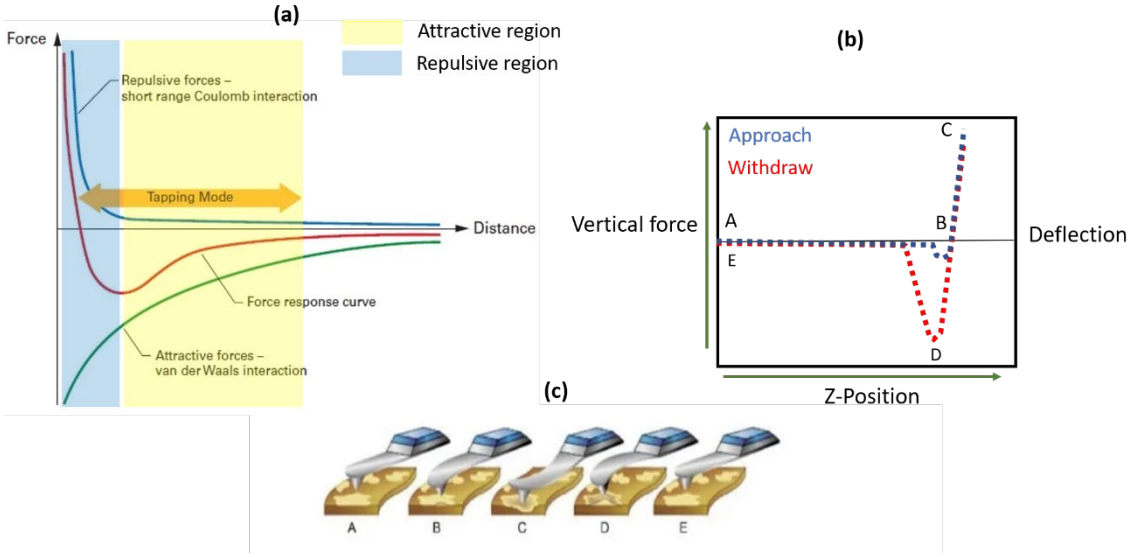

Figure 39: PeakForce tapping mode principle. (a) force-distance curve representing the attractive forces (green line) and repulsive forces (blue line) acting between the tip and the surface. The red line is constructed by adding the short-range repulsive and long-range attractive forces. The attractive and repulsive regions are indicated in yellow and blue, respectively. (b) curve of the vertical force of the tip-surface interaction as a function of the z-position of the tip. (c) drawing of the different aspects of the tip in an approach-withdraw ramp. The points A to E represent each step of the ramp. A: the tip approaches the surface; B: the tip is attracted by the surface (attractive force); C: the tip pushes on the surface until the force set point is reached (repulsive force); D: the tip tries to withdraw but is retained by the attractive force on the surface; E: the tip is withdrawn from the surface.[137]

For this project, the impact of the force applied by the tip was investigated by recording topography images of ferritin nanocages deposited on silicon with increasing applied forces (Figure 40.a). Images show the same area of the sample but with increasing applied forces from 50 pN to 1000 pN. The mean heights of the nanocages (on 60 particles) were measured from these images and displayed in Figure 40.b. No changes in the height of the nanocage are noticed

as the force increases. Therefore, increasing the force set point does not affect the size of the ferritin. In the KPFM experiments, we tried to keep the force setpoint under 1 nN, ideally.

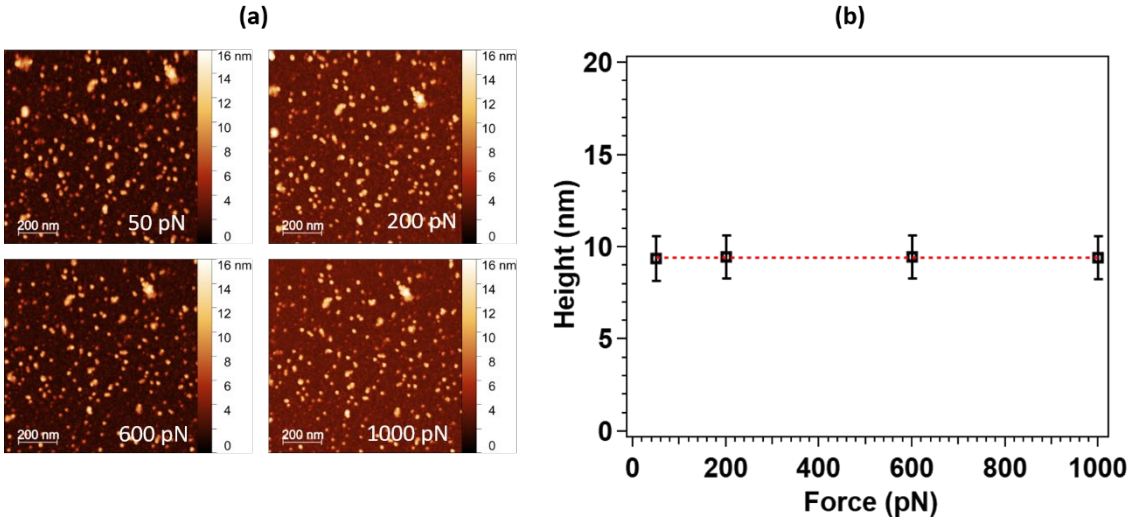

Figure 40 : (a) Topography images (1 µm²) of ferritin nanocages immobilized on a silicon wafer. The four images were recorded in the same area of the sample in PeakForce Tapping mode, with different applied forces. (b) Height mean values of ferritin measured from the topography images with an error bar.

Characteristic of the AFM tips used in this project

During this thesis, two kinds of tips were used for AFM in our work: the ScanAsyst-Air and the SCM-PIT-v2 (Figure 41). Both are commercial tips purchased from *Bruker*. The ScanAsyst-Air tip was used for the *PeakForce Tapping* mode only. It has a triangular-shaped cantilever that makes it less sensitive to lateral and torsional forces. In addition, it has a small spring constant (k = 0.5 N/m) that indicates a mild probe and a weaker interaction between the tip and the sample. The SCM-pit-V2 tip was used for the KPFM mode. The cantilever has a rectangular shape and is made of highly *n*-doped silicon (0.01 – 0.025 Ω.cm). It has a Platinum/ Iridium coated tip (electrically conductive tip) to perform CPD measurement.[138]

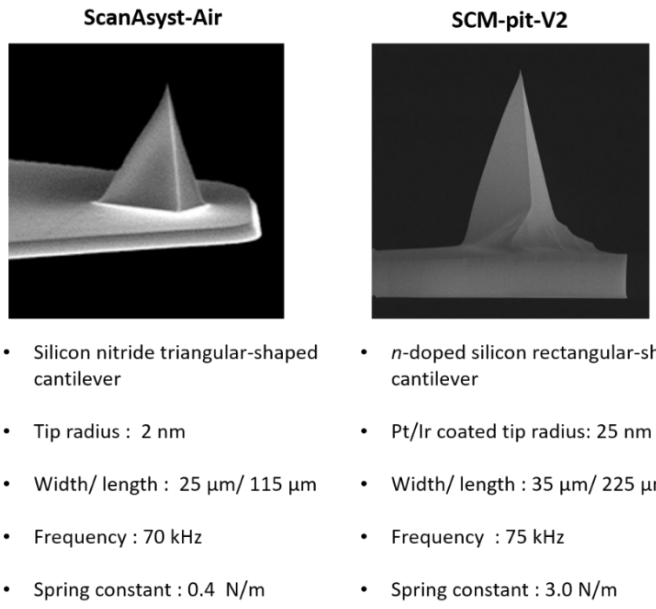

Figure 41: SEM images of a ScanAsyst Air tip (left) and of a SCM-pit-V2 tip (right). The features of these two tips are given under the SEM images.

Measurement of the Contact Potential Difference

The KPFM device measures the local variations of the surface potential by detecting the contact potential difference (CPD) between a sample and a conductive AFM tip. It produces a CPD map. More precisely, when the tip is brought close to the surface, Fermi levels align as a result of charge transfer. The electric charges are reorganized between the tip and the sample, and the CPD builds up (denoted V_{CPD}) (Figure 42.b). The CPD causes the onset of an electrostatic force F_{es} that is nullified by applying an external bias (V_{DC}) with the same magnitude as the V_{CPD} (Figure 42.c). The applied external bias is equal to the difference of work functions between the tip (WF_{tip}) and the sample (WF_{sample}), defined in Equation 3.[139] Here, the Fermi level (E_f) is defined as the highest energy level occupied by an electron at T = 0 K. The energy required to extract an electron from the Fermi level to a position just outside the material (vacuum level) is the work function (noted WF).

$$V_{DC} = V_{CPD} = \frac{WF_{sample} - WF_{tip}}{|q|}$$

Equation 3 : The bias V_{DC} applied by the KPFM device is directly equal to the work function difference between the tip and the sample. Here, $q = -1.6.10^{-19}$ C is the charge of the electron.

By using the Equation 3, it is possible to determine the local work function of the sample surface by knowing the work function of the tip. Beware that this equation is valid only if the potential is applied to the sample, which is the case for our experiments. When V_{DC} is applied to the tip, then $V_{DC} = -V_{CPD}$.

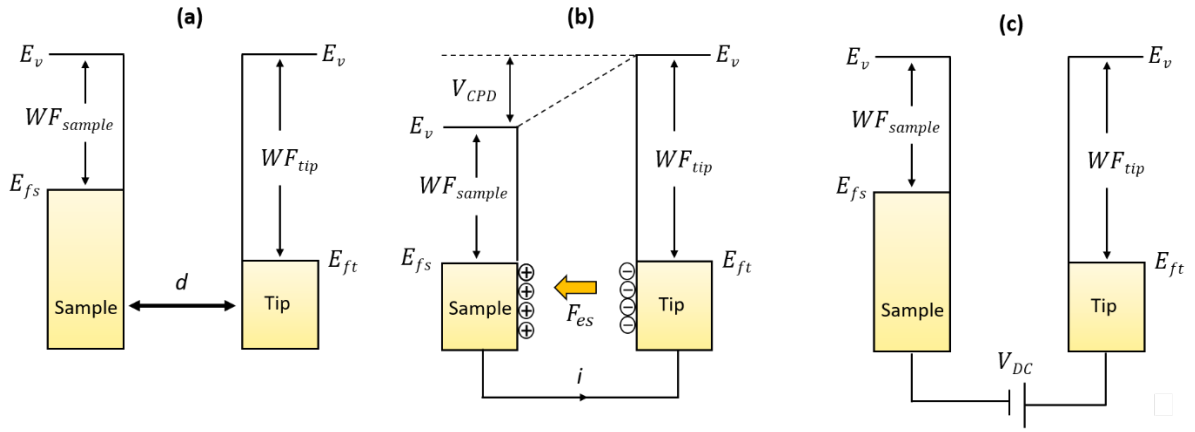

Figure 42: Electronic energy levels of the sample and AFM tip in three cases: (a) tip and sample are separated by a distance d with no electrical contact; (b) tip and sample are in electrical contact; and (c) external bias (V_{DC}) is applied between tip and sample to nullify the CPD and, therefore, the tip-sample electrical force. E_V is the vacuum energy level. E_{fs} and E_{ft} are Fermi energy levels of the sample and tip, respectively.[139]

For the measurement, in addition to the DC voltage V_{DC}, an AC-voltage $V_{AC}.\sin(\omega t)$ is applied, which generates oscillating electrical forces between the tip and the surface. Therefore, the electrostatic force F_{es} derives from the capacitive energy between two parallel metal plates, and its equation is:

$$F_{es}(z) = -\frac{1}{2}\Delta V^2 \frac{dC(z)}{dZ}$$

Equation 4 : Electrostatic force between an AFM tip and a sample surface. Here, $\Delta V(V)$ is the potential difference between the tip and the surface, and $\frac{dC(z)}{dZ}$ is the gradient of the capacitance.

Here, the potential difference ΔV between the tip and the surface is equal to:

$$\Delta V = (V_{DC} - V_{CPD}) + V_{AC}.sin(\omega t)$$

Equation 5 : Potential difference

Substituting Equation 5 in Equation 4 gives the expression of the electrostatic force between the tip and the sample:

$$F_{es}(z,t) = -\frac{1}{2}\frac{\partial C(z)}{\partial z}[(V_{DC} - V_{CPD}) + V_{AC}.\sin(\omega t)]^2$$

Equation 6 : Electrostatic force applied to the tip

Equation 6 can be divided into three-part:

$$F_{DC} = -\frac{\partial C(z)}{\partial z}\left[\frac{1}{2}(V_{DC} - V_{CPD})^2\right] \quad \text{(a)}$$

$$F_{\omega} = -\frac{\partial C(z)}{\partial z}(V_{DC} - V_{CPD}).V_{AC}.\sin(\omega t) \quad \text{(b)}$$

$$F_{2\omega} = -\frac{\partial C(z)}{\partial z}\frac{1}{4}V_{AC}^2[\cos(2\omega t) - 1] \quad \text{(c)}$$

Equations 7 : Components of the electrostatic force on the tip. (a) static deflection of the tip; (b) electrostatic force that creates the oscillation of the cantilever; and (c) force component used for capacitance microscopy.

In Equations 7.b, F_{ω} represents the electrostatic force that causes the cantilever to oscillate at the frequency ω. It is used to determine the V_{CPD}.[139]

The measurement of the CPD by the KPFM can be performed in two distinct modes: amplitude modulation (AM) or frequency modulation (FM). In AM mode, the KPFM measures the electrostatic force F_{ω} directly from the amplitude of the cantilever oscillation induced by the CPD and V_{AC}. In FM mode, KPFM measures the electrostatic force gradient ΔF_{ω} detected from the frequency shift of the cantilever.[140] From an inter-atomic force-distance curve (Figure 43), the electrostatic force gradient, that derives from the electrostatic force, is larger for short distances and becomes insignificant when the distance increases. Therefore, the detection of the electrostatic force gradient is considered a short-range detection and mainly takes place at the apex of the tip. Conversely, the electrostatic force is considered long-range detection, and it included both the tip and the cantilever. The average effect between the tip and the cantilever results in a lower spatial resolution. In AM mode, the spatial resolution is typically 25 nm, whereas in FM it is sub-nanometer and depends on the tip apex.[141] However, detection of the CPD in FM mode is achieved by sending the signal through a frequency demodulator, which generates additional noise. In AM mode, the CPD is detected by the resonance peak of the oscillating cantilever, which increases the signal-to-noise ratio. Therefore, AM mode presents

a higher energy resolution than FM mode. Typically, the energy resolution in AM mode is about 5 mV whereas it is between 10 and 20 mV in FM mode.[139] In our KPFM experiments, we are looking at phenomena that are manifested by small variations of CPD (≃10 mV). Therefore, all the KPFM experiments were carried out in AM mode for better visualization of CPD variations. Only the calibrations of the work function of the tip, presented hereafter, were done in FM mode.

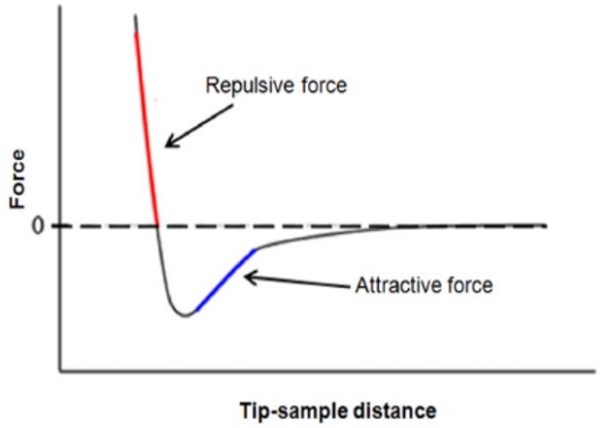

Figure 43 : A typical inter-atomic force vs. distance curve. The force gradient (a derivative of the curve) is limited to the short-range in tip-sample distance, while the force is long-ranged compared to the force gradient.[139]

Before measuring the sample surface, the work function of the tip must be known. To do so, the tip was calibrated using a commercial reference sample (PFKPFM-SML). This sample is made by lithography and is formed by Al and Au films on a *n*-Si substrate (Figure 44.a). By scanning at the junction of Al/Si/Au, we obtained a potential image with a different CPD for each material (Figure 44.b). Because aluminium is less sensitive to humidity, its work function is more stable compared to Au and Si. Therefore, the theoretical work function of Al/Al_2O_3 (a native oxidation layer lies on top of Al) is taken as a reference to measure the work function of the tip. The work function of Al/Al_2O_3 (WF_{sample}) is equal to 3.9 eV. On the CPD profile (Figure 44.c), we measure $V_{CPD} = -1.07$ V for Al/Al_2O_3. Therefore, by using Equation 3 : $WF_{tip} = WF_{sample} - |q|.V_{CPD} = 3.9\ eV + 1.07\ eV = 4.97\ eV$.

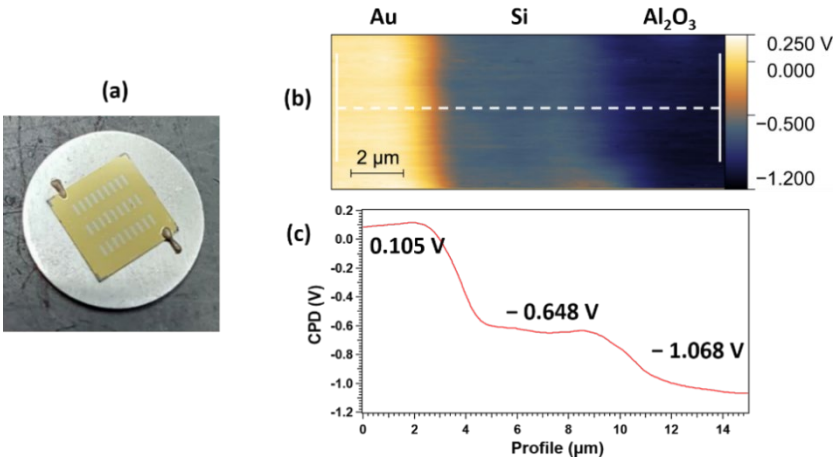

Figure 44 : (a) Au/Si/Al reference sample from Bruker. (b) CPD image obtained by scanning across Au/Si/Al. (c) CPD profile from the obtained CPD image.

The calibration of the tip is an essential step in measuring the work function of a sample. It can also provide more information about the condition of the tip. A change in the work function of the tip after an experiment could be evidence of some damage to the tip or adsorbed particles on it. Therefore, the work function calibration of the tip was systematically realized before and after each of the experiments. In a KPFM measurement, topography and CPD were acquired within two passes above the surface. The tip performs a first pass recording the topography, then lifts at a given lift scan height (LSH) and acquires the CPD, following the recorded topography of the first pass (Figure 45).

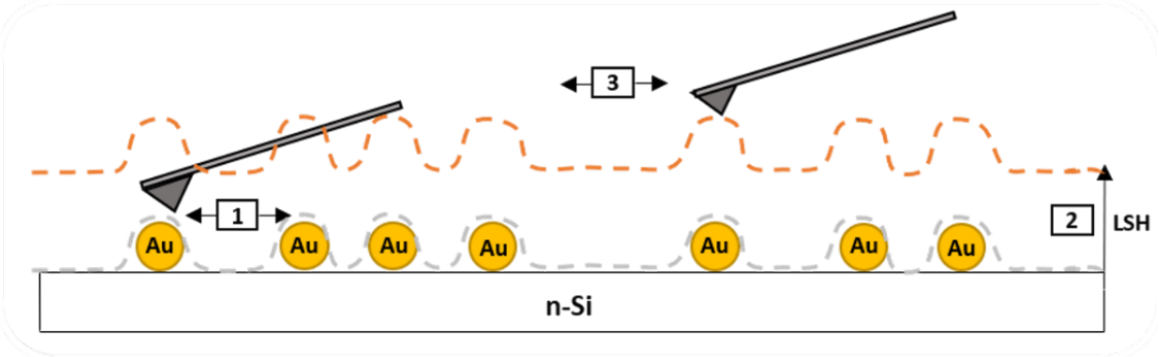

*Figure 45: KPFM two-pass measurement principle: **Step 1**: the surface topography is acquired in PFT mode during a first pass (grey dash line) over one line; **Step 2**: the cantilever ascends to a pre-defined lift scan height (LSH); **Step 3**: the cantilever follows the previously recorded surface topography along the same line and above the sample. It constantly adjusts the value of V_{DC} for cancelling the tip-sample electrostatic force (orange dash line).*

When analysing relatively small nanoparticles with KPFM, the LSH becomes an important parameter as it monitors the spatial resolution that we obtain, which is approximately equal to the value of the LSH. For instance, the CPD of 12 nm nanoparticles on doped silicon cannot be detected with a LSH of 50 nm. This is due to the size of the tip (usually around 25 nm in diameter) that would average the measured CPD, and being too far from the surface will sense mostly the contribution from the silicon. In the Figure 46 below, are shown CPD images of 50 nm gold nanoparticles on doped silicon, that we recorded at different LSHs. At 70 nm, the CPD of particles is slightly blurry compared to 50 nm and 40 nm. At 30 nm, we can see the apparition of artefact (white horizontal lines) on the image arising from the tip that has bumped on the nanoparticles while scanning. At 20 nm, the CPD are barely visible, as the tip was probably too damaged. These results show that the choice of the LSH value is crucial to obtaining high-resolution CPD images as well as keeping the tip safe and clean. Ideally, a good LSH would be a few nanometers above the size of the particle we are measuring. Then, for the 50 nm gold nanoparticles measurements, LSH was set at 50-60 nm and for the 12 nm AfFtn-AA proteins, LSH was set at 15-20 nm.

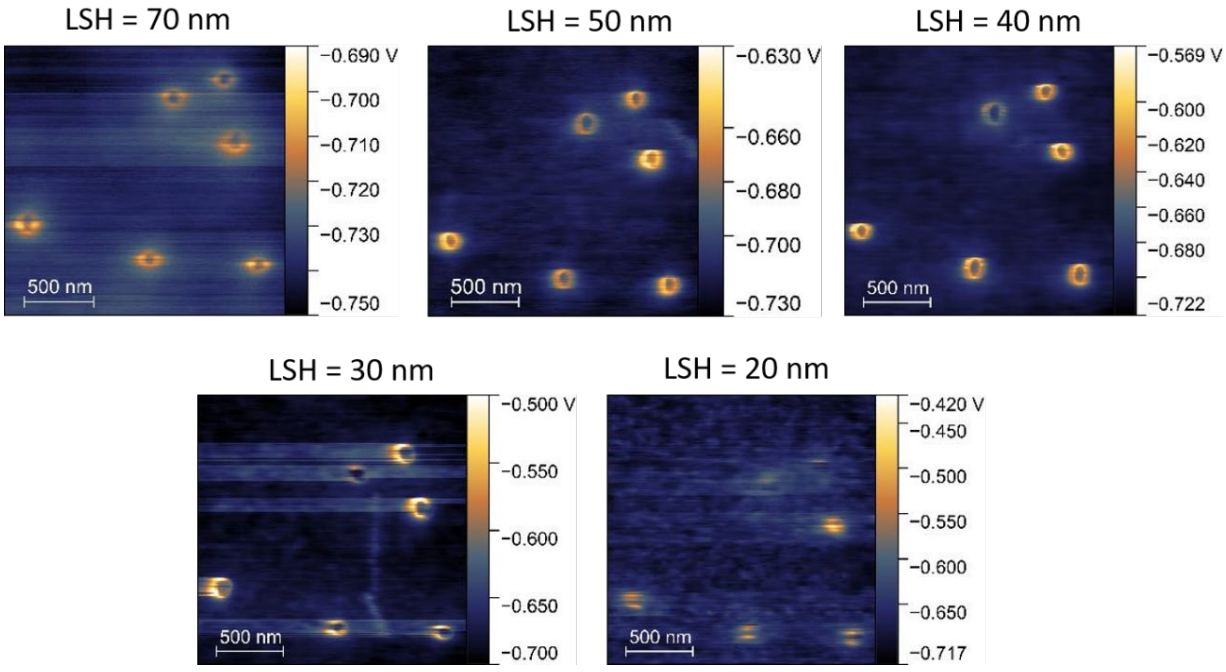

Figure 46 :CPD images of gold nanoparticles on n-doped silicon recorded for different LSH values.

3.2. Dark-Field Optical Microscopy

The dark-field optical microscopy (DFOM) is an observation method using light to identify objects at the surface of a sample. Unlike traditional bright-field (BF) optical microscopy, DFOM senses only the scattered light from the subjects, resulting in an image with a dark background and bright objects on it. Invented in 1830, this technique presents highly sensitive sensing and has been at the heart of numerous developments and applications since 2000: acquisition of high-quality colour photographs and visualization at the single nanoparticle level. Recently, DFOM was used to detect metal nanoparticles[142] for the study of localized plasmon resonance and enzyme biomarkers for human disease diagnosis.[143] The acquisition of images by DFOM is achieved by a dark-field condenser, in which a light stop is used to cut off the central part of the vertical incident light. The outer-side light is directed onto the sample via a condenser lens. The incident light passes along its original path and misses the objective, whereas the scattered light is detected by the objective. Therefore, diffraction spots from the objects can be seen in the recorded image (Figure 47).[144] In fact, the DFOM can "overpass" the angular resolution of a classic optical microscope and detect very small objects. This technique allowed us to rapidly observe the surface of our samples, mainly to confirm the immobilization of the 50 nm AuNPs on doped silicon. All the DFOM images were recorded with a *Nikon Eclipse LV100ND* microscope using a *TU Plan Fluor 100x* objective (numerical aperture = 0.90). The DFOM was operated in reflection (due to the opacity of the silicon) by a *Universal Epi Illuminator*.

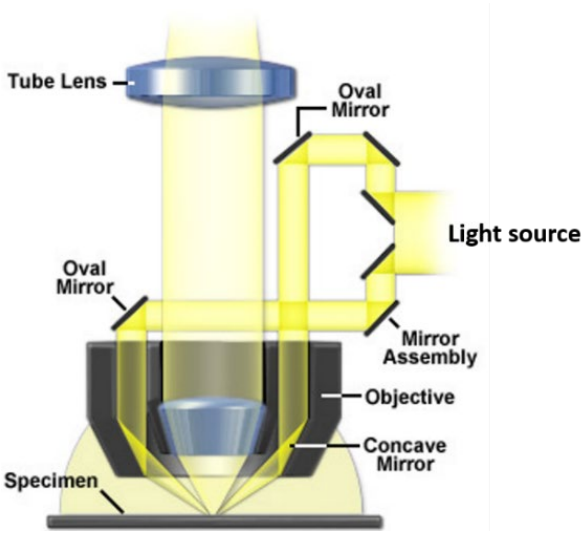

Figure 47: Schematic of the DFOM principle. The light source is directed onto the sample so that only the scattered light can reach the objective.[145]

3.3. *Fourier* Transform Infrared Spectroscopy

In this project, AfFtn-AA nanocages were immobilized on *n*-doped silicon surfaces. Therefore, we needed to assess the presence of the ferritin on the surface after the deposition. However, even if the techniques presented before (KPFM and DFOM) could probe the presence of particles on the surface, none of them provided information about their chemical nature. To do so, we used Fourier transform infrared spectroscopy (FTIR) (see the detailed protocol in the Appendix III-3).

FTIR is an analytic tool that senses the interactions of infrared light with matter. This technique determines the presence of molecular components and functional groups in a solid, liquid, or gaseous sample. It detects the molecular vibrations of the inter-atomic bonds composing the sample. In fact, when infrared light is sent through a sample, molecules inside absorb it and vibrate at specific wavelengths that are recorded by a detector. More precisely, each wavelength corresponds to a mode of vibration of a molecular bond that depends on the atoms involved in it. Therefore, by exciting the sample at different IR frequencies, we can produce an IR spectrum, which informs us about the molecules present in the sample.[146] In FTIR spectroscopy, the IR radiation used ranges from 2.5 µm to 25 µm. The conventional units are the wavenumber (in cm^{-1}): the range is then between 400 and 4000 cm^{-1}. The FTIR spectrometer is based on an optical device called the Michelson interferometer, which is composed of a beamsplitter, one fixed mirror, and one moving mirror, as shown in Figure 48. During a FTIR experiment, the beam coming from the IR source is split into two perpendicular beams by the beamsplitter. One of the beams is reflected toward the fixed mirror, while the other is transmitted through the beamsplitter to the moving mirror. The moving mirror causes the transmitted beam to be delayed compared to the reflected beam, creating a difference in the optical path. The two beams recombine on the beamsplitter and interfere constructively or destructively, depending on the position of the moving mirror. Then, the recombined beam passes through the sample and is detected afterward by a detector, producing an interferogram. The interferogram shows the intensity of the recombined beam as a function of the moving mirror position. It needs to be computed by the Fourier transform to provide a spectrum displaying the intensity as a function of the wavenumber. The FTIR acquisitions were done at INSP with a *Bruker* Tensor 27 (purchased in 2006).

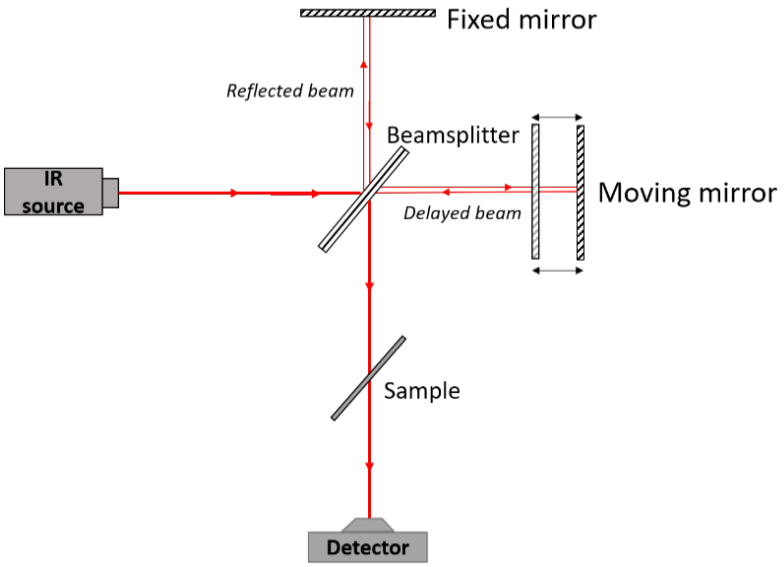

Figure 48: Schematic of the Michelson interferometer used in FTIR spectroscopy. The moving mirror on the right delayed the transmitted beam to create interference with the reflected beam.

In practice, the detection of the AfFtn-AA nanocages on the silicon surface was a two-step process. First, a reference spectrum was recorded on a bare silicon wafer prior to deposition. Then, the AfFtn-AA proteins were drop-casted on the surface of the same silicon wafer, and the sample spectrum was recorded in the same configuration as for the reference. The two spectra were processed by calculating the absorbance difference following the Equation 8, and the resulting spectrum showed the absorbance difference as a function of the wavenumber (cm^{-1}).

$$\Delta A = A_s - A_{ref} = -\log_{10} T_s - \log_{10} T_{ref} = -\log_{10} \frac{I_{ref}}{I_s} + \log_{10} \frac{I_{ref}}{I_0} = \log_{10} \frac{I_{ref}}{I_s}$$

Equation 8 : Absorbance difference (ΔA) between the sample and the reference spectra, where A_s, T_S, and A_{ref}, T_{ref}, are the absorbance and transmittance of the sample and the reference, respectively. I_{ref} and I_s are the intensity of the IR beam passing through the reference and the sample, respectively. I_0 is the intensity of the IR beam without any sample.

The FTIR spectrometer was equipped with a L-alanine doped triglycine sulphate (DLaTGS) thermodetector, a KBr beamsplitter, and was connected to a dryer SDAT from *Specken Drumag* that dries the air before entering the devices. The dryer does not remove the carbon dioxide (CO_2) but reduces the atmospheric water vapor in the spectrometer. However, the presence of

water vapor during the measurements was still visible on the spectrum. To remedy this issue, we recorded a water vapor spectrum that we subtracted from each spectrum. Solutions of AfFtn-AA were drop-casted onto double-sided polished FZ silicon (111) wafers slightly *n*-doped (10-20 Ω.cm with phosphorus dopant). We worked with float-zone (FZ) silicon wafers to avoid intrinsic oxygen. This type of silicon is made by vertical zone melting and provides very pure silicon with very low concentrations of impurities (such as carbon (C), dinitrogen (N_2), or dioxygen (O_2). The IR spectra were recorded in transmission mode at the Brewster angle (or polarization angle), which is here at 70°. At this angle of incidence, there is no reflection of the p-polarized light at the surface. It is entirely transmitted through the wafer, while the s-polarization is totally reflected. Therefore, the detection of modes parallel and perpendicular to the surface is possible.[147]

4. Conclusion

The first part of this chapter presented all the laboratory experiment processes approached in this thesis. All the biochemistry protocols presented here were carried out in the protein laboratory at NTU, mostly during the 2nd year. The production process of ferritin nanocages was done numerous times over the course of this thesis, mostly for AfFtn-AA but for AfFtn-AA mutants, AfFtn-WT. The production of protein was systematically followed by purity (SDS-PAGE), concentration (BradFord Assay), size (DLS), and surface charge (ELS) measurements to create a characteristic list for each batch of protein. These characteristics are important data that helps to understand the behaviour (morphology and CPD) of ferritin in a dry state deposited on silicon. Furthermore, being able to modulate the amount of iron inside the ferritin cages is a real asset. It is a key parameter that is used for KPFM measurements. The second part presented the devices used to characterize the particles on a silicon surface. The DFOM measurement presented here was used for the AuNPs on silicon, where it allows us to rapidly assess the coverage of the particles on the silicon. Furthermore, the DFOM made observations about the plasmonic behaviour of the gold nanoparticles (ring-shape). DFOM could not be used to observe ferritins on the silicon because they are too small. On the other hand, the FTIR measurement was used to confirm AfFtn-AA immobilization on silicon. The KPFM was the most used apparatus during this thesis. Its handling, although laborious, provided us with many new observations and comprehensions of the particles we looked at.

5. References

[104] Alberts B, Johnson A, Lewis J, *et al*., « From DNA to RNA », *Molecular Biology of the Cell*. 4th edition, (2002).

[105] Flyvbjerg F., F. Jülicher, P. Ormos, and F. David, *Physics of Bio-Molecules and Cells.* (2002), 75: 3-4.

[106] Branden Carl and John Tooze. « Basic Structural Principles - The building blocks », *Introduction to Protein Structure - Second Edition*, (1999), Part1.1.

[107] Escherich T, « Die Darmbakterien des Neugeborenen und Säuglinge », *Fortschritte der Medizin*, (1885), 3 ,515–522.

[108] Jeong Haeyoung, Valérie Barbe, Choong Hoon Lee, David Vallenet, Dong Su Yu, Sang-Haeng Choi, Arnaud Couloux, *et al*., « Genome Sequences of Escherichia Coli B Strains REL606 and BL21(DE3) », *Journal of Molecular Biology*, 394, n° 4 (2009): 644-52.

[109] Allocati, Nerino, Michele Masulli, Mikhail Alexeyev, and Carmine Di Ilio. « Escherichia Coli in Europe: An Overview ». *International Journal of Environmental Research and Public Health* 10, no 12 (2013): 6235-54.

[110] Lee Sang Yup, *Systems Biology and Biotechnology of Escherichia Coli*, (2009).

[111] Khan Suliman, Muhammad Wajid Ullah, Rabeea Siddique, Ghulam Nabi, Sehrish Manan, Muhammad Yousaf, and Hongwei Hou, « Role of Recombinant DNA Technology to Improve Life », *International Journal of Genomics,* (2016): 1-14.

[112] William Studier, F., Alan H. Rosenberg, John J. Dunn, and John W. Dubendorff, « Use of T7 RNA Polymerase to Direct Expression of Cloned Genes », *Methods in Enzymology*, (1990), 185:60-89.

[113] Panja Subrata, Swati Saha, Bimal Jana, and Tarakdas Basu, « Role of Membrane Potential on Artificial Transformation of E. Coli with Plasmid DNA », *Journal of Biotechnology,* (2006), 127, nº 1; 14-20.

[114] Carter Matt and Jennifer Shieh, « Gene Delivery Strategies », *Guide to Research Techniques in Neuroscience*, (2015), 239-52.

[115] Bertani G, « STUDIES ON LYSOGENESIS I: The Mode of Phage Liberation by Lysogenic Escherichia Coli », *Journal of Bacteriology,* (1951), 62, n° 3, 293-300.

[116] Egan Alexander J. F. and Waldemar Vollmer, « The Physiology of Bacterial Cell Division: Bacterial Cell Division », *Annals of the New York Academy of Sciences,* 1277, nº 1, (2013): 8-28.

[117] Pletnev P. I., I. A. Osterman, P. V. Sergiev, A. A. Bogdanov, and O. A. Dontsova. « Survival Guide: Escherichia Coli in the Stationary Phase ». *Acta Naturae*, (2015), 7, no 4: 22-33.

[118] Sezonov Guennadi, Danièle Joseleau-Petit, and Richard D'Ari. « *Escherichia Coli* Physiology in Luria-Bertani Broth ». *Journal of Bacteriology*, (2007), 189, no 23: 8746-49

[119] McCue Justin T., « Chapter 25: Theory and Use of Hydrophobic Interaction Chromatography in Protein Purification Applications », *Methods in Enzymology*, (2009), 463:405-14.

[120] U. K. Laemmli, « Cleavage of Structural Proteins during the Assembly of the Head of Bacteriophage T4 », *Nature*, (1970), Vol.227: 680-685.

[121] Schägger Hermann, and Gebhard Von Jagow. « Tricine-Sodium Dodecyl Sulfate-Polyacrylamide Gel Electrophoresis for the Separation of Proteins in the Range from 1 to 100 KDa ». *Analytical Biochemistry,* 166, n° 2, (1987): 368-79.

[122] Bradford Marion M., « A Rapid and Sensitive Method for the Quantitation of Microgram Quantities of Protein Utilizing the Principle of Protein-Dye Binding », *Analytical Biochemistry*, (1976), 72: 248-254

[123] Spencer Virginia A., and James R. Davie, « Isolation of Proteins Cross-Linked to DNA by Cisplatin », *The Protein Protocols Handbook*, (2002) 747-52.

[124] Stetefeld Jörg, Sean A. McKenna, and Trushar R. Patel. « Dynamic Light Scattering: A Practical Guide and Applications in Biomedical Sciences », *Biophysical Reviews*, (2016), 8, n° 4: 409-27

[125] Allen Geoffrey, *Protein: A Comprehensive Treatisen,* (1999) Vol.2: 271-305

[126] Wriedt Thomas, « Mie Theory: A Review ». *The Mie Theory*, 169:53-71, (2012)

[127] Kaszuba M., Sagar C., « A basic introduction to Dynamic Light Scattering (DLS) for particle size analysis», (2017).

[128] Hunter R. J. « Zeta Potential in colloid science. Principles and Applications ». *Zeta Colloid science*, (1981) Ch.1: 1-6.

[129] Kumar Ajeet, and Chandra Kumar Dixit. « Methods for Characterization of Nanoparticles ». In *Advances in Nanomedicine for the Delivery of Therapeutic Nucleic Acids*, (2017), 43-58

[130] Kaszuba Michael, Jason Corbett, Fraser Mcneil Watson, and Andrew Jones. « High-Concentration Zeta Potential Measurements Using Light-Scattering Techniques ». *Philosophical Transactions of the Royal Society A: Mathematical, Physical and Engineering Sciences*, (2010) 368, n° 1927: 4439-51.

[131] DiStefano Johanna K., « Disease Gene Identification: Methods and Protocols », *Methods in Molecular Biology*. (2011), Vol.700, Chap.8

[132] Carter Paul, « Site-Directed Mutagenesis », *Biochem. J.* (1986), 237, 1-7

[133] Schochetman Gerald, Chin-Yih Ou and Wanda K. Jones, « Polymerase Chain Reaction » *The Journal of Infectious Diseases*, (1988), Vol. 158, N°. 6, pp.1154-1157.

[134] Clack Nathan G, Khalid Salaita, and Jay T Groves. « Electrostatic Readout of DNA Microarrays with Charged Microspheres », *Nature Biotechnology,* (2008), 26, nº 7: 825-30

[135] Johnson Daniel, Nidal Hilal, and W. Richard Bowen, « Basic Principles of Atomic Force Microscopy », *Atomic Force Microscopy in Process Engineering*, 1-30,2009.

[136] Stephen B. Kaemmer, « Introduction to Bruker's ScanAsyst and PeakForce Tapping AFM Technology », *Bruker's application note #133*, (2011)

[137] Bruker Nano Surfaces and Metrology, « Using PeakForce Tapping Mode Atomic Force Microscopy to Image the DNA Double Helix », *AZoM*, (2023).

[138] Bruker Nano Surfaces Division, « Atomic Force Microscopy », *AFM Advanced Training class*, 2021.

[139] Melitz Wilhelm, Jian Shen, Andrew C. Kummel and Sangyeob Lee. « Kelvin Probe Force Microscopy and Its Application ». *Surface Science Reports* 66, nº 1 (2011): 1-27.

[140] Glatzel Th., S. Sadewasser, and M. Ch. Lux-Steiner. « Amplitude or Frequency Modulation-Detection in Kelvin Probe Force Microscopy ». *Applied Surface Science* 210, nº 1-2 (m2003): 84-89.

[141] Zerweck Ulrich, Christian Loppacher, Tobias Otto, Stefan Grafström, and Lukas M. Eng. « Accuracy and Resolution Limits of Kelvin Probe Force Microscopy », *Physical Review B,* 71, nº 12 (2005): 125424.

[142] Hu Min, Carolina Novo, Alison Funston, Haining Wang, Hristina Staleva, Shengli Zou, Paul Mulvaney, Younan Xia, and Gregory V. Hartland. « Dark-Field Microscopy Studies of Single Metal Nanoparticles: Understanding the Factors That Influence the Linewidth of the Localized Surface Plasmon Resonance », *Journal of Materials Chemistry* 18, nº 17 (2008): 1949.

[143] Wang Fuyan, Yiliang Li, Yameng Han, Zhongju Ye, Lin Wei, Hai-Bin Luo, and Lehui Xiao. « Single-Particle Enzyme Activity Assay with Spectral-Resolved Dark-Field Optical Microscopy », *Analytical Chemistry* 91, nº 9, (2019): 6329-39.

[144] Gao Peng Fei, Gang Lei, and Cheng Zhi Huang. « Dark-Field Microscopy: Recent Advances in Accurate Analysis and Emerging Applications », *Analytical Chemistry* 93, nº 11 (2021): 4707-26.

[145] Rottenfusser Rudi, Erin E. Wilson, and Michael W. Davidson. « Contrast in Reflected Light Microscopy », *Carl Zeiss Microscopy Online Campus*.

[146] Smith Brian C. *Fundamentals of Fourier Transform Infrared Spectroscopy*. CRC Press, (2011), 2nd edition.

[147] Webb Lauren J., Sandrine Rivillon, David J. Michalak, Yves J. Chabal and Nathan S. Lewis. « Transmission Infrared Spectroscopy of Methyl- and Ethyl-Terminated Silicon (111) Surfaces ». *The Journal of Physical Chemistry B,* 110, nº 14 (2006): 7349-56.

Chapter IV : Gold nanoparticles on doped silicon as an ideal object to mimic ferritin nanocages: Electrostatic study of charged nanoparticles on silicon

Introduction

This chapter describes the work performed during the first year of this thesis in the SU laboratory. The related results were published in the *Nanoscale* journal in March 2023 and presented at the April 2023 session of the *Material Research Society* conference in San Francisco, California. Here, we present an electronic study of gold nanoparticles (AuNPs) immobilized on a doped silicon surface (*n-Si* or *p*-Si). First, we will present the phenomenon of Schottky contact between a metal and a semiconductor and how it is relevant for the nanoelectronic field. Then, the synthesis of the AuNPs and the preparation of our sample will be described, followed by their characterisation by observation techniques such as dark-field microscopy (DFOM) and scanning electron microscopy (SEM). After that, we will present the results of the KPFM characterisation of AuNPs on *n*-Si (or *p*-Si). These results present a model system that sheds light on the mechanism of the Schottky contact, as well as the observation and quantification of the Schottky barrier (SB) for nanostructures. The effects described here are discussed using the classical electrostatic approach. These results will be applied in Chapter V to the case of ferritin nanocages in interaction with silicon. Even if the modelling of a ferritin nanocage with a metallic nanoparticle is a very crude approximation, it helps to understand the effects induced by a partially conducting nano-object on a semiconductor surface.

1. Metal/semiconductor contact: Schottky barrier and band bending

Schottky contact occurs when a metal and a semiconductor are in contact and when their respective work functions are different, with the metal one being larger.[148] This phenomenon has been well established since the 1920s following the work of W.H. Schottky and plays a fundamental role in controlling the electric current in electronic devices, triggering the transfer of electrons in catalysis, and enabling the current onset in photovoltaic cells.[149] The Schottky barrier (SB) reflects a special distribution of charges near the interface that spans over the space charge region (SCR) on the semiconductor side. It is responsible for the onset of a rectifying current. Even if the qualitative behaviour is well documented, the exact calculation of the barrier height is still under debate.[150] Moreover, when dealing with nanostructures, such as metallic nanoparticles in contact with a semiconducting surface, this barrier is even less predictable because the nanoparticles are already significantly charged when their size is small, which

profoundly modifies their apparent work function.[151–153] Moreover, their work function also depends on their diameters.[152–154] Yet, predicting the presence of a Schottky barrier and its height (in millivolt) in the case of nanoparticles has become an important topic.[155] A renewed interest also arises from the field of photocatalysis, where gold nanoparticles are often used for injecting hot electrons into a semiconductor substrate and triggering chemical reactions.[18,156,157] AuNPs are also used for nanoelectronic devices where an electrical contact between a gold nanostructure and a semiconductor is sought: this is essential to properly assess whether the contact is ohmic or of Schottky type (rectifying).[148] In such investigations, KPFM serves as a key instrument since it allows measuring the variations of the local work function through the CPD for individual nanostructures.[149,158] It has recently been applied for AuNPs on TiO_2 by several groups.[18,156,157,159–161] In this thesis, we used KPFM for analysing the profile of electric potential of the Schottky barrier formed by 50 nm AuNPs grafted on silicon with either *n*- or *p*-doping.

2. Gold nanoparticles immobilized on doped silicon wafer

2.1. Experimental methods : synthesis of gold nanoparticles and immobilization on silicon surface

The gold nanoparticles (AuNPs) were synthesized by Yoann Prado, chemical engineer in INSP, using the method explained by Bastús *et al.* (2011)[162]. AuNPs of 50 nm in diameter were obtained following a kinetically controlled seeded growth strategy via the reduction of chloroauric acid ($HAuCl_4$) by sodium citrate ($Na_3C_6H_5O_7$). The sizes of the AuNPs were confirmed by UV-Vis spectroscopy and transmission electronic microscopy (TEM). Citrate molecules were chosen to stabilize the AuNPs because once AuNPs are immobilized on a surface, the citrate molecules can be easily removed via rinses and drying, so they will not interact with the KPFM tip. In this work, *n*-doped and *p*-doped silicon wafers were used as substrates onto which AuNPs were immobilized. For this, we functionalised the silicon wafer via a silanization process with a 3-aminopropyltriethoxysilane (APTES) molecule (Figure 49). First, the silicon wafers were rinsed with ultrapure water and dried under a nitrogen (N_2) flow, and then dipped into an APTES:methanol (volumetric ratio 1:10) solution for 2 hours. The wafers were rinsed with methanol to remove excess APTES and dried under N_2 flow. After that, one drop of AuNPs suspension was drop-casted onto each of the four silicon samples with

an increasing deposition time: 1 min (sample A), 2 min (sample B), 10 min (sample C), and 40 min (sample D). Finally, the samples were rinsed with ultrapure water and dried under N_2 flow (see the detailed protocols and materials in the Appendix IV-1).

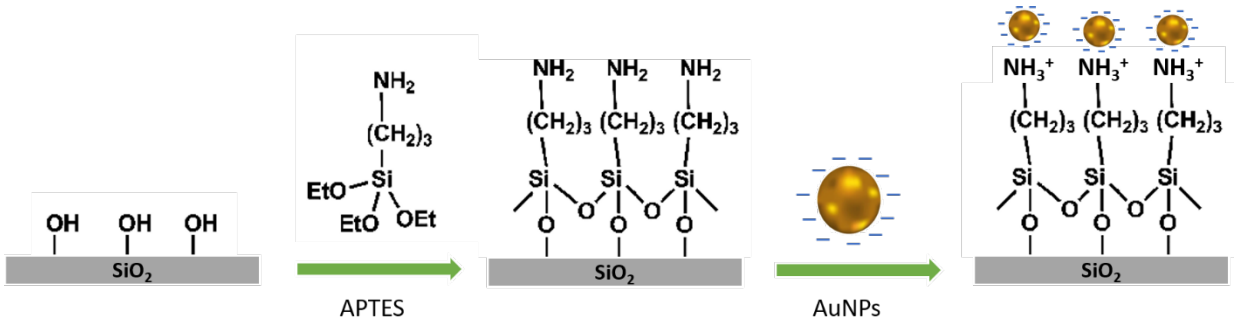

Figure 49 : Schematic of the silicon wafer silanization with APTES. A native oxide layer (SiO_2) lies on top of the silicon surface. Notice that the scheme is not at the correct scale (the scale of molecule has been exaggerated)

2.2. Microscopy measurements: SEM and dark-field optical microscopy

Scanning Electron Microscopy

The obtained samples were characterised by microscopy techniques. First, scanning electron microscopy images (SEM) of sample A were recorded using a Zeiss supra 40 instrument. In Figure 50, a 2 x 1.5 µm² area of the sample is shown. The size distribution of the AuNPs has been measured from five different images from the same sample and on 116 nanoparticles in total (see the inset in Figure 50). More SEM images are shown in the Appendix IV-2. We measured an average diameter of 55 ± 10 nm, which is coherent with the diameter of the synthesised AuNPs. Some of AuNPs are found to be aggregated on the surface, as shown in Figure 50.

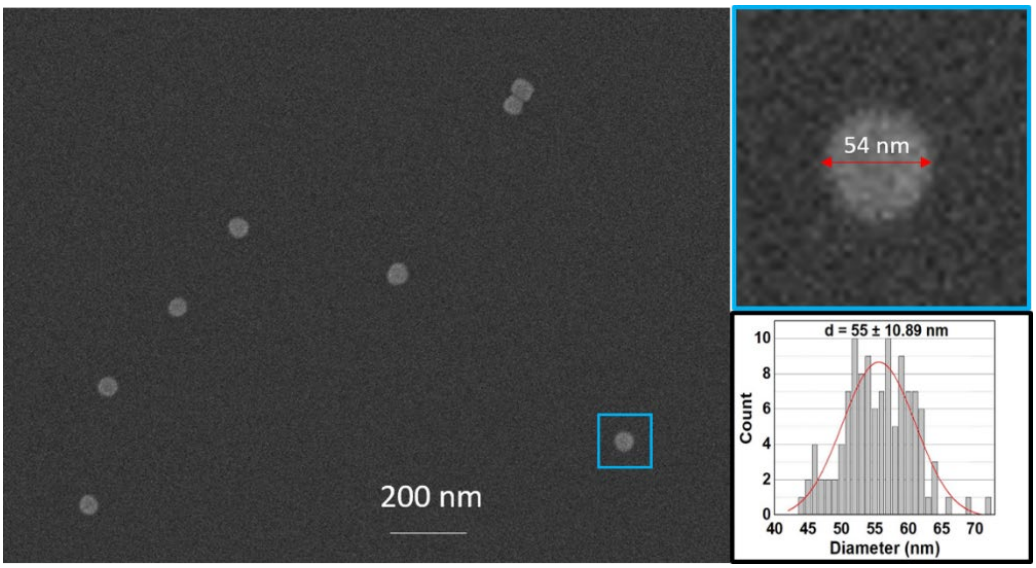

Figure 50: SEM images of gold nanoparticles deposited on a n-doped silicon wafer that was previously functionalized with APTES. The lower inset shows the size distribution of the particles with a Gaussian fit. The average diameter is 55 ± 10 nm.

Dark-Field Optical Microscopy

Dark-field microscopy (DFOM) images of the samples A, B, C, and D were recorded and shown in Figure 51. These images exhibit clear, bright, and green spots that are caused by the optical scattering of AuNPs. This allows a rapid estimation of the surface coverage with AuNPs as long as the AuNPs are not too close to each other. We see an increase in the AuNP coverage on silicon from sample A to sample D as the time of deposition increases. The density of AuNPs was computed as follows: 0.42 NP.μm^{-2} for 1 min, 0.50 NP.μm^{-2} for 2 min, 0.94 NP.μm^{-2} for 10 min, and more than 1.0 NP.μm^{-2} for 40 min. In order to perform a meaningful analysis of the CPD induced by AuNPs, we seek samples with well-separated nanoparticles. On the basis of the DFOM images, we select the sample A and will concentrate on this sample in the following.

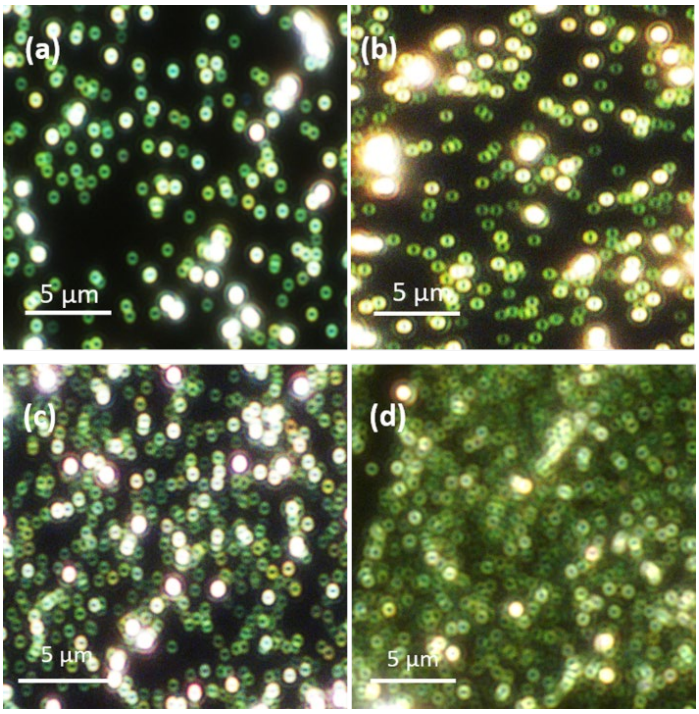

Figure 51 : Dark-field optical microscopy images (20 × 20 µm²) of AuNPs drop-casted on an n-doped silicon wafer for various times: (a) sample A, 1 min; (b) sample B, 2 min; (c) sample C, 10 min; and (d) sample D, 40 min. Light scattered by AuNPs exhibits a typical ring-shaped pattern (see the text below).

Interestingly, we notice in the DFOM images in Figure 51 that AuNPs appear with a green scattering pattern that has a diameter of about 850 nm and, above all, that they exhibit a ring or *doughnut shape*. According to Chen *et al.* (2011)[163], the ring shape of the dark-field scattering pattern is due to the interaction between the substrate and the nanoparticles (see Appendix IV-3). In fact, when AuNPs are excited by light, their localized surface plasmon resonance (LSPR) behaves like a dipole that is oriented parallel or perpendicular to the surface, depending on the orientation of the excitation electric field (which in turn is related to the illumination geometry of the dark-field microscope). This dipole induces an image dipole in the substrate, and both are coupled together. When the excitation electric field is parallel to the surface, the LSPR dipoles present a radiation pattern with a torus shape whose plane is oriented perpendicular to the substrate. It is detected as a bright solid spot. Conversely, when the excitation field is perpendicular to the substrate, the dipolar radiation pattern is a torus oriented parallel to the surface and is detected as a ring-shaped spot. Then, the total intensity of the dark-field scattering pattern will be the sum of the contributions from the dipole and its image. For the parallel one, its image is opposite to the original, and so they will cancel each other partially. On the other hand, the perpendicular one is along the same direction as its image, leading to an

increase in the net dipole. Since the coupling intensity of the radiation and the images is strongly dependent on the dielectric constant of the substrate, when the dielectric constant increases, the magnitude of the coupling increases too. In the present study, silicon has a high dielectric constant, leading to a decrease in the parallel radiation intensity and an increase in the perpendicular one. It results in a ring-shaped scattering pattern on silicon. However, when these AuNPs were deposited on glass, we observed a regular circular pattern and not a ring-shaped one.

3. Electrical characterisation of gold nanoparticles on doped silicon by Kelvin probe force microscopy

In this part, the results obtained by KPFM measurements of sample A are presented. All the KPFM images were acquired within the two-pass mode with values of LSH between 20 nm and 70 nm, at a slow rate (0.15 Hz or 750 nm.s^{-1}) for 1024 x 1024 pixels images. In addition, we studied the parameters that influence the KPFM measurements. Finally, the sphere-plane (gold nanoparticle on silicon) model is described.

3.1. KPFM measurements: ring-shape of AuNPs on *n*-Si

One typical topography image obtained with KPFM on sample A shows a portion of the image with seven AuNPs (Figure 52.a). The diameters of the nanoparticles measured from the heights acquired in AFM are between 51 and 61 nm, which is consistent with the SEM images (Figure 50). The lateral apparent diameter of an AuNP was measured on 12 nanoparticles, and the average value was found to be 90 nm, which is higher than the height due to the convolution with the tip. The APTES monolayer also exhibits small nanograins of typical height of 1 nm and up to 8 nm that were easily distinguished from AuNPs. The corresponding CPD variations were below 1 mV and will not be discussed further because they cannot be confused with AuNPs (see an illustration in the Appendix IV-4). Figure 52.b displays the CPD image of these seven AuNPs. The CPD rises from − 808 mV on the silicon substrate up to − 777 mV close to the AuNPs. The close-up image in Figure 52.d shows that the CPD adopts a ring pattern with a diameter of 120 nm, which exhibits some similarities with the DFOM images, but for completely different reasons, as explained further on. The CPD reaches its maximum value at

the edge of the ring and a minimum value at its center, which is 10 mV below these edges. Figure 52.e−f display the CPD profiles across such rings.

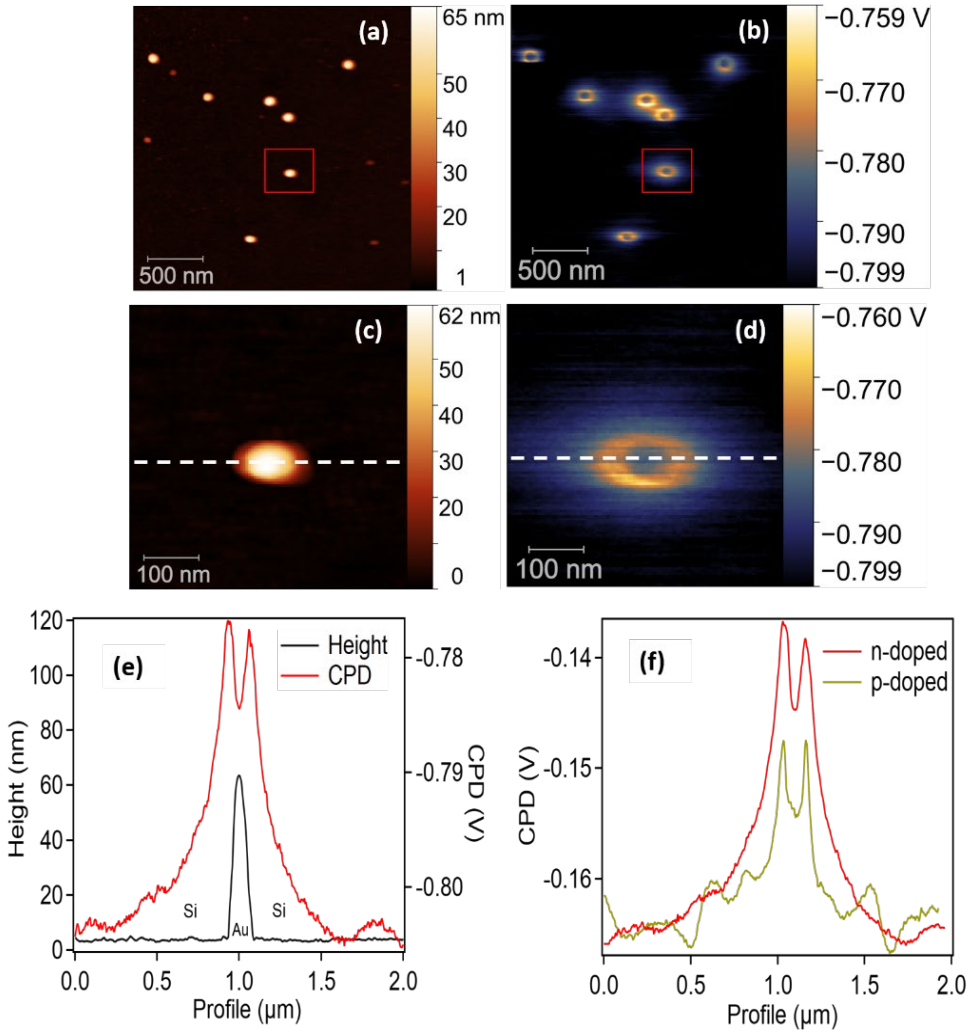

Figure 52 : Topography images (a and c) and their corresponding CPD images (b and d) of gold nanoparticles on n-doped silicon (sample A) measured by KPFM. (e) profile of the height (black line) and of the CPD (red line) for one single AuNP (profile taken along the white dashed lines). (f) CPD profiles for one AuNP on an n-doped (red) and a p-doped (green) sample. Notice that the n-doped curve was shifted vertically to align with the p-doped curve for the sake of comparison.

Similar results can be observed for AuNPs deposited on *p*-doped silicon, showing also a ring-shaped CPD pattern but less pronounced (Figure 53.b). More precisely, Figure 52.e shows the overlap of the topography (black line) and the CPD (red line). It shows that the increase in the CPD occurs above the interfaces between the AuNP and the doped silicon, and that the central drop occurs when the tip is above gold. These results reveal the existence of a potential barrier when scanning from silicon to gold, with a barrier height given by the

difference of the CPD measured above the junction Si/Au ($\phi_{junction}$ = −777 mV on Figure 52.e) and above the silicon (ϕ_{Si} = −808 mV). Such a potential rise ($\Delta CPD = \phi_{junction} - \phi_{Si}$) was measured for a large number of AuNPs on *n*-doped silicon substrates, as well as for *p*-doped substrates. We have measured that the potential rise is higher for AuNPs on *n*-doped silicon than on *p*-doped silicon. Potential barriers were measured for 32 different AuNPs and show an average potential increase of 34.3 ± 0.6 mV for the *n*-doped and 21.2 ± 1.0 mV for the *p*-doped (Figure 53.c−d).

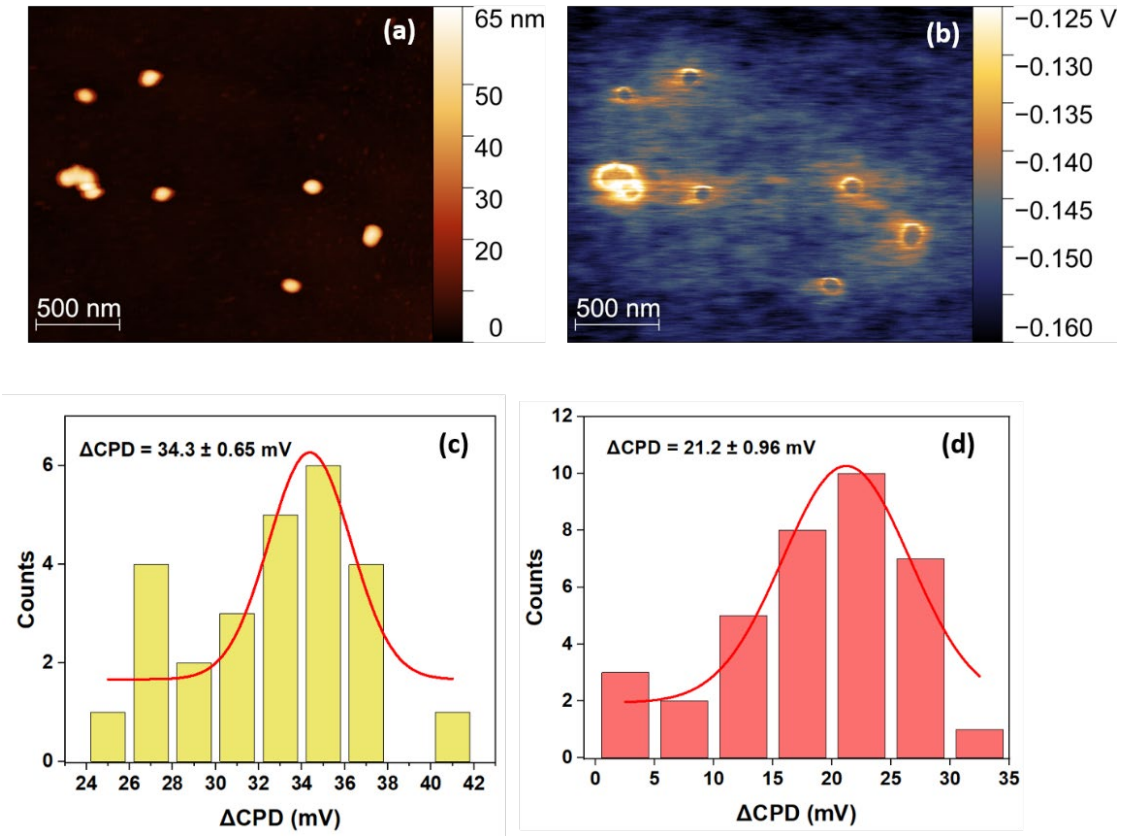

Figure 53: KPFM topography (a) and CPD (b) images of gold nanoparticles on p-doped silicon wafer ($N_D = 10^{14} – 10^{15}$ cm^{-3}). Distributions of ΔCPD measured for gold nanoparticles on n-doped (c) and p doped (d) silicon substrates. In both cases, the dopant concentration was 10^{15} cm^{-3} (10-20 Ω.cm).

In order to rule out the probability that the ring patterns were due to a convolution artefact, additional measurements were carried out at higher scan rates and at different LSHs. In Figure 54, KPFM images obtained on sample A with three different scan rates are shown. All the CPD images exhibit the ring-shaped patterns at every scan rate. This confirms that this pattern in the potential images is not an artefact from this parameter. However, at a high scan

rate (3000 nm/s), the ring tends to become asymmetric. This is why all the other images were recorded with a scan rate of 750 nm.s^{-1}.

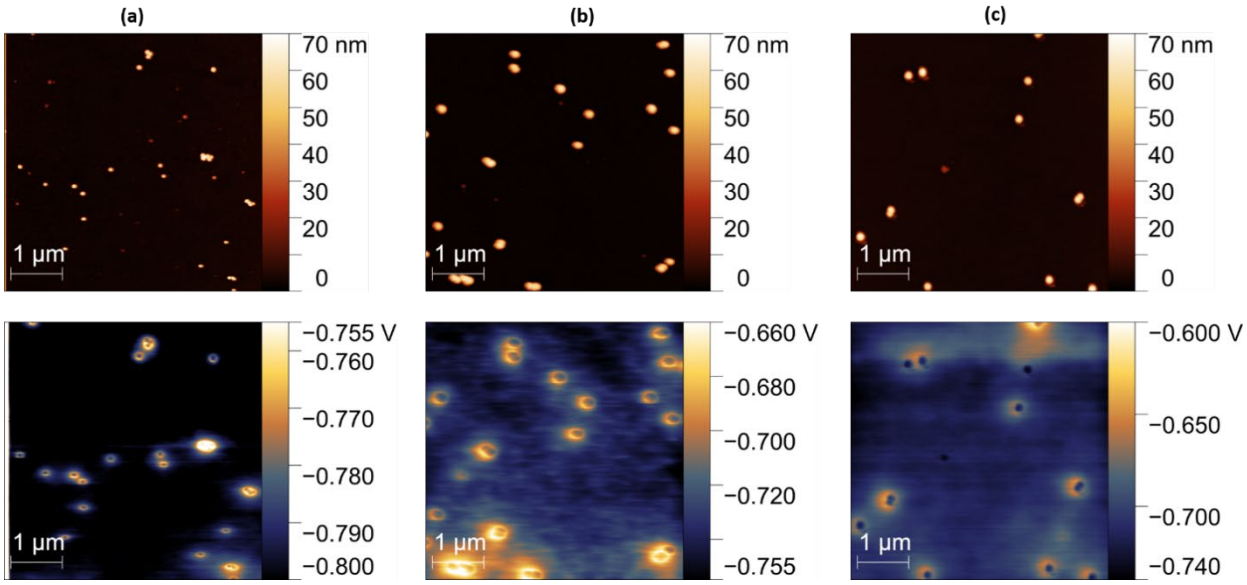

Figure 54 : Topography (top) and relative CPD (bottom) images (5 x 5 µm²) of gold nanoparticles on n-doped silicon obtained at different scan rates: (a) 750 nm.s^{-1}; (b) 2250 nm.s^{-1}; (c) 3000 nm.s^{-1}.

In Figure 55 below, KPFM images of the same area obtained on sample A at five different LSHs are shown. Table 1 summarizes the values of the potential barrier ΔCPD when the LSH is decreased. For LSH < 40 nm, CPD images exhibit a scanning artefact on the gold nanoparticles due to unpredictable contact between the tip and the sample. The values for ΔCPD become unreliable. At LSH = 20 nm, the ring-shaped pattern is no longer visible. As long as the LSH is greater than 40 nm, the CPD images consistently exhibit a ring-shaped pattern.

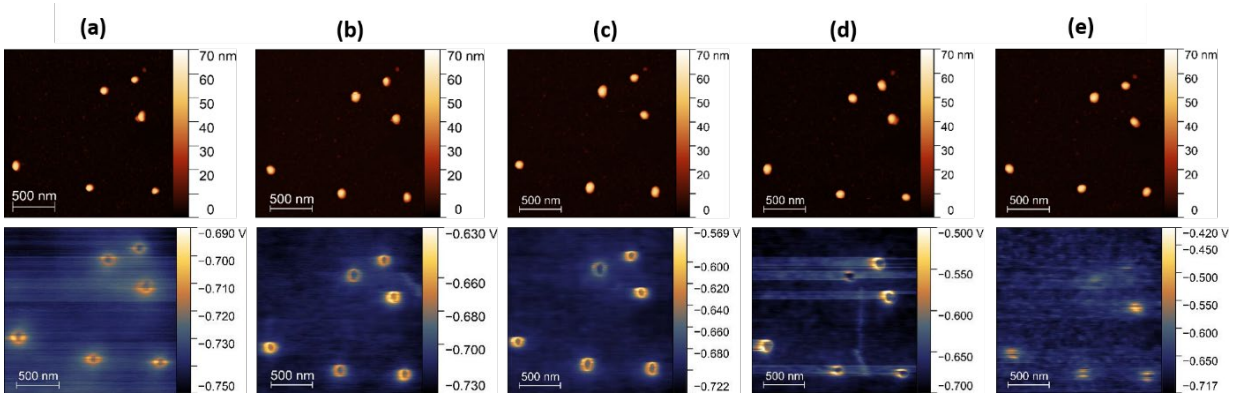

Figure 55 : Topography (top) and relative CPD (bottom) images of 55 nm AuNPs on n-doped silicon obtained at different LSH: (a) 70 nm; (b) 50 nm; (c) 40 nm; (d) 30 nm; (e) 20 nm.

LSH (nm)	70	60	50	40	30	20
ΔCPD (mV)	30	34	65	80	30-120 (*)	0-100 (*)

Table 1 : Values of the ΔCPD for decreasing values of the LSH from 70 to 20 nm. Values marked with (*) indicates unreliable data caused by a too low value of the LSH.

3.2. Band bending at an ideal planar interface

Description and equations of the band bending

The intimate contact between gold and silicon generates a Schottky contact. It results in a local charge reorganization and the built-up of a local electric field (linked to the so-called built-in potential). Since the work function of gold ($q\phi_{Au}$) is higher than that of silicon ($q\phi_{Si}$), electrons tend to accumulate at the metal surface, whereas holes spread next to the semiconductor surface. Charge neutrality requires that positive and negative charges are equilibrated. Since the carrier concentration is relatively low on the semiconductor side, the positive charges are distributed over a rather large barrier region of width W_D, which is the depletion region or space charge region (SCR) (see reference textbooks, e.g., Sze *et al.*[148]). Therefore, the potential energy of an electron on the silicon side (x > 0) writes:

$$E(x) = q\phi_{Si} - \frac{q^2 N_D}{\varepsilon_S}\left(W_D x - \frac{x^2}{2}\right)$$

Equation 9 : Potential energy of an electron on the silicon side for $0 \leq x \leq W_D$

$$E(x) = q\phi_{Si}$$

Equation 10 : Potential energy of an electron on the silicon side for $x > W_D$

In the Equation 9 and Equation 10, q is the elementary charge, N_D (m^{-3}) is the semiconductor dopant concentration, and ε_S ($F.m^{-1}$) is the silicon permittivity. All the quantities are expressed in S.I. units.

The variation of the electron energy in the semiconductor is known as the *band bending*. In the absence of any external electric field, this potential energy is equal to the work function and it corresponds to the contact potential difference (CPD) measured in our experiments within one additional constant linked to the work function of the tip of the KPFM. W_D is calculated by solving the Poisson equation and is related to the built-in potential ϕ_{bi} according to Equation 11 :[148]

$$W_D = \sqrt{\frac{2\varepsilon_S}{qN_D}(|\phi_{bi}| - \frac{kT}{q})}$$

Equation 11 : Value of the depletion layer W_D as a function of the built-in potential ϕ_{bi} .

The corresponding energy band diagram is presented in Figure 56.a and shows the progressive band bending of an amount of ϕ_{bi} over the distance W_D. The CPD profile shown in Figure 52.e corresponds to this evolution and is discussed more in depth in the following. The Schottky barrier height (SBH) is denoted as $\phi_{B,n}$ for the *n*-doped silicon in Figure 56 and can be calculated according to Equation 12 for a semiconductor surface without surface states (ideal case):

$$\phi_{B,n} = \phi_{bi} + \phi_n$$

Equation 12 : Schottky barrier height $\phi_{B,n}$ for a n-doped silicon.

Where ϕ_n is the potential difference between the conduction band and Fermi level E_F, defined as:

$$\phi_n = kT \ln \frac{N_c}{N_D}$$

Equation 13 : Potential difference between the conduction band and the Fermi level E_F. N_C is the effective conduction band density of states at 300 K, $N_C = 3.2.10^{19}$ cm^{-3}.

From Equation 13, the calculation yield ϕ_n = 270 mV for the dopant concentration N_D=10^{15} cm^{-3} used in our experiments. The temperature is set at T = 300 K for all the calculations.

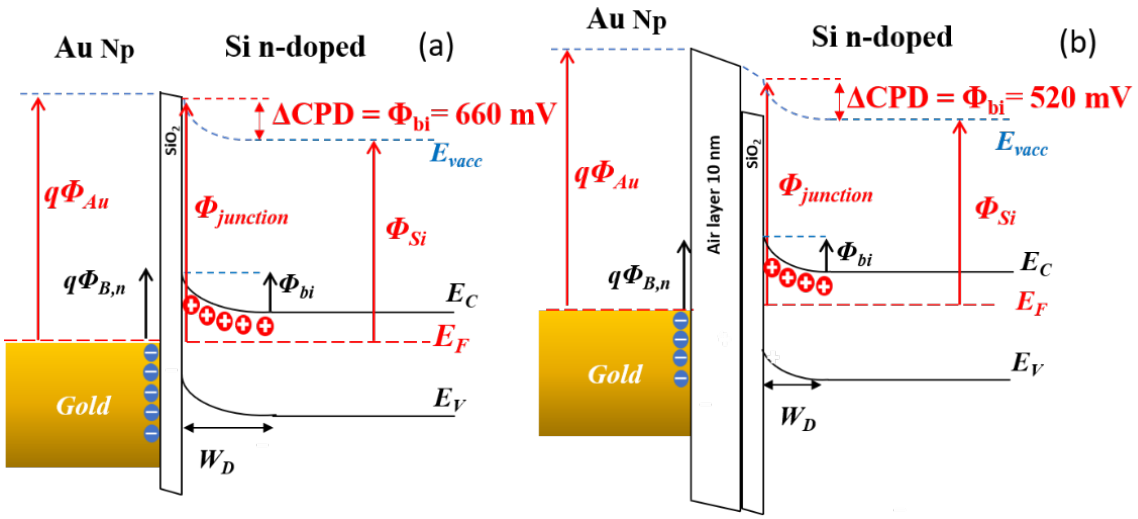

Figure 56 : Schematic of band bending when gold and n-doped silicon are in direct contact (a) and in contact across a 10 nm air layer (b). The SiO_2 native oxide layer is represented on top of the silicon wafer with a thickness of 2 nm.

In a *p*-doped semiconductor, holes in the valence band are the majority carriers, and they usually control the electrical current once they are in contact with a metal. In this case, a Schottky contact appears when the Fermi level of the metal (ϕ_m) is lower than the semiconductor one (ϕ_s): the bands bend downward, and a Schottky barrier for holes $\phi_{B,p}$ appears. On the other hand, when $\phi_m > \phi_s$, bands bend upwards and $\phi_{B,p} = 0$. The contact is ohmic. From the results shown in Figure 52.f, the CPD profile for *p*-doped silicon shows an upward band bending corresponding to an ohmic contact. However, a band bending with a potential barrier (ϕ_{bi} = 21 mV) is still detected by KPFM for the *p*-doped substrate. The value of this barrier is lower than the one obtained on *n*-doped silicon (ϕ_{bi} = 34 mV).

Numerical calculations of the band bending

If we consider this ideal planar model, the values of the built-in potential and the SBH can be easily computed. Calculations are carried out with the software Band Diagram Program developed by Knowlton[164,165] which solves the Poisson equation as briefly explained above. With an Au/*n*-Si junction that includes a 2 nm SiO_2 layer (thermal oxide layer used as received)

this calculation yields: ϕ_{bi} = 660 mV and W_D = 910 nm. The SBH is $\phi_{B,n}$= 930 mV. More details can be found in the Appendix IV-5. However, the calculated value of ϕ_{bi} is far greater than 30 mV measured in our experiments, and so is the calculated SBH for *n*-doped silicon compared to the 10 mV obtained with KPFM. Actually, in the case of nanoparticles, band bending occurs not at a planar interface but at a sphere-plane interface. We need to refine the model and consider that AuNPs and silicon surfaces have only one point of contact (right under the nanoparticle). This is the topic of the following section.

3.3. Calculation of the band bending at the sphere-plane interface

We now consider the spherical AuNP on the planar silicon substrate and use the polar coordinates centered on the AuNP as shown in Figure 57. Only along a vertical line (θ = 0°) gold is in direct contact with the silicon surface. For other angles, there is a gap of air between gold and silicon, denoted as d_{air}. Therefore, the band bending induced by the AuNP can be calculated by varying the polar angle θ between − 90° and + 90°. The case θ = 0° (d_{air} = 0 nm) was already calculated in the previous section, and the following values were computed for the *n*-doped silicon: ϕ_{bi} = 660 mV and W_D = 910 nm. At θ = 45°, geometrical considerations directly yield d_{air} = 10 nm, as shown in Figure 57. These calculations are illustrated in Figure 56.b and yield ϕ_{bi} = 520 mV and W_D = 800 nm (see also in the Appendix IV-5). Figure 57 shows the variation of the SCR for all the possible angles. The orange area represents the geometry of the depletion layer induced below the AuNP and where positive charges accumulate. Interestingly for θ > 86°, this model shows that there is a limit over which there is no more electrostatic influence of the AuNP on the silicon and over which the SCR vanishes to zero. This limit corresponds to d_{air} = 320 nm. This value gives an order of magnitude of the tip–nanoparticle distance under which a CPD change is expected. Actually, Figure 52.d shows that the CPD starts increasing in a circular area of radius between 200 and 300 nm, in agreement with this limit of d_{air} = 320 nm.

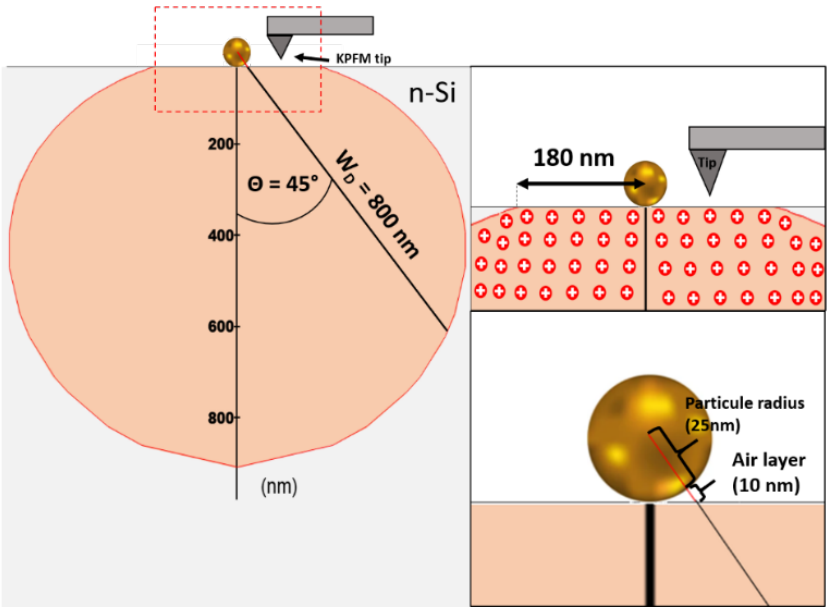

Figure 57 : Graphic of depletion layer lengths W_D calculated as a function of the angle θ (°). Each angle corresponds to a thickness of air layer. At θ = 45°, the air layer is 10 nm and W_D = 800 nm.

Regarding the values for ϕ_{bi}, our calculations are only indicative and cannot reproduce the exact values of the built-in potential and the SBH. One issue is the convolution of the CPD profile with the finite value of the radius of the KPFM tip. In Figure 58 is shown an approached CPD profile that mimics the convolution of the CPD profile with a spherical tip of radius 25 nm. The initial band bending is 46 mV and the convolution leads to a reduction down to 35 mV. This calculation also shows that the SBH is reduced from 66 mV to 20 mV.

Finally, this study shows that on a silicon doped with $N_D = 10^{15}$ cm^{-3}, a 50 nm AuNP induces a ring-shaped space charge region that is positively charged and that spreads some 200 nm around the nanoparticle. It results in a local increase in the surface potential of at least 34 mV. Previous work from Wang *et al.* (2017)[18] also showed a ring-shaped pattern of the CPD for AuNPs deposited on the TiO_2 substrate. They measured a 30 mV potential barrier. Other authors studied 100 nm TiO_2 nanoparticles deposited on Pt and showed that the SBH is reduced to 300 mV in the presence of an insulating layer.[166] However, no clear explanation of the ring pattern in the CPD images was provided.

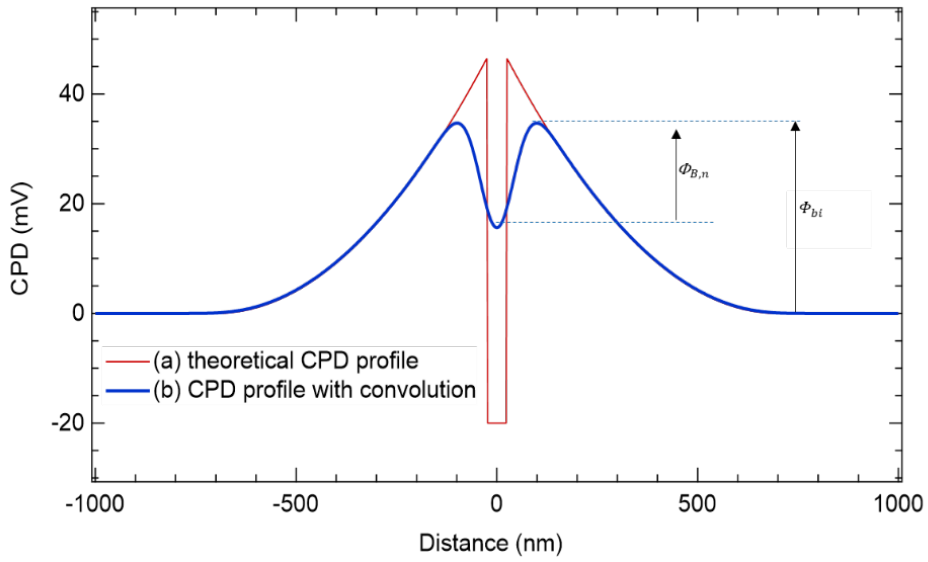

Figure 58 : Simulated CPD profiles of an AuNP/n-Si junction: the ideal profile (red) and the profile including the effect of the tip convolution (blue). For a 50 nm AuNP, the resulting Schottky barrier height is $\phi_{B,n}$ = 20 mV and the built-in potential is ϕ_{bi} = 35mV.

4. Conclusion

In this study, we have investigated how 55 nm AuNPs deposited on a doped silicon surface induce charge transfer and how KPFM data reveal the band bending in silicon. It shows up as ring-shaped patterns of 120 nm diameter around AuNPs in the CPD images, where the CPD rises to 34 mV for *n*-doped substrates and 21 mV for *p*-doped substrates (dopant concentration 10^{15} cm^{-3} in both cases). This circular area probed by KPFM is a visualization of the space charge region, which is positively charged in the case of the Au–Si interface at equilibrium (no external bias was applied). A simple model based on solving the Poisson equation shows that the Schottky barrier height is evaluated at 300 mV in the case of spherical AuNPs on *n*-Si, which turns out to be much lower than in the case of the traditional planar junction Au–Si (SBH = 930 mV). With our KPFM measurements, we have detected the SBH as a 10 mV dip in the centers of the ring patterns in the CPD images. This low value is caused by the limited lateral resolution of KPFM, since the CPD results from the convolution of the potential variation and the curvature of the tip. This detection of the positive charges gathered next to the AuNPs, even at equilibrium, opens up new perspectives for understanding the reactivity of AuNPs and other metallic nanoparticles on semiconductors. These positive charges (holes) around the AuNPs can interact with adsorbed species and be used for different applications such as photocatalysis

or chemical reactions.[155,166] Moreover, knowing the value of the SBH and the band bending area is of great interest for understanding how hot carriers can be generated using the plasmonic properties of AuNPs on doped silicon substrates.[152,159,160,167] This study performed during the first year of the thesis allowed us to become familiar with the parameters of the KPFM and the electronic phenomena (interaction of metal/semiconductor) that influence the measure of the CPD. Therefore, this work is a lead-in for the study of the electrostatic behaviour of ferritin nanocages immobilized on silicon.

5. References

[148] Sze S. M., and Kwok K. Ng. *Physics of Semiconductor Devices*. Third edition. Hoboken, (2007).

[149] Llacer Jaume, David Moerman, Olivier Douhéret, Xavier Noirfalise, Claudio Quarti, Roberto Lazzaroni, Didier Théron and Philippe Leclère. « Nanoscale Studies at the Early Stage of Water-Induced Degradation of $CH_3NH_3PbI_3$ Perovskite Films Used for Photovoltaic Applications ». *ACS Applied Nano Materials* 3, nº 8 (2020): 8268-77.

[150] Tung Raymond T., and Leeor Kronik. « Quantitative Explanation of the Schottky Barrier Height ». *Physical Review B* 103, nº 3 (2021): 035304.

[151] Stehlik Stepan, Tristan Petit, Hugues A. Girard, Jean-Charles Arnault, Alexander Kromka, and Bohuslav Rezek. « Nanoparticles Assume Electrical Potential According to Substrate, Size, and Surface Termination ». *Langmuir* 29, nº 5 (2013): 1634-41.

[152] Zhang Xuming, Yu Lim Chen, Ru-Shi Liu and Din Ping Tsai. « Plasmonic Photocatalysis ». *Reports on Progress in Physics* 76, nº 4 (2013): 046401.

[153] Zhang Yingjie, Jun Kang, Olivier Pluchery, Louis Caillard, Yves J. Chabal, Lin-Wang Wang, Javier Fernandez Sanz and Miquel Salmeron. « Nanoimaging of Organic Charge Retention Effects: Implications for Nonvolatile Memory, Neuromorphic Computing, and High Dielectric Breakdown Devices ». *ACS Applied Nano Materials* 2, nº 8 (2019): 4711-16.

[154] Wood David M. « Classical Size Dependence of the Work Function of Small Metallic Spheres ». *Physical Review Letters* 46, nº 11 (1981) : 749-749.

[155] Žerjav Gregor, Matevž Roškarič, Janez Zavašnik, Janez Kovač andAlbin Pintar. « Effect of Au Loading on Schottky Barrier Height in TiO2 + Au Plasmonic Photocatalysts ». *Applied Surface Science* 579 (2022): 152196.

[156] Gao Yuying, Wei Nie, Qianhong Zhu, Xun Wang, Shengyang Wang, Fengtao Fan, and Can Li. « The Polarization Effect in Surface-Plasmon-Induced Photocatalysis on Au/TiO_2 Nanoparticles ». *Angewandte Chemie* 132, nº 41 (2020): 18375-80.

[157] Kazuma Emiko, and Tetsu Tatsuma. « In Situ Nanoimaging of Photoinduced Charge Separation at the Plasmonic Au Nanoparticle-TiO_2 Interface ». *Advanced Materials Interfaces* 1, nº 3 (2014): 1400066.

[158] Knotek Petr, Tomáš Plecháček, Jan Smolík, Petr Kutálek, Filip Dvořák, Milan Vlček, Jiří Navrátil and Čestmír Drašar. « Kelvin Probe Force Microscopy of the Nanoscale Electrical Surface Potential Barrier of Metal/Semiconductor Interfaces in Ambient Atmosphere ». *Beilstein Journal of Nanotechnology* 10 (2019): 1401-11.

[159] Hammoud Leila, Claire Strebler, Joumana Toufaily, Tayssir Hamieh, Valérie Keller and Valérie Caps. « The Role of the Gold–Platinum Interface in $AuPt/TiO_2$ -Catalyzed Plasmon-Induced Reduction of CO_2 with Water ». *Faraday Discussions*, 2023, 10.1039.D2FD00094F.

[160] Jian Aoqun, Kai Feng, Huaping Jia, Qianwu Zhang, Shengbo Sang, and Xuming Zhang. « Quantitative Investigation of Plasmonic Hot-Electron Injection by KPFM ». *Applied Surface Science* 492 (2019): 644-50.

[161] Lee Hyungbeen, Yoochan Hong, Dongtak Lee, Seungyeon Hwang, Gyudo Lee, Jaemoon Yang, and Dae Sung Yoon. « Surface Potential Microscopy of Surfactant-Controlled Single Gold Nanoparticle ». *Nanotechnology* 31, nº 21 (2020): 215706.

[162] Bastús, Neus G., Joan Comenge, et Víctor Puntes. « Kinetically Controlled Seeded Growth Synthesis of Citrate-Stabilized Gold Nanoparticles of up to 200 nm: Size Focusing versus Ostwald Ripening ». *Langmuir* 27, nº 17 (2011): 11098-105.

[163] Chen Huanjun, Tian Ming, Shouren Zhang, Zhao Jin, Baocheng Yang and Jianfang Wang. « Effect of the Dielectric Properties of Substrates on the Scattering Patterns of Gold Nanorods ». *ACS Nano* 5, nº 6 (2011) : 4865-77.

[164] Southwick R.G., and W.B. Knowlton. « Stacked Dual-Oxide MOS Energy Band Diagram Visual Representation Program (IRW Student Paper) ». *IEEE Transactions on Device and Materials Reliability* 6, nº 2 (2006): 136-45.

[165] Southwick R G, A Sup, A Jain and W B Knowlton. « An Interactive Simulation Tool for Complex Multilayer Dielectric Devices ». *IEEE Transactions on Device and Materials Reliability* 11, nº 2 (2011): 236-43.

[166] Ano Taishi, Fuminao Kishimoto, Shuntaro Tsubaki, Yi-Hsien Lu, J. Nathan Hohman, Masato M. Maitani, Miquel Salmeron, and Yuji Wada. « Controlling the Schottky Barrier at the Pt/TiO_2 Interface by Intercalation of a Self-Assembled Monolayer with Oriented Dipole Moments ». *The Journal of Physical Chemistry C* 125, nº 25 (2021): 13984-89.

[167] Kale Matthew J., Talin Avanesian, and Phillip Christopher. « Direct Photocatalysis by Plasmonic Nanostructures ». ACS Catalysis 4, no 1 (2014): 116-28.

Chapter V: Electrostatic Properties of Ferritin Nanocages on Silicon: a KPFM study

Introduction

In this chapter is presented the work performed in the NTU and SU laboratory. Here, we are presenting a KPFM study of the electrostatic and morphological properties of AfFtn-AA nanocages (produced in the NTU laboratory) deposited on silicon. First, we will give a general description of the adsorption of proteins on solid surfaces. Secondly, we will present the results of the FTIR measurements of AfFtn-AA that confirmed their immobilisation on the surface. Thirdly, the KPFM results of individual AfFtn-AA and AfFtn-AA monolayers will be presented. They will bring strong and valuable information about the electrostatic and morphologic behaviour of AfFtn-AA on the silicon. Fourthly and lastly, we will demonstrate a novel approach to understanding the adsorption mechanisms of proteins on solid surfaces by measuring the electric dipoles of the ferritin directly at the surface. An article about the related results is currently in writing, and this chapter is strongly inspired by the draft of this article.

1. Adsorption of protein on solid surface

In biomolecular electronic applications, proteins adsorb on solid surfaces and must be retained in a bioactive state in order to maximize their functionality. Therefore, the interaction of the protein with the surface and its conformation are fundamental parameters for integrating proteins in electronic devices. However, the way proteins adsorb on a solid surface is difficult to predict, as they are polyampholyte molecules that possess multiple patches (hydrophobic, charged, polar) and their structure (helix α, β sheet, and self-assembly) makes them complex and electrostatically non-uniform molecules. Many studies described the adsorption of proteins (hydrophobin, cytochrome c, and lysozyme) on hydrophobic and charged surfaces through molecular simulations and demonstrated the important role of electrostatics in favourable protein adsorption. In particular, the orientation and conformation of adsorbed proteins were shown to be dictated by their electric dipole.[168–172] By means of the advent of X-ray crystallography and NMR techniques that established the structure of proteins at the atomic level, many dipole moments were determined from calculations[173] and experimentally correlated by electric dichroism and dielectric measurements in bulk solution.[173–176] However, the value of the measured bulk dipole varies because of the mobility of the charged amino acids[177] and differs from the measured dipole after adsorption due to conformational

changes.[171] Previous studies determined the electric dipoles of molecules adsorbed on a solid surface by capacitance measurement[178] or by measuring the surface potential.[179,180] In this thesis, we performed KPFM measurements of AfFtn-AA deposited on a solid surface in order to obtain their electric dipole.

2. Adsorption of AfFtn-AA nanocages on silicon

2.1. Experimental methods: AfFtn-AA deposition on silicon substrate

For the preparation of the samples, silicon wafers were cut into 1x1 cm² (3x1 cm² for FTIR) pieces with a diamond tip, cleaned with acetone and ethanol under sonication, and dried under nitrogen flow. Prior to deposition, AfFtn-AA solutions were filtered with a 0.22 µm filter to remove dust particles and unbound iron. One drop of the solution was drop-casted onto each of the silicon samples. Two deposition times were used: 1 minute to obtain very dispersed particles and 2 hours to produce a monolayer. Finally, samples were thoroughly rinsed with MiliQ water and dried under a nitrogen flow. In total, samples of AfFtn-AA loaded with 5 different iron contents (600Fe, 1200Fe, 2400Fe, 3600Fe and 4800Fe) on silicon wafers were prepared for this study.

2.2. Monitoring the adsorption of AfFtn-AA nanocages on silicon by FTIR

Solutions of AfFtn-AA were drop-casted on a silicon surface without any prior modification of the surface and followed by a thorough rinse and drying. The immobilization of the particles on the silicon surface was confirmed by differential FTIR following the protocol described in the Appendix III-3. In Figure 59 is displayed the IR spectrum obtained for an AfFtn-AA monolayer (red curve). As a test experiment, we also show the IR spectrum obtained with only the HEPES buffer (black curve). It shows that no chemical species have attached after rinsing of the buffer. Whereas, the AfFtn-AA monolayer spectrum shows clearly visible peaks associated with the ferritin structural unit. The 1656 cm^{-1} peak is assigned to the N−H (primary amine) bend vibrations and peaks at 1523 and 1542 cm^{-1} to the C═O bending mode. This association of peaks is known to be the footprint of proteins amino acids.[181,182] Moreover, the FWMH for the N-H peak was measured at 80 cm^{-1} in the KBr pellet (Soriano-Portillo *et al.*),[181] whereas in our case it was measured at 20 cm^{-1}, showing that the ferritins are in a chemically

ordered environment (i.e., a monolayer). Other bands at 2926-2962 cm^{-1} and 3305 cm^{-1} are assigned to CH_2 and −OH binding vibrations, respectively. From these results, we confirmed the immobilization of AfFtn-AA on the silicon surface. Here, particles were deposited on a silicon dioxide surface, SiO_2 (native oxide layer). As the point of zero charge of SiO_2 is around 2.0 – 3.7[183,184] and the pH of the drop-cast solution is 7.4 (HEPES buffer solution), most of the silanol sites (SiOH) are in their basic form (SiO^-) and the surface is negatively charged. From electrostatic potential calculations, the overall external surface of AfFtn-AA shows a dominant negative potential at pH 7.4. However, these calculations also showed localized positive regions of some significance that explain the immobilization of the ferritin onto a negative surface.

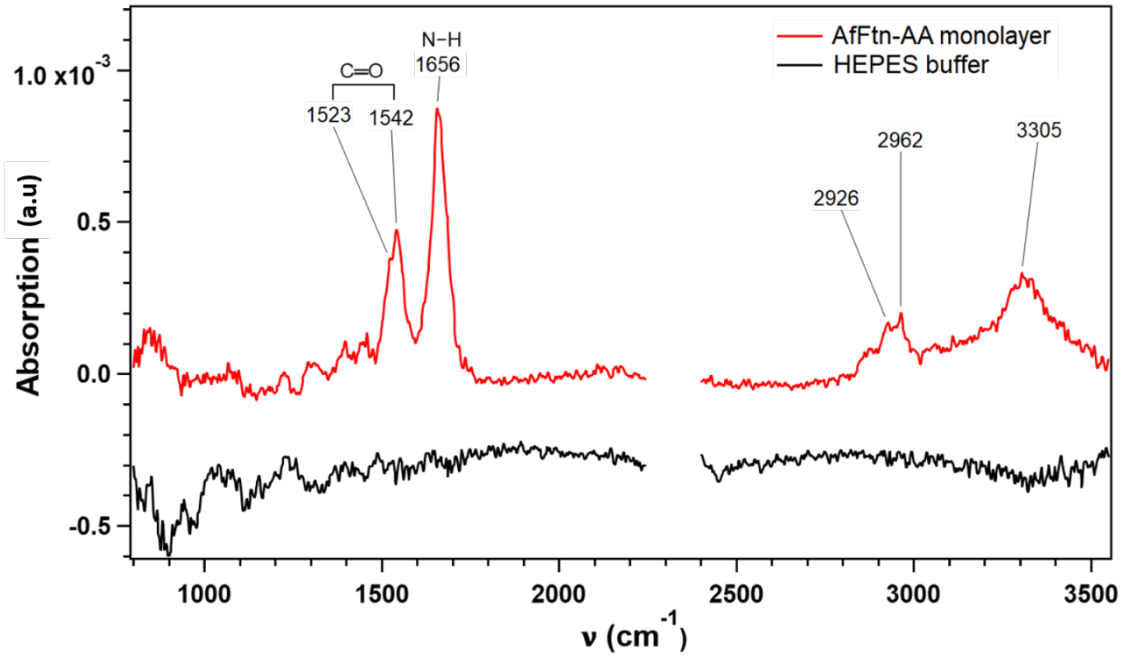

Figure 59: Differential FTIR spectrum (3500−800 cm^{-1}) of a ferritin (AfFtn-AA 4800Fe) monolayer (red curve) and HEPES buffer (black curve) on a silicon wafer (FZ). The blank space at 2250-2400 cm^{-1} corresponded to the CO_2 vibration peaks that were erased on both curves for the sake of clarity.

3. Electrostatic characterisation of AfFtn-AA nanocages on silicon surface by KPFM

In this section, the results of the KPFM measurements of AfFtn-AA on silicon are presented. Topography and CPD images of our samples have been measured using a SCM-PITv2 tip from *Bruker*. The topography was measured by the *PeakForce Tapping*® technique, and the CPD is measured in AM mode. The topography and CPD were acquired within two passes above the surface and at a slow rate (0.5 Hz or 500 nm.s^{-1}) for 512 x 512 px² images. The LSH is set at 15 nm for samples of single ferritins and 20 nm for samples of ferritin monolayers.

3.1. KPFM measurement of individual AfFtn-AA on silicon

Topography images: Size of AfFtn-AA nanocages is affected by the iron content

The Figure 60.a shows an image of a 1 µm² area of the AfFtn-AA 4800Fe sample. Many individual nanostructures (yellow dots) are clearly distinguishable (Figure 60.b), although few aggregates remain. Recorded topographies of other samples, with different loadings, show similar observations (see Appendix V-1). The sizes of the nanostructures were measured from height profiles (Figure 60.c) and show an average height of d = 8.8 ± 0.63 nm, which is coherent with the size of the ferritin in solution (≈ 12 nm). The height distributions and average heights of the five samples were computed from the topography images and displayed in Figure 60.d and Figure 60.e, respectively. These results show that the size of the ferritin decreases with lower iron content until d = 3.63 ± 0.43 nm for the 600Fe sample. The ferritin nanocage tends to shrink when its iron core is not fully loaded. Similar behaviour was observed for AfFtn-AA immobilized on a gold[52] and a graphene surface.[87] For all the loading, the AfFtn-AA lateral width was measured at 32 ± 1.5 nm. However, since the height of the ferritin is decreasing, we would expect to measure an enlargement of the lateral size. Actually, the ferritin nanocage displays a profile in an ellipsoid shape with a height of 8.8 nm and a lateral size of 12 nm, leading to a calculated perimeter of 33 nm. The shrunken shape (at 600Fe) has an equal perimeter but a lower height equal to 3.6 nm, and the lateral size is now 14.4 nm (see Appendix V-2). The ferritin undergoes an enlargement of 2.4 nm due to the reduction of its iron loading. This is not surprising that such a small lateral increase is not detected with the KPFM tip due to the limitation induced by the tip convolution. We showed here that the height of ferritin nanocages on a silicon surface varies linearly with the number of iron atoms inside, forming its core. This variation of shape is strongly linked to a variation of shape of the ferritin.

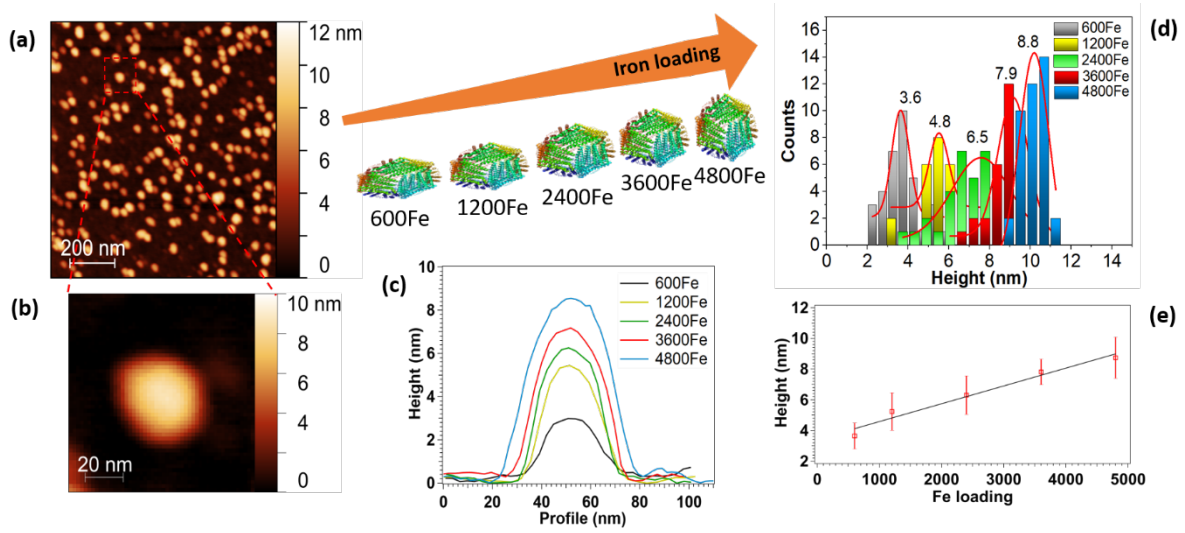

Figure 60: Topography results from KPFM measurements of ferritin (AfFtn-AA) on a silicon surface. (a) topography image (1µm²) of AfFtn-AA 4800Fe on silicon. (b) zoom-in on one AfFtn-AA (100 nm²). (c) height profiles over one ferritin with different loading. (d) height distributions of ferritin with different loading on silicon with Gaussian fit. The average height from each distribution is: 4800Fe: d = 8.8 ± 0.63 nm; 3600Fe: d = 7.93 ± 0.64 nm; 2400Fe: d = 6.5 ± 1.24 nm; 1200Fe: d = 4.78 ± 0.42 nm; 600Fe: d= 3.63 ± 0.43. (e) The average heights of ferritin on silicon as a function of the loading with linear fit.

CPD images : Influence of the iron core on the electrostatic behaviour of the ferritin

The CPD of sample surfaces was recorded simultaneously with the topography, and the LSH was set at 15 nm for all measurements. This value was chosen to both be close to the surface to sense the electrostatic contribution of the ferritin and to keep a reasonable distance from the surface, thus avoiding possible surface contact, which can generate image artefacts.[185,186] In Figure 61.a, the relative CPD image of the AfFtn-AA 4800Fe sample is shown. The CPD of single AfFtn-AA nanocages (Figure 61.b) (in blue) is clearly distinguishable from the silicon one (yellow) and is shown to be negative compared to the CPD of the silicon, with a −25 mV difference. The recorded relative CPD images for other loading (see Appendix V-3) show a less resolved CPD of the particles as the iron content (i.e., the size) decreases. At 600Fe, the CPD of the nanocages are barely distinguishable, and could be explained by the resolution limit of the KPFM, which is closely linked to the LSH parameter. We are showing here that it is possible to visualize, with sufficient resolution, the CPD of a ferritin nanocage on a surface using KPFM in an ambient environment. Moreover, CPD profiles of a single AfFtn-AA at different loading are displayed and overlapped in Figure 61.c. It shows that the CPD value of AfFtn-AA tends to decrease when the iron loading is higher than 2400Fe.

It is confirmed in Figure 61.d, where average CPD values (on 40 ferritins) computed from the five samples are displayed. AfFtn-AA loaded at 600Fe, 1200Fe and 2400Fe (designated hereafter as low-Fe ferritins) show closed values of CPD at −18 mV, −16 mV, and −15 mV, respectively, and AfFtn-AA loaded at 3600Fe and 4800Fe (designated hereafter as high-Fe ferritins) show lower values at − 23 mV and − 25 mV, respectively. These results demonstrate the influence of the iron core on the CPD of AfFtn-AA nanocages. Increasing the size of the nanocages appears to decrease the CPD and, unlike the topography, there is a threshold at 2400Fe.

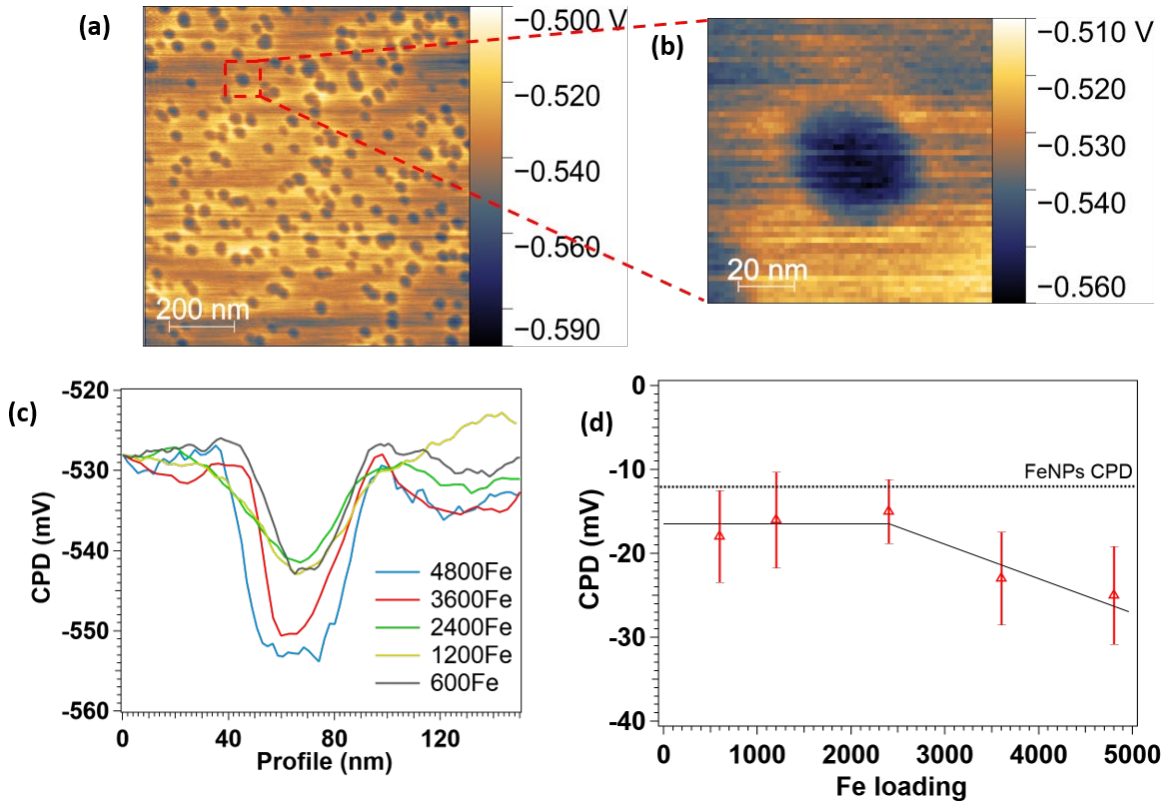

Figure 61: CPD results from KPFM measurements of ferritin (AfFtn-AA) on silicon. (a) CPD image (1 µm²) of single AfFtn-AA 4800Fe on silicon. (b) zoom-in on one ferritin (100 nm²). (c) CPD profiles taken on one ferritin at different loading. The profiles were shifted and superposed for the sake of comparison. (d) average measured CPD of single ferritins with different iron content. CPD of ferritin nanocages is measured compared to the silicon one (i.e., CPD = CPD (ferritin) – CPD (Si)). The black dotted line represents the average CPD of single FeNPs with CPD = −11.7 ± 1.1 mV. Average CPD values of ferritin with error bar are: 600Fe: CPD = −18 ± 5.5 mV; 1200Fe: CPD = − 16 ± 5.7 mV; 2400Fe: CPD = −15 ± 3.8 mV; 3600Fe: CPD = −23 ± 5.5 mV; 4800Fe: −25 ± 5.9 mV.

As the CPD depends on the nature of the nanostructure, we measured the CPD of pure iron nanoparticles to gain more insights about the evolution of the CPD with the iron loading. We compared the CPD values of AfFtn-AA with the CPD values of iron oxide (II, III) nanoparticles (FeNPs), of similar sizes (d = 15 nm), deposited on silicon and obtained by KPFM as well. These FeNPs were chosen because they have the same diameter as the ferritin nanocages. The number of iron atoms inside a 15 nm FeNP was calculated to be around 40,000. The recorded images (Figure 62.a–b) show clear single FeNPs both in topography and CPD. The average measured CPD of FeNPs (−12 mV) is reported in Figure 61.d (black dotted line) and reveals that it is less than for all the AfFtn-AA. This low value of –12 mV tends to show that the more negative value of high-Fe ferritins is not due to the pure effect of the iron work function.

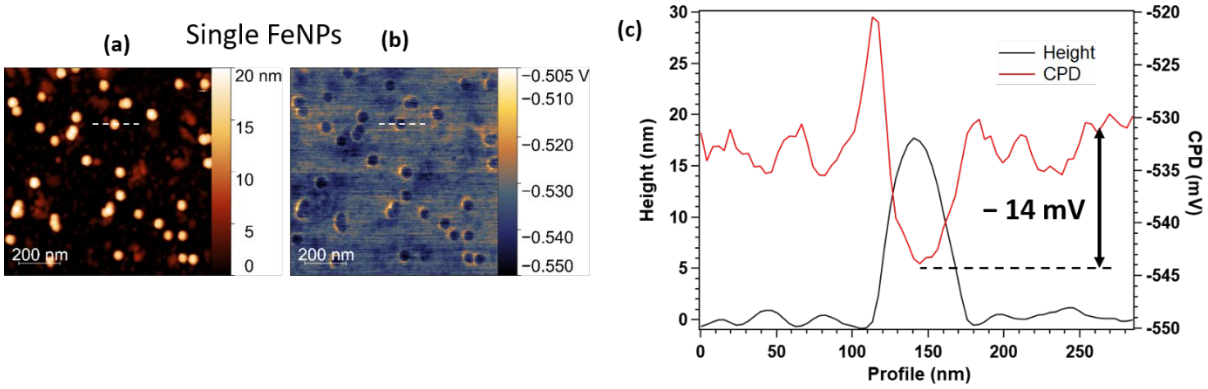

Figure 62: Topography (a) and relative CPD (b) images (1 µm²) of iron nanoparticles (FeNPs) on silicon obtained by KPFM. (c) Height (red) and CPD (black) profiles of one FeNP (following the white dashed line).

3.2. KPFM measurement of AfFtn-AA monolayer on silicon

To confirm and shed light on the behaviour of individual AfFtn-AAs, samples of AfFtn-AA monolayers with different iron loadings and FeNPs monolayers on silicon were made and measured by KPFM. The Figure 63.a shows the topography of the AfFtn-AA 4800Fe monolayer sample recorded at the edge of the AfFtn-AA area. The height of the monolayer is measured at around 8 nm from the height profile (Figure 63.c, black line), which matches exactly with the sizes measured on the single AfFtn-AA 4800Fe sample. On the relative CPD image in Figure 63.b, we can clearly distinguish the AfFtn-AA monolayer (blue) from the Si (yellow), with a CPD drop of – 110mV (Figure 63.c, red line). Topography and CPD images of AfFtn-AA monolayer at other loading and FeNPs monolayer show similar frontiers between Si and AfFtn-AA areas (see Appendix V-4). One CPD profile from each AfFtn-AA monolayer

sample is displayed and overlapped in Figure 63.d, showing a lower CPD value than for single AfFtn-AA. The average CPD of AfFtn-AA monolayers was computed from the KPFM images and reported in Figure 63.e. The low-Fe ferritins show similar CPD values of – 49 mV, − 50 mV, and −43 mV for 600Fe, 1200Fe, and 2400Fe, respectively. After 2400Fe we see a net decrease in the CPD value of −71 mV for 3600Fe and −110 mV for 4800Fe. The CPD of the FeNPs monolayer (− 44mV) is reported in Figure 63.e and, as for single FeNPs, is measured lower than for AfFtn-AA monolayers (except for 2400Fe). In this part, both single AfFtn-AA and AfFtn-AA monolayer measurements show the influence of the iron core on the electrostatic behaviour of the ferritin. Increasing the iron content above 2400Fe clearly induces a CPD threshold. Although, electrostatic behaviour of ferritin cannot be exclusively associated to its iron core. In fact, if we consider the iron core of a ferritin nanocages as an iron oxide nanoparticle, we would expect a decrease in the CPD as the size of the iron nanoparticles increases, as shown by the results. But here, the CPD measured for FeNPs is lower than for 9 nm AfFtn-AA nanocages on the surface. It demonstrates that the iron core of ferritin, and especially its atom content, are not the only parameters that can affect the electrostatic behavior of ferritin. A few parameters involving the amino acid shell and its interaction with the iron core could explain this observation. First, the amino acid shell changes the overall work function and then differs from the iron mineral core's only. Secondly, local charges and dipoles arising from such interaction could be sensed by the KPFM and induce a decrease in the CPD. An interpretation of the charge distribution in the ferritin protein is discussed in the next section.

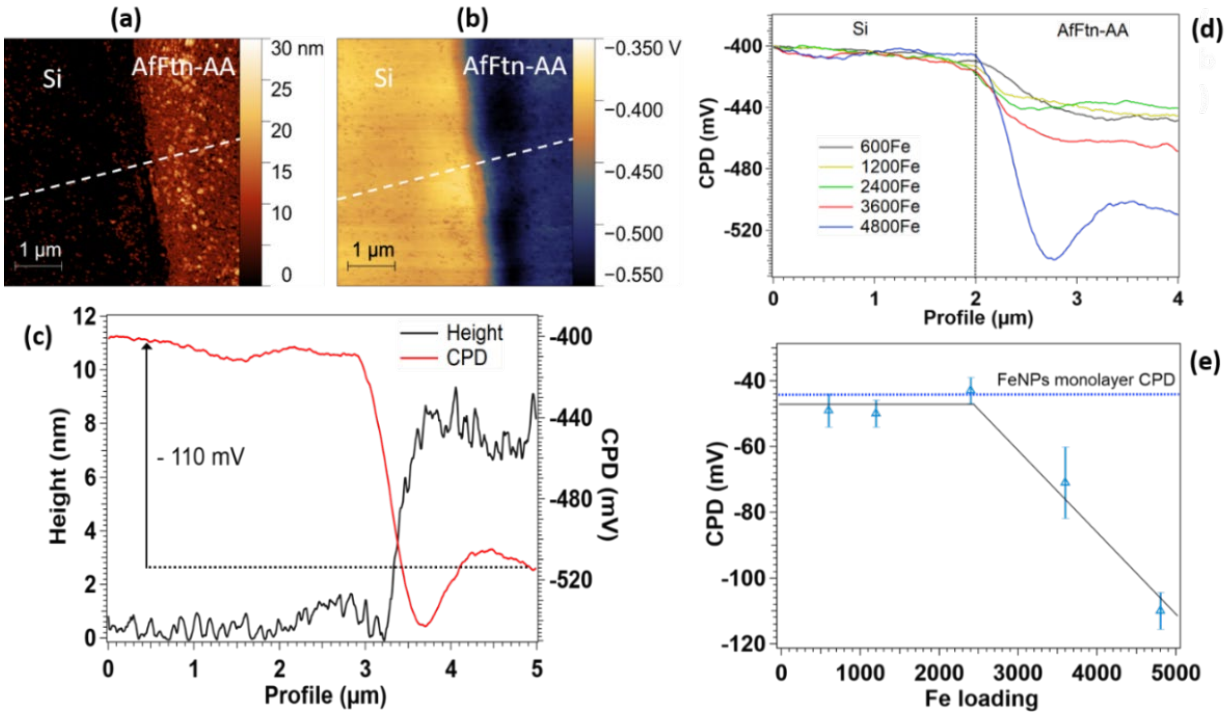

Figure 63: CPD results from KPFM measurements of ferritin (AfFtn-AA) monolayers on silicon. (a) Topography and (b) CPD images (5x5 µm²) of an AfFtn-AA 4800Fe monolayer on silicon. (c) graphic of the CPD (red) and height (black) profiles, following the white dashed lines. (d) CPD profiles taken across the silicon/ferritin monolayer at different loading. (e) average CPD values of ferritin monolayer at different loading, with error bars. The blue dotted line represents the average CPD value of a FeNPs monolayer.

4. Insight about the electrostatic behaviour of AfFtn-AA on silicon

4.1. Comparison of the CPD values of individual AfFtn-AA and AfFtn-AA monolayers

The KPFM results of single ferritin on silicon show similar CPD values for low-Fe ferritins, followed by lower CPD values for high-Fe ferritins. For the KPFM results of ferritin monolayers, a similar trend, but with lower CPD values, is shown. This trend can be explained by the intrinsic resolution limit of the KPFM: above single ferritins dispersed on a surface, the bare silicon area is also sensed by the tip and increases the overall measured CPD. This hinders the probing of low CPD variations between small ferritins (low-Fe ferritins). However, while increasing the ferritin concentration (monolayer), the tip only senses the electrostatic interaction from the ferritins, and the same trend is observed. Therefore, the CPD of ferritin remains constant for low-Fe ferritins and decreases above the 2400Fe loading. However, the comparison

of ferritin CPD values with FeNPs ones excludes the iron core as the principal factor responsible for the CPD changes and orients us toward the influence of the amino acid shell of ferritin.

4.2. Electric dipoles and influence of the iron loading on AfFtn-AA conformation

To adsorb on a solid surface, soft proteins undergo a rearrangement of their structures (secondary and tertiary) in order to increase the contact area with the surface and to relax in an energetically favored state. This phenomenon is especially true for proteins adsorbing on an electrostatically hostile surface (e.g., a negative protein onto a negative surface). In such a configuration, the peptide units released from the structure rearrangement could make hydrogen bonds with the polar surface or interact with the positive ions (from the buffer solution) incorporated between the protein and the surface. Also, it was shown for this adsorption mechanism that the positions of the negatively charged groups of the protein (COOH) are closer to the negative surface than those of the positively charged group of the protein (NH_2) (and conversely for a positive surface charge).[65] The distribution of charges creates an net electric dipole in the protein, whose direction will depend on the substrate and the surface charges of the protein. In our case, ferritin has a net negative surface charge and adsorbs on a negatively charged silicon surface at pH 7.4, which leads to conformational changes clearly shown by the flattening of the ferritin (decreasing of the height) measured by KPFM. However, the change in structure appears strongly related to the iron content of the ferritin. In fact, during the iron loading process, Fe^{3+} atoms bind to subunits on the inner surface of the shell to form the mineral oxide core (Figure 64). For low-Fe ferritin, the mineral core is not binding to all the subunits, and unbound ones are more likely to disrupt their structures upon adsorption. On the other hand, for high-Fe ferritins, all subunits are bound to the mineral core, resulting in a higher resistance to surface-induced structure changes.

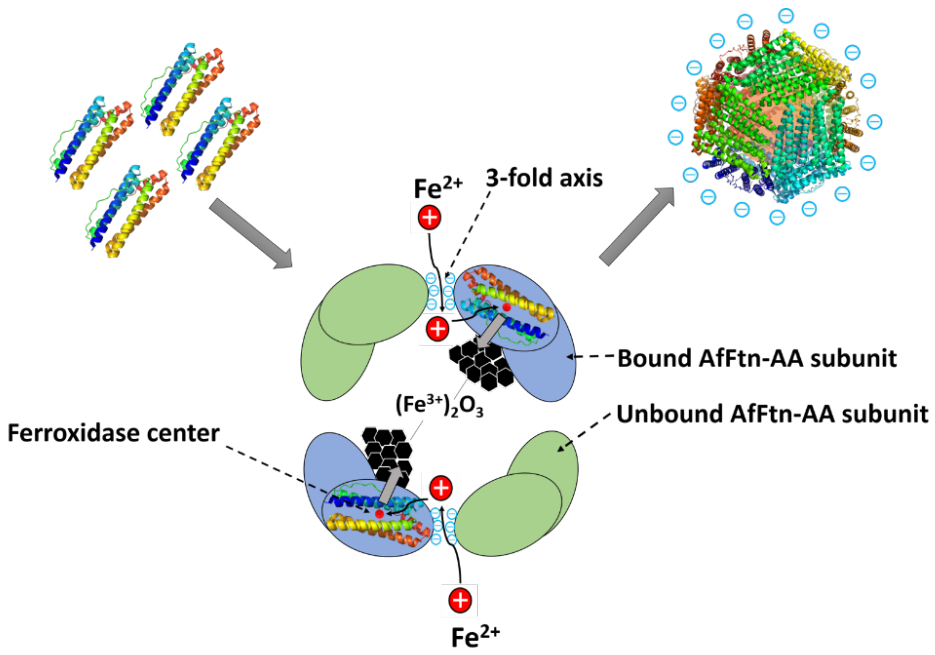

Figure 64: Iron loading mechanism of ferritin nanocages. The dimers (left) self-assembled in presence of iron (II) to form the nanocages (right). The Fe^{2+} atom flow inside the core trough the 3-fold axes and bind to the inner surface of the cage. Subunits bound and unbound to the mineral core are represented in blue and green, respectively.

From the KPFM measurement, value of the electric dipole moment can be extracted from the measured CPD value. First, the negative values of CPD indicated an electric dipole oriented in the same direction for all the loading. In the literature, measured negative CPD values (compared to the substrate) most frequently indicate the presence of a positive charge or an outward dipole at the surface (and conversely for a positive CPD value).[187] Therefore, the sign of the CPD values indicates an outward electric dipole created by the distribution of charge in the ferritin. The electric dipole moments of the ferritins were calculated from the CPD values of AfFtn-AA monolayers, following the equations below:

The net dipole moment p (C.m) is defined by Equation 14:

$$p = q.d$$

Equation 14 : Net dipole moment

with q (C) the electric charge and d (m) the length of the dipole across one ferritin. Here, d = 8 nm .

To obtain the charge q , we determined the electric field $\Delta\varphi$ ($V.m^{-1}$) created by the monolayer of ferritin. It is defined by Equation 15 :

$$\Delta\varphi = -\frac{p}{\varepsilon_0 . A} = -\frac{q . d}{\varepsilon_0 . A}$$

Equation 15 : Electric field

with ε_0 = 8.85.10^{-12} F.m^{-1} the dielectric constant of air and A = 144 nm² the surface formed by four ferritin nanocages.

From the KPFM, the measured CPD corresponds to the electric field created by the ferritin monolayer, which is sensed by the tip.

For a monolayer of AfFtn-AA 4800Fe, the CPD = − 110 mV = − 110 meV = $\Delta\varphi_{4800}$

Therefore, from the Equation 15 the charge q is :

$$q = -\varepsilon_0 . A . \frac{\Delta\varphi_{4800}}{d}$$

Equation 16 : Electric charge

Therefore, the Equation 14 becomes :

$$p = q . d = -\varepsilon_0 . A . \Delta\varphi_{4800}$$

Then, the net dipole moment p_{4800} = 1.4.10^{-28} C.m = 42 D.

The calculated electric dipoles are shown in Table 2. AfFtn-AA 600Fe, 1200Fe, and 2400Fe show similar dipole moments at 19 D, 19 D, and 16 D, respectively, and AfFtn-AA 3600Fe and 4800Fe show higher values at 27 D and 42 D, respectively. These values are smaller than the calculated electric dipole moment of an apo-AfFtn-AA (AfFtn-AA without iron core) in solution, with $\boldsymbol{p_{apo}}$= 79 D.

Ferritin	600Fe	1200Fe	2400Fe	3600Fe	4800Fe	apo-AfFtn in solution[a]
CPD (mV)	−49	−50	−43	−71	−110	nA
$\boldsymbol{p}$ (Debye)	19	19	16	27	42	79

Table 2: Values of the net dipole moment calculated for AfFtn-AA monolayers at different loading and calculated net dipole moment of apo-AfFtn-AA in solution. [a]Value obtained from the protein dipole moment database.[188]

The increase of the electric dipole moment with increasing iron loading could indicate a change in the protein orientation upon adsorption, as it was shown for other proteins such as the cytochrome c[171] or the hydrophobin deposited on SAMs.[172] However, these studies showed that the orientation of the protein strongly depends on the type of surface, and here, on an identical surface, the ferritin orientation is unlikely to change from one loading to another. The variation of the dipole moments probably stems from the different conformations of the ferritin as a function of its loading. The charges on the ferritin rearrange themselves when they sense the electric field of the surface. For low-Fe ferritins, the distribution of charge is similar as shown by the dipolar moment values and changes as the ferritins exhibit a more "spherical shape" for high-Fe ferritins (Figure 65.a−b).

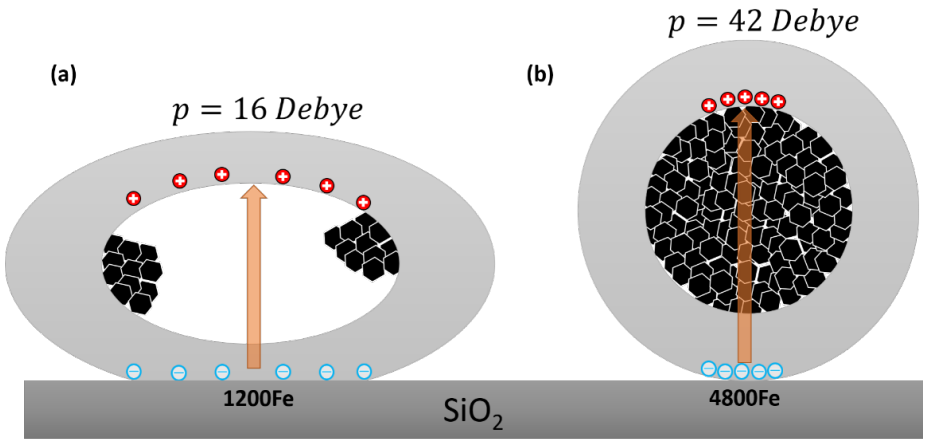

Figure 65: Electric dipoles of AfFtn-AA. Once adsorbed on the silicon surface, the created electric dipoles point toward the exterior (outward dipole). The distribution of charges induced by the contact with the surface leads to a smaller dipole moment for 1200Fe (a) than for 4800Fe (b).

5. Conclusion

In this chapter, we investigated the morphological and electrostatic behaviour of AfFtn-AA deposited on a silicon surface. Through KPFM measurements, we demonstrated how the iron core, of the ferritin, by interaction with the subunits, affect both the morphology and the surface potential of the protein upon adsorption. This was demonstrated by the decreasing height of AfFtn-AA with decreasing iron content and via the constant CPD values for low-Fe ferritin followed by a sudden decrease for high-Fe ferritin. This phenomenon was observed for individual AfFtn-AA and AfFtn-AA monolayers, and the CPD marks a threshold at 2400Fe. In addition, the low CPD value of FeNPs on silicon demonstrated that the amino acid shell has an impact on the overall surface potential of the ferritin. The electric dipoles of the ferritins were calculated and indicated an outward dipole for all the loading, but at a constant value for low-Fe ferritin and an increasing value after 2400Fe. These results showed that the conformation of the ferritin on the silicon surface will change depending on its iron content and is strongly affected by how the iron core binds to the amino acid subunits. This study shows a new method to visualise and to measure the electric dipole of protein directly on a solid surface. It brought valuable information about how the AfFtn-AA adsorbs and conforms when it is in contact with a silicon surface and how the surface charge of the ferritin is affected by it.

6. References

[168] Kubiak, Karina, and Paul A. Mulheran. « Molecular Dynamics Simulations of Hen Egg White Lysozyme Adsorption at a Charged Solid Surface ». *The Journal of Physical Chemistry B* 113, nº 36 (2009): 12189-200.

[169] Kubiak-Ossowska Karina, and Paul A. Mulheran. « What Governs Protein Adsorption and Immobilization at a Charged Solid Surface? » *Langmuir* 26, nº 11 (2010): 7690-94.

[170] Wunderlich M. « The Correlation between Protein Stability and Dipole Moment: A Critical Test ». *Protein Engineering Design and Selection* 19, nº 8 (2006): 355-58.

[171] Zhou Jian, Jie Zheng, and Shaoyi Jiang. « Molecular Simulation Studies of the Orientation and Conformation of Cytochrome c Adsorbed on Self-Assembled Monolayers ». *The Journal of Physical Chemistry B* 108, nº 45 (2004): 17418-24.

[172] Peng Chunwang, Jie Liu, Daohui Zhao, and Jian Zhou. « Adsorption of Hydrophobin on Different Self-Assembled Monolayers: The Role of the Hydrophobic Dipole and the Electric Dipole ». *Langmuir* 30, nº 38 (2014): 11401-11.

[173] Takashima Shiro. « Electric Dipole Moments of Globular Proteins: Measurement and Calculation with NMR and X-Ray Databases ». *Journal of Non-Crystalline Solids* 305, nº 1-3 (2002): 303-10.

[174] Porschke D., C. Créminon, X. Cousin, C. Bon, J. Sussman, and I. Silman. « Electrooptical Measurements Demonstrate a Large Permanent Dipole Moment Associated with Acetylcholinesterase ». *Biophysical Journal* 70, nº 4 (1996): 1603-8.

[175] Keefe S E, and E H Grant. « Dipole Moment and Relaxation Time of Ribonuclease ». *Physics in Medicine and Biology* 19, nº 5 (1974): 701-7.

[176] Takashima Shiro, and Koji Asami. « Calculation and Measurement of the Dipole Moment of Small Proteins: Use of Protein Data Base ». *Biopolymers* 33, nº 1 (1993): 59-68.

[177] Barlow D. J., and J. M. Thornton. « The Distribution of Charged Groups in Proteins ». *Biopolymers* 25, nº 9 (1986): 1717-33.

[178] Cho Yasuo, and Ryusuke Hirose. « Atomic Dipole Moment Distribution of Si Atoms on a Si (111) − (7 × 7) Surface Studied Using Noncontact Scanning Nonlinear Dielectric Microscopy ». *Physical Review Letters* 99, nº 18 (2007): 186101.

[179] Qian Yinping, Peng Wang, Lujia Rao, Changkun Song, Hongjie Yin, Xingyu Wang, Guofu Zhou, and Richard Nötzel. « Electric Dipole of InN/InGaN Quantum Dots and Holes and Giant Surface Photovoltage Directly Measured by Kelvin Probe Force Microscopy ». *Scientific Reports* 10, nº 1 (2020): 5930.

[180] Albrecht F., J. Repp, M. Fleischmann, M. Scheer, M. Ondráček, and P. Jelínek. « Probing Charges on the Atomic Scale by Means of Atomic Force Microscopy ». *Physical Review Letters* 115, nº 7 (2015): 076101.

[181] Soriano-Portillo Alejandra, Miguel Clemente-León, Carlos J. Gómez-García, Eugenio Coronado, Natividad Gálvez, Enrique Colacio, and José M. Domínguez-Vera. « Magnetic Langmuir–Blodgett Films of Ferritin with Different Iron Loadings ». *Synthetic Metals* 148, nº 1 (2005): 7-10.

[182] Clemente-León Miguel, Eugenio Coronado, Vicent Primo, Antonio Ribera, and Alejandra Soriano-Portillo. « Hybrid Magnetic Materials Formed by Ferritin Intercalated into a Layered Double Hydroxide ». *Solid State Sciences* 10, nº 12 (2008): 1807-13.

[183] Cloarec Jean-Pierre, Céline Chevalier, Jonathan Genest, Jacques Beauvais, Hassan Chamas, Yann Chevolot, Thierry Baron, and Abdelkader Souifi. « pH Driven Addressing of Silicon Nanowires onto Si_3N_4/SiO_2 Micro-Patterned Surfaces ». *Nanotechnology* 27, nº 29 (2016): 295602.

[184] Noh Joong S, and James A Schwarz. « Estimation of the Point of Zero Charge of Simple Oxides by Mass Titration ». *Journal of Colloid and Interface Science* 130, nº 1 (1989): 157-64.

[185] Gołek F., P. Mazur, Z. Ryszka, and S. Zuber. « AFM Image Artifacts ». *Applied Surface Science* 304 (2014): 11-19.

[186] Lechaptois Luis, Yoann Prado, and Olivier Pluchery. « KPFM Visualisation of the Schottky Barrier at the Interface between Gold Nanoparticles and Silicon », *Nanoscale*, (2023).

[187] Laurent Nony. PRINCIPLES OF KELVIN PROBE FORCE MICROSCOPY AND APPLICATIONS PRINCIPLES OF KELVIN PROBE FORCE MICROSCOPY AND APPLICATIONS. Doctoral. 2nd German-French summer school on noncontact-AFM Osnabrück, 12th-16th of September (2016), Germany, Germany. 2016.

[188] Felder C. E., J. Prilusky, I. Silman, and J. L. Sussman. « A Server and Database for Dipole Moments of Proteins ». *Nucleic Acids Research* 35, nº Web Server (2007): W512-21.

Chapter VI: Modulation of the surface charge of AfFtn-AA by site-directed mutagenesis

Introduction

This chapter will present the work done, mostly in the 2nd year of the thesis, in the NTU laboratory. It describes the mutations of the AfFtn-AA in order to modulate its surface charge. First, we will give a description of the surface charge of the unmutated ferritin in solution and, particularly, the role of the amino acids. Secondly, we will present a numerical method to perform mutations and calculate the electrostatic surface potential of the ferritin. Thirdly, we will describe the experimental mutations and production of ferritin. Fourthly and lastly, we will present the results obtained by KPFM measurement of ferritin mutants deposited on silicon. We will discuss the effect of the mutations on the electrostatic and morphological behaviour of AfFtn-AA.

1. Surface charges of ferritin nanoparticles in solution

A solution with nanoparticles dispersed in a continuous phase (e.g., an ionic solution) is considered a colloidal system. Inside, the particles are stabilized through steric interactions, with polymers covalently coupled to the particles,[189] or through electrostatic interactions that arise from the ionization of the surface groups of the nanoparticles. The dissociation of acidic groups will create a negatively charged surface, and conversely, a basic surface will create a positive surface charge. Then, the net charge at the surface of the particle will affect the distribution of ions surrounding the particle and increase the concentration of counter-ions close to the surface, forming an electrical double layer. The overlapping of electrical double layers develops repulsive potentials responsible for the stability of the system. The potential of the double layer is the zeta potential (ζ in mV). Finally, the magnitude of the surface charge will depend on the strength of the surface groups and the pH of the solution.[190–192] In our case, ferritin nanocages are composed of various and multiple amino acids, each of which contains two ionizable groups: an acidic group $COOH \rightleftharpoons COO^- + H^+$, a basic group $NH_2 + H^+ \rightleftharpoons NH_3^+$, and a variable group, that can carry an electric charge (positive or negative). Thus, ferritin is a polyelectrolyte species with a complex and non-uniform net surface charge. Furthermore, the quaternary structure of ferritin is formed by hydrophobic interaction between subunits, and the driving force is to minimize the contact between apolar groups and water. It results in more charged groups (hydrophilic) pointing toward the solvent.[193] Thereby, ferritins are stabilized

through electrostatic interactions, and the nature of the amino acids in contact with the ionic solution dictates the strength and sign of the surface charge of the ferritin. Consequently, the modulation of the net surface charge of ferritin can be performed by modification of its amino acid sequence (primary structure), which contains, for one nanocage, 696 and 360 negatively and positively charged amino acids, respectively, that make up a net negative surface charge.

Therefore, our goal is to substitute specific negatively charged amino acids with positively charged ones in order to obtain a positive surface charge. Such operations were experimentally performed by site-directed mutagenesis, and validation of the surface charges was performed by measuring the zeta potential of mutated ferritins via the electrophoretic light scattering method (ELS). The purpose is to shift the isoelectric point (IEP) of the ferritin toward a higher pH so that at physiological pH 7.4, the zeta potential becomes positive. In the literature, such a shift was observed for horse-spleen ferritin tailored with polymer brushes (polyethylene glycol).[194] We chose not to use capping molecules to modulate the charge of the ferritin, as those could hinder the measurement of the ferritin potential by KPFM.

In our experiments, we first determined the IEP of the unmutated ferritin (AfFtn-AA M0). To do so, we measured the zeta potentials of AfFtn-AA M0 solutions at different pHs (from 3 to 10) by following the ELS protocol (see Appendix II-2.4). The results are displayed in Figure 66 (red curve) and show an IEP around 4.2 and a $\zeta = -18$ mV at pH 7.4. This latter value indicates a net negative surface charge, as expected, and low colloidal stability, as it is under the general dividing line between stable and unstable suspension ($\zeta = \pm 30$ mV). However, the colloidal stability can be debated as the zeta potential is proportional to the ionic strength (i.e., the concentration of ions) of the buffer solution. For our experiments, the ionic strength I ($mol.L^{-1}$) was kept low for all the buffer (I = 50 mM) and could explain the ζ value obtained. In addition, by observing our AfFtn-AA M0 solutions over time, no sedimentation was visible (the sedimentation of a ferritin solution can be identified by a blurry solution, notably due to the released irons that precipitate).

In addition, similar ELS measurements were carried out for the wild-type ferritin (AfFtn-WT), and the results are displayed in Figure 66 (green curve). For AfFtn-WT, the ζ value is similar as for AfFtn-AA, but has a higher IEP at 4.8 than AfFtn-AA M0. This small shift is explained by the mutation (K150A/R151A) performed on AfFtn-WT. This mutation replaced two positive amino acids (Lys and Arg) by two hydrophobic amino acids (Ala). The

AfFtn-WT presents a net surface charge slightly more positive than the AfFtn-AA M0, and the difference in surface charges can be sensed by ELS measurements.

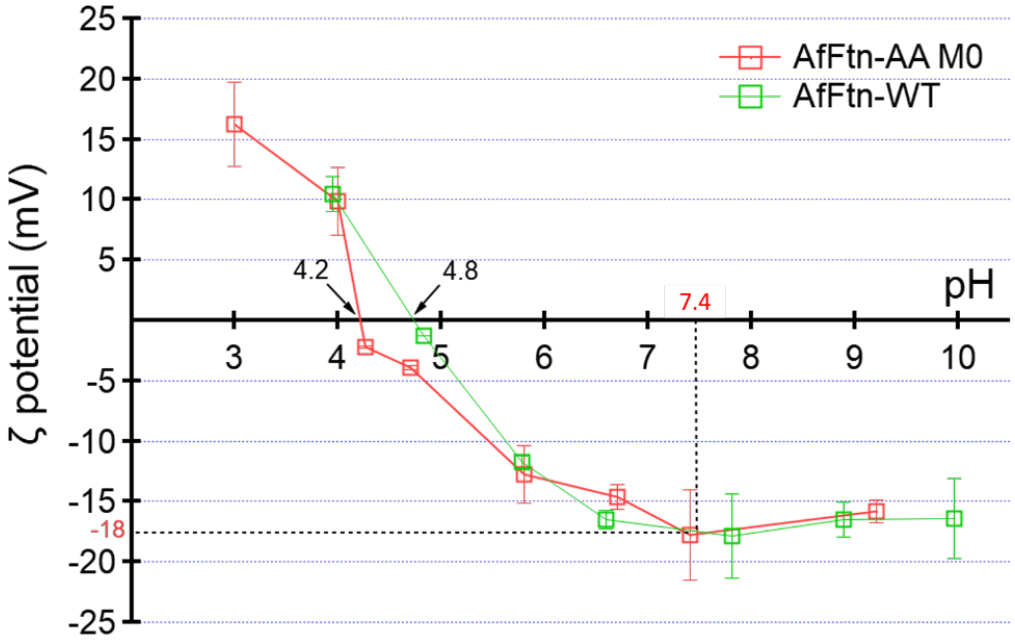

Figure 66 : Curve of ζ vs. pH for unmutated ferritin (AfFtn-AA M0) (red curve) and wild-type ferritin (AfFtn-WT) (green curve). Isoelectric points (IEP) are indicated with black arrows and physiological in red.

2. Design of the mutations

Before experimental site-directed mutagenesis, the first step was to determine the specific amino acids that would be substituted in order to change the surface charge of the ferritin. For this, we used the open-source PyMol software from Schrödinger®.[195,196] This software is a system of molecular visualisations used for structural biology. From the protein data bank code (3KX9 for AfFtn-AA), it displays a 3D ribbon representation of one ferritin nanocage showing the 24 folded subunits (Figure 67.a) and indicates the position of each amino acid in the nanocage. In addition, the software performs mutations on the desired amino acids (see Appendix VI-1) and calculations of the electrostatic surface potential (ESP) of ferritin by solving the Poisson-Boltzmann (PB) equation. In our work, the ESP was calculated for AfFtn-AA and AfFtn-AA mutants in an ionic solution that reproduces the HEPES buffer, i.e., a solution at pH 7.4 with monovalent counter-ions (Na^+ and Cl^-) at an ionic strength I = 50 mM and a temperature set at T = 300 K. The dielectric constants are set at $\varepsilon_W = 78$ and $\varepsilon_f = 3.34$ for

water and ferritin, respectively.[197] As a result, the software displays an electrostatic potential on the molecular surface. In Figure 67.b, the result for AfFtn-AA M0 is shown and presents mostly a negative surface potential (in red). However, we distinguish a few positive areas (in blue) situated around some of the 3-fold axes (Figure 67.c), which originate from lysine amino acids. These are positioned on a helix that forms the exterior surface of the nanocage, giving easy access to the solvent. Furthermore, the lysine has a long alkane side chain terminated with a positively charged amino group (NH_3^+) at physiological pH.

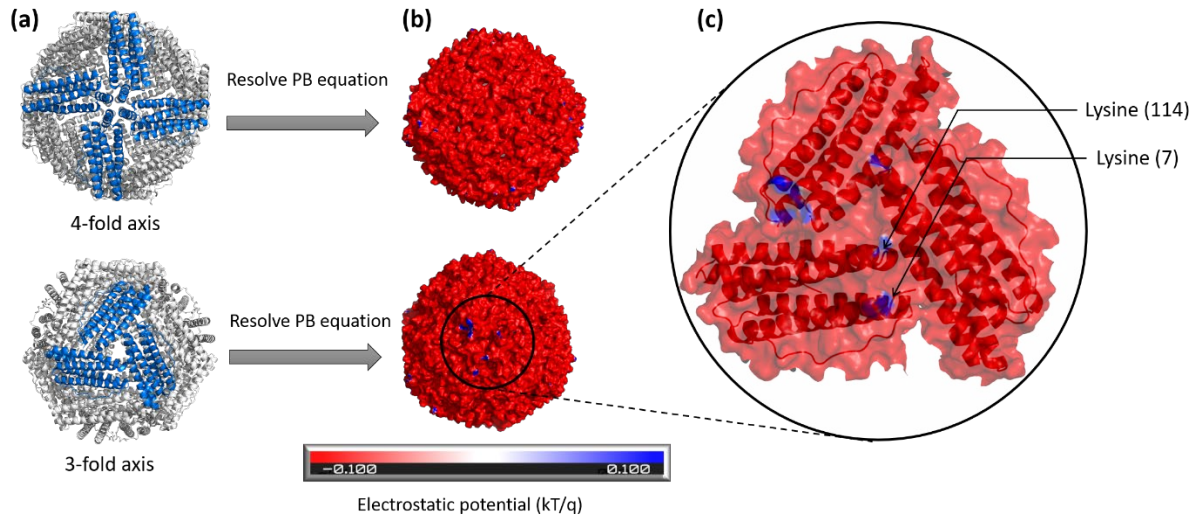

Figure 67: 3D PyMol representations of unmutated ferritin (AfFtn-AA M0) at the 4-fold (top) and 3-fold (bottom) axes. (a) ribbon representations of AfFtn-AA M0. The subunits forming the 3-fold and 4-fold axes are in blue. (b) representations of the electrostatic potential on the molecular surface after resolution of the Poisson-Boltzmann equation. The positive areas are in blue, and the negative areas are in red. The scale is shown at the bottom and ranges from −0.1 to +0.1. (c) zooming in on the 3-fold axis indicates the position of the lysines. The number corresponds to the position of the amino acid in the primary structure.

To improve the mutation process, we chose specific amino acids to substitute that answered some criteria : (1) it must have its side chain preferentially pointing toward the solvent; (2) it must be terminated by a negatively charged group; (3) it must not be on the 3-fold axis because a positive charge around the pores will hinder the flow of iron inside (iron loading); (4) it must not be at positions 150 and 151 because these are the amino acids responsible for the closing of the pores. All the amino acids were substituted with lysine because, as presented in the previous section, lysine amino acids were responsible for the

positive areas present at the surface of AfFtn-AA M0 and therefore are of great interest to obtain a positive surface charge. Finally, four sets of mutations were chosen. Each mutation is noted "AXB" with A being the original amino acid, X being the position of the amino acid in the primary sequence, and B being the substitute amino acid. The glutamic acid (Glu) and aspartic acid (Asp) are noted with the letters "E" and "D", respectively, and both have a side chain terminated with a negatively charged group (COO^-). After each numerical mutation, we calculated the ESP of the mutated ferritin, and the resulting electrostatic potential molecular surfaces are displayed in Figure 68. The mutations are indicated under the 3D representations. Clear positive areas are visible for the mutations M1, M3, and M4, whereas they are barely distinguishable on the mutation M2. The areas where the amino acids were substituted show a positive charge (except for M2), with the intensity increasing with the number of mutated amino acids. Thereby, we see a significant change in the surface charge with at least two amino acids substituted on each subunit. It is important to stress that a mutation is performed on each subunit; therefore, the total number of mutated amino acids is 24 times the number of mutations (e.g., mutation M3 corresponds to 72 amino acids substituted in the entire nanocage, for a total of 3,960 amino acids). These first sets of mutations show the apparition of positively charged areas on the surface, but the negatively charged areas prevail, and it was necessary to increase the number of mutations to obtain a net positive surface charge.

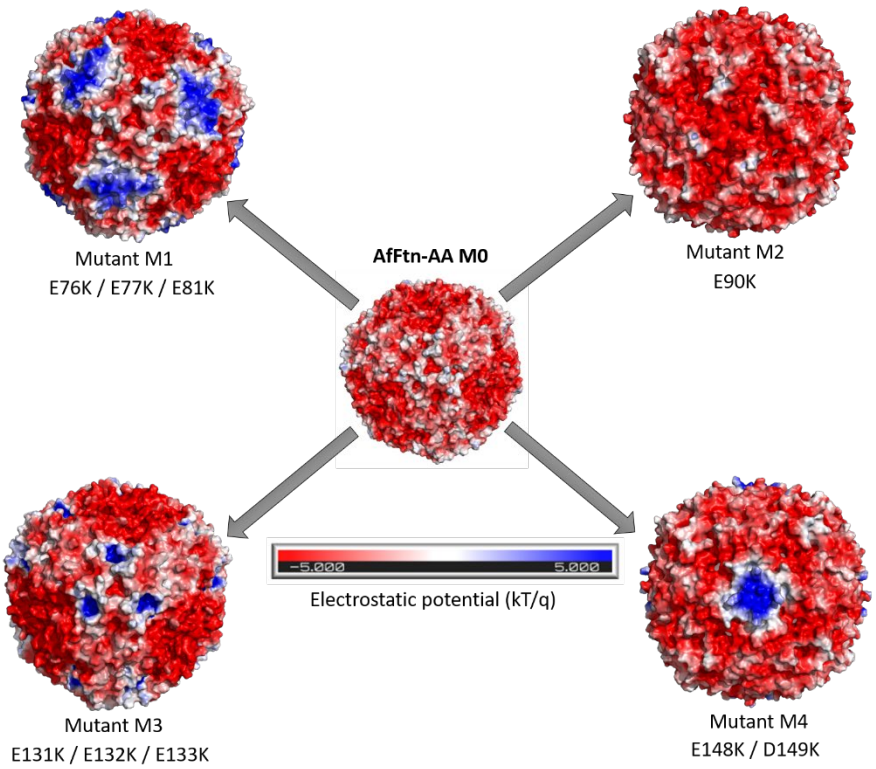

Figure 68: 3D representation of the electrostatic potential molecular surface of ferritin mutants (AfFtn-AA M1, M2, M3, and M4). The ESP is represented by positive (blue), negative (red), and neutral (white) areas. The scale bare ranges from −5.00 to +5.00.

In order to increase the number of mutations, we numerically design new mutants by adding the mutations presented before. In Figure 69, the three new mutants M34, M342, and M3421 (called M9) with 5, 6, and 9 mutations, respectively, are displayed. The number of positively charged areas increases with the number of mutations, and there is a majority of positive surface charge areas for the fully mutated M9. From these results, the M9 mutants seem suitable to obtain a positive ferritin. Experimental mutations of ferritin mutants were carried out by site-directed mutagenesis and are described in the next section.

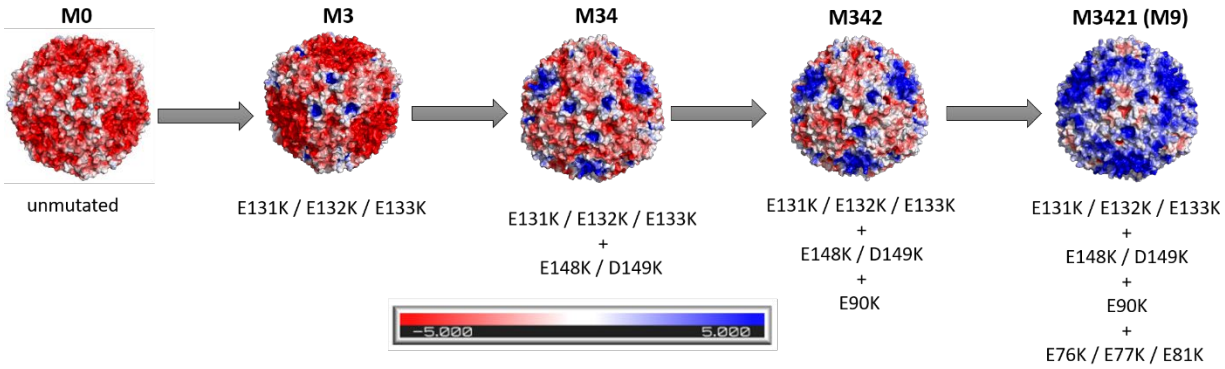

Figure 69: 3D representation of calculated electrostatic surface potentials (ESP) for unmutated ferritin (AfFtn-AA M0) and ferritin mutants (AfFtn-AA M3, M34, M342, and M9). The negative and positive surface charge areas are represented in red and blue, respectively. The mutations are shown with increasing mutated amino acids (from left to right). The scale is represented at the bottom and ranges from −5.00 to +5.00.

3. Production and characterisation of ferritin mutants

3.1. Mutation and purification of the ferritin mutants

Experimentally, site-directed mutagenesis was performed in the NTU laboratory following the PCR protocol (see Appendix III-1.4). The template plasmids were extracted from *E.coli* DH5α cells that contained the AfFtn-AA gene. After PCR reactions, the mutated plasmids were transformed into *E.coli* BL21(DE3)C+ RIL cells for future gene expression and production of the ferritin mutants. Two primers (forward and reverse) were used in the PCR reaction for each set of mutations. In order to make the successive mutations M34, M342, and M9, the mutated plasmids were used as template plasmids in the PCR reaction. For instance, to perform the M34 mutation, M3-mutated plasmids were extracted and used as template plasmids with M4 primers in the PCR reaction. After mutations and transformation of mutated plasmids into competent cells, the ferritin mutants were produced and purified following the protocol described in Appendices III-1.1 and III-1.2. The ferritins AfFtn-AA M0, AfFtn-AA M3, and AfFtn-AA M9 are designated by M0, M3, and M9, respectively, for the rest of this chapter. M3 and M9 were the main ferritin mutants produced during this thesis. For M3, upstream and downstream protocols were similar to those for M0. For the M9, it was required to change the eluent solution to water to collect the purified ferritins. The rest of this section focus on the ferritin purification

protocol. In fact, the purification of ferritin uses the HEPES buffer as eluent. For M3, HEPES buffer elution yielded a high quantity of ferritin, as indicated by a strong peak on the FPLC chromatogram (Figure 70.a, peak n°1 at ≈ 2300 mAU). However, for M9, only a small quantity of ferritin could be collected by HEPES buffer elution (Figure 70.b, peak n°1 < 200 mAU). Then, the elution was carried out with MiliQ water instead, and we see an increase in the absorbance for the water elution peak (Figure 70.b; peak n°2 at ≈ 1000 mAU). The change in the eluent nature could arise from a resistance to the elution for the M9 mutant, and will be discussed later in this chapter. The purity of the collected ferritin solutions was confirmed by SDS-PAGE, following the protocol described. In Figure 70.c−d, the SDS-PAGE pictures related to the FPLC chromatograms are displayed. The wells (1) and (2) correspond to the solution collected at peaks n°1 and n°2, respectively. For M3, SDS-PAGE (Figure 70.c) shows only a clear band at 20 kDa for the wells (2), which confirms the purity of the solution. For M9, SDS-PAGE (Figure 70.d) shows many bands in the wells (1) and only one clear band at 20 kDa in the wells (2). The HEPES buffer elution is not efficient and gives a nonpure solution, whereas water elution gives a pure solution. After that, the purified ferritin mutants were loaded by following the mineralisation protocol. M3 mutants were successfully loaded at 4800Fe. M9 mutants could only be loaded at a maximum of 3600Fe as solutions loaded at a higher iron content showed instability and sedimentation.

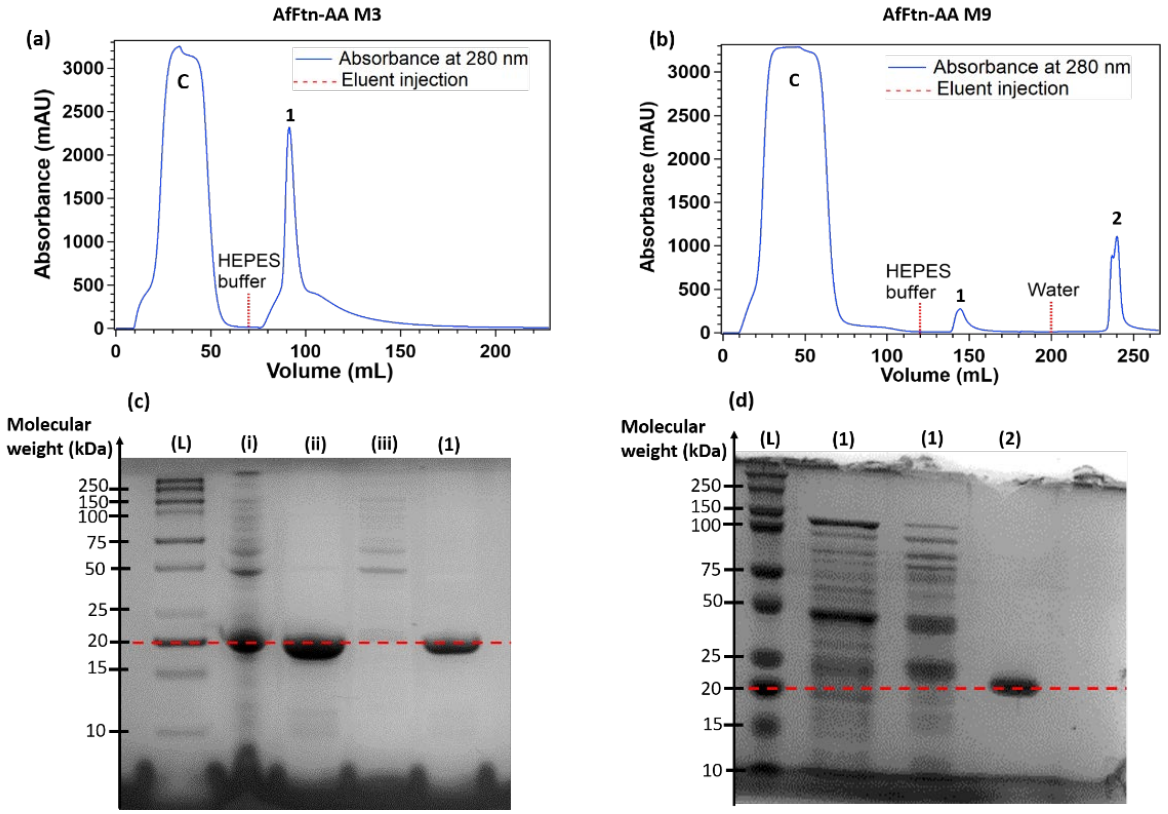

Figure 70: FPLC chromatograms for ferritin mutants M3 (a) and M9 (b) with their corresponding SDS-PAGE pictures (c) and (d), respectively. On the chromatograms, the peak "C" corresponds to the flow through. On the SDS-PAGE pictures, wells are designated as follows: (L) ladder; (i) lysate; (ii) supernatant; (iii) remaining pellets; (1) HEPES buffer elution peak; (2) water elution peak. The molecular weight of a ferritin monomer (20 kDa) is indicated by a red dashed line.

3.2. DLS and ELS characterisation of AfFtn-AA mutants

Ferritin mutants produced, purified, and loaded were characterised by DLS (see the detailed protocol in Appendix III-2.3) to confirm the formation of the 24-mer cages post-loading and, where applicable, to determine their hydrodynamic diameters. The DLS measurements were carried out at pH 7.4 (HEPES buffer), and three runs were recorded for each ferritin mutant solution. In Figure 71, the results showed average diameters, calculated from the three runs, of 25.7 ± 1.5 nm and 26.8 ± 14.0 nm for M3 and M9, respectively, and confirmed the formation of the cages for both mutants. The polydispersity indexes Đ were recorded at around 0.26 and 0.43 for M3 and M9, respectively. The diameter values of both mutants are higher than the value measured for M0 at 13.3 ± 1.8 nm. This increase in diameter could arise from mutations. The lysine amino acids have a different interaction with the ionic solvent than the aspartic acid and glutamic acids, and even though they are all charged, the morphology of their side chains

is different and could affect the size of the double-layer. In the case of M9, the value of Đ is higher than for M0 (Đ = 0.21) and M3 (Đ = 0.26), and the standard deviation between the three runs is high, with one peak at 14.8 nm and two peaks at 33 nm and 30.7 nm. This observation could be the result of particle aggregation.

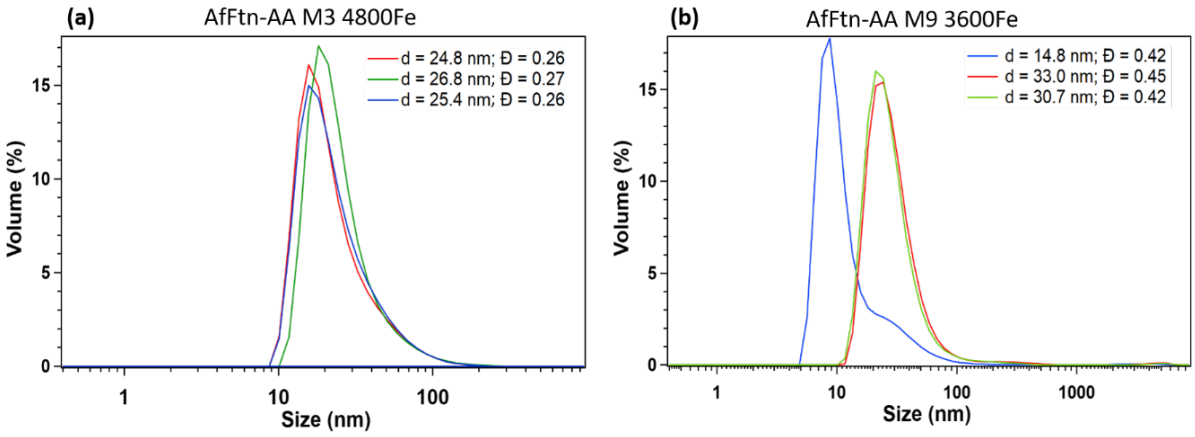

Figure 71: Graphics of the DLS results for ferritin mutants (a) M3 (AfFtn-AA M3) and (b) M9 (AfFtn-AA M9). The size value for each peak is displayed in the inset of the figures with the polydispersity index (Đ).

Then, the zeta potentials of ferritin mutants were measured by ELS methods at pH ranging from 3.0 to 10.0, following the same protocol as for M0. The results are displayed in Figure 72, along with the zeta potential curve obtained for M0 (red curve) from Figure 66. The zeta potential values at pH 7.4 are −18 ± 3.7 mV, −22 ± 5.6 mV, and −9 ± 0.57 mV, and the IEP values are 4.2, 4.8, and 5.9 for M0, M3, and M9, respectively. These results show a shift of the IEP towards higher pH values induced by the mutations, however the zeta potentials remained negative at pH 7.4. Consequently, the substitution of amino acids in the ferritin nanocages significantly modified its electrostatic charge, but the sign of the net surface charge of the ferritin was not changed by the mutations, however, some changes are noticeable and are described hereafter.

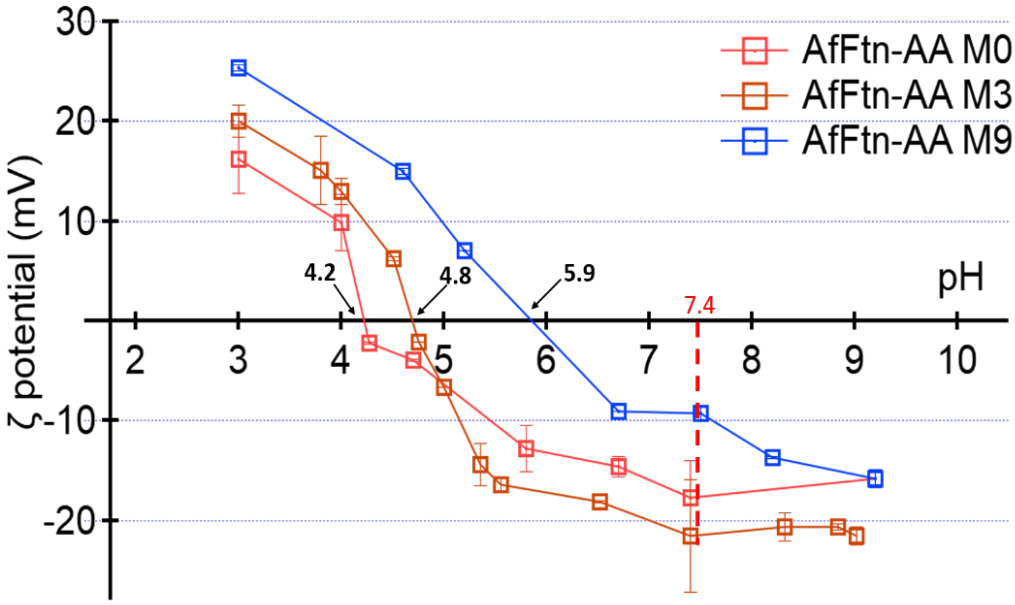

Figure 72: Graphic of zeta potential (mV) vs. pH curves measured for AfFtn-AA M0 (red), M3 (brown), and M9 (blue) as a function of the pH of the solution. The isoelectric points are indicated with black arrow.

3.3. Impact of the mutation on the ferritin

The characterisation of the ferritin mutants clears up the impact of the mutations on the ferritin shape and electrostatic behaviour. The shift of the IEP closer to the pH of the buffer (from 4.2 to 5.9) causes weaker repulsion between ferritins in the solution, as shown by the low zeta potential value (−9 mV) obtained for M9. Therefore, it indicates low stability for the M9 colloidal dispersion, and ferritins inside the solution are more likely to form aggregates, which explains the large diameter deviation (± 14 nm) and the Đ value (0.43) obtained by DLS.

Earlier in this chapter, we mentioned the elution resistance for M9, which can now be explained from the ELS results. In fact, the purification of ferritin by the HIC method is based on interactions between hydrophobic areas present on the ferritin dimers and the hydrophobic ligands attached to the column adsorbent. These interactions are strengthened by adding a high concentration (0.5 mol.L^{-1}) of ammonium sulphate salt in the buffer solution, which reduces the solvation of the ferritin and exposes its hydrophobic patches to promote binding to the column. Thereby, the more the particle is hydrophobic, the more it will bind to the column (for the same concentration of salt). For M9, its IEP is close to the pH of the HEPES buffer (which is also reduced by the addition of ammonium sulphate) resulting in less charged groups on the

ferritin dimer and then an increase in its hydrophobicity. The binding of the M9 to the adsorbent is reinforced, increasing its resistance to elution. Furthermore, the HEPES buffer used for the elution of the ferritin contains NaCl salts (at 0.05 mol.L^{-1}), which also promote hydrophobic interaction[119] and therefore hinder the desorption of the M9 particles from the column adsorbent. However, the solvation of M9 in the buffer solution is low due to its poor colloidal stability in a high salt environment, which results in some M9 dimers aggregating. It causes them to weakly or not bind to the column and to be washed away with other protein contaminants. Consequently, the final concentration of M9 mutants inside the purified solution is low compared to the M0 or M3 purified solution, as shown by the low absorbance measured for the water elution peak (Figure 70.b). In addition, the ferritin yield of the purified solutions, measured by Bradford assay, showed lower values for M9 (< 20 mg) compared to M0 or M3 (> 50 mg).

4. KPFM characterisation of AfFtn-AA mutant on silicon

In this section, we present the KPFM measurement of ferritin mutants on silicon. Solutions of M3 4800Fe and M9 3600Fe were drop-casted for 1 min on a silicon surface. Topography and CPD images of both samples were recorded at a slow rate of 500 nm.s^{-1} (0.5 Hz) for 512 x 512 px² images, and with a LSH set at 25 nm

4.1. Topography of AfFtn-AA mutants on silicon

In Figure 73 a−b, a topography image of a 1.5 µm² area recorded on each sample is displayed and shows many nanoparticles (yellow dots) with few aggregates. The average heights of the particles were computed from height profiles (on 50 particles) at h = 8.8 ± 1.5 nm and h = 9.3 ± 1.5 nm for the M9 sample and M3 sample, respectively. The measured sizes are coherent with the size of a ferritin (around 12 nm). Thus, the two ferritin mutants produced in the laboratory were successfully immobilized on the silicon substrate. Also, the height distributions (Figure 73 c−d) show a few large ferritins with sizes over 12 nm. The results indicate similar sizes for M3 4800Fe and M9 3600Fe, despite the difference in their iron content.

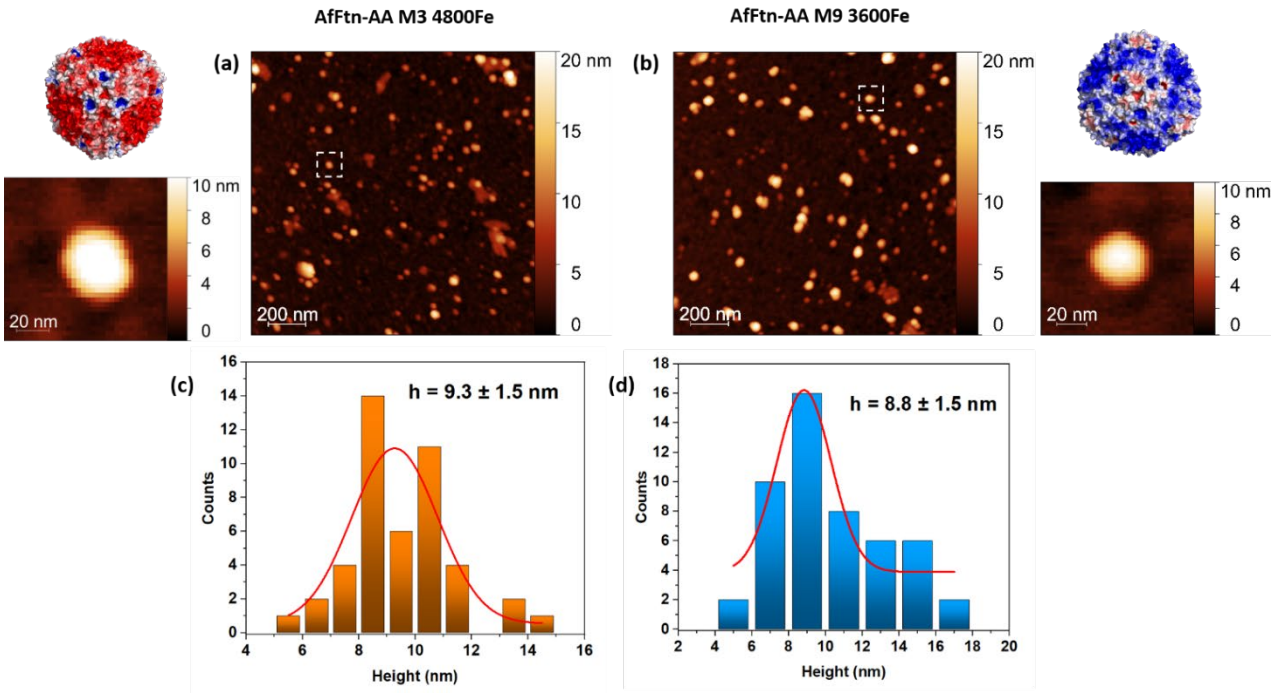

Figure 73: Topography images (1.5 µm²) of ferritin mutants M3 (a) and M9 (b) immobilized on silicon, measured by KPFM. Zoom-in images (100 nm²) of one M3 and one M9 particle are also displayed, along with associated PyMoL 3D representations of the molecular electrostatic potential. Height distributions with a Gaussian fit computed from the height profiles of the M3 (c) and M9 (d) samples.

4.2. Surface potential of AfFtn-AA mutants on silicon

The relative recorded CPD images are displayed in Figure 74 a−b, and many ferritin mutants are distinguishable on both images, although the CPD signals of M3 nanocages are less recognizable than for M9, in spite of their higher sizes as shown above. CPD images of one individual M3 and M9 ferritin are shown in Figure 74.c-d and indicate negative CPD (in blue) compared to the CPD of the silicon (yellow) for both ferritins. The CPD profiles across these two ferritins (Figure 74.e) reveal a slightly higher CPD for M3, which is confirmed by computing the average CPD values for 50 ferritin. The results are CPD = −6 ± 1.4 mV and CPD = −8 ± 3.0 mV for M3 and M9, respectively.

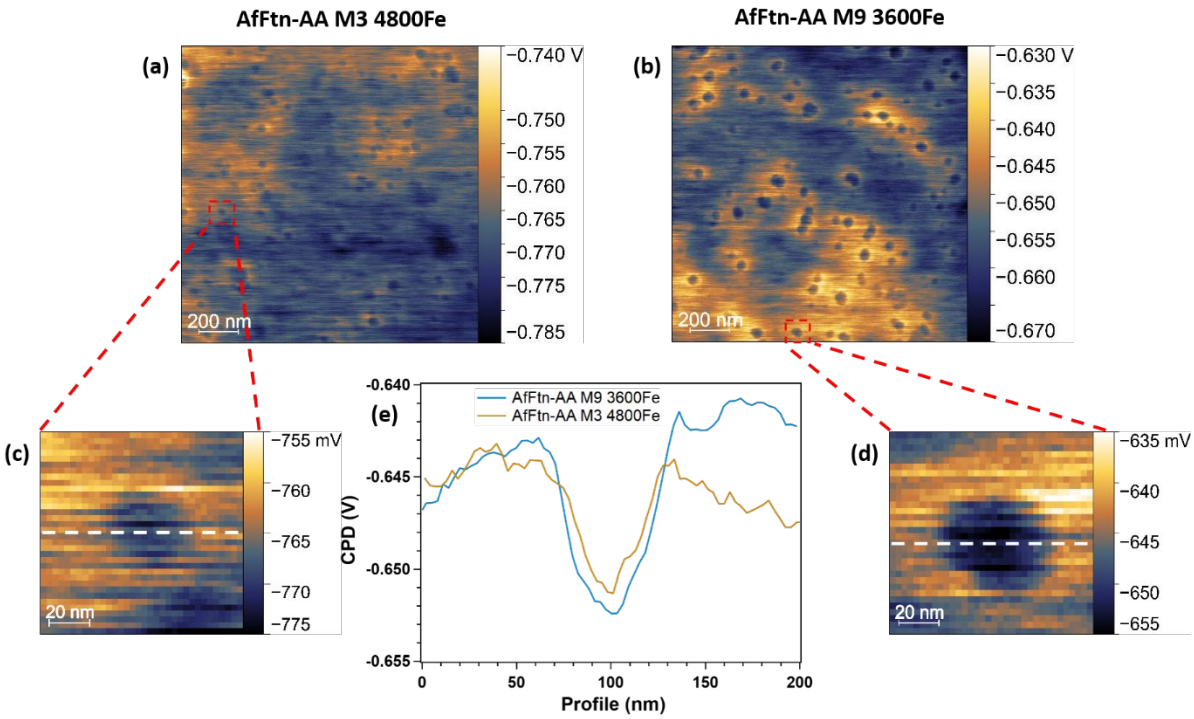

Figure 74: CPD images (1.5 µm²) of M3 (a) and M9 (b) immobilized on silicon, measured by KPFM. Zoom-in images (100 nm²) of one M3 (c) and one M9 (d) particle, along with associated CPD profiles. (e) the scale on the zoomed images is reduced for a better visualisation of the particles. The profile curves were shifted for the sake of comparison.

4.3. Effects of the mutations on the electrostatic and morphological behaviour of AfFtn-AA on a solid surface

From the topography results, we notice significant changes in the morphology of the ferritin mutants compared to the unmutated ferritins. The average height value of M9 loaded at 3600Fe is higher (h =8.8 nm) than for M0 at the same loading (h = 7.9 nm), and we observe the same phenomenon for M3 loaded at 4800Fe (h = 9.3 nm) and M0 loaded at 4800Fe (h =8.8 nm). Therefore, the ferritin mutants present a different behaviour when adsorbed on a surface. As described in the Chapter V, the adsorption interactions are important parameters that explain the change in the morphology of the protein upon adsorption. In this case, M3 and M9 present more positive patches at their surfaces, induced by the mutations, and the negative silicon surface is no longer seen as an electrostatically hostile surface. Thus, the mutants are adsorbed mostly by electrostatic interactions with the surface, and they don't need to undergo conformational change to stabilize on the surface.

The surface potential measurement presented a negative CPD for all the ferritin mutants. The mutations did not change the sign of the surface charge of the ferritin. However, M3 4800Fe and M9 3600Fe present higher CPD values than unmutated ferritin at the same loading, with CPD = −23 mV and CPD = −25 mV for M0 3600Fe and M0 4800Fe, respectively. On the one hand, the value of the LSH set at 25 nm instead of 15 nm for M0 ferritins could explain the difference in the measured values. However, CPD images of the same area of an M0 4800Fe monolayer sample recorded at a LSH from 20 nm to 10 nm (see Appendix VI-2) show a CPD variation of only 4 mV. Therefore, such a difference in LSH (10 nm) is very unlikely to result in a large CPD difference. Consequently, we can consider that the CPDs of ferritin mutants are different from that of unmutated ferritins. The overall surface charge of the ferritin mutants has changed because more positive amino acids are present, and it even becomes a majority for M9 (480 negatives and 576 positives). Here, the electric dipole moments were calculated at 2 D and 3D for M3 and M9, respectively. These values were calculated from the CPD of individual M3 and M9 particles and therefore do not reflect the electric dipole of pure ferritin mutants due to the contribution of the silicon. However, the low values indicate a distribution of charges with more positive charges that would be close to the surface, and creating inward dipoles, the overall net dipole moment of the mutants would decrease. Even though the sign of the CPD has not changed along with the mutations of the ferritin (at least for the fully mutated one), a change in the surface potential of the ferritin mutants is clearly distinguishable from the KPFM results.

5. Conclusion

In this section, we presented the experimental mutations carried out on the ferritin protein (AfFtn-AA) as well as their production in the NTU laboratory. The morphological and electrostatic characterisation in solution by light scattering methods (ELS, DLS) and directly onto a solid surface by KPFM were performed. The results indicated successful mutations and a shift of the IEP of AfFtn-AA in solution from 4.2 to 5.9, as expected. However, the sign of the surface charge in solution (zeta potential) and of the surface potential on the silicon (CPD) remained negative in both cases. By comparing the KPFM results of AfFtn-AA M0 with AfFtn-AA M3 and M9, the impact of the mutations is shown in the morphology of the ferritins, where the heights of the mutants differ from the heights of the unmutated, and it is believed to result from a switch in the adsorption mechanism on the silicon surface. Furthermore, the difference in the CPD values demonstrated a different distribution of charges induced by the mutations and the inversion of the positive/negative amino acid ratio. Finally, the site-directed mutagenesis performed on the AfFtn-AA nanocages allows us to modulate the surface charge of the ferritin and to create a new ferritin that could be incorporated, with the negative ferritin, as an electronically active layer in a future transistor devices.

6. References

[189] Lourenco C. « Steric Stabilization of Nanoparticles: Size and Surface Properties ». *International Journal of Pharmaceutics* 138, nº 1 (1996): 1-12.

[190] Derjaguin B.V., and L. Landau. « Theory of the stability of strongly charged lyophobic sol and of the adhesion of strongly charged particles in solutions of electrolytes », nº 14 (1941): 633-.

[191] Verwey E. J. W., and J. T. G. Overbeek. « Theory of Stability of Lyophobic Colloids », (1948).

[192] Lekkerkerker Henk N.W., and Remco Tuinier. *Colloids and the Depletion Interaction*. Vol. 833. Lecture Notes in Physics. Dordrecht: Springer Netherlands, 2011.

[194] Sengonul Merih, Josef Ruzicka, Athula B. Attygalle, et Matthew Libera. « Surface Modification of Protein Nanocontainers and Their Self-Directing Character in Polymer Blends ». *Polymer* 48, nº 13 (2007): 3632-40.

[193] Walstra Pieter. *Physical Chemistry of Foods*. Food Science and Technology 121, (2003).

[195] DeLano L. Warren, and Sarina Bromberg. « PyMOL User's Guide », (2004)

[196] DeLano Warren. « CCP4 NEWSLETTER ON PROTEIN CRYSTALLOGRAPHY », (2002), 11

[197] Amin Muhamed, and Jochen Küpper. « Variations in Proteins Dielectric Constants ». *ChemistryOpen* 9, nº 6 (2020): 691-94.

[198] Varadi Mihaly, Stephen Anyango, Mandar Deshpande, Sreenath Nair, Cindy Natassia, Galabina Yordanova, David Yuan, and al. « AlphaFold Protein Structure Database: Massively Expanding the Structural Coverage of Protein-Sequence Space with High-Accuracy Models ». *Nucleic Acids Research* 50, nº D1 (2022): D439-44.

[199] Jumper John, Richard Evans, Alexander Pritzel, Tim Green, Michael Figurnov, Olaf Ronneberger, Kathryn Tunyasuvunakool, and al. « Highly Accurate Protein Structure Prediction with AlphaFold ». *Nature* 596, nº 7873 (2021): 583-89.

Conclusions and Perspectives

In this thesis, we presented the ferritin nanocage as a promising biomolecule for the biomolecular electronic field and especially to be incorporated into solid-state electronic devices (junction, transistor). In such a configuration, the ferritin is adsorbed on a conductive or semiconductor surface, and the aim of this thesis is to propose a deep analyse of the morphology and electrostatic behaviour of the ferritin immobilized on a solid surface. These two parameters are important to understand the adsorption mechanisms and enhance the functionality of the ferritin. Moreover, this study will help to fully understand the charge transport mechanism through a ferritin. The approach of this thesis was to characterise one particular ferritin, the AfFtn-AA that we immobilized on a doped silicon surface and characterised by KPFM. Furthermore, we aimed for the modulation of the surface charge of the AfFtn-AA through bioengineered mutations, in order to design a future active monolayer of AfFtn-AA ferritin that could be deposited on transistor-like devices. These mutations were monitored by the ELS technique, and our goal was to shift the isoelectric point (IEP) of the ferritin with increasing mutations.

Throughout this thesis, AfFtn-AA particles were successfully produced from the *E.coli* bacteria, purified and loaded with different iron contents. In solution, the characterisations of AfFtn-AA demonstrated constant hydrodynamic diameters at all loadings, a net negative surface charge ($\zeta = -19$ mV), and an IEP around 4.2. In order to obtain a ferritin nanocage with a positive surface charge, we substituted specific negative amino acids of the ferritin with positive ones. The substituted amino acids were carefully chosen after extensive numerical calculations of the electrostatic surface potential of different ferritin mutants by solving the PB equation, and it was demonstrated that the substitution of nine amino acids significantly alters the overall electrostatic surface potential of the ferritin, from negative to positive. The mutations were successfully performed in the laboratory by the site-directed mutagenesis (SDM) method and were successfully produced in the laboratory. As expected, ELS characterisation of the mutated ferritins indicated a shift of the IEP from 4.2 to 4.8 and 5.9 for the M3 and M9 mutants, respectively. However, the net surface charge of the ferritin mutants and especially the fully mutated remained negative ($\zeta = -9$ mV for M9). This was not expected from the numerical calculations and indicated a difference between the zeta potential and the theoretical electrostatic surface potential. Regarding these results, we did not obtain a positive ferritin, but the mutations did change the surface charge of the ferritin. The shift of the IEP is a clear indicator, and experimental observations regarding the purification of the ferritins also suggested an increase in the ferritin hydrophobicity resulting from the mutations.

The results of in-solution characterisations gave us important electrostatic properties for the ferritin and mutants, which makes it a good starting point for the study of the ferritin in a dry state (on a solid surface). But the goal of making a positive ferritin is not yet complete, and to go further, we could increase the number of mutations to obtain a larger shift in the IEP. However, we need to be aware that substituting a high number of amino acids could hinder the ferritin dimers to self-assembling into a nanocage. Furthermore, the stability of the ferritin solution (i.e., colloidal stability) should be properly monitored because mutations induce the IEP of the ferritin to approach the working pH of 7.4, and the risk of aggregation or sedimentation becomes higher. Therefore, a large amount of mutation is required for the IEP to shift over the working pH and to obtain a positive ferritin. Although, the ionic strength, the pH, and the type of counter-ions are parameters involved in the dynamic and electrostatic of the ferritin in solution and would be of a great interest to be investigated. Finally, the ferritin mutants were taken over by another PhD student in the NTU laboratory to form hyper structures by mixing them with unmutated ferritins.

Ferritins loaded with different iron contents were immobilized on bare doped silicon. After confirming the immobilization of the ferritin on the silicon by FTIR, the surface potentials of the sample were measured by KPFM. Topographic results showed a linear decrease in the ferritin size with decreasing iron content, showing that AfFtn-AA tends to flatten on the silicon surface when not fully loaded. Such a phenomenon is widely known for proteins that rearrange their secondary and tertiary structures to relax into an energetically favoured state, in particular for the soft proteins, of which ferritin is arguably one. Unlike the topography, the surface potential of a single AfFtn-AA showed a clear non-linear variation of the CPD as a function of the iron content. The CPD remains constant for low-Fe ferritin (≤2400Fe) and decreases significantly for high-Fe ferritin (>2400Fe). A threshold appears at 2400Fe, which was confirmed by repeating the measurements for AfFtn-AA monolayers. Moreover, the CPD of 15 nm iron oxide nanoparticles, that mimic the iron core of ferritin, was measured higher than for the low-Fe ferritins, which clearly indicates that the ferritin iron core is not the only parameter involved in the variation of CPD. Our assumption is that there is an interaction between the iron core and the amino acid shells. To investigate this assumption, we interested ourselves in the electric dipole that is formed by the distribution of charge in the amino acid shell of the ferritin.

The electric dipoles of AfFtn-AA were calculated from CPD values and showed outward dipoles whose magnitudes followed the same trend as the CPD values. Many conclusions can

be drawn from these results, but we need to focus first on the adsorption mechanism of the ferritin on the silicon. At neutral pH, the silicon surface (SiO_2) is negatively charged, and the ferritin has a net negative surface charge due to the larger number of negatively charged amino acids in its primary structure. But positive patches from the positive amino acids (mainly the lysine in this case) are also present, creating a way for the ferritin to electrostatically adsorb on the silicon. Although, these positive patches are few and have a too low intensity for the ferritin to overpass the repulsion force. For proteins, it is known that their soft feature is what makes them adsorbed on electrostatically hostile surfaces. The loss of the structure and the release of counter-ions create high entropic contributions that mainly drive the adsorption process. In this case, it is understandable that ferritin adsorbed onto the silicon surface. However, the complexity of the ferritin structure makes it difficult to predict the exact mechanism for its adsorption. Although, the ferritin could adsorb via electrostatic interactions between charged amino acids and the silicon, it could also adsorb via the released counter-ions incorporated in the protein-surface contact regions, and via hydrogen bonds between basic silanol sites (SiO^-) and the N, C terminals of amino acids. Through these observations, we assess that the variation of the calculated electric dipoles arises from different charge distributions in proteins, which are directly linked to the way ferritin is adsorbed on the silicon, which is also profoundly linked to the iron core and its content. By bonding to the different subunits of the ferritin, the iron core would soften or harden the protein, changing the way it adsorbs. Furthermore, the KFPM measurements of the ferritin mutants deposited on the silicon reinforce our assumption. The height of the ferritin mutants were higher than the unmutated ferritin ones at equal iron content, which clearly shows that increasing the positive patches around the surface of the ferritin, makes it adsorb easily via electrostatic interaction and therefore does not require it to flatten to adsorb on the silicon. On the other hand, even though they are still negative, the CPD values of ferritin mutants clearly show a change in the surface charge induced by the mutation.

The results and observations expounded during this thesis opened the door for many future works. On the one hand, and as a proof of concept, the AfFtn-AA ferritins would be deposited as a monolayer on a pseudo-MOSFET. The monolayer, acting as a second gate and controlling the source-drain current, could be modulated by varying the iron content of the ferritin and seeking for a transistor response. Furthermore, the incorporation of a ferritin mutant monolayer on the transistor could possibly lead to development of a ferritin mutation sensor. However, the road to using ferritins as a proper biomolecular electronic component is long, as the interactions between semiconductors and particles are plentiful. In this thesis, we also studied one of these

phenomena, using gold nanoparticles as model particles that we immobilized on silicon. We demonstrated the presence of a Schottky barrier at the semiconductor/metal interfaces by KPFM, and we showed that the silicon areas around the gold nanoparticles are filled with positive charges that could possibly be used for catalysis chemical reactions or generate hot electrons. In fact, in a project briefly started during this thesis, we tried to form a gold nanoparticle/ferritin complex and deposit it on the silicon. By using laser irradiation, the idea would be to create hot electrons that would be injected into the ferritin.

Appendices

Appendices – Chapter I

1. The 20 primary amino acids and the proline

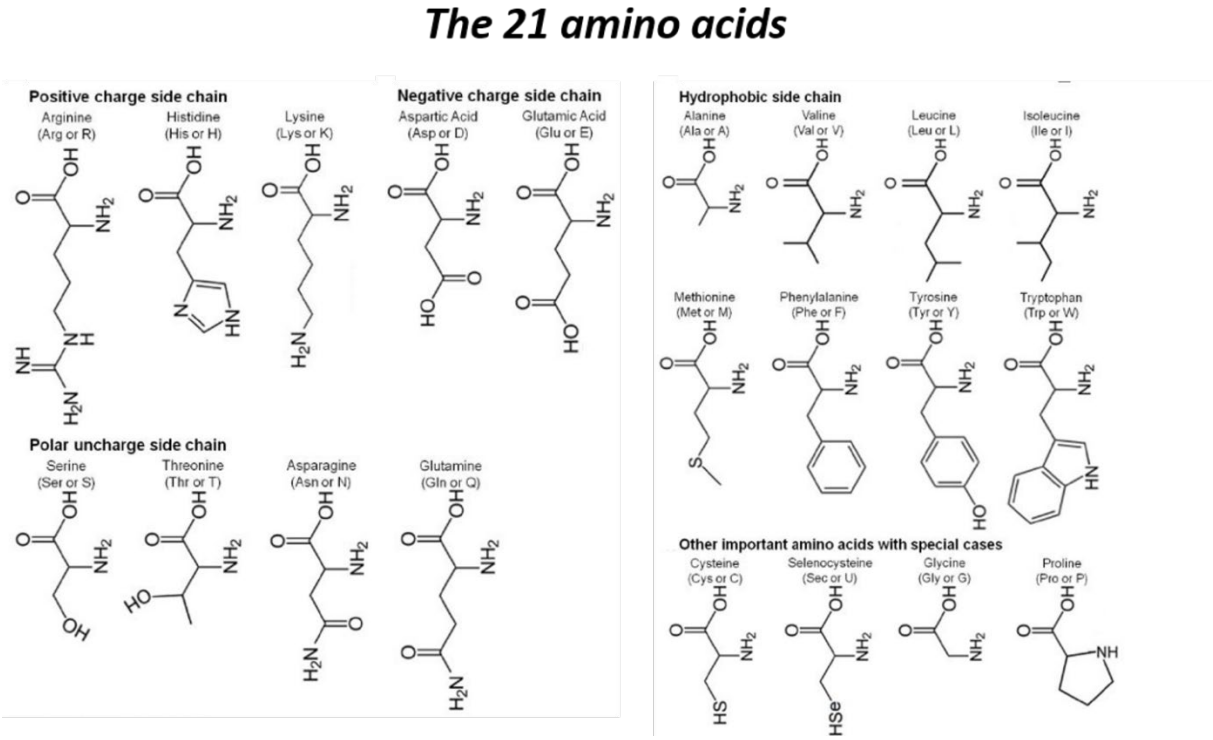

Figure S1 : The 21 amino acid molecules. Each amino-acid is designated with either one letter (e.g., R for Arginine) or the three first letters of its name (e.g., Arg for Arginine).

Appendices – Chapter III

1. Biochemistry protocols

1.1. Upstream protocol

The production of AfFtn-AA nanocages is carried out in two parts: the upstream protocol (culture and harvest of the cells) and the downstream protocol (protein extraction and protein purification). Prior to the culture of the cells, a few preparations need to be made. One ampicillin solution in DI water (100 $mg.mL^{-1}$) and one chloramphenicol solution in ethanol (50 $mg.mL^{-1}$) are prepared. These two solutions are antibiotic solutions that protect cells as they grow in the air, and many contaminants could hinder their proliferation. Then, 1 L of culture solution is prepared in a 3 L conical flask (the extra volume of air inside the flask is required for the cells to grow). The culture solution is made of LB media prepared by dissolving 25 g of LB Miller powder in 1 L of MiliQ water. The LB Miller powder is composed of 10 $g.L^{-1}$ of NaCl 10 $g.L^{-1}$ of tryptone and 5 $g.L^{-1}$ of yeast. The conical flask is then sealed with aluminium foil and autoclaved to remove contaminants. After that, the flask is left at room temperature to cool down (usually overnight). Once autoclaved, the culture solution can only be opened under a BSC (biosafety cabinet) to avoid contamination. In fact, all the manipulation described hereafter needs to be done inside a BSC (except for the harvesting part). Next, inoculum solutions of 2x20 mL of autoclaved LB media with 20 µL of each antibiotic are prepared in test tubes. The total inoculum volume is chosen to be between 2 % and 10 % of the total culture solution volume, and the volume of antibiotic is 1/1000 of the inoculum volume. Then, inoculums are inoculated with the desired *E.coli* cell stock using a sterilized spatula. This step is realized quickly because the *E.coli* stock is very sensitive to temperature. Inoculated solutions are put in a shaker-oven at 37 °C for 14-16 hours in order for the cells to grow. As for the culture solution, an extra volume of air is left above the inoculum solutions, and the caps of the tubes have to be slightly loose for the air to flow inside.

Once cells are grown inside inoculum solutions, (recognized by a blurry solution), they are poured into the 1 L culture solution, inside which 1 mL of each of the antibiotics has been previously introduced. The culture solution is incubated in a shaker-oven at 37 °C for 3 hours. After this time, the optical density (OD_{600}) of the culture solution is measured with a spectrometer. For this, 1 mL of the solution is swabbed and put in a quartz cuvette, which is

introduced into the spectrometer. The reference is done with 1 mL of LB media. When the OD_{600} reaches 0.6, 1 mL of isopropyl-β-d-thiogalactopyranoside (IPTG) is added to the culture solution to overexpress the cells. The culture goes back to the shaker-oven for 4 hours at 37 °C. The cells are then harvested by centrifugation. For this, the culture solution is poured into two 500-mL plastic recipients and put inside the centrifuge device. The centrifugation is set at 4500 rpm (rotation per minute) for 1 hour. This step will attract all the cells at the bottom of the recipient in the form of pellets. The pellets are removed from the bottom of the recipients by sonication, resuspended in about 40 mL of the culture solution inside a test tube, and centrifuged again for 10 minutes at 4500 rpm. The supernatant solution is then discarded, and the pellets inside test tubes are put in the freezer at −80 °C. Each test tube corresponds to 500 mL of culture solution made into pellets.

1.2. Downstream protocol

This protocol follows the upstream protocol and starts with frozen *E.coli* pellets. First, it needs the preparation of two distinct buffer solutions: buffer A, composed of 25 $mmol.L^{-1}$ of HEPES (acid 4-(2-hydroxyéthyl)-1-pipérazine ethane sulfonic) and 50 $mmol.L^{-1}$ of sodium chloride (NaCl) inside MiliQ water. And buffer B with the same composition as buffer A with 0.5 $mol.L^{-1}$ of ammonium sulphate ($NH_2SO_4^{2-}$) in addition. All the buffers are filtrated with a 0.22 µm filter and degassed (the degassing removes air bubbles inside the buffer that might enter the FPLC device).

Breaking cells: Pellets are resuspended in a beaker with 40 mL of buffer A (40 mL for 500 mL pellets) and put inside the ultrasound device. During the experiment, the beaker is put on ice to avoid overheating the protein solution. The ultrasound device is set at 37% with an alternance of 5 seconds ON and 5 seconds OFF. The cells are broken for 30 minutes ON (one hour in total). When sufficient cells are broken and the solution becomes clear, the beaker is put in a water bath and heated at 85 °C for 10 minutes.

Centrifugation: The heated protein solution is centrifuged with an ultracentrifuge Optima XE-100 from *Beckman Coulter*, for one hour at 40,000 rpm. Special tubes are used for this step, inside which the protein solution is poured. The tubes need to be balanced prior to centrifugation. After this, the supernatant is collected and the pellets discarded.

FPLC: The supernatant containing the protein is filtrated with a 0.22 µm filter, and ammonium sulphate is added inside. The concentration of ammonium sulphate inside the solution needs to match the concentration of buffer B, (i.e., 0.5 mol.L^{-1}). An *HiPrep*^{TM} PhenylFF (high sub) 16/10 column (Figure S2.b) is mounted on the FPLC device, washed with DI water, and equilibrated with buffer B. The protein solution is injected inside the FPCL and flows through the column at a rate of 1.5 mL.min^{-1}. Then, the column is rinsed with buffer B and eluted with buffer A. The eluted solution is collected in 10 mL test tube fractions. The purification of the protein solution is monitored by an UV spectrometer set at 280 nm that detects the presence of molecules flowing through the column. On the Figure S2.a, the first peak between 10 mL and 80 mL corresponds to the impurities flowing through the column and being discarded; during this time, the column, is washed with buffer B (100%). After 90 mL, the column is eluted with buffer A (buffer B at 0%), and the solution flowing through the column is collected by the tube test fraction (vertical red line). The second peak contains only purified ferritin in buffer A. About 20 mL of purified protein can be collected from here.

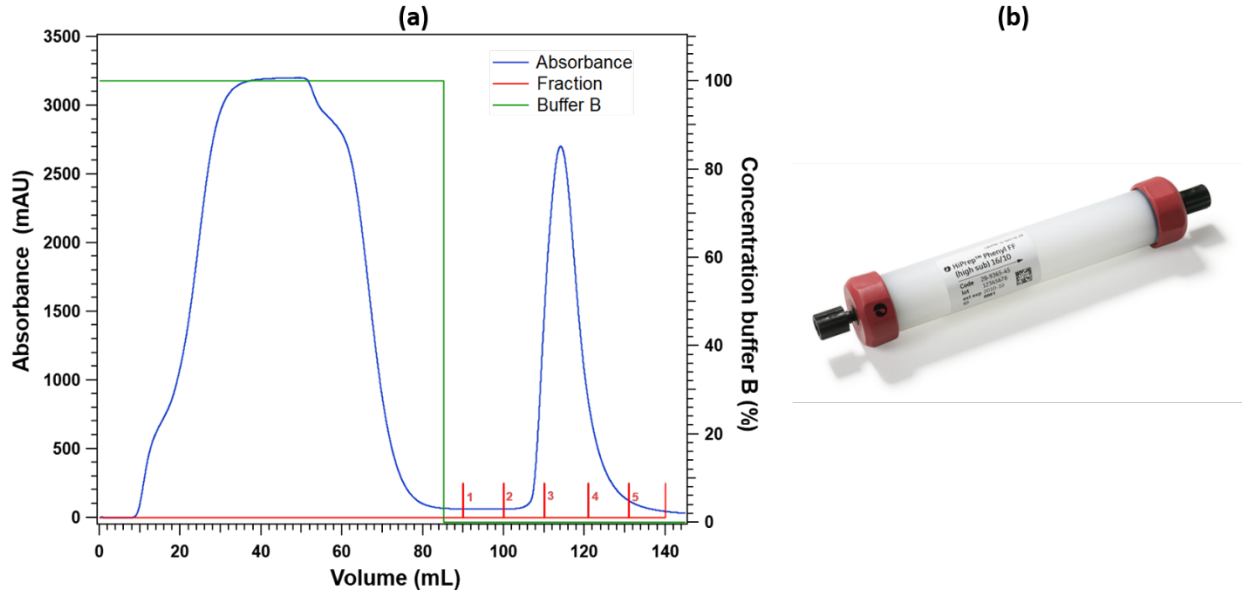

Figure S2: (a) Chromatogram of AfFtn-AA purification by FPLC. The blue curve represents the absorbance detected at 280 nm. The red vertical lines represent the test tube fraction (10 mL), inside which the purified solution is collected. The green curve represents the percentage of buffer B flowing in the FPLC system. (b) picture of an HIC HiPrep^{TM} *PhenylFF (high sub) 16/10 column.*

Iron loading: The loading of iron requires the preparation of an iron stock solution and the measurement of the protein solution concentration. The stock solution is 100 mmol.L^{-1} ($C_{solution,Fe}$) solution of iron (II) sulphate heptahydrate ($Fe_2SO_4^{2-}\cdot 7H_2O$) + 0.1 % chloric acid (HCl). The protein solution is always loaded at a concentration of 0.3 mg. mL^{-1} ($M_{protein}$). To load 10 mL (V_{sample}) of protein solution at 1200 Fe/cage, the volume of iron stock solution to add in the protein solution ($V_{solution,Fe}$) is calculated as follows:

We calculate the ratio of the protein concentration to the molecular weight of one empty ferritin nanocage (m_{cage}) :

$$\frac{M_{protein}}{m_{cage}} = \frac{300}{475} = 632\ nmol.L^{-1}$$

We multiply this value with the number of iron atoms wanted inside each cage, to obtain the concentration of iron stock needed inside the protein solution:

$$C_{sample,Fe} = 632 \times 1200 = 758\ \mu mol.L^{-1}$$

Then, we calculate the volume of the iron stock solution that needs to be introduced into the protein solution to reach this concentration:

$$V_{solution,Fe} = \frac{C_{solution,Fe}}{C_{sample,Fe}} \times V_{sample} = \frac{10\ (mL)}{132} = 76\ \mu L$$

The volume of iron is introduced by adding ten times 7.6 µL. After each addition, the solution is slowly shaken and left for 5 minutes. After the loading, the solution is left 1 hour at room temperature and then overnight at 4 °C.

Desalting: The loaded protein solution is filtered with a 0.22 µm filter and a *HiPrep*^{TM} 26/10 desalting column is mounted on the FPLC devices. The column is rinsed with DI water and equilibrated with buffer A. The sample is injected into the device, flows through the column at a rate of 5 mL.min^{-1} and is collected in test tube fractions.

Inductively-coupled plasma mass spectroscopy (ICPMS): This technique is used after protein desalting to confirm the amount of iron atoms loaded inside cages. For this, 100 µL of nitric acid (HNO_3) is added to a 1 mL AfFtn-AA solution at 1 µg.mL^{-1} and then incubated for

1 hour at room temperature. Then, 9 mL of DI water is added, and the total solution is filtrated with a 0.22 µm filter. The solution is then analysed by the ICP-MS apparatus.

1.3. Plasmid extraction

The method of plasmid extraction is used to take out a plasmid from a cell. Here, we perform this technique for the AfFtn-AA mutation, for which we need to extract the AfFtn-AA plasmid that will be mutated. The plasmids are extracted from *E.coli* DH5-α cells. To do so, a 15 mL LB media preculture solution is prepared (only ampicillin antibiotic is added) and inoculated with the *E.coli* stock that contains the gene of interest (AfFtn-AA gene). The culture is incubated at 37 °C in a shaker-oven for 16 hours. After this, the preculture is spun down at 4500g for 5 minutes, the supernatant is discarded, and the cells are in pellet form. For the next steps, we use an AxyPrep Plasmid Miniprep Kit from *Axygen Biosciences* containing DNA extraction buffer solutions, purification (wash) buffer solutions, an eluent solution, and Miniprep columns with silica membrane. In Figure S3, the different steps for plasmid extraction are shown. The bacterial cell pellets are resuspended in a resuspension buffer (50 mM Tris-HCl, 10 mM EDTA, and 100 µg.mL^{-1} RNase at pH 8.0) and treated with a lysis buffer (200 mM NaOH, and 1% (w/v) SDS) to break open the cells and liberate the plasmid. Then, a neutralization buffer (3.0 M potassium acetate at pH 5.0) is added to neutralize the resulting lysate. The impurities (precipitated proteins or cell debris) are pelleted by centrifugation, and the supernatant is loaded onto a Miniprep column. The column is washed first with a buffer (guanidine salt + ethanol) to remove contaminants such as fatty acids, proteins, and carbohydrates. Other contaminants (salts, metabolites) are removed by washing the column with an ethanolic buffer (1.0 M NaCl, 50 mM MOPS, and isopropanol (v/v) 15% at pH 7). The pure plasmids are eluted with an alkaline buffer (5 mM Tris-HCl at pH 8.5) and stored at −20 °C. The concentration of the plasmid solutions is monitored by measuring their absorbance at 280 nm with a NanoDrop ND-1000 spectrophotometer. The extracted plasmid DNA is used for the PCR experiment described below.

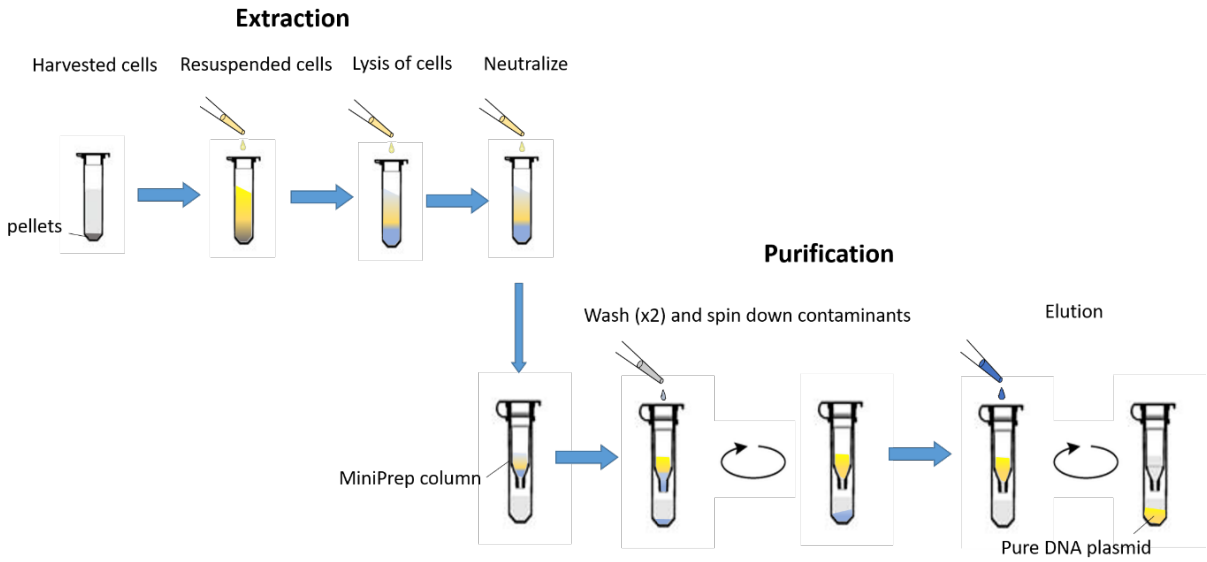

Figure S3: Schematic of the plasmid DNA extraction process. The plasmid DNA are extracted from the cells and dispersed in solution. The plasmid DNAs are purified inside a silica column (Miniprep column).

1.4. Polymerase chain reaction

The polymerase chain reaction, or PCR, is used here to mutate a parent plasmid by substituting a part of its sequence with a short DNA sequence specifically designed (primers). The forward and reverse primers (sequences) are required to perform the PCR. Here, extracted AfFtn-AA plasmids are used as parent DNA. Inside a tube, a ready-to use master mix from *ThermoFisher*, containing a *DreamTaq*^{TM} DNA polymerase, dNTPs (solution of nucleotides) and $MgCl_2$ (cofactor for DNA polymerase), is mixed with 1 µL of forward and reverse primers, 0.5 µL of extracted plasmid DNA solution, and 10.5 µl of DI water (Figure S4.a). Then, the tube is put inside an *Applied Biosystem* Veriti 96-well programmable thermocycler, which is set for 10 cycles (Figure S4.b). After that, 2 µL of dpn1 (digestion enzyme) is added to the tube (which removes the parent DNA) and incubated at 37 °C for 30 minutes (Figure S4.c). The mutated plasmids are stored at 4 °C for future experiments.

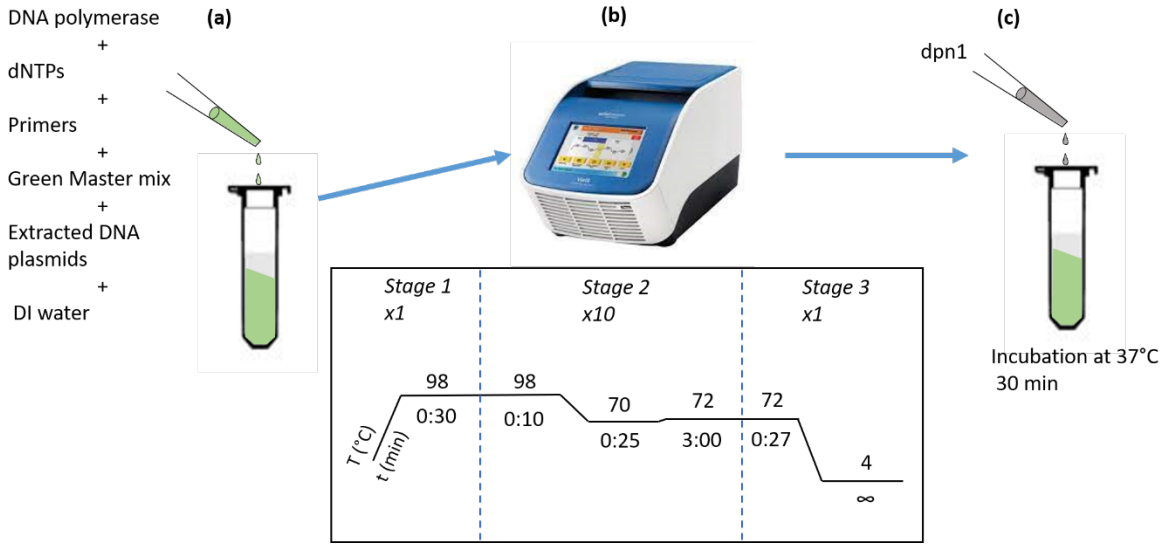

Figure S4: Schematic of the PCR protocols. (a) the extracted plasmid DNA solution is mixed with PCR reagents in a tube. (b) the tube is inserted in a thermocycler which undergoes 10 cycles (stage 2). The apparatus is heated to 98 °C in stage 1 and cooled down at 4 °C in stage 3. (c) the tube is taken out of the thermocycler and incubated at 37 °C for 30 minutes after addition of the dpn1 solution.

1.5. Transformation

The transformation process injects plasmid into competent cells. Here, mutated plasmids of AfFtn-AA are transformed inside *E.coli* DH5α or *E.coli* BL21(DE3)C+ RIL competent cells. Some culture plates are previously prepared with a LB agar solution mixed with DI water (with the addition of ampicillin). The solution is autoclaved and poured into a petri dish. When cooled down, the LB agar solution hardens and makes culture plates onto which cells can proliferate. Inside a BSC, competent cells in tubes are incubated for 5 minutes on ice. Then, 10 µL of the extracted plasmid DNA solution is added and incubated on ice again for 20 minutes. The tubes are heat-shocked for 45 seconds at 42 °C and are put back in ice. After 2 minutes, 500 µL of LB media is added, and tubes are incubated for 1 hour at 37 °C. The cells are concentrated by spin down at 4000g for 5 minutes, and the supernatant is partially discarded (≈ 500 µL). Cells are resuspended with the remaining solution and spread onto culture plates with a sterilized spatula. One control plate is made with competent cells without extracted plasmid. The Culture plates are incubated overnight at 37 °C. After colonies have grown on the culture plates (distinguishable as small white dots), 3x5 mL of LB media (+ ampicillin) culture solutions are inoculated with three different colonies and incubated at 37 °C overnight. Once

the cells are grown, glycerol stocks are made by mixing 0.9 µL of cell culture with 0.6 µL of glycerol. Stocks are stored at −80 °C for further experiments.

2. Protein characterisation techniques

2.1. SDS-PAGE

SDS-PAGE experiments were usually done after protein purification and iron loading. It is used to assess the purification of the ferritin solution. The first step is the preparation of two gels: the resolving gel (or running gel) inside which proteins flow, and the stacking gel inside which solutions are loaded into wells. The chemical composition of the gels is described in Table 3. The resolving gel is first poured between two glass plates (10 x 20 cm) filled up to ¾, covered with ethanol (99%) to remove air bubbles, and left for 20 minutes for the gel to polymerize. After that, the stacking gel is poured to the top, and a well-forming comb is inserted into the opening between the glass plates (Figure S5.a). After 20 minutes, the comb is withdrawn, the glass plates are inserted in a running module and they are put inside a gel box filled with a 10 % SDS running buffer. Prior to loading into the gel, samples need to be prepared by adding 9 µL of protein solution with 3 µL of a buffer solution containing 27 µL of Lameli buffer (dye) and 3 µL of β-mercaptoethanol (reducing agent). The solution is heated at 95 °C for 10 minutes to denature proteins, and centrifuged at 15,000 rpm for 10 minutes. Then, 8 µL of the prepared protein solutions and 5 µL of the molecular mass protein marker solution are loaded into the gel wells. The gel box is closed with a lid that connects the electrodes to the running module (Figure S5.b). Then, a 120 V potential is applied between the electrodes. We usually run the gel for 1 hour (until each protein reaches the bottom of the gel). After, the gel is taken off the glass plates, rinsed with DI water, and stained for 1 hour with a *Coomassie* brilliant blue stain, an organic dye that makes complexes with amino acids, and allows the visualization of proteins inside the electrophoresis gel. Finally, the gel is destained overnight with DI water and images of the gel are recorded using a G-box imaging system.

Reagents	Function in the gel	Volume in the resolving gel	Volume in the stacking gel
Deionized water	Solvent	4.1 mL	6.1 mL
30% Acrylamide/Bis	Polymerized to form the gel	3.3 mL	1.3 mL
Buffer 1.5 M Tris-HCl (pH 8.8)	Regulate the pH	2.5 mL	0 mL
Buufer 0.5 M Tris-HCl (pH 6.8)	Regulate the pH	0 mL	2.5 mL
10% SDS	Anionic headgroup binding to the protein	100 µL	100 µL
10% ammonium persulfate (APS)	Form free radicals Induce the polymerisation	32 µL	100 µL
TEMED	Free radical stabilizer, promote polymerisation	10 µL	10 µL

Table 3 : Composition of the resolving and stacking gel. Reagents are mixed inside a test tube. TEMED and APS induce the polymerization (hardening) of the gel and are therefore added in to the mix just before pouring the gel.

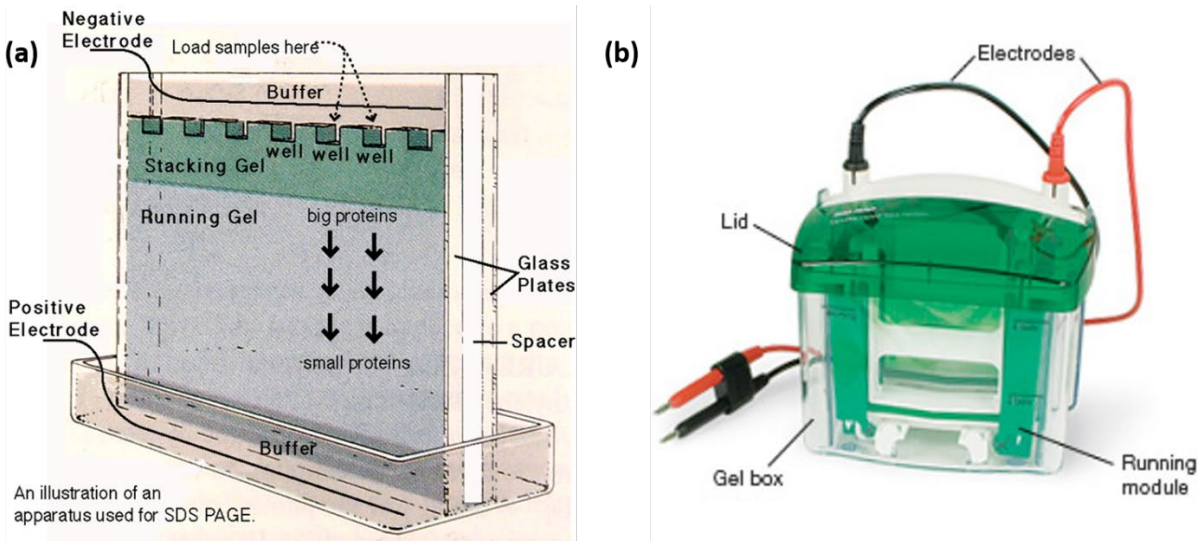

Figure S5: (a) Drawing of the glass plates inside which gels are poured. The comb forms the wells at the top of the stacking gel, inside which solutions will be loaded. (b) SDS-PAGE apparatus: the running module contains the gel and is put inside a gel box filled with a 10% SDS buffer. Both electrodes are connected to the running module via the lid.

2.2. *Bradford* assay

The Bradford assay determines the concentration of a protein solution. For this experiment, we use a 96-well plate from *ThermoFisher* that will contain the solutions to analyse. 10 µL of sample solutions and standard solutions (bovine serum albumin) with known concentrations (ranging from 0.05 $mg.mL^{-1}$ to 0.6 $mg.mL^{-1}$) are loaded in the 96-well plate as shown in Figure S6.a. DI water is also loaded as a blank. Each solution is loaded into three different wells to increase the accuracy of the measurement. Then, 200 µL of Coomassie blue G-250 dye is added and mixed inside each well. The solution is added slowly to avoid air bubbles inside the wells. After 5 minutes, the 96-well plate is put inside the spectrometer, which measures the absorbance of each well at 595 nm (Figure S6.b). From the standard absorbance results, we compute a calibration curve of the standard absorbance as a function of the standard concentrations. Therefore, the protein concentration is determined from the calibration curve by knowing its absorbance (Figure S6.c). Sometimes, the protein solution is too concentrated and doesn't fit in the calibration curve range. The solution is then diluted with buffer A.

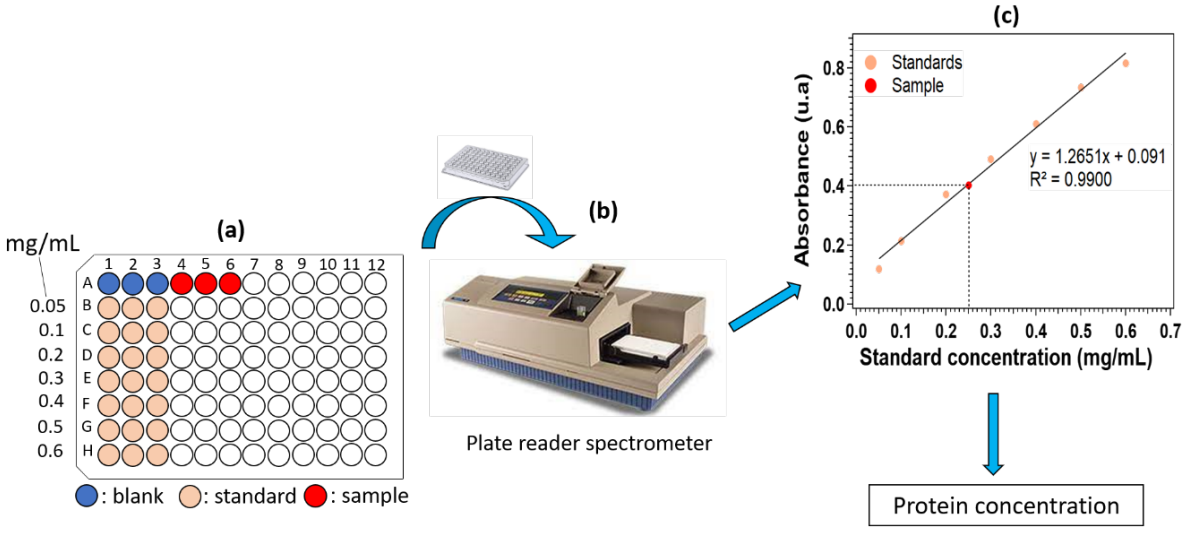

Figure S6: Schematic of the Bradford assay protocol. (a) a 96-well plate filled with DI water as a blank (blue), standard solutions at different concentrations (pink), and the sample solutions (red). (b) the 96-well plate is introduced into the spectrometer, which measures the absorbance of each well at 595 nm. (c) from the spectrometer results, we draw an absorbance vs. standard concentration calibration curve, from which the protein concentration is determined.

2.3. Dynamic light scattering

The dynamic light scattering (DLS) technique measures the hydrodynamic diameter of ferritin dispersed in buffer A. For this, 1.5 mL of a purified AfFtn-AA solution is filtrated with a 0.22 µm filter and centrifuged for 10 minutes at 15,000 rpm to remove the aggregates. Then, 1 mL of the supernatant is taken and poured inside a transparent quartz cuvette. The cuvette is inserted inside the Zetasizer device (Figure S7.a), and the temperature is equilibrated at 25 °C. Each sample is measured three times.

2.4. Electrophoresis light scattering

The electrophoresis light scattering (ELS) technique measures the zeta potential of ferritins dispersed in various buffers. As for the DLS, the AfFtn-AA solution is filtrated and centrifuged before the measurement. The AfFtn-AA solution is injected into a DTS 1070 capillary cell with a 1 mL syringe. This cell is in the form of a capillary with one electrode on each side and is closed with caps (Figure S7.b). The cell is inserted inside the Zetasizer device and the temperature is equilibrated at 25 °C. Then, the zeta potential is recorded five times with an interval of 180 seconds to avoid overheating the cell. The zeta potential of the AfFtn-AA nanocages is recorded for different pH. Therefore, a 50 mM Tris-HCl buffer is used for pH in the range from 8 to 10, and a 50 mM sodium acetate $C_2H_3NaO_2$ + 50 mM acetic acid (CH_3COOH) is used for pH in the range from 5 to 3. For neutral pH, ferritins are in buffer A.

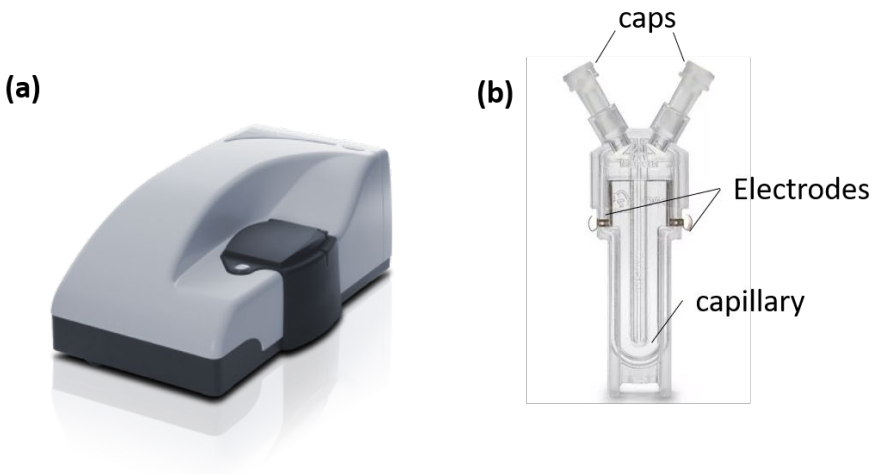

Figure S7 : (a) Picture of the Zetasizer apparatus, and (b) picture of a folded capillary cell for electrophoresis light scattering measurement.

3. *Fourier* transform spectroscopy

For FTIR measurement, a 3x1 cm^2 of FZ silicon wafer, cut with a diamond tip, is rinsed with acetone and ethanol in an ultrasound bath. The silicon wafer is placed on the sample holder of the spectrometer. The laser alignment is checked by maximizing the amplitude received by the detector. Then, we wait 15 minutes to purge the spectrometer. After that, three reference spectra are recorded. Each spectrum is made by 500 scans recorded between 4000 and 800 cm^{-1}, in absorbance mode. The silicon wafer is withdrawn, one drop of an AfFtn-AA solution is drop-casted on it, and it is left for 2 hours. Finally, the silicon wafer is placed again on the sample holder, and the sample spectra are recorded with the same configuration as for the reference.

Appendices – Chapter IV

1. AuNPs on Si : material and methods

Materials: For our experiments, *n*-doped (doped with phosphorus) and *p*-doped (doped with boron) silicon wafers were cut into 1 × 1 cm² pieces with a diamond tip. *n*-doped silicon wafers ⟨100⟩ with a dopant concentration of 10^{14}–10^{15} cm^{-3} (1–10 Ω.cm) and *p*-doped silicon wafers with a dopant concentration of 10^{14}–10^{15} cm^{-3} (10–20 Ω.cm) were purchased from ITME. MilliQ water (18.3 MΩ.cm) was used for solution preparation and rinses. 3-Aminopropyltriethoxysilane (APTES) was purchased from Aldrich and methanol from VWR Chemicals. AuNPs of 50 nm diameter used for this study were synthesised following the seeded-growth method explained by Bastús *et al.* and they are stabilized by citrate molecules.

Silanization: First, silicon samples were cleaned with acetone and ethanol under sonication and dried under nitrogen flow. Next, they were dipped into an APTES : methanol solution (volumetric ratio 1:10) for 2 hours, followed by three successive rinses in methanol under sonication in order to remove the excess APTES. The functionalized samples were dried under a nitrogen flow. One drop of AuNP suspension was drop-casted onto each of the four silicon samples with an increasing deposition time: 1 min (sample A), 2 min (sample B), 10 min (sample C), and 40 min (sample D). Finally, the samples were thoroughly rinsed with ultra-pure water and dried under a nitrogen flow.

2. SEM images of gold nanoparticles

SEM images of 55 nm gold nanoparticles (AuNPs) deposited on sample A were recorded. AuNPs are immobilized with a monolayer of APTES.

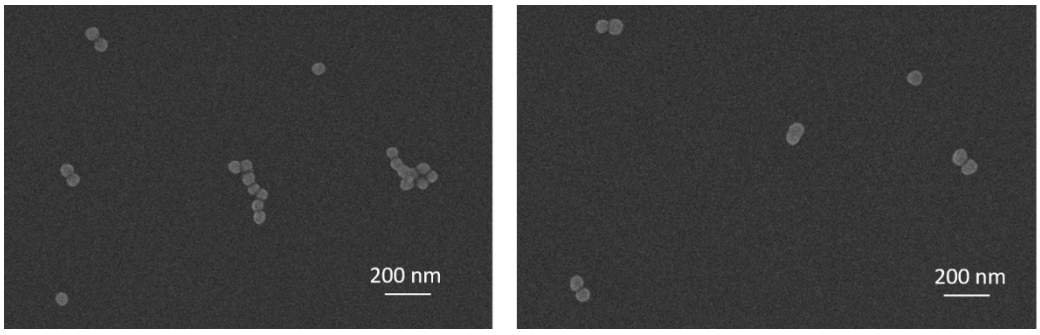

Figure S8: SEM images (2 x 1.5 µm²) of gold nanoparticles on n-doped silicon.

3. Ring-shaped pattern of AuNPs on silicon

In Figure S9 is represented a schematic, from Chen et *al.* (2013) [163], showing the far-field scattering patterns from the differently oriented electric dipoles of gold nanorods. This figure helps understanding the phenomenon of ring-shape pattern for AuNps on silicon described in the main text.

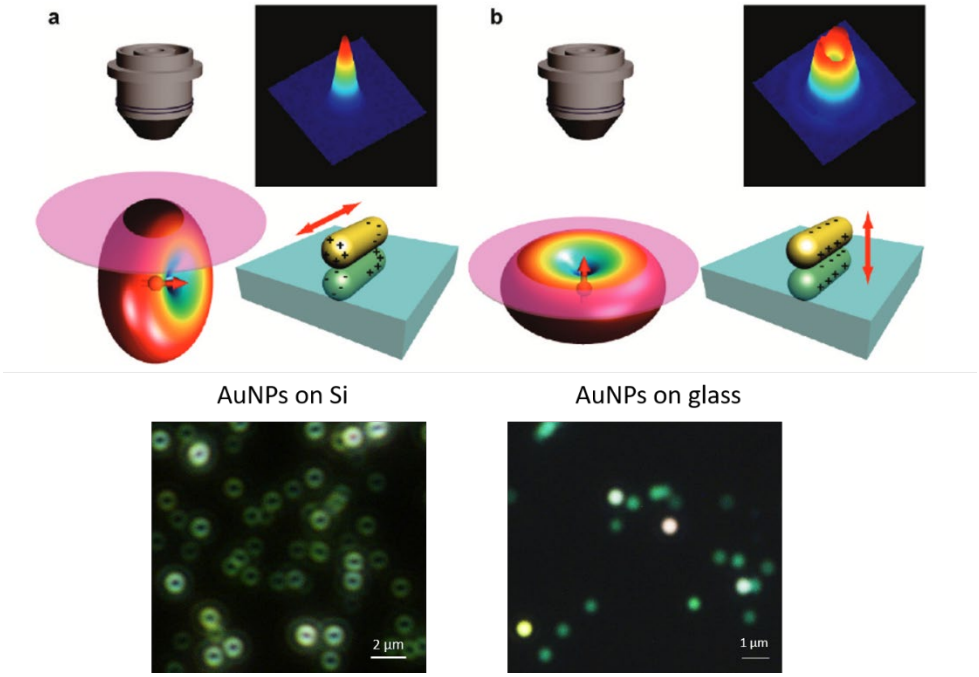

Figure S9: Schematic showing the far-field scattering patterns from the differently oriented electric dipoles. (a) Excitation field aligned parallel to the length axis of the nanorod. (b) Excitation field aligned perpendicular to the substrate. The pink plates on the radiation torus denote the regions that can be collected by the objective. The red arrows indicate the direction of the excitation polarization. The nanorod with charges is rotated relative to the dipole in the radiation torus in order to show clearly the original dipole and the image dipole in the substrate. [163] At the bottom are displayed dark-field images of AuNPs on silicon (left) and AuNPs on glass (right).

4. KPFM measurement: checking the uniformity of the APTES monolayer

These images in Figure S10 below emphasize the small irregularities of the APTES monolayer. The topographic image in Figure S10.a shows small grains originated from APTES aggregates of typically 1 nm. The corresponding CPD variations are around 1 mV. These small variations do not screen the CPD variations induced by the AuNPs which are in the order of magnitude of 30 mV.

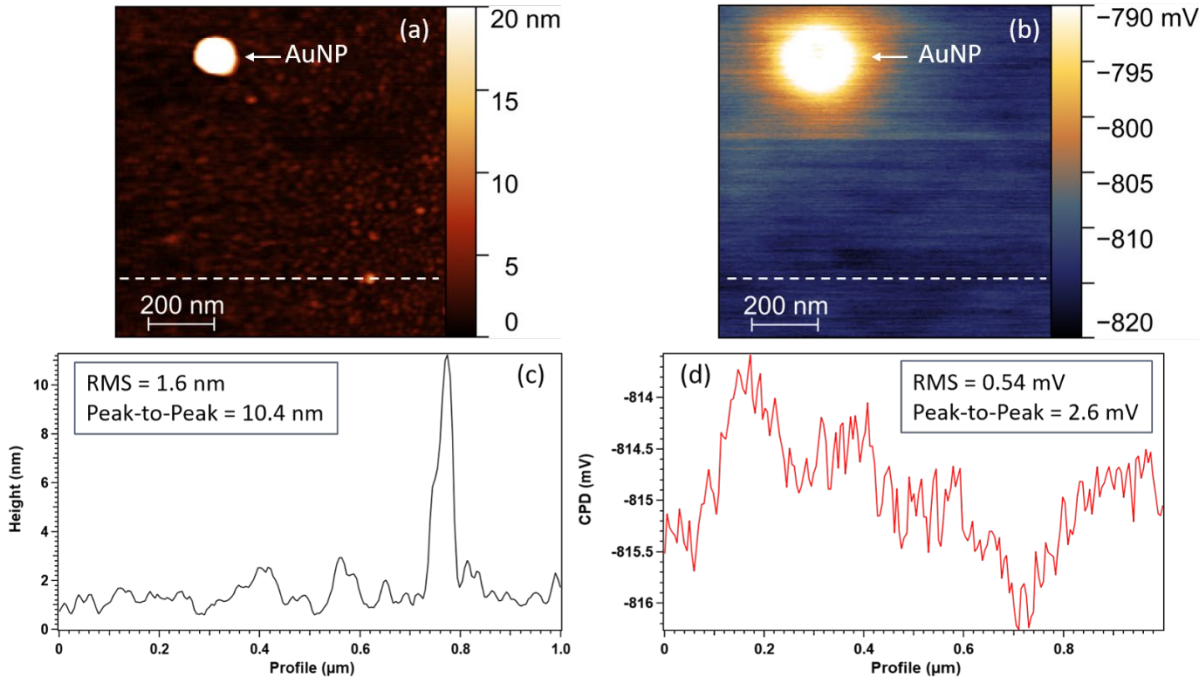

Figure S10 : Topography image (a) and its corresponding CPD image (b) of one gold nanoparticle on n-doped silicon (sample A). Profiles (from the white dashed line) below show the height (c) and CPD (d) of a part of the APTES monolayer. Root Mean Square (RMS) and Peak-to-Peak values along these lines are displayed in the inset of the graphs.

5. Band bending calculation for *Band Diagram Program*

Figure S11 is a representation of the results obtained with the *Band Diagram Program* developed by Knowlton in the two cases of Figure 56 in section 3.2 of the chapter IV. The top band diagram of Figure S11 corresponds to a planar ideal interface of gold/SiO_2/Si. It results in a built-in potential of 660 mV. The second band diagram corresponds to the system that includes a gap of 10 nm of air and mimics the situation of the silicon surface in the vicinity of the AuNPs and not exactly below it. This crude description demonstrates that the built-in potential reduces to 520 mV. As explained in the main text, this explains the progressive CPD increase when the KPFM tip approaches an AuNP.

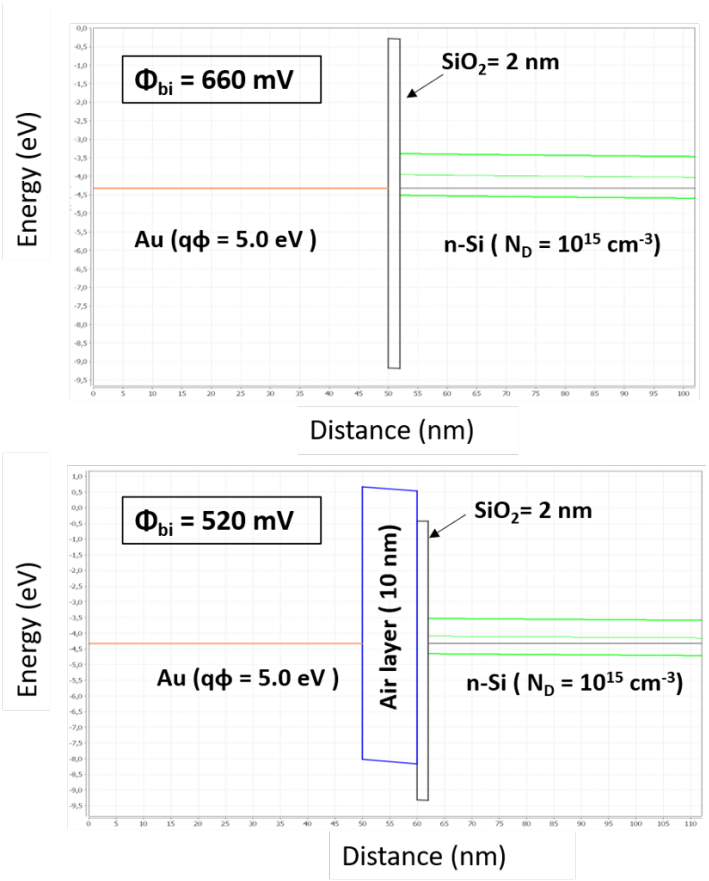

Figure S11 : Band Bending simulation with an air layer of 320 nm (top) and 10 nm (bottom). Respective ϕ_{bi} are 660 mV and 520 mV.

Appendices – Chapter V

1. Topography images of AfFtn-AA nanocages on silicon

The topography images obtained from KPFM measurements of ferritin (AfFtn-AA) on silicon are shown below (Figure S12). Images show a 1 µm² area of the sample surfaces where AfFtn-AAs have been deposited. The height distributions in the main text are computed from the Figure S12.

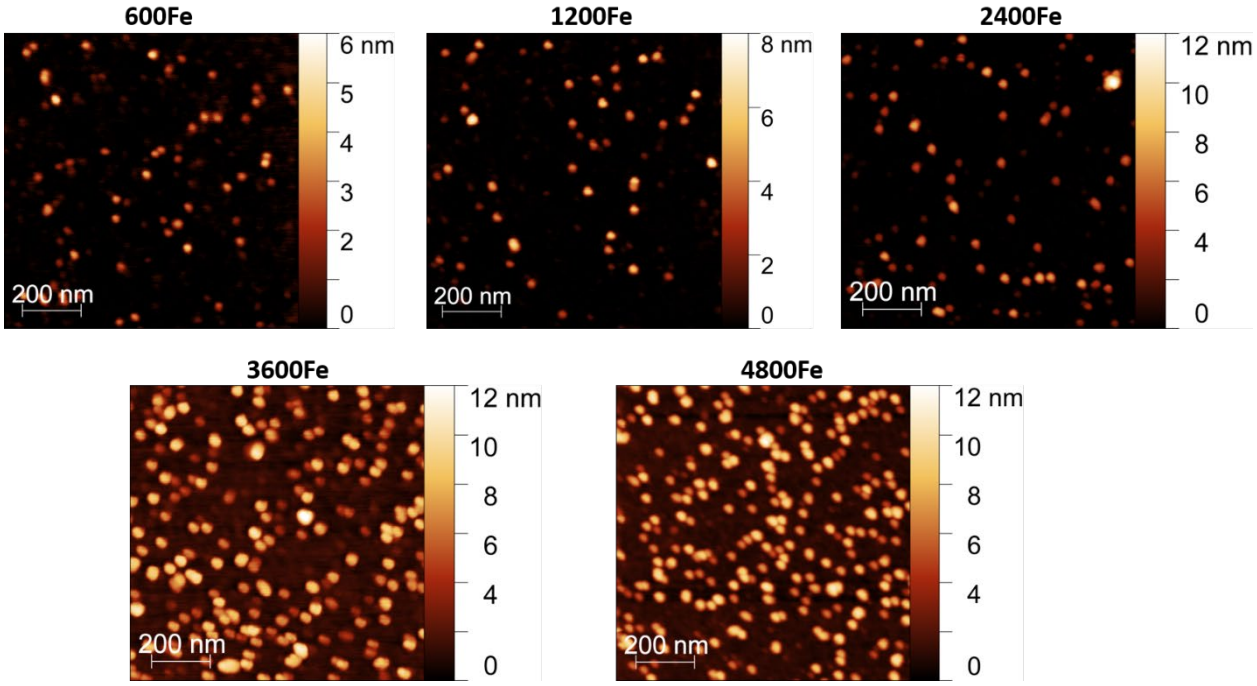

Figure S12: Topography images (1 µm²) of ferritin (AfFtn-AA) with different iron content on silicon obtained by KPFM.

2. Calculation of the enlargement of AfFtn-AA nanocage

The Figure S13 below shows a simple representation of two ferritin nanocages with different loading immobilized on a surface. For a constant perimeter, but with a lower height, the low loaded ferritin undergoes an enlargement.

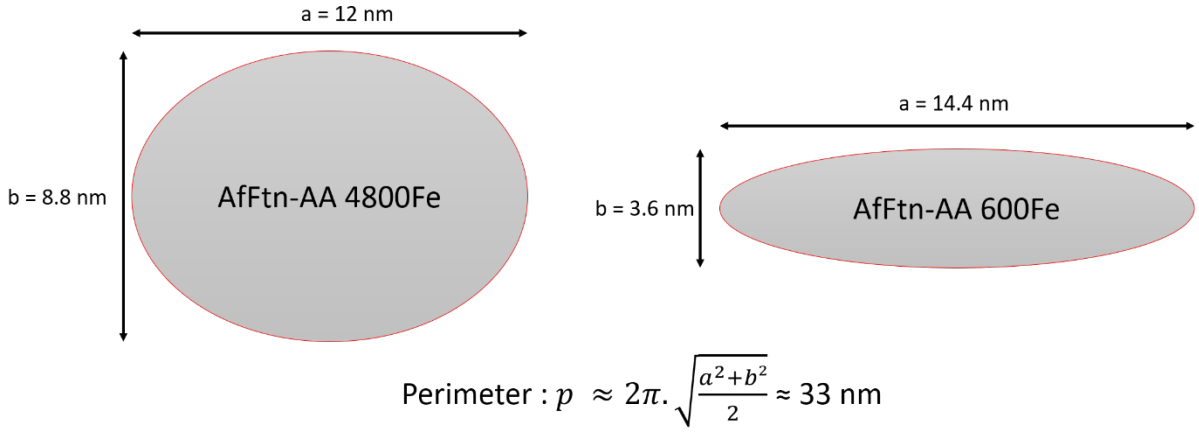

Figure S13: Schematic of a ferritin nanocage loaded with, 4800Fe (left) and 600Fe (right). The circumference (perimeter) of the two ferritins remains equals (≈ 33 nm). The height values b are from the topography.

3. CPD images of AfFtn-AA nanocages on silicon

The CPD images obtained from KPFM measurements of ferritin (AfFtn-AA) on silicon are shown below (Figure S14). Images show a 1 µm² area of the sample surfaces where AfFtn-AAs have been deposited. The average CPD values in the main text are computed from the Figure S14.

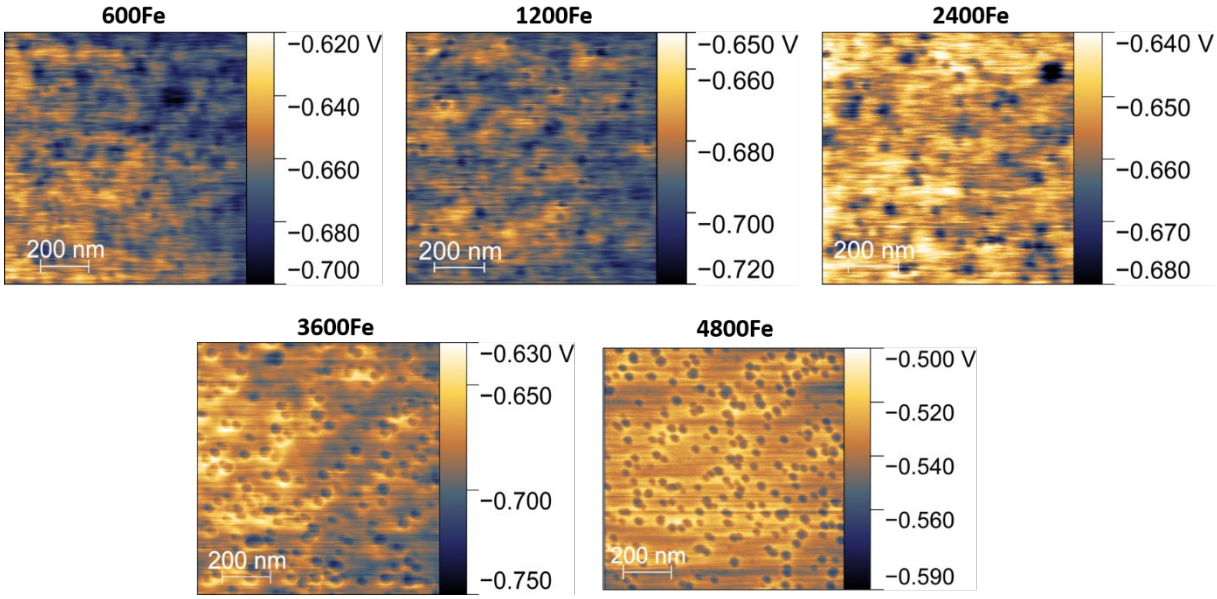

Figure S14: Relative CPD images (1 µm²) of ferritin with different iron content deposited on silicon obtained by KPFM measurements.

4. Topography and CPD images of AfFtn-AA nanocages and FeNPs monolayers

Topography and CPD images obtained from KPFM measurements of AfFtn-AA monolayers and FeNPs deposited on silicon are shown below (Figure S15). Images show a 5 µm² area of the samples surface where ferritins and FeNPs have been deposited as a monolayer. The CPD profiles in the main text are from the CPD images, and profiles are taken perpendicular to the silicon/AfFtn-AA boundaries.

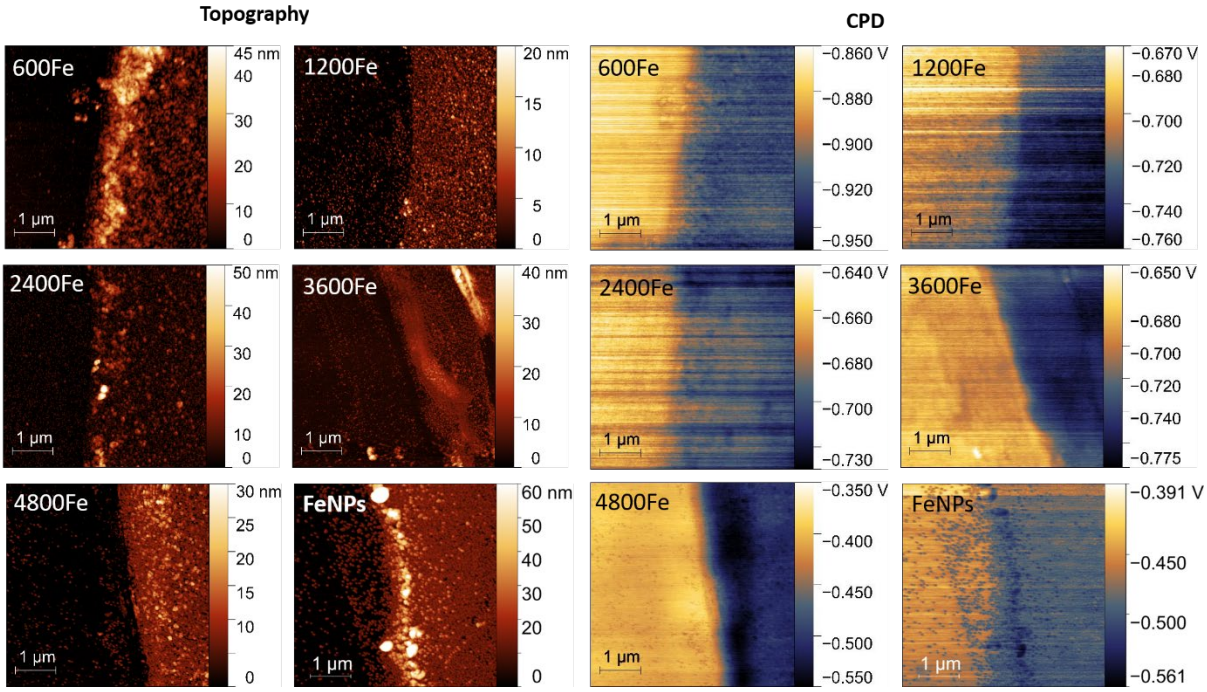

Figure S15: Topography (left) and relative CPD (right) images (5 µm²) of ferritin monolayer with different iron content and FeNPs deposited on silicon, obtained by KPFM measurements.

Appendices – Chapter VI

1. Mutation of amino acid with PyMol

The numerical mutations of AfFtn-AAs were carried out with the Mutagenesis plugin of the PyMol. We used a script (in Python language) that is displayed in the Figure S16.

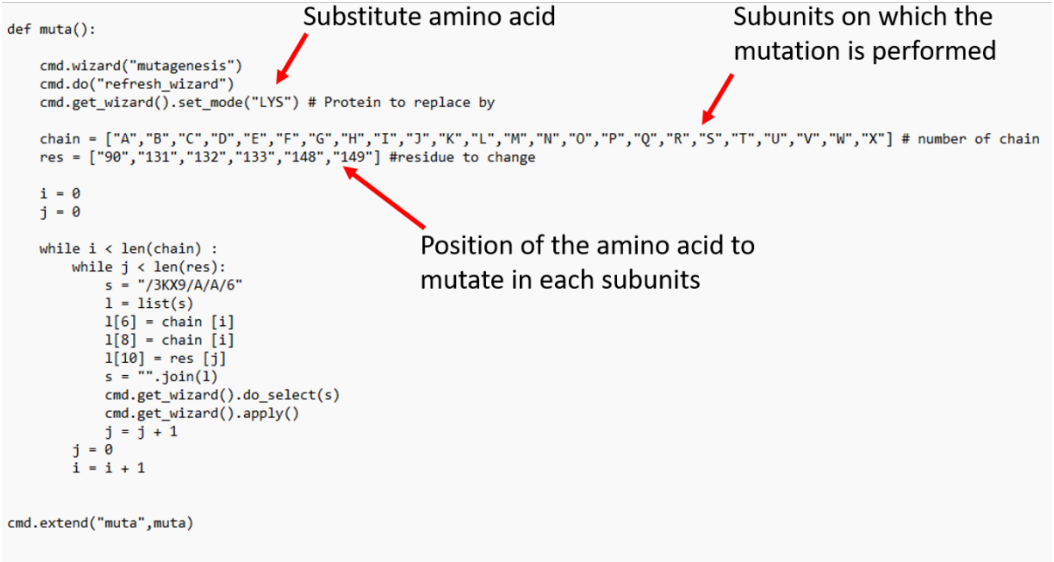


```
def muta():

    cmd.wizard("mutagenesis")
    cmd.do("refresh_wizard")
    cmd.get_wizard().set_mode("LYS") # Protein to replace by

    chain = ["A","B","C","D","E","F","G","H","I","J","K","L","M","N","O","P","Q","R","S","T","U","V","W","X"] # number of chain
    res = ["90","131","132","133","148","149"] #residue to change

    i = 0
    j = 0

    while i < len(chain) :
        while j < len(res):
            s = "/3KX9/A/A/6"
            l = list(s)
            l[6] = chain [i]
            l[8] = chain [i]
            l[10] = res [j]
            s = "".join(l)
            cmd.get_wizard().do_select(s)
            cmd.get_wizard().apply()
            j = j + 1
        j = 0
        i = i + 1


cmd.extend("muta",muta)
```

Figure S16: Script for the mutagenesis plugin of the PyMol software.

2. Influence of the LSH on the CPD

In Figure S17 below, are displayed CPD images of the same area measured on a sample of AfFtn-AA 4800Fe immobilized on silicon for 2 hours (monolayer sample). The images are recorded at different LSHs at 10 nm, 15 nm, and 20 nm, showing CPD value of the ferritin compared to the silicon at 124 mV, 128 mV, and 126 mV, respectively. Values are determined from CPD profiles extracted from the three images and displayed on the graphic shown in the figure.

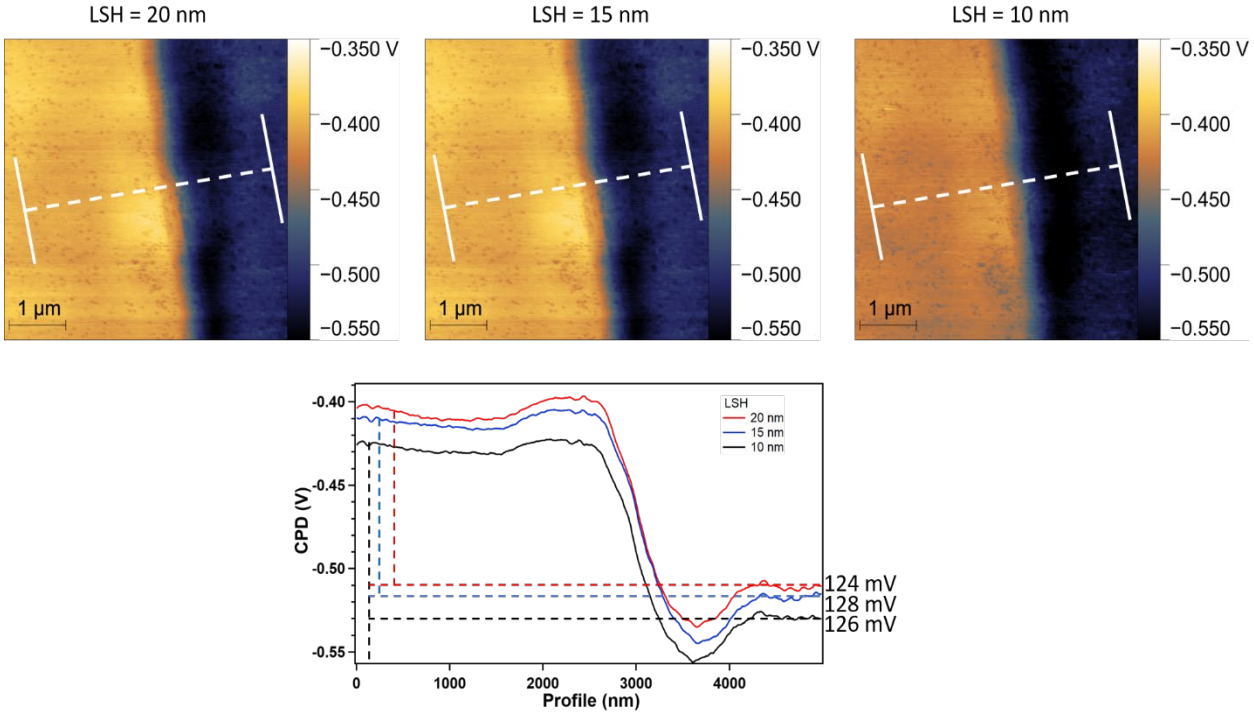

Figure S17. Variation of the CPD as a function of the LSH. At the top are shown CPD images of the same area (5µm²) of an AfFtn-AA 4800Fe monolayer sample, at different LSH = 20 nm (left), LSH = 15 nm (center), and LSH = 10 nm (right). At the bottom are shown CPD profiles taken from the CPD images (from the white dashed line) across the ferritin monolayer silicon intersection. The values of the ferritin CPD compared to the silicon CPD are shown to the right of the graphic for each LSH value.

Résumé :

Les nanocages de ferritine sont des protéines omniprésentes et largement connues pour leur capacité à manipuler des atomes de fer à l'intérieur de nombreuses espèces vivantes. Cette protéine possède une architecture unique composée d'une coquille d'acide aminé avec un noyau de fer et est apparue comme un candidat attrayant pour être incorporée dans un dispositif électrique (jonction, transistor à l'état solide). L'objectif de cette thèse est de caractériser les propriétés électrostatiques, les états de charge et les interactions avec une surface semi-conductrice des ferritines pour l'électronique biomoléculaire. De plus, la surface globale de la ferritine (naturellement chargée négativement) peut être modulée par des techniques de bio-ingénierie (mutagénèse dirigée) pour être chargée positivement. Au cours de cette thèse, les nanocages de ferritine ont été produits et bio-ingéniés dans le laboratoire de NTU à Singapour, et ont été caractérisés en solution à l'aide de techniques de diffusion de la lumière (ELS, DLS). Les mutations des ferritines ont été réalisées en remplaçant les acides aminés négatifs par des acides aminés positifs, et les ferritines mutantes ont montré un décalage de leur point isoélectrique (IEP). Afin d'étudier le comportement électrostatique des protéines de ferritine sur une surface solide, elles ont été déposées sur un substrat de silicium dopé, et les surfaces des échantillons ont été scannées par la microscopie de force à sonde de Kelvin (KPFM), qui est une technique avancée de la microscopie à force atomique qui mesure simultanément la topographie et le potentiel de surface d'une surface d'échantillon. La caractérisation de la ferritine immobilisée sur une surface de silicium par KPFM révèle un changement de la morphologie de la ferritine (aplatissement) et de ses propriétés électrostatiques (potentiel de surface) en fonction de sa teneur en fer. De plus, ces résultats présentent une nouvelle méthode pour déterminer l'orientation et la conformation des protéines directement sur une surface solide en mesurant leur dipôle électrique. Pour les ferritines mutées, le potentiel de surface mesuré par KPFM ne montre aucun changement dans le signe de la charge de surface (de négatif à positif), mais des changements significatifs sont perceptibles et indiquent la modulation de la charge de surface des ferritines mutées. Cette étude donne un bon aperçu de l'incorporation possible de la ferritine dans des dispositifs électroniques. Pour cela, d'autres interactions électrostatiques restent à étudier lorsqu'une nanoparticule est déposée sur un semi-conducteur, comme la formation d'une barrière Schottky, qui a été étudiée au cours de cette thèse avec une particule modèle (nanoparticules d'or de 50 nm) déposée sur du silicium et mesurée par KPFM. Sur la base de l'étude électrostatique de la ferritine (et des nanoparticules d'or), l'une des prochaines idées serait de réaliser une monocouche mixte active de ferritine positive et négative qui serait déposée sur une structure pseudo-MOSFET. La modification du rapport entre les particules positives et négatives modulera le courant source-drain.

Mots clés : Ferritines, Mutations, KPFM, potentiel de surface, comportement électrostatique

Abstract :

Ferritin nanocages are ubiquitous proteins, widely known for their ability to handle iron atoms inside many living species. This particular protein has a unique architecture made of an amino acid shell with an iron core and has appeared as an attractive candidate to be incorporated into an electrical device (junction, solid-state transistor). The goal is to characterise the electrostatic properties, charge states, and interactions with a semi-conductor surface of ferritins for biomolecular electronics. Furthermore, the overall surface of ferritin (naturally negatively charged) can be modulated through bioengineering techniques (site-directed mutagenesis) to be positively charged. During this thesis, the ferritin nanocages were produced and bioengineered in the NTU laboratory in Singapore, and were characterised in solution using light scattering techniques (ELS, DLS). The mutations of the ferritins were performed by substitution of negative amino acids with positive ones, and the ferritin mutants showed a shift in their isoelectric point (IEP). In order to study the electrostatic behaviour of the ferritin proteins on a solid surface, they were deposited on a doped silicon substrate, and the sample surfaces were scanned by Kelvin Probe Force Microscopy (KPFM), which is an advanced technique of the atomic force microscopy that simultaneously measures the topography and the surface potential of a sample surface. The characterisation of ferritin immobilized on a silicon surface by KPFM reveals a change in the ferritin morphology (flattening) and electrostatics properties (surface potential) as a function of their iron content. Moreover, these results present a new method to determine the orientation and conformality of proteins directly on a solid surface by measuring their electric dipole. For the mutated ferritins, the surface potential measured by KPFM showed no change in the sign of the surface charge (from negative to positive), but significant changes are noticeable and indicate the modulation of the surface charge of the mutated ferritins. This study gives strong insight into the possible incorporation of the ferritin inside electronic devices. For this, other electrostatic interactions remain to be studied when a nanoparticle is deposited on a semi-conductor such as the formation of a Schottky barrier, which was investigated during this thesis with a model particle (50 nm gold nanoparticles) deposited on silicon and measured by KPFM. Based on the electrostatic study of the ferritin (and gold nanoparticles), one of the next ideas would be to achieve an active mixed monolayer of positive and negative ferritin that will be deposited onto a pseudo-MOSFET structure. The change in the positive/negative particle ratio will modulate the source-drain current.